THESE DE DOCTORAT

Présentée à

L'UNIVERSITE DE LILLE

Ecole Doctoral Sciences Pour l'Ingénieur Lille Nord-de-France

Pour obtenir le grade de

DOCTEUR EN SCIENCES

Dans la spécialité:

Electronique, microélectronique,nanoélectronique et micro-ondes

par

YUAN ZHANG

PREPARTION OF MULTI-METAL SULFIDES FOR ELECTROCHEMICAL SUPERCAPACITORS

PREPARATION DE SULFURES MULTIMETALLIQUES POUR SUPERCONDENSATEURS ELECTROCHIMIQUES

Directeur de thèse:

Dr. Rabah BOUKHERROUB

Co-directrice de thèse:

Prof. Sabine SZUNERITS

Soutenue le 02 July 2020 devant le jury composé de

Prof. Thierry DJENIZIAN	Rapporteur	Ecole Nationale Supérieure des Mines de Saint-Etienne
Prof. Nathalie JOB	Rapporteur	University of Liège
Dr. Mathieu MORCRETTE	Président	Université de Picardie Jules Verne
Prof. Sorin MELINTE	Examinateur	Université Catholique de Louvain

ABSTRACT

In recent years, electrochemical supercapacitors (ESs), as environmentally-friendly energy storage systems, are facing several challenges associated with the performance, functionality, and durability of key materials. Among different types of ESs, hybrid supercapacitors, the combination of electrodes with different energy storage mechanisms, especially the combination of electrochemical double layer capacitance (EDLC) and battery-type behavior, are expected to offer enhanced electrochemical performance.

Concerning hybrid supercapacitors consisting of EDLC//battery-type electrode materials, carbonaceous materials, owing to their excellent electrical conductivity, electrochemical stability, and large specific surface area, are the most promising candidates for electrode materials with EDLC-type behavior. For electrode materials with battery-type behavior, owing to the faradaic charge transfer reactions involved in the electrochemical process, transition metal compounds can store plenty of energy and represent one of the most promising candidates for electrode materials with battery-type behavior.

In this thesis, different carbonaceous materials, such as reduced graphene oxide (rGO), porous reduced graphene oxide (PrGO), and poly-ethylene dioxythiophene-Fe-900 (PF-9), are prepared through chemical oxidation and reduction methods. Moreover, transition metal compounds, such as CoS/carbonaceous support (rGO or PF-9), ZnCoS, ZnS/Ni_3S_2 and Sb_2S_3/CoS_2/CrOOH, are synthesized *via* chemical co-precipitation and ion-exchange method.

A variety of different techniques, including XPS, SEM, ICP-AES, TEM, XRD, BET, and Raman, are used to investigate the physicochemical performance of as-prepared materials. Their corresponding electrochemical performance is also evaluated through a 3- electrode system. Additionally, hybrid supercapacitors consisting of as-prepared carbon and transition metal electrodes are assembled, respectively, and their electrochemical performance is evaluated through the 2- electrode system.

Key words: Electrochemical capacitors, Supercapacitors, Energy-storage, Electrode materials, Metal sulfides, Transition metal compounds, Oxyhydroxydes

RÉSUMÉ

Ces dernières années, les supercondensateurs électrochimiques (SE), en tant que systèmes de stockage d'énergie respectueux de l'environnement, sont confrontés à plusieurs défis liés aux performances, à la fonctionnalité et à la durabilité des matériaux clés. Parmi les différents types de supercondensateurs électrochimiques, les supercondensateurs hybrides combinent des électrodes avec différents mécanismes de stockage. En particulier, la combinaison d'électrodes à double couche (EDLC) et de type batterie devrait offrir une performance électrochimique améliorée.

En ce qui concerne les supercondensateurs hybrides à comportement EDLC // type batterie, il a été largement reconnu que les matériaux en carbone, en raison de leur excellente conductivité électrique, de leur stabilité électrochimique et de leur grande surface spécifique, sont les candidats les plus prometteurs pour les matériaux d'électrode avec un comportement de type EDLC. En ce qui concerne les matériaux d'électrodes ayant un comportement de type batterie, il a été prouvé qu'en raison des réactions de transfert de charge faradiques impliquées dans le processus électrochimique, les matériaux à base de métaux de transition ont la capacité de stocker beaucoup de l'énergie et sont des candidats prometteurs pour les matériaux d'électrodes avec un comportement de type batterie.

Dans cette thèse, différents matériaux d'électrodes en carbone, tels que l'oxyde de graphène réduit (rGO), l'oxyde de graphène réduit poreux (PrGO) et le polyéthylène-dioxythiophène-Fe-900 (PF-9), ont été préparés par une méthode d'oxydation et de réduction chimiques. De plus, des matériaux d'électrodes composés de métaux de transition, tels que CoS / support carboné (rGO ou PF-9), ZnCoS, ZnS / Ni_3S_2 et Sb_2S_3 / CoS_2 / CrOOH ont été synthétisés par co-précipitation chimique et méthode d'échange d'ions.

Une variété de techniques différentes (MES, MET, DRX, XPS, ICP-AES, BET, Raman) ont été utilisées pour caractériser les propriétés physico-chimiques des matériaux d'électrodes ainsi préparés. Leur performance électrochimique est également évaluée dans une cellule à 3 électrodes. Enfin, des supercondensateurs hybrides ont été assemblés et leur performance électrochimique a été évaluée dans un système à deux électrodes.

Mots clés: Condensateurs électrochimiques, Supercondensateurs, Énergie-Stockage, Électrodes-Matériaux, Sulfures Métalliques, Métaux De Transition-Composés, Oxyhydroxydes

ACKNOWLEDGEMENTS

This research work is carried out in the NanoBioInterfaces (NBI) group at the Institute of Electronics, Microelectronics and Nanotechnology (IEMN, UMR CNRS8520). I would like to express my deepest gratitude to all those people who have helped and encouraged me in the successful completion of my doctoral study.

First and foremost, I would like to give my most sincere thanks to my supervisors, Dr. Rabah Boukherroub and Professor Sabine Szunerits, for their guidance, kindness, stimulating discussion, continued advice, and permanent support over the past four years, as well as the time and patience they spent in reading and correcting the manuscript of this dissertation. With their enormous help and supervision, I have obtained a lot of precious research experience such as scientific thinking, knowledge in chemistry and materials, as well as laboratory techniques. It is truly a great pleasure and privilege to study under their mentorships.

My special thanks goes to Professor Ning Cao from China University of Petroleum. Professor Cao is such as a virtuous, kind and generous mentor who provided me with guidance, encouragement and support for my study and career plans. I respect and appreciate him very much.

I would like to express my thanks to Professor Thierry Djenizian and Professor Nathalie Job for accepting to be the reviewers of the manuscript of my thesis and the committee members of my defense. I'm so grateful for their time and precious opinions. I would like to sincerely thank Dr. Mathieu Morcrette and Professor Sorin Melinte for accepting to be the committee members of my defense. I truly appreciate your time and your helpful comments.

My heartfelt thanks go to all my colleagues for all the help, discussions, and sharing. Thanks for all those generous help and valuable advice.

I would like to thank my friends, Pang Liuqing, Li Min, Miao Yuanyuan, Xu Yanni, Yan Xiang … for their friendship and big support.

In particular, I wish to thank the China Scholarship Council (CSC), which offered me the opportunity to pursue my PhD study in France.

Finally, my parents and husband are always there for me with their supports and unconditional love throughout, for which my mere expression of gratitude does never suffice.

ZHANG Yuan

ACKNOWLEDGEMENTS

Villeneuve d'Ascq, France

25/04/2020

TABLE OF CONTENTS

ACRONYMS

ASCs	-	Asymmetric supercapacitors
BET	-	Brunauer-Emmett-Teller
C	-	Pseudocapacitance
C_F	-	Faradaic capacitance
C_L	-	Limit capacitance
CNTs	-	Carbon nanotubes
CPE	-	Constant phase element accounting for the faradaic pseudocapacitor capacitance
CPs	-	Conducting polymers
CTAB		Cetyltrimethylammonium bromide
CV	-	Cyclic voltammerty
CVD	-	Chemical vapor deposition
DFT	-	Density functional theory
E_d	-	Energy density
EDLC	-	Electrochemical double layer capacitance
EDOT		3,4-Ethylenedioxythiophene
EIS	-	Electrochemical impedance spectroscopy
EG	-	Ethylene glycol
ESs	-	Electrochemical supercapacitors
GCD	-	Galvanostatic charge/discharge
GO	-	Graphene oxide
HSCs	-	Hybrid supercapacitors
ICP-AES	-	Inductively coupled plasma atomic emission spectroscopy
LDH	-	Layered double hydroxide
NMP	-	N-Methyl-2pyrrolidone
P_d	-	Power density
PF-9	-	Poly-ethylene dioxythiophene-Fe-900

PrGO	-	Porous reduced graphene oxide
PVDF	-	Polyvinylidene fluoride
PVP	-	Poly(N-vinylpyrrolidone)
R_{ct}	-	Charge transfer resistance
rGO	-	Reduced graphene oxide
R_s		Series resistance
SAED	-	Selected area electron diffraction
SCs	-	Symmetric supercapacitors
SEM	-	Scanning electron microscopy
SSA	-	Specific surface area
TAA	-	Thioacetamide
TEM	-	Transmission electron microscopy
W	-	Warburg resistance (diffusion resistance)
XPS	-	X-ray photoelectron spectroscopy
XRD	-	X-ray diffraction

GENERAL INTRODUCTION

In recent years, electrochemical supercapacitors (ESs), as environmentally-friendly energy storage systems, are facing several challenges associated with the performance, functionality, and durability of key materials. It has been widely recognized that advanced transition metal-based electrode materials, such as metal sulfides, oxides/hydroxides, selenides, and phosphides, and so on, can store much more energy than that of carbon materials, owing to the faradaic charge transfer reactions involved in the electrochemical process. Therefore, these advanced transition metal-based electrode materials have been extensively studied to overcome the major challenges cited above and achieve breakthroughs in practical applications.

In this PhD thesis, a general review on ESs, including brief history and background, structures, energy storage principle, characteristic features and electrode materials, allows to gain a better understanding on the performance evaluation criteria of different types of ESs as well as different energy storage mechanisms of the corresponding electrode materials. From this review study, the literature data revealed that the combination of electrochemical double layer capacitors (EDLC), commonly carbon materials, and Faradaic battery-type characteristics (transition metal based electrode materials) represents an appealing and promising configuration to achieve high performance, owing to the high energy storage of batteries, and high power and long lifetime of EDLC. Thus, the development of two types of electrode materials with improved performances relative to existing electrode materials is the most important approach to overcome these challenges (**Chapter 1**).

Among various transition metal-based electrode materials, cobalt sulfide (CoS_x), a promising anode material for lithium ion batteries, exhibiting multi-valence states and a theoretical capacity of 870 mA h g^{-1}, has attracted our attention. In **chapter 2**, we described the preparation of CoS-based electrode materials by chemical precipitation and ion-exchange process, evaluated their electrochemical performance and identified their shortcomings. Based on the discussion on transition metal electrode materials, the construction of composites and multi-metal compounds are regarded as the most promising strategy to prepare electrode materials with improved electrochemical performance. Therefore, by introducing different types of conducting carbonaceous matrixes (reduced graphene oxide (rGO) or poly-ethylene dioxythiophene (PEDOT)-Fe-900 ℃ (PF-9)), the electrochemical performance of the composite electrode materials (CoS/rGO, CoS/PF-9) was evaluated.

The performance of the synthesized composite electrode materials was assessed using different electrochemical techniques and the results revealed that the composite materials exhibited improved electrochemical performance, but not remarkable. Therefore, in the following step, we evaluated the electrochemical performance of multi-metal sulfides by introducing different metal cations. ZnS, a wide band gap material (3.5-3.8 eV), has attracted our attention. Owing to the high theoretical capacity of CoS_x, ZnCoS electrode materials were synthesized by introducing Co into the ZnS lattice and the results indicated that ZnCoS electrode materials exhibit a remarkable electrochemical performance (**Chapter 3**).

In **chapter 4**, we have examined Ni-based sulfide electrode materials, owing to their rich oxidation states, high theoretical capacity (873 mA h g-1 for NiS2) and cost effectiveness. Some published results have demonstrated that Ni-based bimetal sulfides electrode materials could provide enhanced electrochemical performance. Therefore, bi-metal (ZnS/Ni_3S_2) composites were prepared and their electrochemical performance was assessed.

Based on our previous work, bi-metal sulfides proved to exhibit an enhanced electrochemical performance than mono metal sulfides. In addition, transition metal oxy-hydroxides have also been regarded as one of the most promising electrode materials. However, little work was focused on employing the composites of transition-metal sulfides and oxides as electrode materials for SCs. Hence, $Sb_2S_3/CoS_2/CrOOH$ composite materials were synthesized and investigated as electrode materials for SCs. The results indicated that these electrode materials could achieve an enhanced electrochemical performance (**Chapter 5**).

CHAPTER 1. INTRODUCTION

The utilization of renewable and clean energy sources is expected to decrease our reliance on non-renewable fossil fuels. However, the bottleneck for their practical application is that they will influence the power system if being integrated to the grid directly because most of them are weather or geographic dependent. The best way will be to store this energy before being connected to the network. Therefore, worldwide attention and increasing research interests have been paid to develop highly efficient, low cost, and environmentally friendly energy storage systems.

Based on advantages such as high efficiency, versatility, and flexibility, electrochemical energy storage systems (Electrochemical supercapacitors (ES), Batteries, and fuel cells) are believed to be one of the most promising candidates for energy storage devices[1]. Among them, electrochemical supercapacitors (ESs), as convenient electrochemical energy storage devices, have attracted substantial attention owing to their higher specific capacitance/capacity compared to traditional capacitors, high power storage capability, and much higher charging/discharging rate capability efficiency than primary/secondary batteries [2]. They have additional advantages, such as almost maintenance-free, no memory effect, and safe as the bridging function for power/energy gap between traditional dielectric capacitors (high power) and batteries/fuel cells (high energy storage) [3]. These advantages propelled ES devices at the forefront of growth in mobile electronic devices, smart grids, and so on. ESs also present the possibility of providing energy in specific areas where public grids are not available or where heavy cost comes from wiring for providing electricity.

1.1 Historical background of ESs

The beginning of capacitor technology goes back to the invention of Leyden Jar (1745) (**Fig. 1.1**), which consists of a glass jar with metal foil cemented to the inside and outside surfaces [4]. The metal foil and jar acted as electrodes and a dielectric plate, respectively. In the charging process, positive charges accumulated on one electrode and negative charges on the other. A discharging process would take place after these two charges were connected using a metal wire. Until 1879, the description of the capacitive performance of an electric double-layer was first made by Hermann von Helmholtz. However, the first ES patent (electrochemical double-layer supercapacitors-EDLC) was filed by Becker at the General Electric Corporation in 1957 [5]. After Becker, researchers in Sohio Corporation developed the first electric double-layer

capacitor for commercial purposes using porous carbon in a non-aqueous electrolyte in 1969 [6]. The first commercial application of the supercapacitor product for the memory back up device was licensed by Nippon Electric Company (NEC) in 1971 [2]. Further developments revealed that ES could be an important candidate in the field of energy storage by bridging the power/energy gap between traditional dielectric capacitors and batteries/fuels. During 1975-1980, B.E. Conway explored RuO_2 pseudo-capacitors extensively [3]. It was only in the 1990s that ES technology started to attract attention in the field of hybrid electric vehicles. Today, many companies such as ECOND, ELTRAN, and SAFT, and NESS and several others invested massively in ESs.

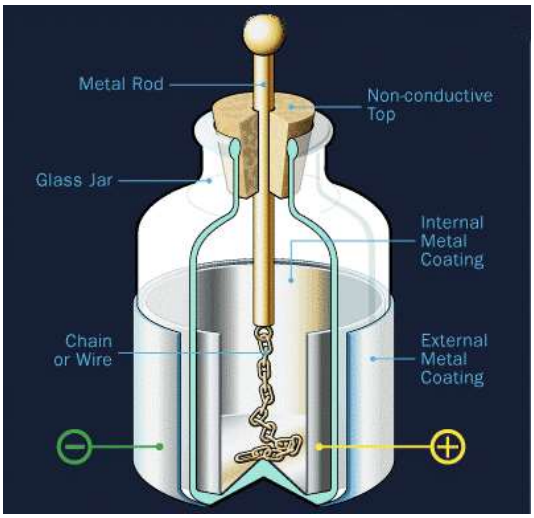

Figure 1.1: The Leyden jar [4].

Although significant major progress has been made in theoretical and practical research for the development of ESs. The disadvantages of ESs, including low energy density (E_d) and high production cost, have still been identified as major challenges for the further development of ESs technologies [3]. It is well known that the performance of ES devices (energy and power density) is dominated by the active materials chosen. Therefore, understanding of the characteristic behavior of active materials at atomic and molecular levels will provide an important future direction for improving these shortcomings. In the following part, the energy storage mechanism of active materials and ES fundamentals will be introduced in detail.

1.2 Fundamentals, classifications and applications of ESs

An ES storage device is generally made up of two electrodes (collectors with active materials), an electrolyte, and a separator that electrically isolates the two electrodes (**Fig. 1.2**).

The two electrodes are insulated by the separator and impregnated with the electrolyte. The separator only allows the mobility of ions but prevents the direct contact of the two electrodes.

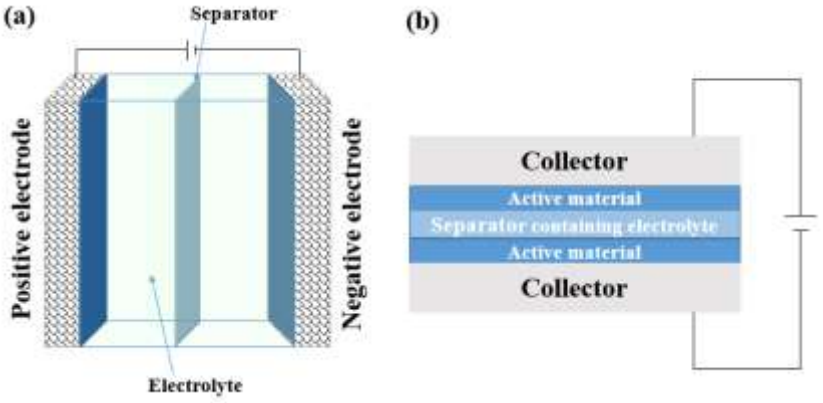

Figure 1.2: Schematic representation of an ES configuration (a) and the ES structure (b).

1.2.1 Energy storage mechanism

In this part, the charge storage mechanism of different electroactive materials including electrical double layer capacitance (EDLC), pseudo-capacitance and battery-type capacity will be discussed.

1.2.1.1 Electrochemical double layer capacitance (EDLC)

The behavior of EDLC electrode materials in ES devices is associated with an electrode-potential-dependent accumulation of electrostatic charges at the interface. The mechanism of surface electrode charge generation includes surface dissociation as well as ion adsorption from both the electrolyte and crystal lattice defects. These processes operate solely on the electrostatic accumulation of surface charge. As shown in **Fig. 1.3a**, this electrical double-layer capacitance arises from electrode material particles at the interface between the carbon particles and electrolyte, where excess or deficit of electric charges is accumulated on the surface of an electrode, and electrolyte ions with counterbalancing charge are built upon the electrolyte side to meet electro-neutrality.

During the process of charging, the electrons travel from the negative electrode to the positive electrode through an external load. Within the electrolyte, cations move towards the negative electrode, while anions move towards the positive electrode. During discharge, the reverse processes take place. In this way, the electrical energy of such a supercapacitor is supposed to be stored in the double-layer interface through a reversible ion adsorption process, and this process also acts on the electrostatic accumulation of surface charges. The performance

of EDLC is associated with the accumulation of electrostatic charges at the surface or inside pores of electrodes.

In this type of ESs, no charge transfers across the electrode/electrolyte interface, and net ion exchanges occur between the electrode and the electrolyte. This implies that the electrolyte concentration remains constant during the charging and discharging processes. Moreover, the performance of EDLC electrode materials are characterized by nearly rectangular cyclic voltammetry (CV) curves and triangle galvanostatic charge-discharge (GCD) curves (**Fig. 1.3b**).

It is important to note that the EDLC-type behavior is due to the adsorption of Colombian charge near the electrode-electrolyte boundary. The capacitance is measured using the general capacitance equation 1-1 [7]:

$$C = \frac{A \times \epsilon_0}{d} \qquad 1\text{-}1$$

Where C denotes the capacitance measured in farads, A the surface area, ϵ_0 the permittivity of free space, and d the effective thickness of the electric double layer also termed as Debye length.

The thickness of the double layer (d) is associated with the electrolyte concentration and size of ions. This value ranges from 5 to 10 Å for concentrated electrolytes [7]. To increase the capacitance value of EDLC, one has to put efforts in increasing the values of specific surface area (SSA). Thus, the electrode materials with high specific surface area (SSA) are required to obtain supercapacitors with good performance.

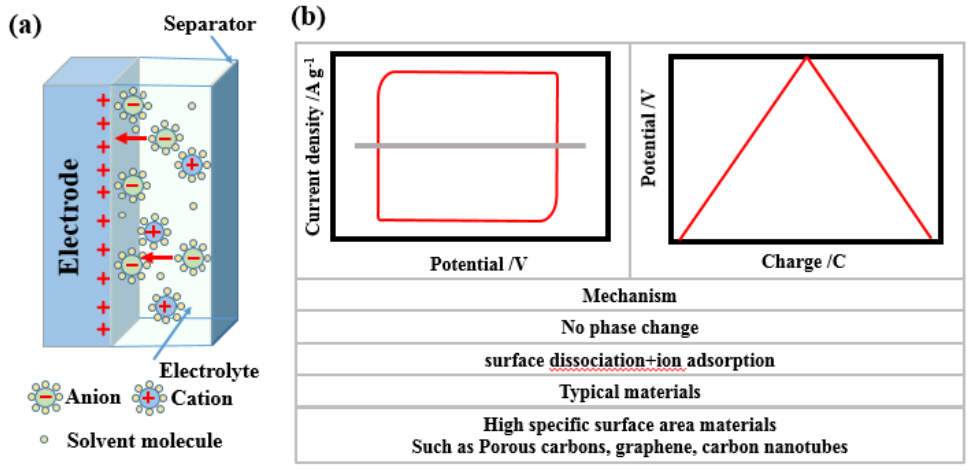

Figure 1.3: The schematic illustration of electrical double layer capacitance (EDLC) (a), summary of characteristic metrics such as CV, GCD, key mechanism descriptions and typical materials (b) [8, 9].

1.2.1.2 Pseudo-capacitance

"Pseudo-capacitance" describes the properties of electrode materials (RuO_2, MnO_2) displaying a capacitor-type behavior in their electrochemical signature. When a potential is applied to this type of electrode, a fast and reversible faradic reaction takes place on the electrode material and involves the passage of charge across the double layer. This type of electrode material has the electrochemical signature of a capacitive electrode (carbon materials), while the charge storage originates from different reaction mechanisms, including surface redox reactions and intercalation mechanism (**Fig. 1.4a and b**) [10].

Concerning surface redox pseudo-capacitance process, it normally stores charges through adsorption-desorption of electrolyte cations and anions on the surface of electrode material where faradic redox reactions occur. Materials dominated by surface redox pseudo-capacitance behave just like EDLC based materials with nearly rectangular CV curves (**Fig. 1.4 c**). The electrode materials exhibiting pseudo-capacitance behavior are mainly comprised of metal oxides/sulfides and conductive polymers.

The energy storage process in the intercalation pseudo-capacitance process involves reversible intercalation/de-intercalation of electrolyte cations (Na^+, K^+, Li^+, H^+, etc) into the crystal structure of electrode materials (**Fig. 1.4 b**), and it should be noted that no material phase change occurs in the intercalation pseudo-capacitance process. Materials dominated by intercalation pseudo-capacitance behave could be distinguished through the broad redox peaks observed in CV curves.

The pseudo-capacitance behavior takes place at the electrode surface where the faradic charge storage mechanism applies and the value of C_s is given by the derivative of charge acceptance (Δq) and change in potential (ΔV)[11]:

$$C_s = \frac{d(\Delta q)}{d(\Delta V)} \qquad 1\text{-}2$$

The pseudo-capacitance behavior allows pseudo-capacitors to attain much higher charge storage capacity compared to EDLCs, the capacitance value is 10–100 times more than that of normal EDLCs [7]. However, electrode materials with pseudo-capacitance behavior are more likely prone to swelling and shrinking during the charge/discharge process, and thus lead to poor mechanical stability and low cycling stability.

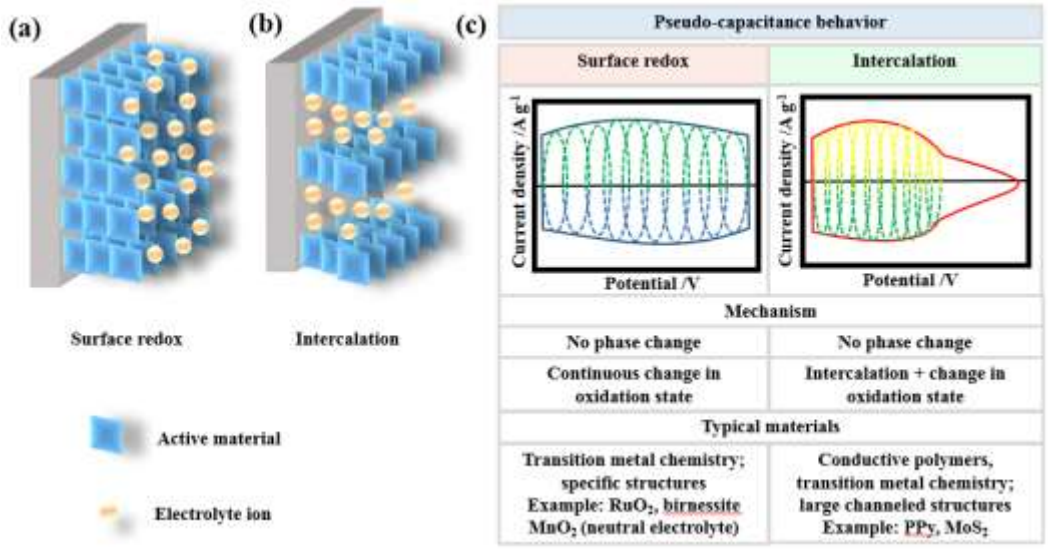

Figure 1.4: The schematic illustration of pseudo-capacitance behavior: (a) surface redox capacitance behavior, (b) intercalation capacitance behavior; (c) summary of characteristic metrics such as CV, key mechanism descriptions and typical materials of corresponding capacitance behavior [8, 12].

1.2.1.3 Battery-type behavior

Despite the definition of pseudo-capacitance, many electrode materials that experience phase change during the charge/discharge process have long been mistreated as pseudo-capacitive materials. Recently, the electrochemistry community has distinguished the difference between electrode materials that present battery-type behavior and that exhibit traditional pseudo-capacitance behavior.

Compared with pseudo-capacitance electrode materials, the electrochemical reactions of battery-type materials are controlled by electrolyte ion diffusion and normally experience "phase-transformation" ion intercalation and/or alloying reactions (**Fig. 1.5a**), which is reflected in the CV curves with obvious redox peaks. To GCD curves, during the charging process, the low valence transition metals are oxidized to higher valence state to release electrons and then reduced to the original state in the reverse discharging process. Therefore, the low valence compounds experience at least one phase change in each charge and discharge process, resulting in the occurrence of the potential plateau in GCD curves [13]. Based on the new definition, electrode materials that present potential plateau during charge/discharge electrochemical process and obvious redox CV peaks should belong to "battery-type" electrode materials (**Fig. 1.5b**).

For the evaluation of charge storage ability, like batteries, battery-type electrode materials usually provide high charge storage capacity. Furthermore, the battery-type electrode materials

with specially designed nanostructures are expected to possess a high specific surface area and afford abundant active sites for redox reactions and shorter distance for the diffusion of electrolyte ions. However, low rate performance and poor cycling stability due to the sluggish kinetics associated with the slow material phase transformation could also be detected during the process of charge/discharge.

In contrast to EDLC- and pseudo-capacitance-type behavior, the concept of "capacitance (F)" is not suitable for battery-type behavior. Based on previous reports, capacitance is the ability of a body to store an electrical charge. This capacitance is constant over a given potential window and can be used to calculate the charge stored using equation **1-2**. However, the "capacitance" of a battery-type electrode is definitely not constant over the whole potential window available, and the value of "capacitance" corresponds to an "average" value calculated over a limited potential window, and if a wider or narrower potential window is chosen, the calculated specific capacitance will change [14]. In this case, "capacity" (mA h or coulomb C) is the most appropriate and meaningful metric to use. The capacity of battery-type electrodes is given by the derivative of charge acceptance (Δq) and change in potential (ΔV) [15, 16]:

$$C\ (mA\ h\ g^{-1}) = \frac{Q}{M} = \frac{I \times \Delta t}{3600 \times M} \qquad 1\text{-}3$$

Where C (mA h g^{-1}) is the specific capacity, Q is the quantity of charge, M (g) is the mass of the active material, I (mA) is the constant discharge current and Δt (s) is the discharge time.

$$C(C\ g^{-1}) = \frac{Q}{M} = \frac{I\Delta t}{M} \qquad 1\text{-}4$$

Where C (C g^{-1}) is the specific capacity, Q is the quantity of charge, M (g) is the mass of the active material, I (A) is the constant discharge current and Δt (s) is the discharge time.

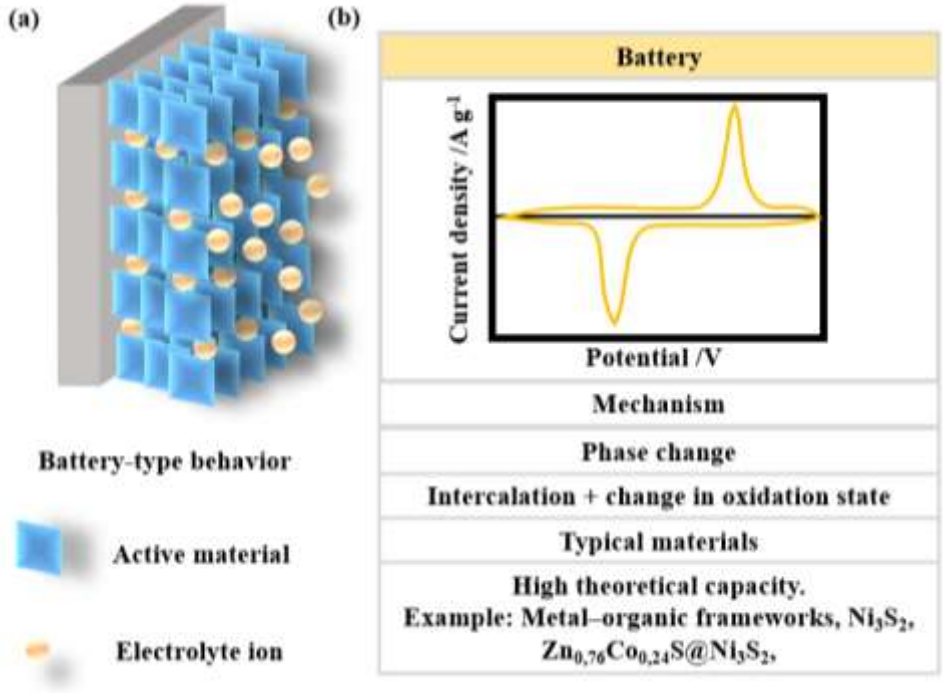

Figure 1.5: (a) The schematic illustration of battery-type behavior, (b) summary of characteristic metrics such as CV, key mechanism descriptions and typical materials [8, 12].

1.2.2 Classification of ESs

Based on the chemical responses and the architecture of an ES device, it could be classified into three types: i) symmetric supercapacitors (SCs), ii) asymmetric supercapacitors (ASCs), and iii) hybrid supercapacitors (HSCs) [8].

Typically, SCs are made up of two electrodes of same weight, thickness, material and so on. Therefore, in designing supercapacitors, it is essential to recognize that SCs might not be optimal. The ES is commonly expected to exhibit optimized performance, thus, ASCs are produced. The ASCs could be optimized through the mass match of positive and negative electrodes (charge balance) (equation **1-5** and **1-6**). This configuration favors their application in energy storage systems [17].

$$q = C \times \Delta E \times M \qquad 1\text{-}5$$

$$\frac{M_+}{M_-} = \frac{C_- \times \Delta E_-}{C_+ \times \Delta E_+} \qquad 1\text{-}6$$

Where q is the stored charges in the electrodes, C (F g^{-1}) is the specific capacitance, ΔE (V) is the working potential window range, and M (g) is the mass of the electrode.

The definition of an ASC is very broad because ACSs are fabricated with different electrodes. This could be two electrodes made up of the different or same material, but having different thicknesses (masses).

In recent years, a more distinct type of ESs (hybrid supercapacitors) is fabricated. In this case, the combination of two different storage mechanisms together constitutes the energy storage mechanism, and it is expected that this type of ESs could offer enhanced performance, as compared with SCs and ASCs. For example, an EDLC-type behavior electrode and a Faradaic battery-type behavior electrode are utilized as negative and positive electrodes, respectively. In this case, one-half of the hybrid supercapacitor acts as EDLC, while the other half behaves as faradic battery-type. In this configuration, hybrid supercapacitors exhibit high energy from batteries and high power and long lifetime from ESs. Furthermore, under the conception of ASCs, the supercapacitor could be optimized through the mass match of positive and negative electrodes (charge balance) (equation **1-5** and **1-6**).

1.2.3 Applications of ESs

As we discussed in the history background of ESs, an increasing number of developers and manufacturers pay attention to the development and utilization of ESs. With the ever-improving performance, there is a constant increasing utilization of ESs in public sector, automobiles and transport, defense and military, and industrial applications (**Fig. 1.6**). Take the applications in electric vehicles as an example, even though the materializing process has been quite slow, a few applications have been commercialized. These include hybrid-electric transit buses in the United States and China, electric braking systems in passenger cars, and recently in stop-go hybrid vehicles [18]. Among them, the fast-charge e-buses introduced by Aowei Technology Co., Ltd (Shanghai, China) can be fully charged within 90 s and drive 7.9 km at a time with an average and maximum speed of 22 and 44.8 km h^{-1}, respectively [7]. In addition, the tramcar working on EDLC configuration with charging time of 30 s and distance range of 3-5 km has been developed by CSR Co. Ltd. (China) [19].

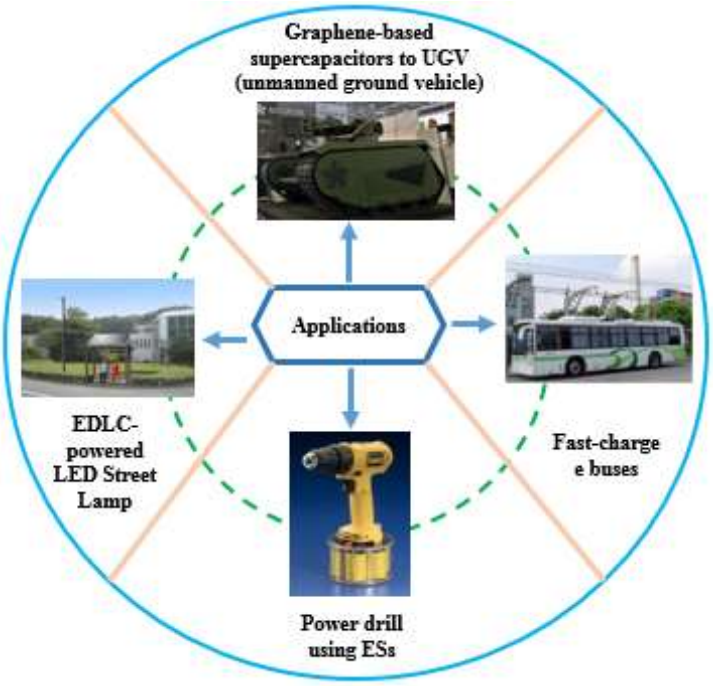

Figure 1.6: Applications of supercapacitors [7, 20, 21].

1.3 Characteristic features of ESs

The concept of the characteristic features of ES devices is necessary to evaluate the performance of corresponding ES devices, and their performance could be investigated through the following two criteria: 1) how much energy it can store (energy density, E_d, in Wh kg^{-1}), 2) how fast the stored energy can be released (power density, P_d, W kg^{-1}). Therefore, the decisive characteristics related to ESs performance are the specific energy and power density; besides, specific capacitance and electrochemical impedance along with other features like cycling stability, rate efficiency, and coulombic efficiency (ŋ) are also important criteria to evaluate the performance of an ES device.

1.3.1 The energy and power densities

Fig. 1.7 compares the energy and power densities of supercapacitors and batteries. Capacitors and batteries (fuel cells) exhibit high power density and high energy density, respectively. SCs, ASCs, and hybrid supercapacitors all provide an improved energy density value along with a high-power density value, as compared with capacitors. Also, hybrid supercapacitors could deliver higher energy density as compared with SCs, ASCs. Furthermore, the energy density provided by hybrid supercapacitors is comparable to that of batteries, indicating their widespread use for next-generation electronics and energy-storage devices. As

a consequence, extensive attention has been paid in the exploration, construction, and development of hybrid supercapacitors.

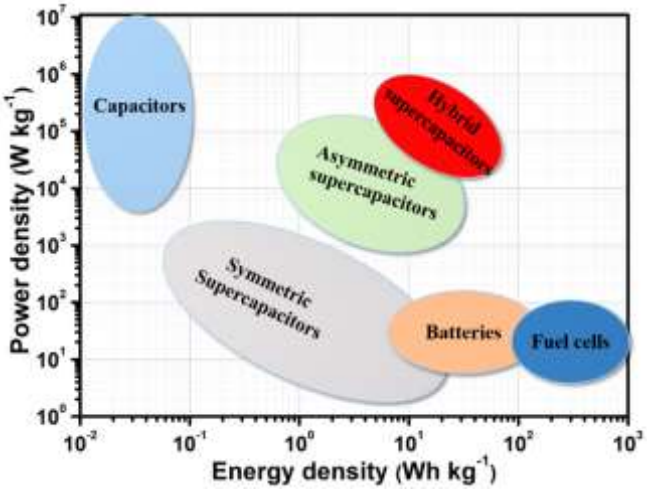

Figure 1.7: Ragone plot comparing the energy and power densities of various capacitors and batteries [22].

In an ES cell, E_d can be evaluated by using equation **1-7**, and the maximum instantaneous power density P_{max} depends on the potential and the internal resistance R as follows [7, 23]:

$$E_d = \int_{t1}^{t2} C(V_1 + V_2)\,(V_2 - V_1) \qquad 1\text{-}7$$

$$P_{max} = \frac{V^2}{4R} \qquad 1\text{-}8$$

$$P_d = \frac{E}{\Delta t} \qquad 1\text{-}9$$

Where E_d (Wh kg^{-1}) is the energy density, C (F g^{-1}) is the capacitance of an ES, and V_2-V_1 (V) is the corresponding potential window of the device, Δt (s) is the discharge time, P_{max} (W kg^{-1}) is the maximum power density, R (ohm cm^{-2}) is the equivalent inner resistance, and P_d (W kg^{-1}) is the power density of the ES device.

Obviously, to improve the values of E_d and P_d of an ES, one has to put efforts in increasing both values of V and C while decreasing the R value. Moreover, the values of both E_d and P_d are proportional to the square of V. Therefore, more efforts should be paid in widening the operating voltage window, V. It is known that the value of V depends on the materials used for the electrode and the chosen electrolyte. Commonly, considering their low cost, aqueous electrolytes are still the best choice. Therefore, the selection of the type of electrode materials

and design of electrodes with optimized structures are the most promising approaches to obtain an extended value of V. With respect to the value of C, an increased value of C could be achieved by improving the specific capacitance of both electrodes; the specific capacitance/capacity of each electrode is dominated by the energy storage mechanism of chosen electrode materials (EDLC-, pseudocapacitance- or battery- type) as well as the corresponding specific surface area. That is to say, the choice of suitable electrode materials, especially battery-type electrode materials, and the development of advanced electrode materials with the large specific surface area should be the key approach in ESs research and development.

1.3.2 Specific capacitance

Specific capacitance (C) is one of the important variables determining the ESs' performance. it can be expressed using the following equation [7]:

$$C = \frac{I}{M(dV/dt)} \qquad 1\text{-}10$$

Where C (F g^{-1}) denotes the specific capacitance, M (g) the total mass of the electrode, I (A) the average current in amperes and dV/dt the potential scanning rate.

1.3.3 Electrochemical impedance spectroscopy (EIS)

It is well known that EIS is an extremely informative method for electrochemical nature (the charge transfer and the capacity) of electrode materials used in electrochemical supercapacitors. Furthermore, the resistance of an ES device, another important variable determining the power density (equation **1-8**), could also be reflected through the EIS measurements at a specific potential. The voltage amplitude for such measurements is low ranging from 5 mV to 10 mV, corresponding to the wide frequency limits between 0.01 Hz and 100 kHz. The series resistance, charge-transfer resistance, and diffusion resistance could be obtained by specific plots (called Nyquist plots) for ESs.

The Nyquist plots are usually made up of three regions (**Fig. 1.8**). The intercept at the region of higher frequency (larger than 10^4 Hz) is assigned to the internal resistance from the electrolyte and the contact between the electrode material and the collector. The second region in the high to medium frequency (10^4 to 10^1 Hz) marking a semicircle in the plots describes the resistance of charge transfer. The third region in the low frequency (less than 1 Hz) presenting a vertical line on the plot represents the capacitive behavior.

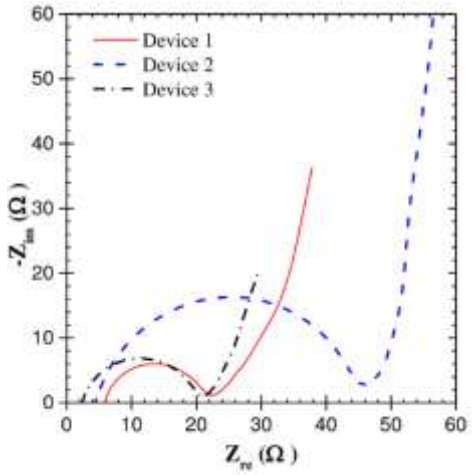

Figure 1.8: Nyquist plots of three experimental EDLC devices with activated carbon electrodes in different electrolytes (1M $LiPF_6$ in EC (Ethylene Carbonate): DMC (Dimethyl Carbonate) (1:1), 1M citric acid in DI water, 1M TEATFB (Tetraethylammonium Tetrafluoroborate) in acetonitrile, corresponding to devices 1, 2 and 3, respectively) [24].

In general, a smaller value for internal resistance indicates a higher instantaneous power density. A smaller value for charge transfer resistance stands for a faster speed for charge transfer.

1.3.4 Coulombic efficiency

Coulombic efficiency (η), also called faradaic efficiency, describes the efficiency with which charge electrons are transferred in a system facilitating an electrochemical reaction, and is determined by the ratio of discharge capacity and charge capacity. Here, the coulombic efficiency of a supercapacitor is given by the following equation [7]:

$$\eta = \frac{t_D}{t_C} \times 100 \qquad 1\text{-}11$$

Where t_D (s) and t_C (s) are the time for discharging and charging processes, respectively.

1.4 Active electrode materials for ESs

As discussed above, the charge storage mechanism and the performance of an ES are closely related to the electrode material. Thus, developing new electrode materials with improved performance relative to existing electrode materials is the most important strategy to overcome challenges such as improving the specific capacitance of EDLC-type capacitance, enhancing the power density of pseudo-capacitance, and boosting the cycling stability of pseudo-capacitance and battery-type capacity. Therefore, to gain a good understanding of electrode

materials and their advantages/disadvantages is of paramount importance. In general, the electrode materials of ES can be categorized into three types: 1) carbon materials, 2) conducting polymers and 3) transition metal-based materials [25].

1.4.1 Carbon materials

Carbon materials are considered as prospective electrode materials for industrialization due to their high availability and advantages including abundance, non-toxicity, higher specific surface area, good electronic conductivity, high chemical stability, and wide operating temperature range [2]. Normally, carbon materials belong to EDLC type behavior electrode materials. Therefore, carbon materials, utilized in the commercially available EDLC supercapacitors, should have a high specific surface area (> 1000 m^2g^{-1}). Onion-like carbon, carbon nanotubes, graphene, activated carbons, and carbide-derived carbons are the most promising candidates [11]. Among them, active carbon, carbon nanotubes, and templated porous carbons and graphene (**Table 1-1**), will be discussed in the following part.

Table 1-1: Properties and characteristics of carbon structures used for ESs [9, 11, 26-31].

Material		Active carbon	Carbon nanotubes	Templated porous carbons	Graphene
Dimensionality		3-D	1-D	3-D	2-D
Conductivity		Low	High	Low	High
Volumetric		High	Low	Low	Moderate
Cost		Low	High	High	Moderate
Capacitance ($F\ g^{-1}$)	Aqueous electrolyte	< 200	50-100	120-350	< 298
	Organic electrolyte	< 100	<60	60-140	120-348
Structure		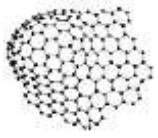	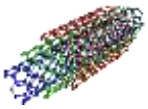		

1.4.1.1 Activated carbon

Activated carbon is a form of carbon processed to have small, low-volume pores that increase the active surface area. It could be obtained from carbon-rich organic precursors after

physical and/or chemical treatment. The precursor of activated carbon is usually from natural renewable resources such as woods, textile products, crop shell, and fossil-fuel-derived such as pitch, coal, or coke. Physical treatment is usually done at high temperatures under oxidizing atmosphere (CO_2, H_2O, and so on), whereas chemical treatment is commonly performed on amorphous carbons previously mixed with chemicals such as alkalis, carbonates or acids. A porous network in the bulk of carbon materials could be obtained after physical or chemical treatment. The pore size distribution (micropores (<2 nm), mesopores (2-50 nm) and macropores (>50 nm)) and specific surface area could be calculated through Brunauer-Ennett-Teller (BET) characterization.

Owing to the porous network and relatively low cost, activated carbon is the most widely used electrode material for supercapacitor negative electrodes. Some commercially available devices, composed of activated carbon electrodes and organic electrolytes, can achieve a specific capacitance of 100-120 F g^{-1} and their operating cell voltage could be extended up to 2.7 V [32, 33]. In aqueous electrolytes, the operating cell voltage is limited to 0.9 V and the specific capacitance could reach 300 F g^{-1} [34].

1.4.1.2 Carbon nanotubes (CNTs)

Carbon nanotubes (CNTs) are tubes made of carbon with diameters typically in the nanometer size. CNTs exhibit remarkable electrical conductivity, fully accessible external surface area, and exceptional tensile strength and thermal conductivity. These properties are expected to be valuable in many fields of technology, such as electronics, optics, energy storage, and other applications of materials science.

CNTs could be produced in sizable quantities using various methods, including arc discharge, laser ablation, chemical vapor deposition (CVD) and high pressure carbon monoxide disproportionation (HiPCO). However, the as-prepared CNTs always have impurities such as other forms of carbon (amorphous carbon, fullerene, etc.) and non-carbonaceous impurities (the metal used as catalyst). The performance of CNTs is greatly influenced by the purity of the material, therefore, these impurities need to be removed to make use of CNTs.

The specific capacitance of purified CNT powders is in the range of 20 to 80 F g^{-1}, which could be enhanced by subsequent oxidative processes up to about 130 F g^{-1} [23, 35, 36]. Recently, many efforts have been devoted to the improvement of the electrochemical performance of CNTs through chemical activation (nitric acid or potassium hydroxide), introducing pseudo-capacitive behavior materials, etc.

1.4.1.3 Templated porous carbons

Templated porous carbons are obtained from the synthesis of ordered nanostructured carbons through templating techniques. The well-controlled pore size distributions, ordered pore structures, large specific surface area, and interconnected pore network of templated porous carbons make them promising candidates for supercapacitor electrode materials. Generally, the production of a templated porous carbon comprises the following five steps [37]: i) synthesis of an inorganic template; ii) impregnation of the template with an organic template; iii) polymerization of the precursor; iv) carbonization of the organic material and v) leaching of the inorganic template.

Various carbon structures with well-controlled micropores, mesopores and/or macropores produced from different types of templates and carbon precursors have been studied for supercapacitor applications. For example, a functionalized microporous carbon material was obtained by using zeolite Y as a template, and the resultant carbon material possessed a high gravimetric capacitance of about 340 F g^{-1} in aqueous electrolyte with good stability (over 10,000 cycles) [38]. Ordered porous carbons containing meso/macro/micropores with large surface areas have been synthesized by Yamada's group by a colloidal-crystal templating technique. A high EDLC capacitance of 200-350 F g^{-1} was achieved in an acidic electrolyte solution [39].

Investigations on pore-dependent capacitance properties have revealed that a narrow pore size distribution, well-adapted pore size to the electrolyte ions and ordered straight pore channels are better for use as high-energy-density electrode materials. Moreover, a well-controlled porous structure also provides efficient use of pseudo-capacitance from the N and O functionalities of the carbon materials. Thus, many efforts have been put into the modification of the porous structure of templated porous carbons, such as using different templates, leaching with HF, HCl or NaOH, impregnation from the liquid and gas phase, and carbonization at different temperatures.

1.4.1.4 Graphene

Graphene is an allotrope of carbon in the form of a single layer of atoms in a two-dimensional hexagonal lattice in which one atom forms each vertex. It was discovered in 2004 through a process of scotch tape peeling and is being studied in nearly every field of science and engineering due to its excellent electrical conductivity, large theoretical surface area (2630 m^2g^{-1} of a mono-layer), high surface to volume ratio, short diffusion distance, and structural

flexibility, and thermal and chemical stability. Although the production of pristine graphene by mechanical exfoliation has led to the rapid development and characterization of graphene's potential, this method does not apply to some particular applications, which require larger material quantities. Therefore, some alternative processes including chemical vapor deposition (CVD), chemically derived graphene, total organic synthesis, and unzipping of carbon nanotubes… have been developed [40-42].

Graphene is regarded as a natural competitor for electrode materials of ESs, owing to its chemical stability, large surface area, and high conductivity. Reports of various graphene and heteroatom-doped graphene materials also proved that they are better than many high surface area activated carbons used in the industry. However, the tendency of graphene materials to re-stack prevents the utilization of graphene's full surface area (2630 m^2g^{-1}) and leads to irreversible capacity loss and decrease of the initial coulombic efficiency.

To avoid the re-stacking of graphene sheets, different approaches have been investigated. As an example, composites made of graphene and transition metals/conductive polymers were proposed as an interesting strategy to overcome the above hurdles [43, 44]. On the one hand, transition metals/conductive polymers prevent graphene from agglomeration and re-stacking and also increase the specific surface area (SSA). On the other hand, graphene helps the formation of transition metals/conductive polymers with uniformly dispersed controlled morphologies, suppressing the volume change and agglomeration of transition metals/conductive polymers.

The second strategy is the design and development of porous frameworks, such as graphene foams, porous graphene, or hydrogels [45]. Benefiting from its many advantages such as large specific surface area (SSA), abundant porosity, admirable electronic conductivity, and unique mechanical characteristics as well as ultrafast electron transport kinetics, graphene with porous structure exhibits excellent electrochemical properties and has been extensively applied in energy storage and conversion.

The third strategy is the heteroatom doping into graphene [46]. It is believed that the introduction of heteroatom could change the electro-neutrality of graphene, affecting its electronic conductivity and chemical reactivity, and thus allowing fast access of ions and electrolytes to the electrode surface, resulting in increased capacitance. Doping graphene with single heteroatoms such as N, S, P, and B has been extensively studied, and the obtained data indicate that single doping can improve the electrochemical performance of graphene to varying degrees.

By combining the above methods, it is highly anticipated that the modified graphene with a designed framework will achieve superior electrochemical performance at a relatively low cost.

1.4.2 Transition metals

Transition metals are another important class of ESs electrode materials expected to store much more energy than carbon materials, owing to the faradaic charge transfer involved in the electrochemical process. In the past decades, worldwide attention has been focused on transition metal oxides/hydroxides, sulfides, phosphides based electrode materials. Three different types of transition metal materials distinguished by their corresponding energy storage mechanism are shown in **Table 1-2** and discussed in the following parts.

Table 1-2: Transition metals distinguished by their corresponding energy storage mechanism [12].

Energy storage mechanism		Typical materials
Pseudo-capacitance	surface redox	Mn and Fe oxides/oxyhydroxides
	intercalation	V_2O_5, WO_3, Nb_2O_5, MoS_2, etc
Battery-type capacity		Ni, Co, Cu, Zn based oxides/hydroxides, sulphides and phosphides

1.4.2.1 Surface redox pseudo-capacitive materials

Manganese oxide/oxyhydroxide materials such as MnO_2, Mn_3O_4, and MnOOH are reported as typical surface redox pseudo-capacitive materials [47, 48]. Iron (Fe) oxides/oxyhydroxides also show surface redox pseudo-capacitive behavior only in a relatively narrow voltage range of 0 to -0.8 V vs. Ag/AgCl. These types of electrode materials are abundant, possess high theoretical capacitance and low cost. The electric charge storage of this class of electrode materials involves a change of oxidation state with the participation of alkali cations or protons. Taking MnO_2 material as an example, the general charge storage mechanism can be described as [49]:

$$MnO_2 + C^+ + e^- \leftrightarrow MnOOC \qquad 1\text{-}12$$

Where C^+ stands for protons or alkali cations (Na^+, K^+, Li^+, etc). The performing MnO_2 materials are characterized by rectangular cyclic voltammogram curves and triangular galvanostatic charge–discharge (GCD) plots.

The pseudo-capacitive properties of these electrode materials are dominated by their crystallinity and crystallographic structures. As the charge storage process is accompanied by adsorption-desorption of protons and alkali cations, structures with sufficient spaces for the diffusion of these ions are useful for supercapacitor applications. Concerning manganese oxide/oxyhydroxide, α-MnO_2 and δ-MnO_2 exhibit great potential for SCs, because α-MnO_2 has a large tunnel size (ca. 0.46 nm) and δ-MnO_2 has a large interlayer space (ca. 0.7 nm), while other crystallographic structures normally show negligible charge storage ability due to the narrow tunnels in the structure (**Fig. 1.9**) [50]. However, the bottleneck for these electrode materials is their poor structural stability, poor electrical conductivity, and low life cycle stability. Moreover, the charge storage ability of Mn-based materials is limited, because only the surface thin layer of Mn-based materials can store charges. To solve these problems, the design of composites was proposed as an alternative approach, because composites could provide abundant active sites and improve electron transport efficiency, and cycling stability [51, 52].

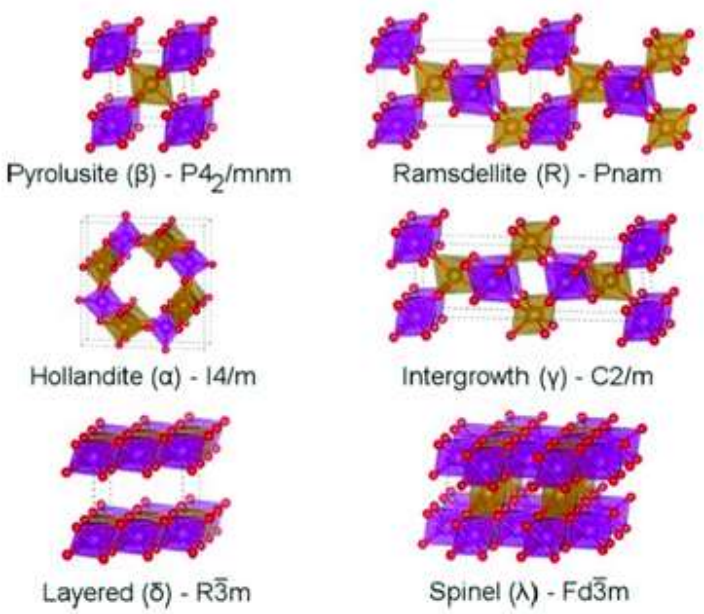

Figure 1.9: Illustration of the crystal structures of selected common manganese oxides [50].

1.4.2.2 Intercalation pseudo-capacitive type materials

Transition metal oxides such as V_2O_5, WO_3, MoO_3, Nb_2O_5, and TiO_2 and two-dimensional (2D) metal sulfides MS, where M represents Mo, V, Ti, etc [53-59] are found to possess intercalation pseudo-capacitive characteristic. One typical feature for intercalation based materials is that they normally have a 2D layered structure or 3D interconnected channels, which enable fast electrolyte ion transport during the charge-storage process. Taking V_2O_5 as

an example (**Fig. 1.10**) [60], the electrochemical behavior was assessed by density functional theory (DFT). It was found that the migration pathway of K ions is along the V_2O_5 channels and the charge storage process was not limited to the surface. Instead, the whole bulk material participates in the electrochemical process during the SC charge/discharge process. Therefore, increasing the electrical conductivity and enlarging the interlayer spaces are very important for better performance, especially for rate performance.

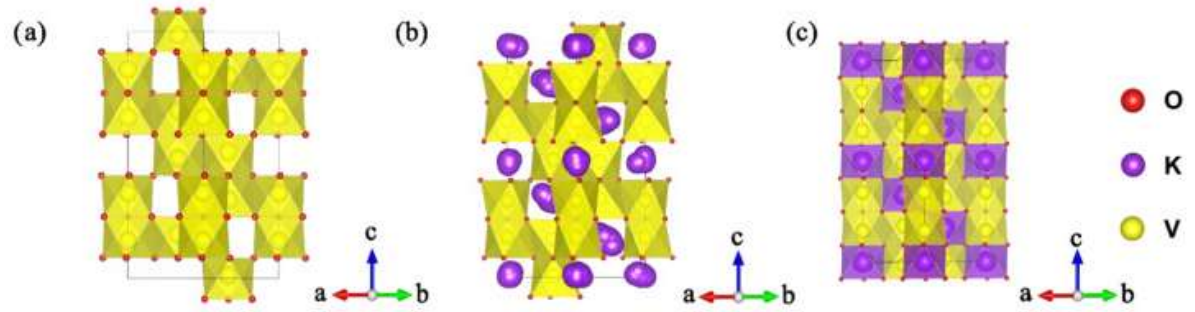

Figure 1.10: Electrochemical behavior calculated by DFT; a) optimized structure of V_2O_3, b) trajectories of K ions in KV_2O_3 obtained by the ab initio molecular dynamics (AIMD) simulation at 2000K for 4ps, c) optimized structures of KV_2O_3 [60].

1.4.2.3 Battery-type materials

Transition metals (Ni, Co, Cu, Cd, Mn^{II} and Fe) based oxide/hydroxide, sulfide, selenide, and phosphide materials are distinguished as battery-type electrode materials because they react with OH^- in alkaline media and experience a phase change during the charge/discharge process and display obvious redox CV peaks. These materials are very attractive for hybrid supercapacitors because they exhibit comparable kinetics as capacitor-type materials after special designing while possessing high electrochemical activity due to the battery charge-storage process. The battery-type electrode materials are discussed in the following part.

I) Transition metal hydroxides

Transition metal hydroxides store charges through deprotonation/protonation (i.e. O-H bond breaking/reconstitution) reaction with the participation of OH^- in the electrolyte. The redox reaction can be expressed as [61]:

$$M(OH)_2 + OH^- \leftrightarrow MOOH + H_2O + e^- \qquad 1\text{-}13$$

Transition metal hydroxides contain α (hydrotalcite-like and turbostratic-disordered structures) and β (brucite-like structure) phase crystal structures (**Fig. 1.11**). The α-form

hydroxides generally have a larger interlayer spacing (> 7.0 Å) than β-phase (4.6 Å), resulting in a much higher electro-activity than the latter. However, the α phase material is normally structurally vulnerable and can be reversibly transformed into β phase in alkaline electrolyte. The β phase is a low electrical conductive p-type semiconductor and has a metastable crystal structure, resulting in a sluggish charge storage process and therefore a poor capacity retention rate and short cycle lifetime.

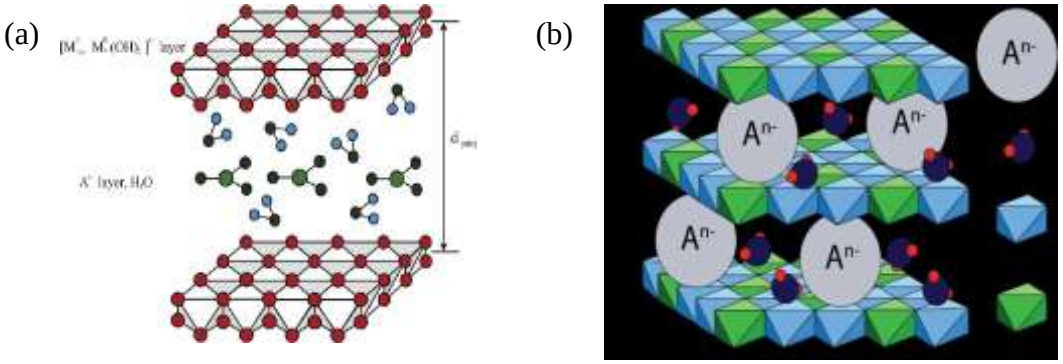

Figure 1.11: Hydrotalcite-like (a), and brucite-like (b) structures [62, 63].

The design of ultrathin hydroxide structures and introduction of additional metal cations have been reported to solve the cycling problems [64]. In addition, binary metal cation based layered double hydroxide (LDH) materials and transition metal oxyhydroxides also have the potential of delivering high cycling lifetime in supercapacitors [61, 65].

II) Transition metal oxides

Transition metal oxides such as Co_3O_4, NiO, and Fe_2O_3 have been extensively investigated as electrode materials mainly because of their high theoretical capacity, natural abundance, and simple synthetic approaches to achieve controlled morphologies, structures, sizes, and compositions. Some reports have demonstrated that these transition metal oxides can be very stable for long-term charge/discharge processes. However, in most cases, it is challenging to achieve such high cycling performance, because of their poor electrical conductivity due to their semiconducting or even insulating nature, and reduced electrochemical activity compared to hydroxides.

Based on previously published reports [66-69], multiple metal oxides normally show much higher electric conductivity and electro-capacitive activity than mono metal oxides. Therefore, the construction of multiple metal oxides is regarded as one of the best ways to obtain enhanced electrochemical performance.

III) Transition metal sulfides

Besides hydroxides and oxides, transition metal sulfides are important candidates as battery-type materials for supercapacitors, because of their desirable properties including higher electric conductivity, improved electrochemical activity, and the diversity of stoichiometric chemistry compared to metal oxides.

Similar to oxides, transition metal sulfides exhibit battery charge storage behavior through reversible surface redox reactions of transition metal ions with OH^-. The process can be expressed as:

$$MS + OH^- \leftrightarrow MSOH + e^- \qquad 1\text{-}14$$

Where M represents the transition metal. To utilize the redox reaction, alkaline electrolytes must be used because they are essential for the surface redox reaction. Despite the fact that most of the transition metals can coordinate with sulfur, only those with multi-valence states are feasible for redox reactions. Furthermore, only a few transition metal sulfides have demonstrated cycling stability higher than 10,000 cycles.

Many attempts have been made to overcoming these barriers, and researchers are inspired by building of micro-nano transition metal sulfide structures and the construction of other bimetal sulfides [70-73].

IV) Transition metal selenides and phosphides

Inspired by the excellent performance of transition metal sulfides, metal selenides and phosphides have also been investigated for ESs [74-76]. Selenium and phosphorus have lower electronegativity and larger atomic radius than sulfur and oxygen, and their corresponding metal selenides and phosphides lead to different physical or chemical properties compared to their sulfide and oxide counterparts. Most selenides and phosphides are battery-type materials, which involve surface redox reactions of Ni, Co-based cations in an alkaline electrolyte for charge storage. Therefore, the redox reaction is determined by the properties of the metal cations.

1.4.3 Conducting polymers

Conducting polymers (CPs) are organic polymers that conduct electricity. Such compounds may have metallic conductivity or can be semiconductors. They possess many advantages

making them suitable materials for ESs, such as low cost, high conductivity in a doped state, high potential window, high storage capacity/porosity/reversibility, and adjustable redox activity through chemical modification. They offer capacitance behavior through the redox process. When oxidation takes place, ions are transferred to the polymer backbone, and when reduction occurs, the ions are released from its backbone into the electrolyte. Early researchers termed the oxidation-reduction processes as 'doping'. As shown in **Fig. 1.12**, the positively-charged polymers, introduced by oxidation of the repeating units of polymer chains, are termed as 'p-doped', while negatively-charged polymers generated by reduction are termed as 'n-doped'. These reactions in the CP come about throughout its entire bulk, not just on the surface.

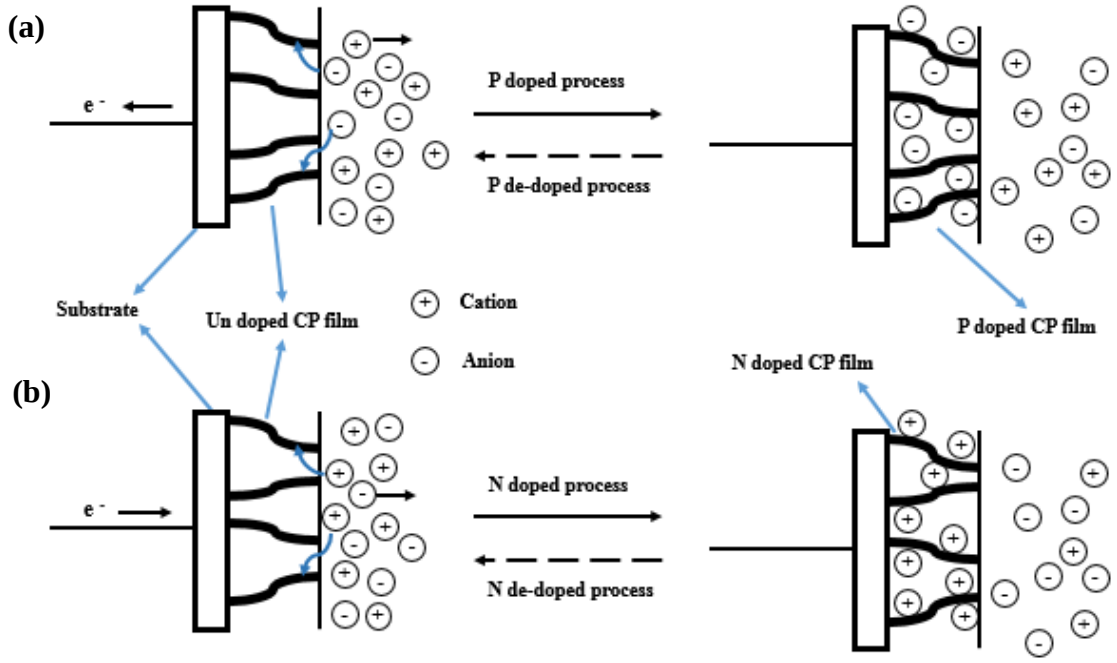

Figure 1.12: Schematic representation of electrochemical doping of CPs: (a) p-doping and (b) n-doping [77].

Several CPs have been produced and are widely in use, as illustrated in **Fig. 1.13**. CPs-based ES systems have been investigated in three different configurations (**Table 1-3**): i) Type I (symmetric p-p doped). In this type, both electrodes use the same p-doped polymer. When fully charged, one electrode is in the full p-doped (positive) state and the other in the uncharged state, ii) Type II (asymmetric p-p' doped). In this type, two different p-doped polymers with a different range of oxidation and reduction electro-activities are used, and iii) Type III (symmetric n-p doped). Electrodes use the same polymer, which can be both p- and n-doped in the same molecule. Particularly, the n-p type configuration has huge potential for high E_d and P_d.

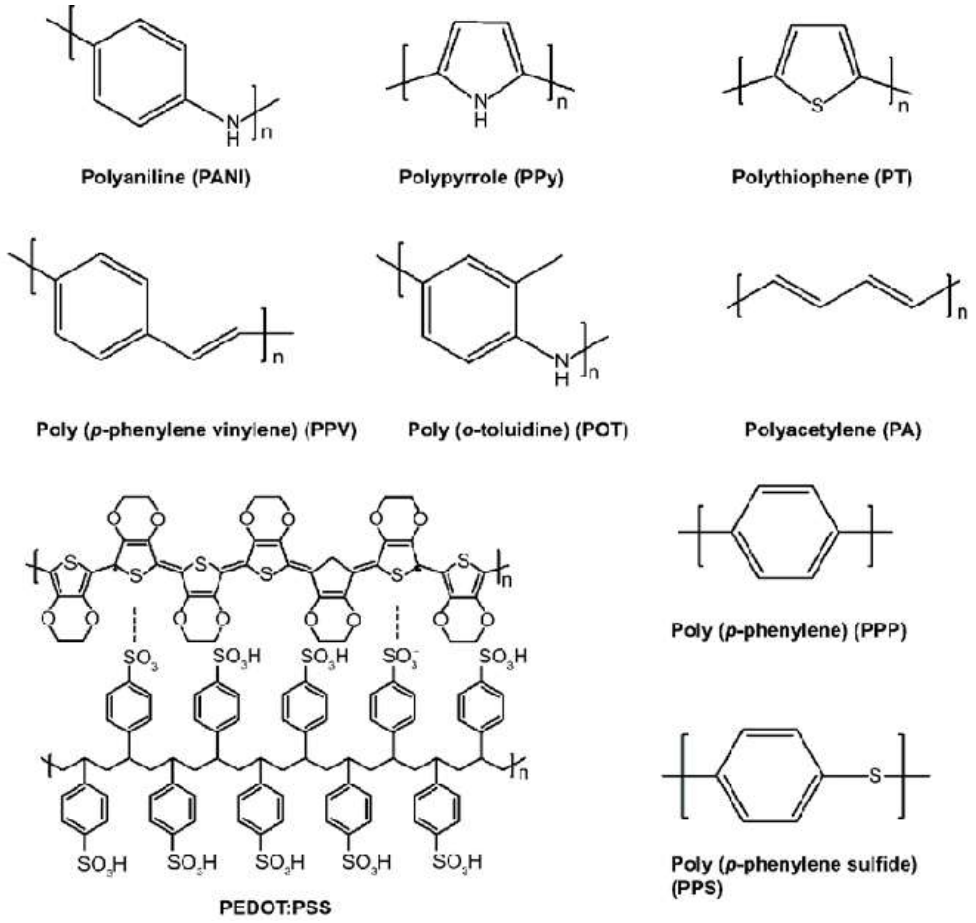

Figure 1.13: Chemical structures of representative conducting polymers [77].

Table 1-3: Configurations of CPs-based ES systems [25, 78].			
Type		Electrode materials	Typical materials
I	Symmetric p-p doped	Same p-doped polymer	Polyaniline (PANI), Polypyrrole (PPy)
II	Asymmetric p-p' doped	Two different p-doped polymers	PPy/polythiophene (PTh)
III	Symmetric n-p doped	Same polymer which can be p- and n-doped in the same molecule	PTh and its derivatives

Unfortunately, CPs in n-doped configuration exhibit poor stability than those in the p-doped state, and the swelling and shrinking of CPs may occur during the intercalating/de-intercalating process. These problems often lead to mechanical degradation of the electrode and fading electrochemical performance during cycling, which compromises CPs as electrode materials. To improve CPs stability, following attempts have been made [25, 44, 79]: i) Nanostructured CPs such as nanofibers, nanorods, nanowires, and nanotubes; ii) Hybridizing ESs with a p-

doped CP as the positive electrode and carbon material as the negative electrode; iii) fabricating composite electrode materials.

1.5 Conclusion and future prospects

This chapter provides information about ESs including brief history and background, structures, energy storage principle, characteristic features, and electrode materials. Based on the above information, ESs devices show potential applications in mobile electronic devices, smart grids, and so on. However, the disadvantages of ESs including low energy density (E_d) and high production cost limit their further application. Moreover, the limitation of current ESs devices exposes fundamental gaps in our understanding of atomic- and molecular-level processes that govern their operation, performance, and failure. To overcome this limitation, the understanding of the energy storage principle of active materials and configuration types of ES devices indeed provides future direction.

Based on the three configuration types of ESs, different energy storage mechanisms of the corresponding electrode materials and the performance evaluation criteria of ESs, hybrid supercapacitors, particularly, the combination of the EDLC and Faradaic battery-type characteristics, is expected to be the most promising configuration with enhanced performance. Therefore, one has to put efforts in the construction and development of hybrid supercapacitors.

As a hybrid supercapacitor consists of electrodes with different energy storage mechanisms, it is of prime importance to design well-matched electrodes in terms of mass and capacity. It is also well known that the performance of ES cells (energy and power density) is proportional to the square of the value of cell voltage window (V) and the value of V is dependent on the chosen electrolyte and electrode materials. Therefore, special efforts should be concentrated on the exploration and development of suitable electrolytes with low production cost and the preparation of advanced electrode materials with improved performance relative to the existing ones.

1.6 Thesis objectives

The thesis objective is to prepare advanced electrode materials with improved performance relative to the existing ones. The thesis strategy is based on the increase of electroactive sites for charge storage of electrode materials through synergistic effects between different compounds and the construction of hybrid supercapacitors through a ‘smart’ balance of two electrodes. The hypothesis of this approach is based on the development of electrode materials

capable of meeting the followings criteria: 1) increased density of electroactive sites, 2) improved electrical conductivity, 3) the ability to operate an extended potential window without material distortion, 4) meet the demand of the practical application.

To achieve this goal, it is necessary to identify the shortcomings of the selected materials and the role that the introduced compound plays in. An example is mono metal sulfides, which are supposed to provide good electronic, chemical properties, and high theoretical capacity. However, the poor intrinsic conductivity and agglomeration of mono metal sulfides greatly limit their performance. Therefore, our strategy for improving the performance of metal sulfides is to introduce conducting matrix or construct multi-metal sulfide compounds. This approach has led to remarkable changes in material morphology such as the modification of the distribution of metal sulfide particles and the design of porous structures on the material surface. The obtained enhanced electrochemical performance of modified metal sulfide electrode materials will be discussed in the following chapters.

1.7 References

[1] C. Liu, F. Li, L. P. Ma, H. M. Cheng, Advanced Materials for Energy Storage, Adv. Mater. 22 (2010) E28-62.

[2] L. Zhang, X. S. Hu, Z. P. Wang, F. C. Sun, D. G. Dorrell, A Review of Supercapacitor Modeling, Estimation, and Applications: A Control/Management Perspective, Renew. Sustain. Energy Rev. 81 (2018) 1868-1878.

[3] Poonam, K. Sharma, A. Arora, S. K. Tripathi, Review of Supercapacitors: Materials and Devices, J. Energy Storage 21 (2019) 801-825.

[4] A. C. Okaro, C. O. Ugwuoke, O. S. Okwundu, Recent Trends in Non-Faradaic Supercapacitor Electrode Materials, Metall. Mater. Eng. 25 (2019) 105-138.

[5] H. J. Becker, V. Ferry, a. t. G. E. C. N.Y., Low Voltage Electricity Capacitor, United States Patent Office (1957).

[6] D. L. Boos, O. G. Heights, assignor to The Standard Oil Company, , O. Cleveland, a corporation of Ohio, Electricity Capacitor Having Carbon Paste Electrodes, United States Patent Office (1970).

[7] A. Muzaffar, M. B. Ahamed, K. Deshmukh, J. Thirumalai, A Review on Recent Advances in Hybrid Supercapacitors: Design, Fabrication and Applications, Renew. Sust. Energy Rev. 101 (2019) 123-145.

[8] M. R. Lukatskaya, B. Dunn, Y. Gogotsi, Multidimensional Materials and Device Architectures for Future Hybrid Energy Storage, Nat. Commun. 7 (2016) 12647 DOI: 12610.11038/ncomms12647

[9] X. L. Chen, R. Paul, L. M. Dai, Carbon-based Supercapacitors for Efficient Energy Storage, Natl. Sci. Rev. 4 (2017) 453-489.

[10] V. Augustyn, P. Simon, B. Dunn, Pseudocapacitive Oxide Materials for High-rate Electrochemical Energy Storage, Energy Environ. Sci. 7 (2014) 1597-1614.

[11] L. L. Zhang, X. S. Zhao, Carbon-Based Materials as Supercapacitor Electrodes, Chem. Soc. Rev. 38 (2009) 2520-2531.

[12] T. Wang, H. C. Chen, F. Yu, X. S. Zhao, H. X. Wang, Boosting the Cycling Stability of Transition Metal Compounds-based Supercapacitors, Energy Storage Mater. 16 (2019) 545-573.

[13] W. Zuo, R. Li, C. Zhou, Y. Li, J. Xia, J. Liu, Battery-Supercapacitor Hybrid Devices: Recent Progress and Future Prospects, Adv. Sci. 4 (2017) 1600539.

[14] T. Brousse, D. Bélanger, J. W. Long, To Be or Not To Be Pseudocapacitive?, J. Electrochem. Soc. 162 (2015) A5185-A5189.

[15] Y. X. Chen, D. Ni, X. W. Yang, C. C. Liu, J. L. Yin, K. F. Cai, Microwave-assisted Synthesis of Honeycomblike Hierarchical Spherical Zn-doped Ni-MOF as a High-Performance Battery-Type Supercapacitor Electrode Material, Electrochim. Acta 278 (2018) 114-123.

[16] Y. M. Lv, A. F. Liu, Z. X. Shi, H. W. Che, J. B. Mu, Z. C. Guo, X. L. Zhang, Construction of Hierarchical Zinc Cobalt Sulfide@Nickel Sulfide Core-Shell Nanosheet Arrays for High-Performance Asymmetric Solid-state Supercapacitors, Chem. Eng. J. 349 (2018) 397-407.

[17] R. Sahoo, A. Pal, T. Pal, Proportion of Composition in a Composite Does Matter for Advanced Supercapacitor Behavior, J. Mater. Chem. A 4 (2016) 17440-17454.

[18] A. Burke, H. B. Zhao, Applications of Supercapacitors in Electric and Hybrid Vehicles, 5th ESSCAP (2015).

[19] Y. Wang, Y. Song, Y. Xia, Electrochemical Capacitors: Mechanism, Materials, Systems, Characterization and Applications, Chem. Soc. Rev. 45 (2016) 5925-5950.

[20] N. C. C. Corporation, Nippon Chemi-Con, Stanley Electric and Tamura announce: Development of "Super CaLeCS", an Environment-Friendly EDLC-powered LED Street Lamp, Press Release (2010).

[21] https://milremrobotics.com/milrem-robotics-introduces-the-new-generation-multi-purpose-unmanned-ground-vehicle/.

[22] N. Choudhary, C. Li, J. Moore, N. Nagaiah, L. Zhai, Y. Jung, J. Thomas, Asymmetric Supercapacitor Electrodes and Devices, Adv. Mater. 29 (2017) 1605336.

[23] A. G. Pandolfo, A. F. Hollenkamp, Carbon Properties and their Role in Supercapacitors, J. Power Sources 157 (2006) 11-27.

[24] B. A. Mei, O. Munteshari, J. Lau, B. Dunn, L. Pilon, Physical Interpretations of Nyquist Plots for EDLC Electrodes and Devices, J. Phys. Chem. C 122 (2017) 194-206.

[25] G. Wang, L. Zhang, J. Zhang, A Review of Electrode Materials for Electrochemical Supercapacitors, Chem. Soc. Rev. 41 (2012) 797-828.

[26] P. Simon, Y. Gogotsi, Capacitive Energy Storage in Nanostructured Carbon-Electrolyte Systems, Acc. Chem. Res. 46 (2013) 1094-1103.

[27] P. Simon, A. Burke, Nanostructured Carbons: Double-layer Capacitance and More, Electrochem. Soc. Interface (2008) 38-43.

[28] https://en.wikipedia.org/wiki/Carbon_nanotube.

[29] A. D. Roberts, X. Li, H. Zhang, Porous Carbon Spheres and Monoliths: Morphology Control, Pore Size Tuning and Their Applications as Li-ion Battery Anode Materials, Chem. Soc. Rev. 43 (2014) 4341-4356.

[30] https://en.wikipedia.org/wiki/Graphene.

[31] P. J. F. Harris, Z. Liu, K. Suenaga, Imaging the Atomic Structure of Activated Carbon, J. Phys. Condens. Matter. 20 (2008) 362201.

[32] K. Jurewicz, C. Vix-Guterl, E. Frackowiak, S. Saadallah, M. Reda, J. Parmentier, J. Patarin, F. Béguin, Capacitance Properties of Ordered Porous Carbon Materials Prepared by a Templating Procedure, J. Phys. Chem. Solids 65 (2004) 287-293.

[33] J. A. Fernández, T. Morishita, M. Toyoda, M. Inagaki, F. Stoeckli, T. A. Centeno, Performance of Mesoporous Carbons Derived from Poly(vinyl alcohol) in Electrochemical Capacitors, J. Power Sources 175 (2008) 675-679.

[34] P. Simon, Y. Gogotsi, Materials for Electrochemical Capacitors, Nat. Mater. 7 (2008) 845-854.

[35] S. Talapatra, S. Kar, S. K. Pal, R. Vajtai, L. Ci, P. Victor, M. M. Shaijumon, S. Kaur, O. Nalamasu, P. M. Ajayan, Direct Growth of Aligned Carbon Nanotubes on Bulk Metals, Nat. Nanotechnol. 1 (2006) 112-116.

[36] A. González, E. Goikolea, J. A. Barrena, R. Mysyk, Review on Supercapacitors: Technologies and Materials, Renew. Sust. Energy Rev. 58 (2016) 1189-1206.

[37] B. Sakintuna, Y. Yurum, Templated Porous Carbons: a Review Article, Ind. Eng. Chem. Res. 44 (2005) 2893-2902.

[38] C. O. Ania, V. Khomenko, E. Raymundo-Piñero, J. B. Parra, F. Béguin, The Large Electrochemical Capacitance of Microporous Doped Carbon Obtained by Using a Zeolite Template, Adv. Funct. Mater. 17 (2007) 1828-1836.

[39] H. Yamada, H. Nakamura, F. Nakahara, I. Moriguchi, T. Kudo, Electrochemical Study of High Electrochemical Double Layer Capacitance of Ordered Porous Carbons with Both Meso/Macropores and Micropores, J. Phys. Chem. C 111 (2007) 227-233.

[40] V. Chabot, D. Higgins, A. P. Yu, X. C. Xiao, Z. W. Chen, J. J. Zhang, a Review of Graphene and Graphene Oxide Sponge: Material Synthesis and Applications to Energy and The Environment, Energy Environ. Sci. 7 (2014) 1564-1569.

[41] P. Avouris, C. Dimitrakopoulos, Graphene: Synthesis and Applications, Mater. Today 15 (2012) 86-97.

[42] V. Singh, D. Joung, L. Zhai, S. Das, S. I. Khondaker, S. Seal, Graphene Based Materials: Past, Present and Future, Prog. Mater. Sci. 56 (2011) 1178-1271.

[43] H. L. Wang, Casalongue, H. S. , Y. Y. Liang, H. Dai, $Ni(OH)_2$ Nanoplates Grown on Graphene as Advanced Electrochemical Pseudocapacitor Materials, J. Am. Chem. Soc. 132 (2010) 7472-7477.

[44] D. W. Wang, I. Gentle, F. Li, J. P. Zhao, G. Q. Lu, H. M. Cheng, W. C. Ren, Z. G. Chen, J. Tan, Z. S. Wu, Fabrication of Graphene/Polyaniline Composite Paper via In Situ Anodic

Electropolymerization for HighPerformance Flexible Electrode, ACS Nano 3 (2009) 1745–1752

[45] H. Yamada, H. Nakamura, F. Nakahara, I. Moriguchi, T. Kudo, Electrochemical Study of High Electrochemical Double Layer Capacitance of Ordered Porous Carbons with Both Meso/Macropores and Micropores, J. Phys. Chem. C 111 (2007) 227-233.

[46] K. Gopalakrishnan, A. Govindaraj, C. N. R. Rao, Extraordinary Supercapacitor Performance of Heavily Nitrogenated Graphene Oxide Obtained by Microwave Synthesis, J. Mater. Chem. A 1 (2013) 7563-7565.

[47] S. Li, L. L. Yu, R. B. Li, J. Fan, J. T. Zhao, Template-free and Room-temperature Synthesis of 3D Sponge-like Mesoporous Mn_3O_4 with High Capacitive Performance, Energy Storage Mater. 11 (2018) 176-183.

[48] N. Liu, Y. Su, Z. Wang, Z. Wang, J. Xia, Y. Chen, Z. Zhao, Q. Li, F. Geng, Electrostatic-Interaction-assisted Construction of 3D Networks of Manganese Dioxide Nanosheets for Flexible High-Performance Solid-state Asymmetric Supercapacitors, ACS Nano 11 (2017) 7879-7888.

[49] H. T. Tan, W. P. Sun, L. B. Wang, Q. Y. Yan, 2D Transition Metal Oxides/Hydroxides for Energy-storage Applications, ChemNanoMat. 2 (2016) 562-577.

[50] Z. P. Ye, J. M. Giraudon, N. De Geyter, R. Morent, J. F. Lamonier, The Design of MnO_x Based Catalyst in Post-plasma Catalysis Configuration for Toluene Abatement, Catalysts 8 (2018) 91;doi.org/10.3390/catal8020091.

[51] J. Zhu, J. He, Facile Synthesis of Graphene-wrapped Honeycomb MnO_2 Nanospheres and Their Application in Supercapacitors, ACS Appl. Mater. Interfaces 4 (2012) 1770-1776.

[52] P. Li, Y. Yang, E. Shi, Q. Shen, Y. Shang, S. Wu, J. Wei, K. Wang, H. Zhu, Q. Yuan, A. Cao, D. Wu, Core-Double-Shell, Carbon Nanotube@Polypyrrole@MnO_2 Sponge as Freestanding, Compressible Supercapacitor Electrode, ACS Appl. Mater. Interfaces 6 (2014) 5228-5234.

[53] J. Feng, X. Sun, C. Wu, L. Peng, C. Lin, S. Hu, J. Yang, Y. Xie, Metallic Few-layered VS_2 Ultrathin Nanosheets: High Two-dimensional Conductivity for In-plane Supercapacitors, J. Am. Chem. Soc. 133 (2011) 17832-17838.

[54] T. Zhai, X. Lu, Y. Ling, M. Yu, G. Wang, T. Liu, C. Liang, Y. Tong, Y. Li, a New Benchmark Capacitance for Supercapacitor Anodes by Mixed-valence Sulfur-doped V_6O_{13-x}, Adv. Mater. 26 (2014) 5869-5875.

[55] M. Zhu, W. Meng, Y. Huang, Y. Huang, C. Zhi, Proton-insertion-enhanced Pseudocapacitance based on The Assembly Structure of Tungsten Oxide, ACS Appl. Mater. Interfaces 6 (2014) 18901-18910.

[56] M. Acerce, D. Voiry, M. Chhowalla, Metallic 1T Phase MoS_2 Nanosheets as Supercapacitor Electrode Materials, Nat. Nanotechnol. 10 (2015) 313-318.

[57] M. S. Javed, S. G. Dai, M. J. Wang, D. L. Guo, L. Chen, X. Wang, C. G. Hu, Y. Xi, High Performance Solid State Flexible Supercapacitor Based on Molybdenum Sulfide Hierarchical Nanospheres, J. Power Sources 285 (2015) 63-69.

[58] X. Xiao, C. F. Zhang, S. Z. Lin, L. Huang, Z. M. Hu, Y. L. Cheng, T. Q. Li, W. M. Qiao, D. H. Long, Y. H. Huang, L. Q. Mai, Y. Gogotsi, J. Zhou, Intercalation of Cations into Partially Reduced Molybdenum Oxide for High-Rate Pseudocapacitors, Energy Storage Mater. 1 (2015) 1-8.

[59] X. Zang, C. Shen, E. Kao, R. Warren, R. Zhang, K. S. Teh, J. Zhong, M. Wei, B. Li, Y. Chu, M. Sanghadasa, A. Schwartzberg, L. Lin, Titanium Disulfide Coated Carbon Nanotube Hybrid Electrodes Enable High Energy Density Symmetric Pseudocapacitors, Adv. Mater. 30 (2018).

[60] T. Jin, H. X. Li, Y. Li, L. F. Jiao, J. Chen, Intercalation Pseudocapacitance in Flexible and Self-standing V_2O_3 Porous Nanofibers for High-rate and Ultra-stable K Ion Storage, Nano Energy 50 (2018) 462-467.

[61] T. Wang, S. Zhang, X. Yan, M. Lyu, L. Wang, J. Bell, H. Wang, 2-Methylimidazole-Derived Ni-Co Layered Double Hydroxide Nanosheets as High Rate Capability and High Energy Density Storage Material in Hybrid Supercapacitors, ACS Appl. Mater. Interfaces 9 (2017) 15510-15524.

[62] Z. X. Yang, H. Fischer, J. Cerezo, J. M. C. Mol, R. Polder, Aminobenzoate Modified MgAl Hydrotalcites as A Novel Smart Additive of Reinforced Concrete for Anticorrosion Applications, Constr. Build. Mater. 47 (2013) 1436-1443.

[63] R. Dębek, M. Motak, T. Grzybek, M. Galvez, P. Da Costa, A Short Review on the Catalytic Activity of Hydrotalcite-Derived Materials for Dry Reforming of Methane, Catalysts 7 (2017) 32; doi:10.3390/catal7010032.

[64] J. A. Syed, J. Ma, B. G. Zhu, S. C. Tang, X. K. Meng, Hierarchical Multicomponent Electrode with Interlaced $Ni(OH)_2$ Nanoflakes Wrapped Zinc Cobalt Sulfide Nanotube Arrays for Sustainable High-Performance Supercapacitors, Adv. Energy Mater. 7 (2017) 1701228.

[65] J. Yang, C. Yu, X. M. Fan, J. J. Qiu, 3D Architecture Materials Made of NiCoAl-LDH Nanoplates Coupled with NiCo-Carbonate Hydroxide Nanowires Grown on Flexible Graphite Paper for Asymmetric Supercapacitors, Adv. Energy Mater. 4 (2014) 1400761.

[66] B. Zhu, S. Tang, S. Vongehr, H. Xie, J. Zhu, X. Meng, $FeCo_2O_4$ Submicron-Tube Arrays Grown on Ni Foam as High Rate-Capability and Cycling-Stability Electrodes Allowing Superior Energy and Power Densities with Symmetric Supercapacitors, Chem. Commun. 52 (2016) 2624-2627.

[67] J. Zhou, Y. Huang, X. Cao, B. Ouyang, W. Sun, C. Tan, Y. Zhang, Q. Ma, S. Liang, Q. Yan, H. Zhang, Two-dimensional $NiCo_2O_4$ Nanosheet-Coated Three-dimensional Graphene Networks for High-rate, Long-cycle-life Supercapacitors, Nanoscale 7 (2015) 7035-7039.

[68] S. j. Peng, L. L. Li, H. B. Wu, S. Madhavi, X. W. D. Lou, Controlled Growth of $NiMoO_4$ Nanosheet and Nanorod Arrays on Various Conductive Substrates as Advanced Electrodes for Asymmetric Supercapacitors, Adv. Energy Mater. 5 (2015) 1401172.

[69] X. B. Wang, J. J. Hu, W. D. Liu, G. Y. Wang, J. An, J. S. Lian, Ni–Zn Binary System Hydroxide, Oxide and Sulfide Materials: Synthesis and High Supercapacitor Performance, J. Mater. Chem. A 3 (2015) 23333-23344.

[70] H. Chen, J. Jiang, L. Zhang, H. Wan, T. Qi, D. Xia, Highly Conductive $NiCo_2S_4$ Urchin-like Nanostructures for High-Rate Pseudocapacitors, Nanoscale 5 (2013) 8879-8883.

[71] J. Wang, D. L. Chao, J. L. Liu, L. L. Li, L. F. Lai, J. Y. Lin, Z. X. Shen, Ni_3S_2@MoS_2 Core/Shell Nanorod Arrays on Ni Foam for High-Performance Electrochemical Energy Storage, Nano Energy 7 (2014) 151-160.

[72] R. Kumar, P. Rai, A. Sharma, Free-standing NiV_2S_4 Nanosheet Arrays on a 3D Ni Framework via an Anion Exchange Reaction as a Novel Electrode for Asymmetric Supercapacitor Applications, J. Mater. Chem. A 4 (2016) 17512-17520.

[73] X. Wang, S. X. Zhao, L. B. Dong, Q. L. Lu, J. Zhu, C. W. Nan, One-step Synthesis of Surface-enriched Nickel Cobalt Sulfide Nanoparticles on Graphene for High-performance Supercapacitors, Energy Storage Mater. 6 (2017) 180-187.

[74] A. Banerjee, S. Bhatnagar, K. K. Upadhyay, P. Yadav, S. Ogale, Hollow $Co_{0.85}Se$ Nanowire Array on Carbon Fiber Paper for High Rate Pseudocapacitor, ACS Appl. Mater. Interfaces 6 (2014) 18844-18852.

[75] K. Zhou, W. J. Zhou, L. J. Yang, J. Lu, S. Cheng, W. J. Mai, Z. H. Tang, L. G. Li, S. W. Chen, Ultrahigh-Performance Pseudocapacitor Electrodes Based on Transition Metal Phosphide Nanosheets Array via Phosphorization: a General and Effective Approach, Adv. Funct. Mater. 25 (2015) 7530-7538.

[76] X. Chen, M. Cheng, D. Chen, R. Wang, Shape-Controlled Synthesis of Co_2P Nanostructures and Their Application in Supercapacitors, ACS Appl. Mater. Interfaces 8 (2016) 3892-3900.

[77] A. U. Agobi, H. Louis, T. O. Magu , P. M. Dass, A Review on Conducting Polymers-Based Composites for Energy Storage Application, J. Chem. Rev. 1 (2019) 19-34.

[78] A. Laforgue, P. Simon, C. Sarrazin, J. F. Fauvarque, Polythiophene-based Supercapacitors, J. Power Sources 80 (1999) 142-148.

[79] C. Zhou, Y. Zhang, Y. Li, J. Liu, Construction of High-capacitance 3D CoO@polypyrrole Nanowire Array Electrode for Aqueous Asymmetric Supercapacitor, Nano Lett. 13 (2013) 2078-2085.

CHAPTER 2. THE PREPARATION OF COBALT SULFIDE/ CARBONACEOUS (REDUCED GRAPHENE OXIDE (RGO) OR POLY-ETHYLENEDIOXYTHIOPHENE-FE-900 (PF-9))

2.1 Introduction

Thanks to their excellent physical, chemical, electronic and optical properties, metal sulfides such as nickel [1-3], cobalt [4-7] and copper sulfides [8-10] have been utilized in various fields such as catalysis [11-15], electrochemical supercapacitors [16-19], and Li-ion batteries [20-22]. Among them, cobalt sulfides [23-25] such as Co_9S_8, CoS_2, CoS, and so on, are considered as one of the most promising candidates for electrode materials for supercapacitors, owing to their high theoretical specific capacity (870 mA h g^{-1}), different crystalline phases, various metal valence states, and low cost. For instance, cobalt sulfide nanotubes, synthesized by Wan et al.[26], displayed a maximum specific capacitance of 285 F g^{-1} at 0.5 A g^{-1}; however, the value decreases to 96 F g^{-1} as the current density increases to 10 A g^{-1} and about 86.5% of the initial specific capacitance was retained after 1000 cycles. The poor rate capability and/or cycling stability caused by poor intrinsic conductivity and agglomeration of cobalt sulfide materials greatly affect their performance as electrodes in supercapacitors.

To overcome these problems, many researchers constructed composite materials of carbonaceous materials and cobalt sulfides [27, 28]. Here, carbonaceous materials used as conducting matrices are expected to enhance the electrochemical performance through enhancing the electrical conductivity and dispersion of cobalt sulfide nano-materials. In this line, the 3D cobalt sulfide/ graphene hydrogel (CoSGH), synthesized by Meng et al. [29], exhibited an improved specific capacitance (435.7 F g^{-1} at 0.5 A g^{-1}) than that of bare cobalt sulfide (304.2 F g^{-1}) and graphene (84.9 F g^{-1}) at the same current density. However, graphene sheets tend to agglomerate together during their formation, because of van der Waals interactions, and this may result in reduced surface area and makes it difficult for ion exchange between electrode materials and electrolytes.

Based on Bhanges' work [30], poly-ethylene dioxythiophene (PEDOT)-Fe-900 ℃ (PF-9), prepared by simple oxidative polymerization of ethylene dioxythiophene in aqueous solution followed by an annealing process under an inert atmosphere, displays a crumbled morphology of graphene sheets and flakes with a high surface area (632 m^2g^2). Hence, it is believed that PF-

9 could provide a large surface area for homogeneous deposition of CoS particles, and the formed CoS/PF-9 composite is expected to exhibit an improved supercapacitor performance.

In the present work, reduced graphene oxide (rGO) and PF-9 are used as conducting matrices for CoS nanoparticles. Here, CoS, CoS/rGO, and CoS/PF-9 electrode materials are synthesized *via* chemical precipitation and ion-exchange reaction method.

Experimental section

2.2 Preparation of cobalt sulfide (CoS)

Here, a two-step ion-exchange sulfurization method is used to prepare CoS material (**Fig. 2.1**).

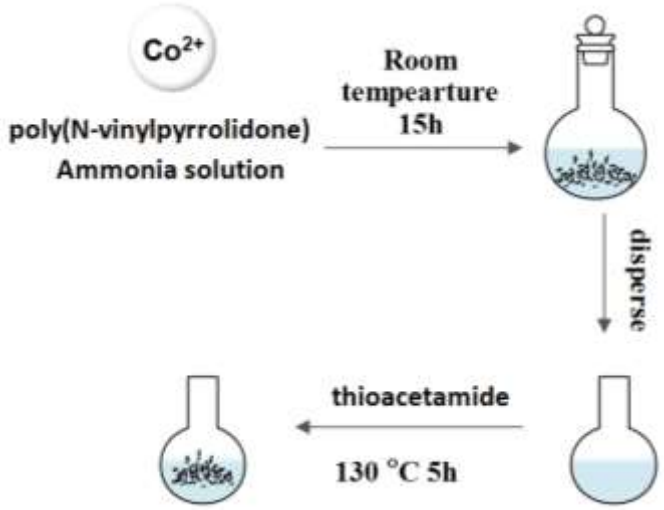

Figure 2.1: Illustration of the synthesis route of CoS electrode through a two-step ion-exchange sulfurization method.

238 mg of $CoCl_2$•$6H_2O$ was added to 20 mL aqueous solution containing 1g of PVP. After that, 286.5 μL of ammonia (35 wt%) was dropped into the above solution under vigorous magnetic stirring at room temperature for overnight. The formed precipitate was washed with water and ethanol until the pH was about 7. The obtained product was re-dissolved in 30 mL aqueous solution for further use.

100 mg of thioacetamide (TAA) were dissolved into 10 mL Milli-Q water, and then mixed with 10 mL of above solution under magnetic stirring at room temperature. After 30 min, the solution was heated at 130 ˚C for 5 h. After natural cooling to room temperature, the resulting

black solid product was collected through centrifugation, then washed with water and ethanol and dried at 60 ˚C overnight.

2.3 Characterizations of CoS

2.3.1 Structural characterization of CoS

X-ray photoelectron spectroscopy (XPS) analysis was performed on obtained CoS electrode material to gain information on the chemical composition and oxidation states of surface elements. The XPS full spectrum of CoS material is depicted in **Fig. 2.2a**. Five elements including C_{1s} (~284.8 eV), N_{1s} (~399.9 eV), O_{1s} (~531.6 eV), Co_{2p} (~779.1 eV), and S_{2p} (~162.4 eV) are observed. The C, N, O signals are most likely due to the PVP stabilizer.

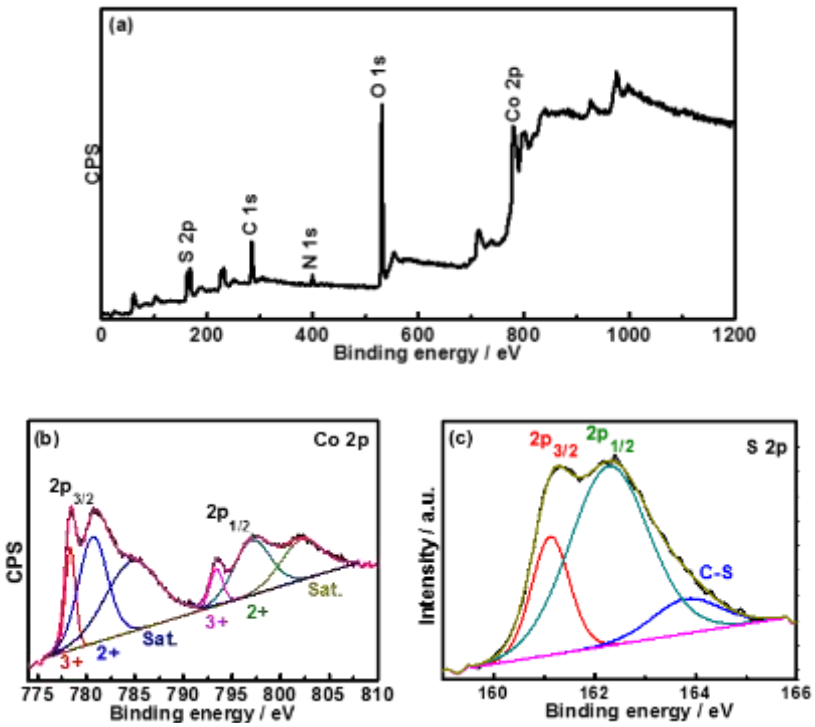

Figure 2.2: XPS analysis of CoS electrode material: (a) full spectrum, (b) high resolution spectra of Co_{2p}, and (c) S_{2p}. "Sat." in **Fig. 2.2** denotes satellite peaks.

The high-resolution spectrum of Co_{2p} (**Fig. 2.2b**) are curve-fitted with several components ascribed to $Co_{2p3/2}$ and $Co_{2p1/2}$ of Co^{2+} and Co^{3+} along with satellite peaks. The peaks at ~778.3 and 793.6 eV are assigned respectively to $2p_{3/2}$ and $2p_{1/2}$ core levels of Co^{3+}, whereas the peaks at ~780.7 and 797.2 eV are attributed to $2p_{3/2}$ and $2p_{1/2}$ core levels of Co^{2+}, respectively. The difference of the binding energy between $Co_{2p1/2}$ and $Co_{2p3/2}$ is larger than 15 eV, revealing the

co-existence of Co^{3+} and Co^{2+} in the CoS material [11, 14]. The bands at ~785.0 and 802.4 eV are shake-up satellite peaks. The XPS high resolution spectrum of S_{2p} are deconvoluted in two bands at ~161.2 and 162.3 eV due to $S_{2p3/2}$ and $S_{2p1/2}$, respectively (**Fig. 2.2c**). The peak at ~163.3 eV is attributed to the C-S bond [11]. The existence of C-S could originate from the interfaces between CoS and PVP. From XPS analysis results, the obtained CoS sample consists of Co^{2+}, Co^{3+}, and S^{2-}.

The crystal structure of obtained sample is investigated by XRD technique (**Fig. 2.3a**). Diffraction peaks at 2Θ= ~30.8 ° and 54.8 ° attributed to (100) and (110) crystal planes can be indexed to diffraction planes of CoS (JCPDS card No. 65-3418). In addition, a broad peak ranging from about 15 ° to 28 ° confirms the existence of PVP, while other diffraction peaks between 15.0 ° and 25.0 ° indicate the formation of orthorhombic sulfur impurities in the obtained sample (JCPDS card No. 08-0247).

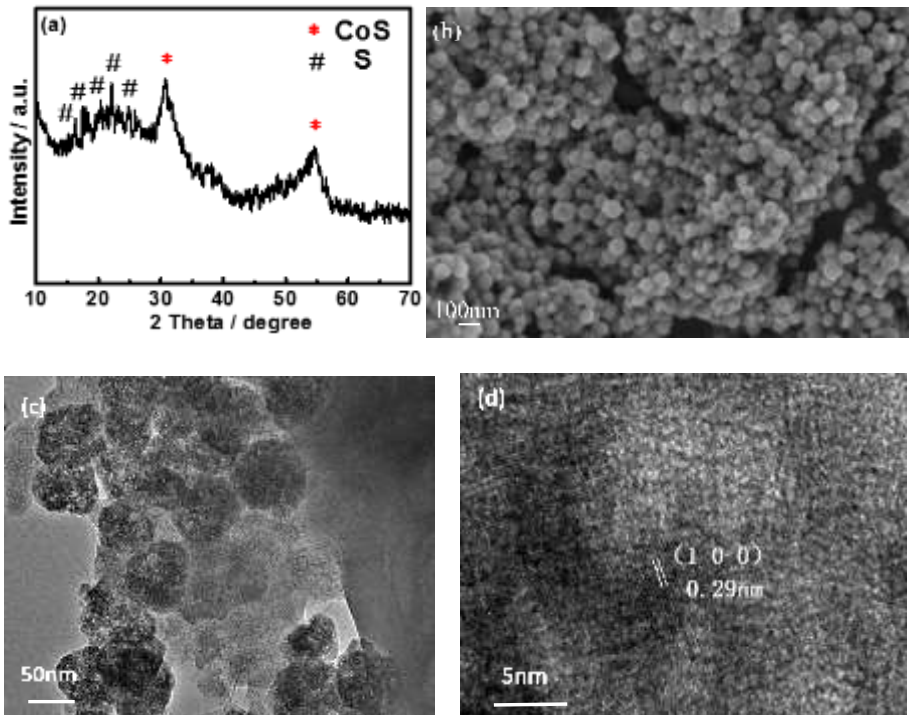

Figure 2.3: XRD pattern (a), SEM (b), TEM (c) and HRTEM (d) images of CoS sample.

The morphology and detailed microstructures of the CoS sample are examined by SEM and TEM. The SEM image (**Fig. 2.3b**) reveals nano-sphere morphology. It can be seen clearly that nano-sphere shaped CoS particles are dispersed in the entire sample. However, the formed CoS particles still tend to agglomerate together even with the help of PVP stabilizer. The TEM image of obtained CoS particles exhibits a nano-sphere like structure (**Fig. 2.3c**). The size of the nano-

sphere shaped CoS particles ranges from 60 to 100 nm (**Fig. 2.3b** and **c**). From HRTEM images in **Fig. 2.3d**, the lattice fringes of 0.29 nm match well with the interplanar distance d calculated from the XRD pattern of CoS sample (**Fig. 2.3a**).

2.3.2 Electrochemical performance of CoS

The electrochemical behavior (CV, GCD, and EIS plots) of the prepared CoS electrode is investigated using a 3-electrode system comprising the CoS material as a working electrode, Pt foil as a counter electrode, and Hg/HgO as a reference electrode (**Fig. 2.4**).

The redox peaks observed in the CV curves of CoS electrode indicate the existence of faradaic reactions (**Fig. 2.4a**). The shape of the CV curves is maintained when the scan rate increases from 5 to 100 mV/s, indicating the excellent rate performance. According to the literature, two electrochemical reactions are proposed [29]:

$$CoS + OH^- \leftrightarrow CoSOH + e^-$$

$$CoSOH + OH^- \leftrightarrow CoSO + H_2O + e^-$$

The corresponding specific capacity, calculated according to equation **7-1**, is shown in **Fig. 2.4b**. The specific capacity decreases from ~190 to 108 C g^{-1} as the scan rate increases from 5 to 100 mV/s. The decrease of the specific capacity, calculated from the CV curves, is mainly caused by less effective redox reaction at the interface of electrode/electrolyte under high scan rate [31].

The GCD plots of CoS, conducted in the potential range of 0 to +0.55V, are depicted in **Fig. 2.4c**. A very small IR drop (~3 mV) at the beginning of the discharge curves at a current density of 0.5 A g^{-1} could be detected, suggesting a rapid I/V response and an excellent electrochemical reversibility. Based on the discharge curves, the corresponding specific capacity is calculated according to equation **1-4**, and these values are plotted in **Fig. 2.4d**. The relatively low value of the specific capacity (~161 C g^{-1} at 0.5 A g^{-1}) is mainly attributed to the agglomeration of CoS particles, which produces more "inactive" surface, thus lowering the availability of active surface area.

EIS analysis is an extremely informative method to monitor the frequency-dependent electrochemical processes occurring at the electrode/electrolyte interface. **Fig. 2.4e** depicts the Nyquist plots and the corresponding equivalent circuit. The Nyquist plots display a depressed semi-circle in the high-medium frequency region, which is assigned to the charge-transfer

process between the electrode material and the electrolyte [32]. A sloped line is detected in the low-frequency region ascribed to electrolyte ion (OH^-) diffusion in the electrode materials [33]. Based on the fitted equivalent circuit, the values of R_s and R_{ct} are determined to be 1.07 and 143.10 ohm cm^{-2}, respectively.

Fig. 2.4f shows the cycling performance of the CoS electrode at 5 A g^{-1}. A slight decrease (from ~105 to ~90 C g^{-1}) is observed after 1,000 cycles.

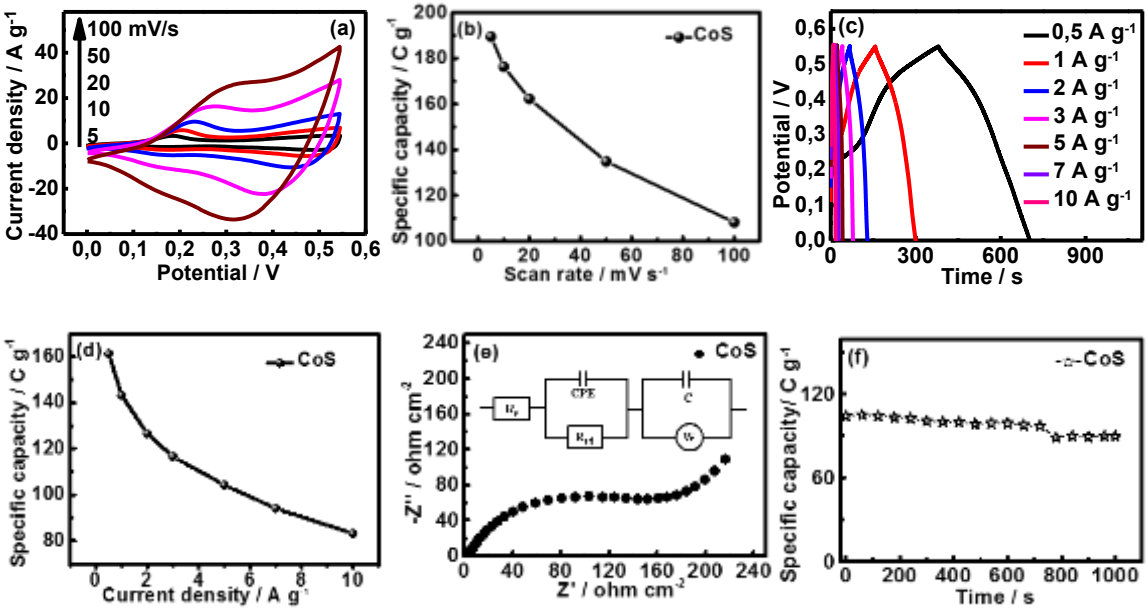

Figure 2.4: Electrochemical performance of the CoS sample: CV curves at different scan rates (a), the corresponding specific capacity (b); GCD curves at various current densities (c); the corresponding specific capacity (d); Nyquist plot (e), the inset in (e) is the corresponding equivalent circuit; stability performance at 5 A g^{-1} in 2M KOH for 1,000 cycles (f).

The specific capacity achieved by CoS electrode is relatively low and the stability performance is also poor. These results are attributed to the agglomeration of the synthesized CoS particles. Therefore, to overcome this limitation, some conducting matrixes such as carbonaceous supports [11], and transition metal compounds [34] are used to prevent the agglomeration of CoS particles.

2.4 Preparation of CoS/rGO and CoS/poly-ethylenedioxythiophene (PEDOT)-Fe-900 ℃ (PF-9)

Here, both rGO and PF-9 are used as conducting matrix, respectively.

2.4.1 Preparation of reduced graphene oxide (rGO)

2.4.1.1 Preparation of graphene oxide (GO)

GO is prepared using the modified Hummers' method [35]. 40 mL of H_2SO_4 (98 wt%) was added to a mixture of 1 g of graphite powder and 1 g of $NaNO_3$ under stirring while keeping the temperature at 0~5 ℃ in an ice bath. After that, 6 g of $KMnO_4$ was added slowly. The mixture was stirred for 90 min at 0~5 ℃ and another 90 min at 35 ℃. Subsequently, 200 mL of Milli-Q water and 10 mL of H_2O_2 (30 wt%) were added into the solution. The obtained GO was washed repeatedly with HCl (5 wt%) aqueous solution (3 times) and Milli-Q water (4 times). The suspension was centrifuged at 2000 rpm for 5 times and the supernatant was kept.

2.4.1.2 Preparation of rGO

50 mL of a homogeneous (2.3 wt %) GO aqueous solution were placed in a round-bottom flask and sonicated for 30 min. After that, 3 mL of ammonia (35 wt%) was added with mechanical stirring. After 30 min, 200 μL of hydrazine was added to the mixture with mechanical stirring. Then, the flask was heated at 90 ~100℃ After 12 h, the obtained black rGO precipitate was washed with water and ethanol until the pH reached 7.

2.4.2 Preparation of PF-9

Based on Bhanges' work [30], 2 mL of EDOT monomer was dissolved in 80 mL of 1 M HCl solution using 1 g of CTAB as the surfactant at room temperature. 5 g of ammonium persulfate in 20 mM of 1 M HCl was added dropwise to the EDOT solution to initiate the polymerization reaction. It was followed by the addition of 9.1 g of iron chloride hexahydrate solution into 20 mL of 1 M HCl solution. This mixture was kept for a period of 24 h with constant stirring. The suspension containing the polymer and transition metal salt was dried at 80 ℃ with stirring. This product was termed as PEDOT-Fe. PEDOT-Fe was annealed for 1 h at 900 ℃ in an argon atmosphere for carbonization. The resulting black colored powder was dispersed in 0.5 M H_2SO_4 and stirred at 80 ℃ for 8 h. The acid-washed sample was further annealed for 1 h in an argon atmosphere to get the final product. The product named as PF-900 represents the annealed PEDOT-Fe at 900 ℃.

After that, composite materials of CoS/rGO and CoS/PF-9 were prepared by using rGO or PF-9 as a conducting matrix, respecitvely (**Fig. 2.5**).

2.4.3 Preparation of CoS/rGO

238 mg of $CoCl_2$•$6H_2O$ were added to 20 mL of an aqueous solution containing 1g of PVP and certain amounts of rGO. After that, 286.5 μL of ammonia (35 wt%) were dropped into the above solution under vigorous magnetic stirring at room temperature. After 24 h, the formed precipitate was washed with water and ethanol until the pH was about 7. The obtained product was re-dissolved into 30 mL of water for further use.

The sulfurization process was similar to that used for the preparation of CoS. Here, 100 mg of thioacetamide (TAA) was dissolved into 10 mL Milli-Q water, and then mixed with 10 mL of the above solution under magnetic stirring at room temperature. After 30 min, the solution was heated at 130 ℃ for 5 h. After natural cooling to room temperature, the resulting black solid product was collected through centrifugation, then washed with water and ethanol, and dried at 60 ℃ overnight.

The sample was labeled as CoS/rGO. To know the effect of rGO on electrochemical activity, the process was repeated using different amounts of rGO (10, 15, 20 mg) keeping 0.05 M concentration of the $CoCl_2$•$6H_2O$. The samples were labeled as CoS/rGO 10, CoS/rGO 15, CoS/rGO 20, respectively.

2.4.4 Preparation of CoS/ PF-9

Similarly, the CoS/PF-9 sample was synthesized through a similar method, where rGO was replaced by PF-9.

238 mg of $CoCl_2$•$6H_2O$ was added to 20 mL of an aqueous solution containing 1g of PVP and 15 mg PF-9. After that, 286.5 μL of ammonia (35 wt%) was dropped into the above solution under vigorous magnetic stirring at room temperature. After 24 h, the formed precipitate was washed with water and ethanol until the pH was about 7. The obtained product was re-dissolved into 30 mL of water for further use.

100 mg of thioacetamide (TAA) was dissolved into 10 mL Milli-Q water and then mixed with 10 mL of the above solution under magnetic stirring at room temperature. After 30 min, the solution was heated at 130 ℃ for 5 h. After natural cooling to room temperature, the resulting black solid product was collected through centrifugation, then washed with water and ethanol, and dried at 60 ℃ overnight.

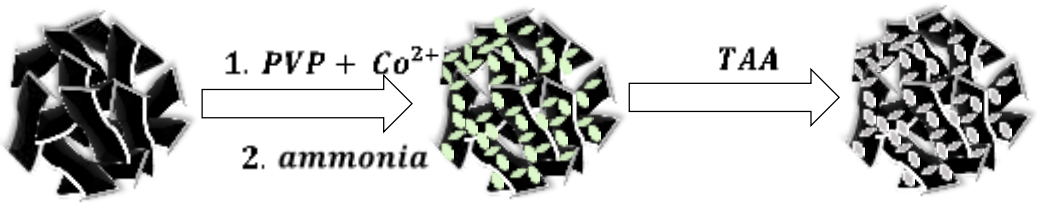

Figure 2.5: Schematic illustration of the synthesis of CoS/rGO and CoS/PF-9 composites, respectively.

2.5 Characterization of CoS/carbonaceous (rGO or PF-9)

2.5.1 Structural characterization of CoS/rGO

The crystal structure of as-prepared CoS/rGO15 composite was determined by XRD technique (**Fig. 2.6a**). Diffraction peaks at 2θ values of ~30.7˚, 35.6˚, 47.1˚ and 54.9˚, corresponding to the (100), (101), and (102) and (110) diffraction planes, respectively, can be well indexed to the hexagonal phase of CoS (JCPDS card No. 65-3418). Apart from CoS peaks, a broad peak ranging from ~ 15.0 °to 28.0 °confirms the presence of rGO and PVP, while other diffraction peaks between 15.0 ° and 25.0 ° indicate the formation of orthorhombic sulfur impurities in the composite (JCPDS card No. 08-0247). In addition, the presence of weak and broad diffraction peaks suggest that the composite has a low crystallinity.

The morphology of the prepared CoS/rGO 15 sample was examined by SEM (**Fig. 2.6b**), where flake-like rGO sheets covered with CoS nano-spheres can be easily distinguished. This 3D architecture seems to be helpful to prevent the agglomeration of CoS particles, and is expected to exhibit an improved electrochemical performance than bare CoS particles.

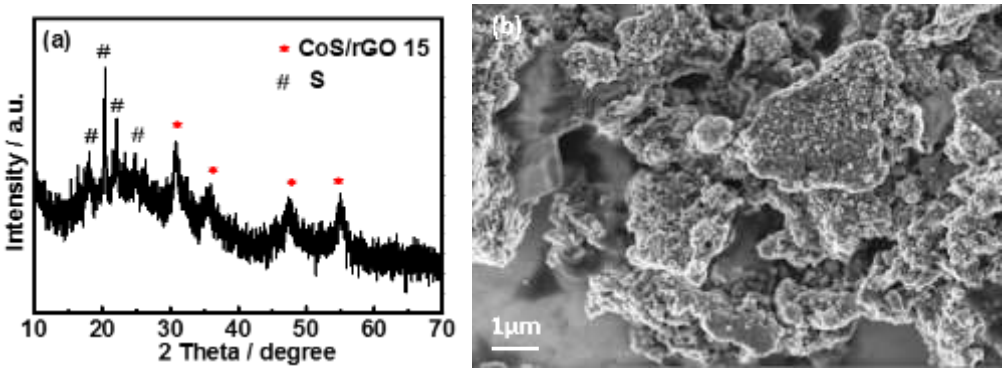

Figure 2.6: XRD pattern (a), and SEM image of CoS/rGO 15 sample (b).

2.5.2 Electrochemical performance of CoS/rGO electrodes

The CV curves of CoS/rGO 10 at different scan rates are depicted in **Fig. 2.7a**. Redox peaks, observed within the operating potential window (0 to +0.55V), are attributed to the reversible faradaic redox reactions of CoS to CoSOH and CoSOH to CoSO, respectively. Furthermore, the current response enhances as the scan rate increases from 5 to 100 mV/s, while the general shape of the CV plots is not altered, indicating that the electrode exhibits a good rate capability.

Fig. 2.7b and **c** depict the CV plots of CoS/rGO 15 and CoS/rGO 20 electrodes, respectively. The CV shapes of both electrodes are similar to those recorded for CoS/rGO 10 electrode, except the current response. Indeed, the current density of CoS/rGO 15 electrode within the potential window is much larger than that of CoS/rGO 10 electrode and slightly larger than that of CoS/rGO 20 electrode, indicating that the CoS/rGO 15 electrode material has higher electrochemical activity.

The CV curves of different CoS/rGO electrodes at a scan rate of 10 mV/s are depicted in **Fig. 2.7d**. The current response and the integrated area of the CoS/rGO 15 electrode within the operating potential window are larger than that of other CoS/rGO electrodes, indicating that the CoS/rGO 15 electrode material has higher electrochemical activity. Moreover, the specific capacity, deduced from the CV curves (**Fig. 2.7e**), further confirms an enhanced specific capacity of the composite electrode materials and CoS/rGO 15 exhibits the highest specific capacity value (~241 C g^{-1}), as compared to CoS/rGO 20 (~207 C g^{-1}), CoS/rGO 10 (~195 C g^{-1}) and CoS (190 C g^{-1})).

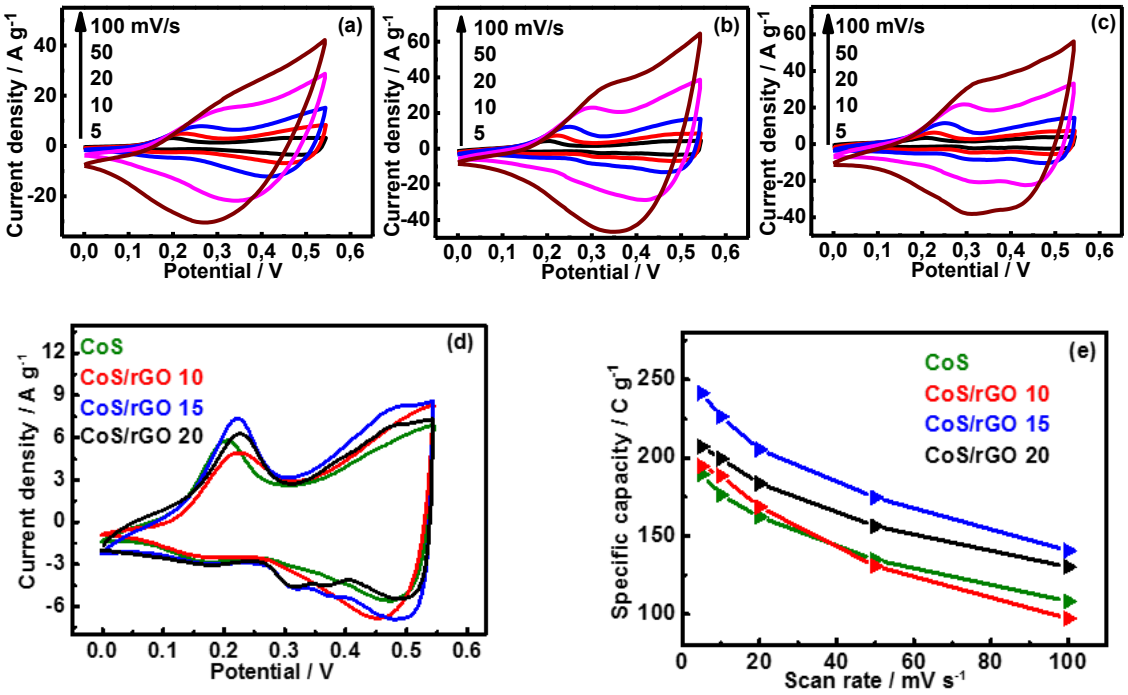

Figure 2.7: CV curves of CoS/rGO 10 (a), CoS/rGO 15 (b), CoS/rGO 20 (c) electrodes, comparison of CV curves at a scan rate of 10 mV/s (d), specific capacity of all CoS/rGO electrodes at different scan rates (e).

The GCD plots of CoS/rGO electrodes, prepared using different amounts of rGO during the precipitation process, are recorded and the corresponding GCD curves at different current densities are displayed in **Fig. 2.8a**, **b**, and **c**. Here, the humps detected in all GCD curves confirm the existence of faradaic reactions. Moreover, consistent with obtained results from the CV curves, CoS/rGO 15 electrode (**Fig. 2.8b**) displays a prolonged time for the charging/discharging process at the same current density, demonstrating higher electrochemical activity.

The discharging curves of all CoS/rGO electrodes at 1 A g^{-1} are also depicted in **Fig. 2.8d**. The time for discharging process (242s) of CoS/rGO 15 is larger than that of other electrodes (CoS/rGO 20 (220s), CoS/rGO 10 (202s) and CoS (142s)). This electrode displays a maximum specific capacity of ~243 C g^{-1} at a current density of 0.5 A g^{-1} (**Fig. 2.8e**), which is higher than that of CoS/rGO 20 (~221 C g^{-1}) and CoS/rGO 10 (~210 C g^{-1})) and is about 1.5 times larger than that of bare CoS electrode (~161 C g^{-1}), indicating that the addition of rGO as a conducting matrix has a pronounced effect on the electrochemical properties. Furthermore, the electrode maintains ~ 80% of its initial specific capacity, as the current density increases from 0.5 to 10 A g^{-1}.

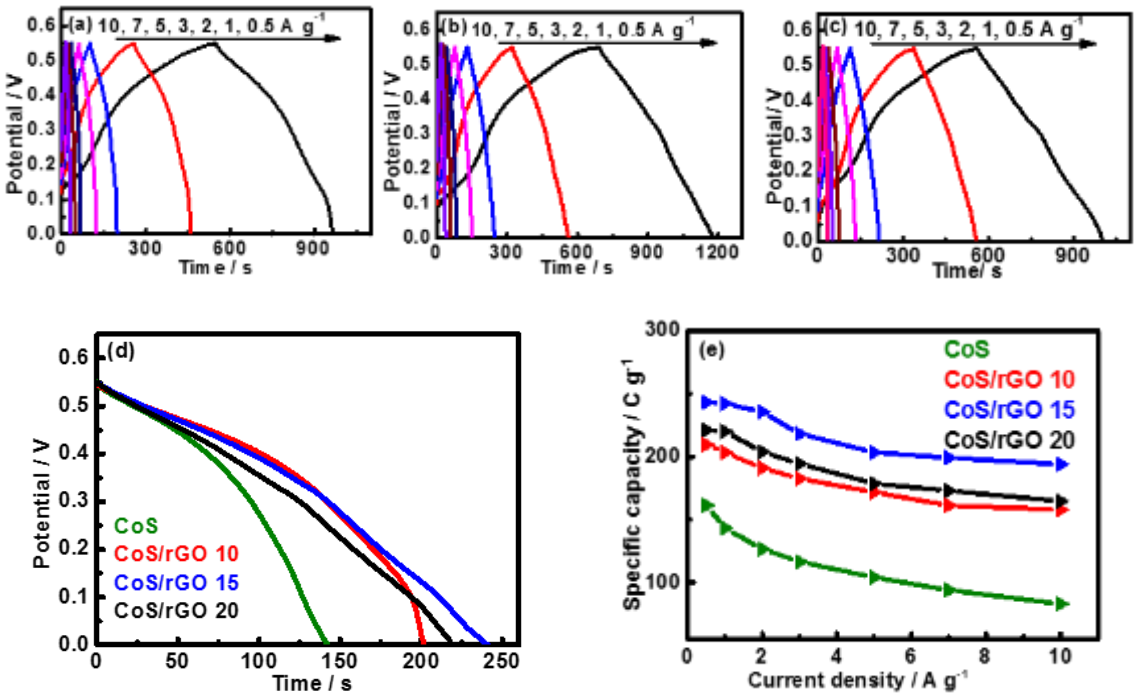

Figure 2.8: GCD curves of CoS/rGO 10 (a), CoS/rGO 15 (b), and CoS/rGO 20 (c) electrodes, comparison of discharge curves at a scan rate of 1 A g^{-1} (d), specific capacity of all CoS/rGO electrodes at different current densities (e).

EIS analysis is used to investigate the frequency-dependent behavior of different CoS/rGO electrodes. **Fig. 2.9a** depicts the Nyquist plots of all CoS/rGO electrodes. The depressed semi-circles in the high-medium frequency region and sloped lines in the low-frequency region could be detected in all Nyquist plots, and this phenomenon is ascribed the electrolyte ion (OH^-) diffusion. From the fitted equivalent circuit (**Fig. 2.9b**), R_s and R_{ct} values for all CoS/GO electrodes are determined (**Table 2-1**). The R_s and R_{ct} values of CoS/rGO electrodes are smaller than that of bare CoS electrode, indicating that the addition of rGO as a conducting matrix could improve the electrical conductivity, and among them, the CoS/rGO 15 electrode exhibits the smallest series resistance (0.90 ohm cm^{-2}) and charge transfer resistance (4.25 ohm cm^{-2}).

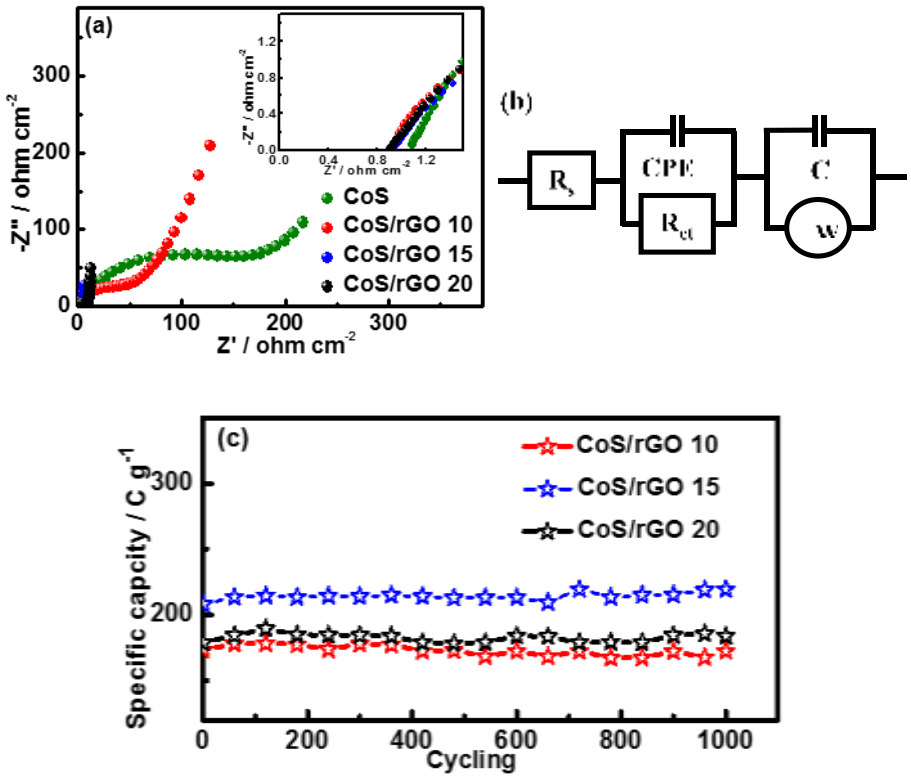

Figure 2.9: Nyquist plots of all CoS/rGO electrodes (a), the corresponding equivalent circuit (b), stability performance of all CoS/rGO electrodes at 5 A g^{-1} in 2M KOH for 1,000 cycles (c).

Table 2-1: Values of R_s and R_{ct} for all CoS/rGO electrodes.

Electrode	R_s (ohm·cm^{-2})	R_{ct} (ohm·cm^{-2})
CoS	1.07	143.10
CoS/rGO 10	0.94	79.05
CoS/rGO 15	0.90	4.25
CoS/rGO 20	0.91	9.27

Fig. 2.9c shows the stability performance of all CoS/rGO electrodes at 5 A g^{-1}. Almost no obvious decrease is detected in the cycling plots after 1,000 cycles, demonstrating the good cycling stability of CoS/rGO electrodes. CoS/rGO 15 electrode achieves the highest specific capacity during the stability test (from ~208 C g^{-1} in the 1st cycle to ~219 C g^{-1} in the 1,000th cycle at 5 A g^{-1}), as compared with that of other CoS/rGO electrodes (CoS/rGO 20 (from ~179 C g^{-1} in the 1st cycle to ~184 C g^{-1} in the 1,000th cycle) and CoS/rGO 10 (from ~173 C g^{-1} in the 1st cycle to ~172 C g^{-1} in the 1,000th cycle) at 5 A g^{-1}).

Based on the results of electrochemical measurements, all CoS/rGO electrodes exhibited enhanced supercapacitor performance with CoS/rGO 15 being the best electrode.

2.5.3 Structural characterization of CoS/PF-9

The crystal structure of the as-prepared CoS/PF-9 composite was assessed by the XRD technique (**Fig. 2.10a**). Diffraction peaks at 2θ values of ~30.7 °and 54.9 °, corresponding to the (100) and (110) diffraction planes, respectively, can be well indexed to the hexagonal phase of CoS (JCPDS card No. 65-3418). Apart from CoS peaks, a broad peak ranging from ~15 °to 28 ° reveals the presence of PF-9 and PVP, while other diffraction peaks between ~15.0 °and 25.0 ° indicate the formation of orthorhombic sulfur impurities in the obtained sample (JCPDS card No. 08-0247). Besides, the presence of weak and broad diffraction peaks in the XRD pattern suggests that the composite has a low crystallinity.

XPS measurements were carried out to analyze the chemical composition of the CoS/PF-9 composite. **Fig. 2.10b** displays the XPS survey spectrum of CoS/PF-9. It consists of C_{1s} (~284.8 eV), Co_{2p} (~780.1 eV), S_{2p} (~162.1 eV), O_{1s} (~531.6 eV) and N_{1s} (~399.6 eV). The presence of high oxygen signal may be due to the remaining PVP stabilizer. The high-resolution spectrum of the Co_{2p} (**Fig. 2.10c**) comprises $Co_{2p3/2}$ and $Co_{2p1/2}$ spin-orbit peaks at ~780.4 and 795.7 eV, respectively, suggesting the existence of Co (II). No peak assigned to Co (III) could be detected, indicating that the addition of PF-9 could prevent the oxidation of Co during the chemical precipitation and ion-exchange reaction processes. The S_{2p} core level spectrum (**Fig. 2.10d**) can be deconvoluted with two peaks at ~161.2 and 162.6 eV attributed to the $S_{2p3/2}$ and $S_{2p1/2}$, respectively. From XPS analysis results, the CoS in CoS/PF-9 consists of Co^{2+} and S^{2-}.

The morphology of CoS/PF-9 composite was examined using SEM (**Fig. 2.10e** and **f**). As a comparison, the SEM image of bare PF-9 is also presented in **Fig. 2.10g**. From the SEM image of CoS/PF-9 (**Fig. 2.10e**), similar to that of CoS/rGO 15 (**Fig. 2.6b**), CoS nano-spheres are uniformly and densely anchored throughout the sheet-like framework of PF-9. By comparing the SEM images of both CoS/PF-9 (**Fig. 2.10f**) and bare PF-9 (**Fig. 2.10g**), the framework of CoS/PF-9 is much more compact than that of bare PF-9 due to the introduction of CoS nanospheres. Besides, a crumbled nature made up of flakes and nanoparticles could be observed from the surface of PF-9 **(Fig. 2.10g**). These flakes and nanoparticles are expected to provide a large number of nucleation sites for the growth of CoS particles.

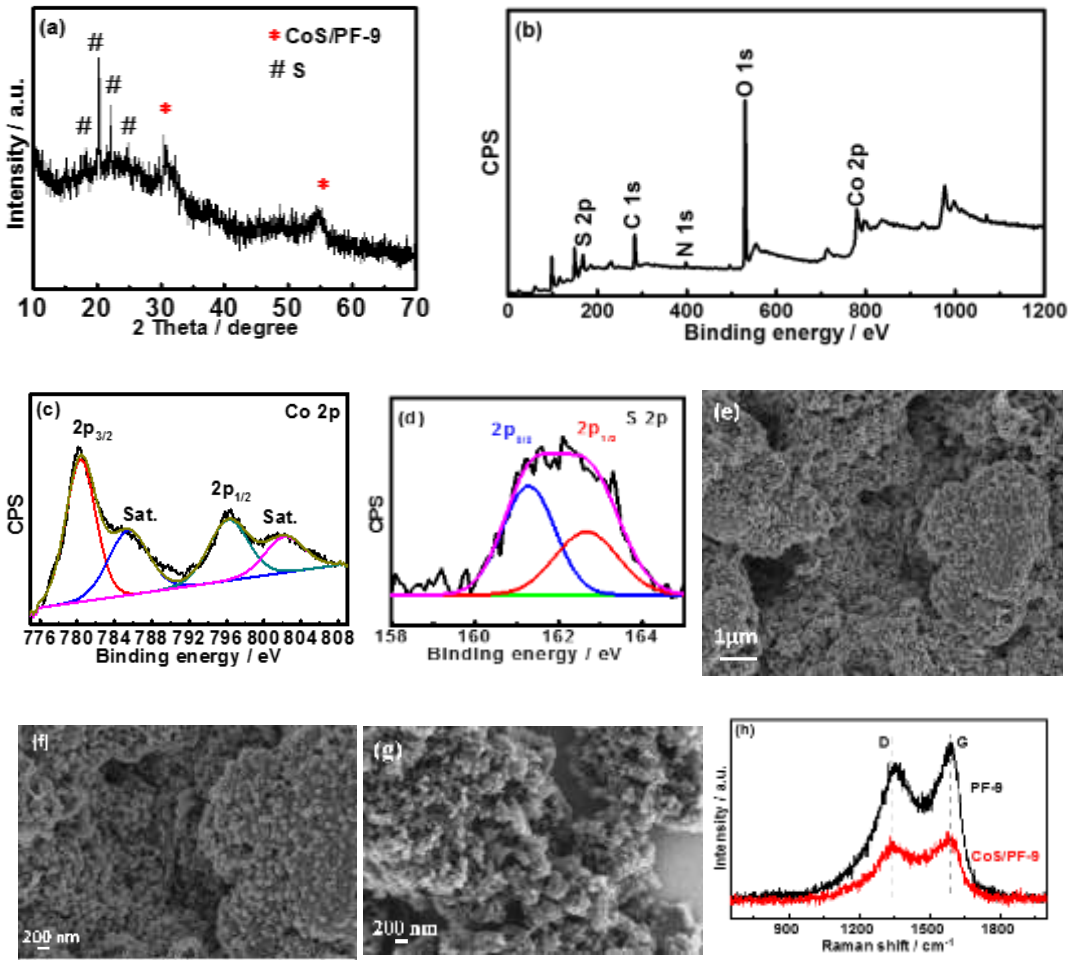

Figure 2.10: Structural characterization of CoS/PF-9: XRD pattern (a); XPS full spectrum (b), and high-resolution spectra of Co_{2p} (c) and S_{2p} (d); SEM image of CoS/PF-9 (e); SEM images of bare PF-9 (f), (g), Raman spectra of bare PF-9 and CoS/PF-9 (h).

Raman spectroscopy of bare PF-9 and CoS/PF-9 is also provided in **Fig. 2.10h**. For bare PF-9, two peaks at ~1346 and 1590 cm^{-1}, assigned respectively to the D and G bands, are observed. The D band, corresponding to the breathing mode of sp^2 atoms in rings in carbonaceous material, is related to structural defects and disorders, and the G band is due to the bond stretching of all pairs of sp^2 atoms in both rings and chains. The appearance of both D and G bands in PF-9 suggests that there are abundant defects and amorphous carbon [29]. The ratio of I_D/I_G peak intensity is used to quantify the defects present on carbonaceous composites. Compared with PF-9, the I_D/I_G intensity ratio of the CoS/PF-9 (~0.96) is slightly higher than that of bare PF-9 (~0.89), indicating that the decoration of CoS particles on the surface of PF-9 results in a more disordered carbon structure and decrease of sp^2 carbon domains when CoS nanoparticles are inserted throughout the framework of PF-9 [36, 37].

2.5.4 Electrochemical performance of CoS/PF-9

Fig. 2.11 summarizes the electrochemical characterization of CoS/PF-9. **Fig. 2.11a** corresponds to the CV curves of CoS/rGO, CoS/PF-9, and bare CoS electrodes at a scan rate of 10 mV/s. Oxidation and reduction peaks, observed in all CV curves within the operating potential window (0 to +0.55V), are believed to be caused by the reversible faradaic redox reaction of Co-S-OH. Furthermore, the CoS/PF-9 electrode, compared with CoS and CoS/rGO electrodes, gives the largest integrated cyclic area. The area enclosed by CV curves are assigned to charge storage capability, and the larger area the electrode offers, the higher charge storage ability it could provide. Obviously, CoS/PF-9 electrode has the best charge storage ability. **Fig. 2.11b** displays the CV curves of CoS/PF-9. Oxidation and reduction peaks could be observed in all CV curves in the selected potential region. The appearance of redox peaks indicates that there are faradaic reactions of CoS/PF-9 in 2M KOH. Moreover, as the scan rate increases, the position of redox (oxidation and reduction) peaks shifts to more positive and negative potential, respectively, which may be caused by the limitation of the ion interaction [8]. The specific capacity, calculated according to obtained CV curves, is shown in **Fig. 2.11c**. For comparison, the calculated specific capacity values of rGO/CoS and CoS are also given. Among them, the CoS/PF-9 electrode demonstrates the highest specific capacity of ~264 C g^{-1} at 5 mV s^{-1}, which is about 1.4 times that of bare CoS (~190 C g^{-1}), and about 1.1 times that of CoS/rGO (~241 C g^{-1}). In addition, it could be seen that the specific capacity decreases as the scan rate increases and this phenomenon is believed to be caused by the reduction of effective interaction between the ions and electrode surface. There is not enough time for OH^- ions to intercalate through the interface between the electrolyte and electrode at a larger scan rate.

The GCD curves of CoS/rGO, CoS/PF-9, and bare CoS, conducted at a current density of 1 A g^{-1} in the potential range of 0 to +0.55 V, are depicted in **Fig. 2.11d.** The GCD curves of all electrodes show some slight curvature, signifying the existence of faradaic reactions. The discharge time is also assigned to a specific capacity. The longer discharge time the electrode offers; the larger the specific capacity it provides. Based on the discharge time from GCD curves (**Fig.2.11e**), the specific capacity is calculated (**Fig. 2.11f**). For comparison, the calculated specific capacity values of CoS and CoS/rGO electrodes are also provided. CoS/PF-9 electrode exhibits a specific capacity of ~275 C g^{-1} at 0.5 A g^{-1}, which is about 1.7 times that of pure CoS nanoparticles (~161 C g^{-1}), and about 1.1 times that of CoS/rGO (~243 C g^{-1}).

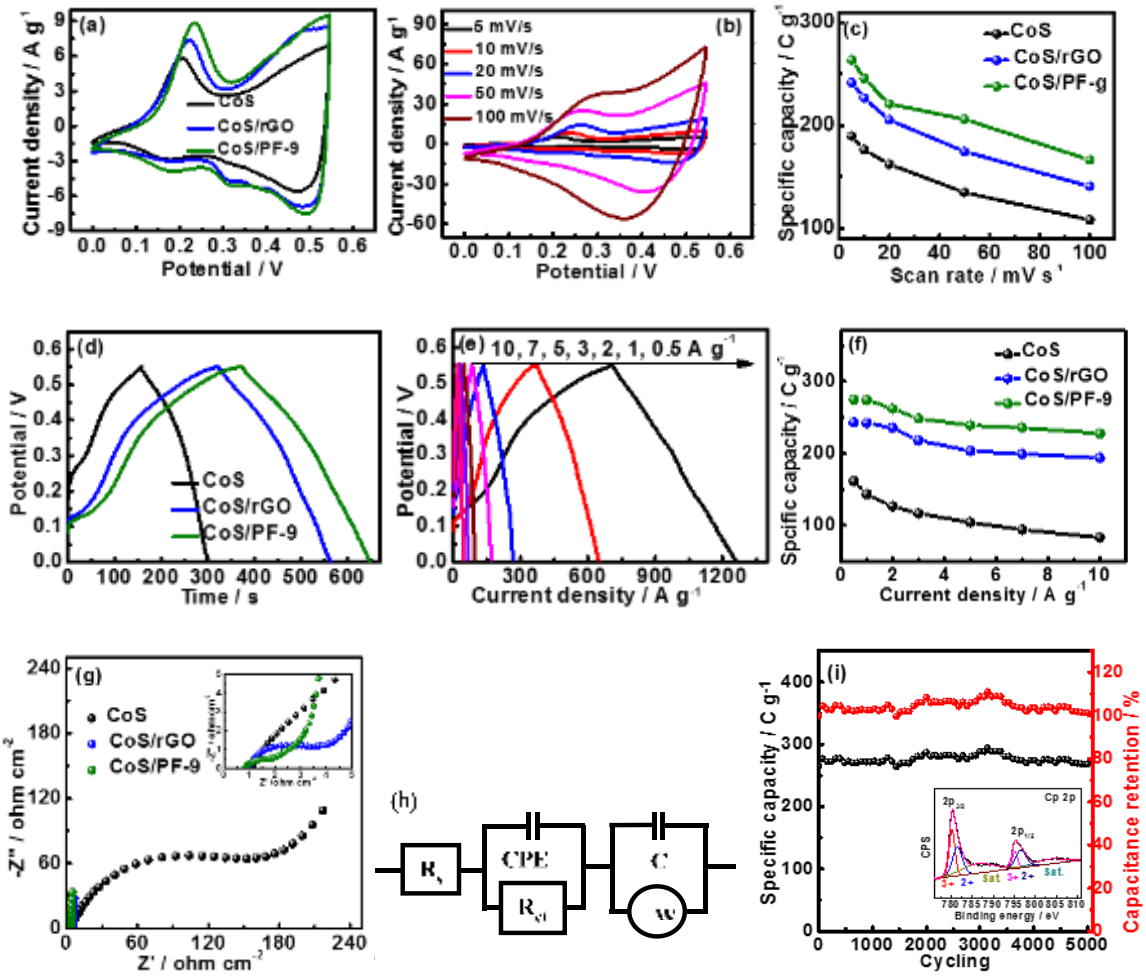

Figure 2.11: Electrochemical properties of CoS/PF-9 in KOH (2 M): (a) CV curves of CoS, CoS/rGO, and CoS/PF-9 at a scan rate of 10 mV s^{-1} in the potential window of 0 to +0.55V; (b) CV curves of CoS/PF-9 at different scan rates, (c) the corresponding specific capacity deduced from (b), (d) GCD profiles at a current density of 1 A g^{-1}; (e) GCD curves of CoS/PF-9 at various current densities, (f) the corresponding specific capacity calculated from (d), (g) Nyquist plots; (h) the corresponding equivalent circuit; (i) Cycling performance of CoS/PF-9 nanocomposite at 5 A g^{-1} for 5000 cycles, inset shows Co_{2p} spectrum of CoS/PF-9 after 5,000 cycles.

Fig. 2.11g displays the Nyquist plots of CoS/rGO, CoS/PF-9, and bare CoS electrodes in the frequency range of 100 kHz to 0.01 Hz. It could be observed that all electrodes have incomplete depressed semi-circles in the high-medium frequency region. As the intercept at the high-frequency region stands for the series resistance (from the electrolyte and the contact between the electrode material and the collector), it could be seen that all electrodes exhibit a similar series resistance. Originally, a bigger semi-circle indicates the electrode has a larger charge transfer resistance (R_{ct}). Therefore, CoS/rGO and CoS/PF-9 materials exhibited much smaller R_{ct} values with R_{ct} of CoS/PF-9 being slightly smaller than that of CoS/rGO. A sloped

line, associated with the diffusion of electrolyte OH^-, is also detected in the low-frequency region. Based on the fitted equivalent circuit (**Fig. 2.11h**), the values of R_s and R_{ct} for all electrodes are summarized in **Table 2-2**. The electrode CoS/PF-9 displays the smallest values for R_s (0.81 ohm cm^{-2}) and R_{ct} (2.73 ohm cm^{-2}).

Table 2-2: Values of R_s and R_{ct} for all electrodes.

Electrode	R_s (ohm·cm^{-2})	R_{ct} (ohm·cm^{-2})
CoS	1.07	143.10
CoS/rGO	0.90	4.25
CoS/PF-9	0.81	2.73

CoS/rGO and CoS/PF-9 electrodes achieve higher capacity than CoS nanoparticles under the same conditions (**Fig. 2.11c** and **f**), and the CoS/PF-9 electrode provides a slightly higher value than CoS/rGO and smaller values for R_s and R_{ct}.

Moreover, the cycling ability and capacity retention of CoS/PF-9 is also investigated at a current density of 5 A g^{-1} for 5,000 cycles. From **Fig. 2.11i**, it could be seen that there is no noticeable decrease after 5,000 cycles, indicating good cycling stability of the as-prepared CoS/PF-9 electrode. The high-resolution XPS spectrum of CoS/PF-9 after 5,000 cycles (inset of **Fig. 2.11i)** shows the presence of $Co_{2p3/2}$ and $Co_{2p1/2}$ spin-orbit peaks. The peaks at ~779.9 and 794.9 eV are assigned respectively to the $2p_{3/2}$ and $2p_{1/2}$ core levels of Co^{3+}, whereas the peaks at ~781.2 and 796.3 eV are ascribed to the $2p_{3/2}$ and $2p_{1/2}$ core levels of Co^{2+}, respectively, suggesting that part of the Co (II) turned into Co (III) oxidation state after 5,000 cycles.

2.6 Electrochemical evaluation of PF-9//CoS/PF-9 asymmetric supercapacitor

To further evaluate the practical usage of the CoS/PF-9 electrode, an ASC device, made up of CoS/PF-9 as a positive electrode and PF-9 as a negative electrode, is fabricated. The working voltage window of the asymmetric supercapacitor is optimized based on the working potential range of PF-9 and CoS/PF-9 in a 3-electrode system.

2.6.1 Electrochemical performance of PF-9 as a negative electrode

The electrochemical performance of bare PF-9 is depicted in **Fig. 2.12.** No obvious oxidation and reduction peaks could be detected in the selected potential region (-0.7 to +0.3 V) (**Fig. 2.12a**), suggesting that energy storage takes place mainly through EDLC behavior.

The CV curves of PF-9 electrode remain nearly rectangular without obvious distortion, even when the scan rate increases to 100 mV/s, revealing that an efficient electric double layer is established in the electrode. Based on equation **7-2**, the specific capacitance of prepared PF-9 is calculated and shown in **Fig. 2.12b**. The electrode PF-9 provides a maximum specific capacitance of ~ 60 F g^{-1} at 5 mV/s.

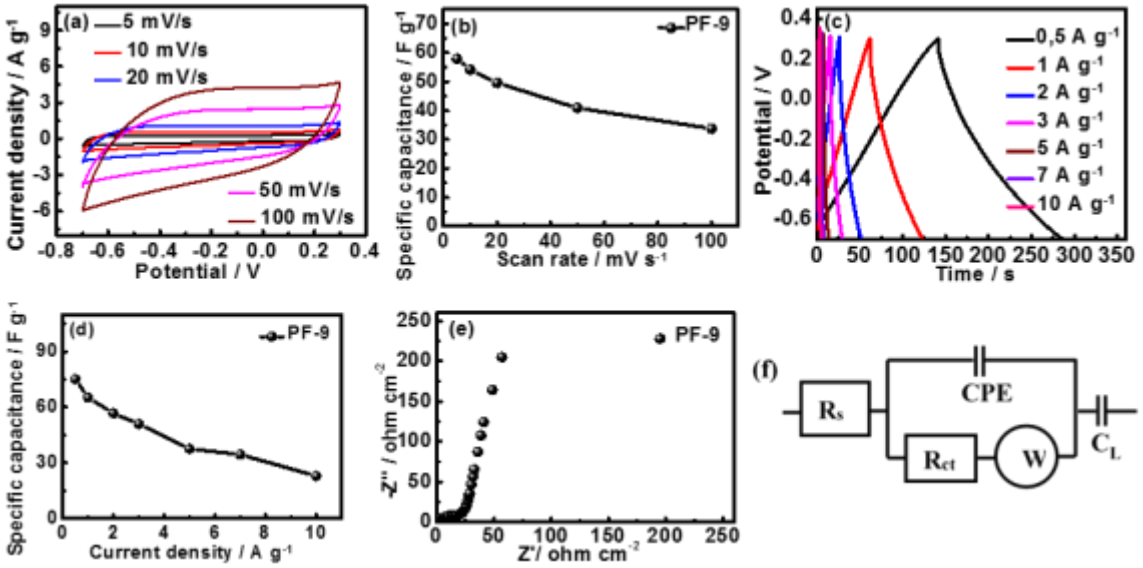

Figure 2.12: Electrochemical performance of PF-9. CV curves (a), the corresponding specific capacitance at different scan rates (b), GCD curves (c), the corresponding specific capacitance at different current densities (d), Nyquist plots (e), and the corresponding equivalent circuit (f).

Typical GCD curves of PF-9 electrode in the operating potential window from -0.7 to +0.3 V at different current densities (0.5 to 10 A g^{-1}) are displayed in **Fig. 2.12c**. The shape of all GCD curves is triangle-like, proving also that no redox pseudocapacitive behavior occurs. Using equation **7-3**, the specific capacitance of the electrode PF-9, calculated from **Fig. 2.12c** is depicted in **Fig. 2.12d**. The electrode PF-9 provides a maximum value of ~75 F g^{-1} at 0.5 A g^{-1}). **Fig. 2.12e** and **f** display the Nyquist plot and the equivalent circuit, respectively. The values of R_s and R_{ct} are determined to be ~ 0.84 and 22.95 ohm cm^{-2}, respectively.

2.6.2 Electrochemical evaluation of the PF-9//CoS/PF-9 asymmetric supercapacitor

Fig. 2.13a depicts the working potential window of PF-9 (-0.7~+0.3 V *vs.* Hg/HgO) and CoS/PF-9 (0~+0.55 V *vs.* Hg/HgO) electrodes at a scan rate of 10 mV/s. According to the individual electrode potential range, the cell voltage of the fabricated ASC is fixed at 1.25 V.

To investigate the range of operating cell voltage window of the fabricated ASC, a series of CV curves of the assembled ASC at different cell voltage windows are acquired at 50 mV/s (**Fig. 2.13b**). The fabricated ASC could maintain the shape of CV curves as the cell voltage window increases to 1.5 V. The GCD curves of the fabricated ASC at different cell voltage windows are also determined (**Fig. 2.13c**). Based on the CV and GCD curves of the fabricated ASC, 1.5V is chosen as the cell voltage for further characterization of the electrochemical properties.

The typical CV curves of the fabricated ASC in a cell voltage window of 1.5 V (**Fig. 2.13d**) show no obvious oxidation or reduction peaks, and also, no noticeable change in the shape of the CV curves could be observed as the scan rate increases from 10 to 75 mV/s. The GCD curves of the fabricated ASC in the operating cell voltage window of 1.5V at various current densities ranging from 0.5 to 5A g^{-1} are depicted in **Fig. 2.13e**. Here, the humps detected in all GCD curves confirm the existence of faradaic behavior of electrode materials. Typical Nyquist plots of the fabricated ASC cell and the equivalent circuit are both shown in **Fig. 2.13f**. R_s and R_{ct} values of ~ 0.53 and 7.30 ohm cm^{-2} are obtained respectively for the fabricated ASC device. The variation of the specific capacity, calculated from the CV curves, is given in **Fig. 2.13g**. A maximum specific capacity of the flexible ASC device is determined to be ~ 30 C g^{-1} at a scan rate of 10 mV s^{-1}.

According to equations **7-4** and **7-5**, the E_d and P_d values are calculated and compared with other ASCs from recent the literature [4, 24, 38, 39]. The Ragone plot of the fabricated ASC at the cell voltage of 1.5V is depicted in **Fig. 2.13h**. The energy density increases from 4.8 W h kg^{-1} to 7.6 W h kg^{-1} as the power density decreases from 4176 W kg^{-1} to 380 W kg^{-1}.

The cycling stability of the fabricated ASC is evaluated at a current density of 1 A g^{-1} over 5,000 cycles (**Fig. 2.13i**). The fabricated ASC device presents a good stability performance with an improved capacity retention (~ 1.4 times of its initial capacity) after 2,000 cycles. While, a slight decrease could be observed after 4,000 cycles, but still higher than that recorded after the 1^{st} cycle. The increase of the capacity retention is probably due to the activation process, in which electrolyte ions gradually penetrate the electrode material. Therefore, the capacity retention of the fabricated ASC cell increases at the early stage of repeated charging-discharging cycles. After 5,000 cycles, the capacity retention could remain at ~ 1.3 times of its initial specific capacity.

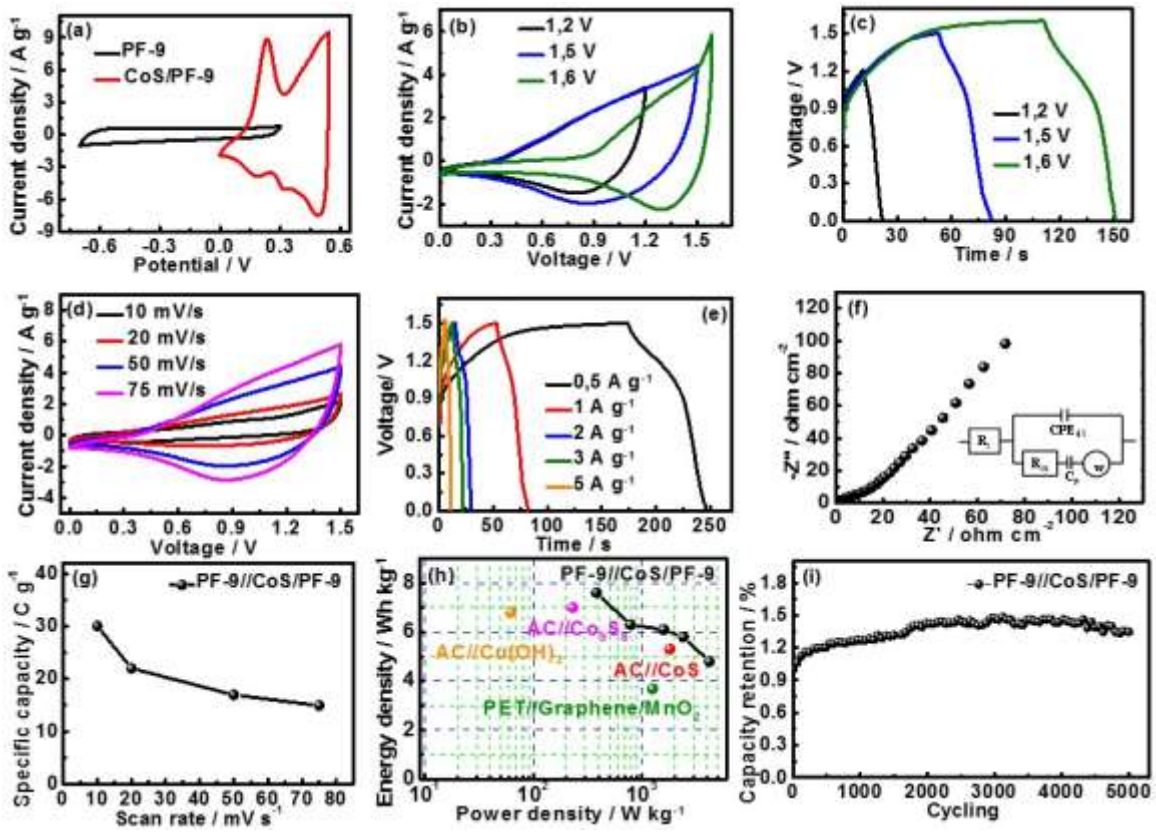

Figure 2.13: CV curves of the positive and negative electrodes at a scan rate of 10 mV/s (a), CV curves of ASC at different cell voltages recorded at a scan rate of 50 mV/s (b), GCD curves of the ASC at different cell voltages acquired at a current density of 1 A g^{-1} (c), CV curves of the ASC at different scan rates (5, 10, 20, and 50 and 100 mV s^{-1}) (d), GCD curves at different current densities (e), Nyquist plots (f), Specific capacity *vs.* scan rate (g), Ragone plot (P_d vs. E_d) (h), cycling stability at 1 A g^{-1} (i), the inset in (f) is the corresponding equivalent circuit.

In addition, in order to investigate the mechanical stability of the fabricated ASC, CV curves at 50 mV/s are also measured at different bending angles (from flat condition to 135 °), **Fig. 2.14.** As shown in **Fig. 2.14c**, no significant distortion in the CV curves could be observed even when the bending angle reaches 135 °, confirming a good flexibility of the fabricated ASC.

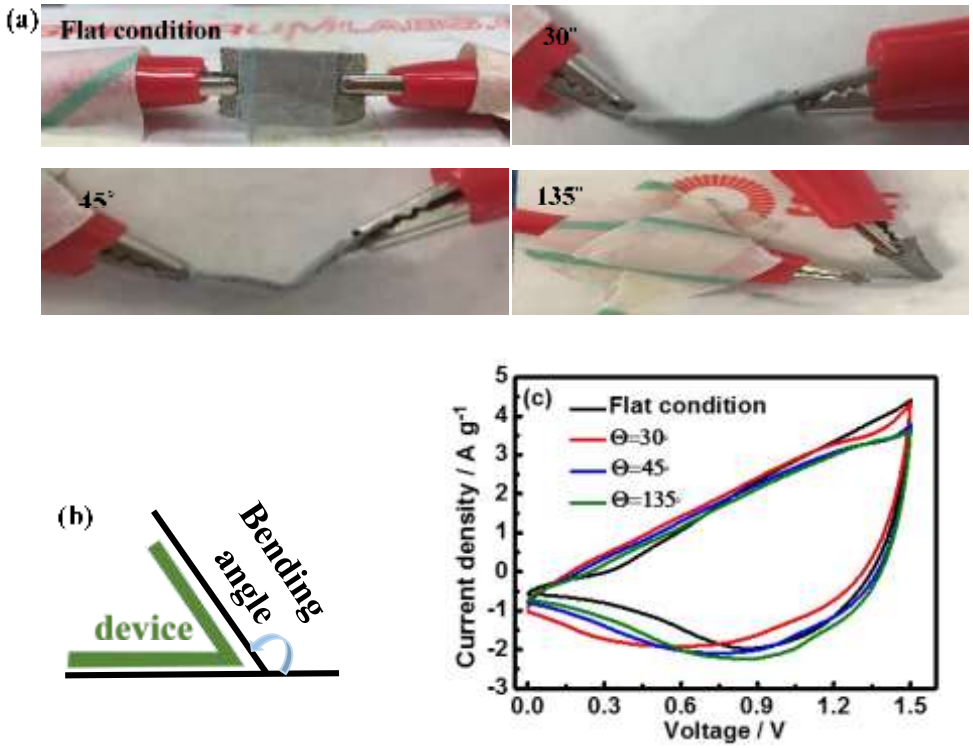

Figure 2.14: (a) Images of the bent cells, (b) Schematic illustration of the bent cell, (c) CV curves of the ASC at 50 mV/s under different bending angles of 0-135˚.

2.7 Conclusion

In summary, CoS and CoS/carbonaceous materials (rGO or PF-9) are synthesized through simple chemical precipitation and ion-exchange reaction method. The as-prepared CoS/ (rGO or PF-9) composites show enhanced electrochemical specific capacity values in comparison with bare CoS. In addition, CoS/PF-9 exhibits a slightly better electrochemical specific capacity (~275 C g^{-1} at 0.5 A g^{-1}) compared with that of CoS/rGO (~243 C g^{-1} at 0.5 A g^{-1}). Furthermore, the CoS/PF-9 composite also reveals good cycling stability with no obvious capacity decrease after 5,000 cycles. Moreover, a flexible asymmetric supercapacitor is assembled by using CoS/PF-9 and PF-9 as positive and negative electrodes, respectively. No significant distortion in the CV curves could be observed when the bending angle was varied from 0 ° to 135 °, confirming the good flexibility of the fabricated ASC cell. The ASC cell achieves an energy density of 7.6 W h kg^{-1} at a power density of 380 W kg^{-1}. The stability test also shows good cycling performance. After 5,000 cycles, the capacity retention remains at ~ 1.3 times of its initial specific capacity. The overall improved electrochemical performance of the CoS/PF-9 composite makes it a promising electrode material for practical applications.

2.8 References

[1] W. Li, S. Wang, L. Xin, M. Wu, X. Lou, Single-crystal β-NiS Nanorod Arrays with a Hollow-structured Ni_3S_2 Framework for Supercapacitor Applications, J. Mater. Chem. A 4 (2016) 7700-7709.

[2] Z. Dai, X. Zang, J. Yang, C. Sun, W. Si, W. Huang, X. Dong, Template Synthesis of Shape-Tailorable NiS_2 Hollow Prisms as High-Performance Supercapacitor Materials, ACS Appl. Mater. Interfaces 7 (2015) 25396-25401.

[3] J. Wang, K. Y. Ma, J. Zhang, F. Liu, J. P. Cheng, Template-free Synthesis of Hierarchical Hollow NiS_x Microspheres for Supercapacitor, J. Colloid Interface Sci. 507 (2017) 290-299.

[4] K. Subramani, N. Sudhan, R. Divya, M. Sathish, All-solid-state Asymmetric Supercapacitors based on Cobalt Hexacyanoferrate-derived CoS and Activated Carbon, RSC Adv. 7 (2017) 6648-6659.

[5] F. Luo, J. Li, H. Yuan, D. Xiao, Rapid Synthesis of Three-dimensional Flower-like Cobalt Sulfide Hierarchitectures by Microwave Assisted Heating Method for High-performance Supercapacitors, Electrochim. Acta 123 (2014) 183-189.

[6] Z. Yang, C. Y. Chen, H. T. Chang, Supercapacitors Incorporating Hollow Cobalt Sulfide Hexagonal Nanosheets, J. Power Sources 196 (2011) 7874-7877.

[7] F. L. Luo, J. Li, H. Y. Yuan, D. Xiao, Rapid Synthesis of Three-dimensional Flower-like Cobalt Sulfide Hierarchitectures by Microwave Assisted Heating Method for High-performance Supercapacitors, Electrochim. Acta 123 (2014) 183-189.

[8] J. X. Guo, X. Q. Zhang, Y. F. Sun, X. H. Zhang, L. Tang, X. Zhang, Double-shell CuS Nanocages as Advanced Supercapacitor Electrode Materials, J. Power Sources 355 (2017) 31-35.

[9] K. L. Jin, M. Zhou, H. b. Zhao, S. X. Zhai, F. Y. Ge, Y. P. Zhao, Z. S. Cai, Electrodeposited CuS Nanosheets on Carbonized Cotton Fabric as Flexible Supercapacitor Electrode for High Energy Storage, Electrochim. Acta 295 (2019) 668-676.

[10] T. L. Li, Z. C. Liu, L. Zhu, F. Dai, L. Hu, L. Zhang, Z. B. Wen, Y. P. Wu, Cr_2O_3 Nanoparticles: a Fascinating Electrode Material Combining both Surface-controlled and Diffusion-limited Redox Reactions for Aqueous Supercapacitors, J. Mater. Sci. 53 (2018) 16458-16465.

[11] L. L. Feng, M. H. Fan, Y. Y. Wu, Y. P. Liu, G. D. Li, H. Chen, W. Chen, D. J. Wang, X. X. Zou, Metallic Co_9S_8 Nanosheets Grown on Carbon Cloth as Efficient Bnder-free Electrocatalysts for The Hydrogen Evolution Reaction in Neutral Media, J. Mater. Chem. A 4 (2016) 6860-6867.

[12] J. Hao, W. Yang, J. Hou, B. Mao, Z. Huang, W. Shi, Nitrogen Doped NiS_2 Nanoarrays with Enhanced Electrocatalytic Activity for Water Oxidation, J. Mater. Chem. A 5 (2017) 17811-17816.

[13] T. Zhu, L. Zhu, J. Wang, G. Ho, In Situ Chemical Etching of Tunable 3D Ni_3S_2 Superstructures for Bifunctional Electrocatalysts for Overall Water Splitting, J. Mater. Chem. A 4 (2016) 13916-13922.

[14] A. Farisabadi, M. Moradi, S. Borhani, S. Hajati, M. A. Kiani, S. A. Tayebifard, Synthesis and Electrochemical Properties of Mg-doped Chromium-based Metal Organic Framework/Reduced Graphene Oxide Composite for Supercapacitor Application, J. Mater. Sci-mater. El. 29 (2018) 8421-8430.

[15] X. Zheng, X. Han, Y. Zhang, J. Wang, C. Zhong, Y. Deng, W. Hu, Controllable Synthesis of Nickel Sulfide Nanocatalysts and Their Phase-dependent Performance for Overall Water Splitting, Nanoscale 11 (2019) 5646-5654.

[16] N. Zhang, W. Wang, C. Teng, Z. Wu, Z. Ye, M. Zhi, Z. Hong, Co_9S_8 Nanoparticle-decorated Carbon Nanofibers as High-performance Supercapacitor Electrodes, RSC Adv. 8 (2018) 27574-27579.

[17] S. Venkateshalu, P. Goban Kumar, P. Kollu, S. K. Jeong, A. N. Grace, Solvothermal Synthesis and Electrochemical Properties of Phase Pure Pyrite FeS_2 for Supercapacitor Applications, Electrochim. Acta 290 (2018) 378-389.

[18] K. Krishnamoorthy, P. Pazhamalai, S. J. Kim, Ruthenium Sulfide Nanoparticles as a New Pseudocapacitive Material for Supercapacitor, Electrochim. Acta 227 (2017) 85-94.

[19] R. K. Mishra, G. W. Baek, K. Kim, H. I. Kwon, S. H. Jin, One-step Solvothermal Synthesis of Carnation Flower-like SnS_2 as Superior Electrodes for Supercapacitor Applications, Appl. Surf. Sci. 425 (2017) 923-931.

[20] J. He, Y. Chen, P. Li, F. Fu, Z. Wang, W. Zhang, Self-assembled CoS_2 Nanoparticles Wrapped by CoS_2-quantum-dots-anchored Graphene Nanosheets as Superior-capability Anode for Lithium-ion Batteries, Electrochim. Acta 182 (2015) 424-429.

[21] Y. N. Ko, S. H. Choi, S. B. Park, Y. C. Kang, Preparation of Yolk-Shell and Filled Co_9S_8 Microspheres and Comparison of Their Electrochemical Properties, Chem. Asian J. 9 (2014) 572-576.

[22] Z. Ma, X. Yuan, Z. Zhang, D. Mei, L. Li, Z. F. Ma, L. Zhang, J. Yang, J. Zhang, Novel Flower-like Nickel Sulfide as an Efficient Electrocatalyst for Non-aqueous Lithium-air Batteries, Sci. Rep. 5 (2015) 18199.

[23] R. Ren, M. S. Faber, R. Dziedzic, Z. H. Wen, S. H. Jin, S. Mao, J. H. Chen, Metallic CoS_2 Nanowire Electrodes for High Cycling Performance Supercapacitors, Nanotechnology 26 (2015) 494001.

[24] R. B. Rakhi, N. A. Alhebshi, D. H. Anjum, H. N. Alshareef, Nanostructured Cobalt Sulfide-on-fiber with Tunable Morphology as Electrodes for Asymmetric Hybrid Supercapacitors, J. Mater. Chem. A 2 (2014) 16190-16198.

[25] L. Zhang, Y. Wang, W. Zhou, G. Song and S. Cheng, Facile Synthesis of Hollow Co_9S_8 Nanospheres for High Performance Pseudocapacitor, Int. J. Electrochem. Sci. 11 (2016) 1541-1548.

[26] H. Z. Wan, X. Ji, J. J. Jiang, J. W. Yu, L. Miao, L. Zhang, S. W. Bie, H. C. Chen, Y. J. Ruan, Hydrothermal Synthesis of Cobalt Sulfide Nanotubes: The Size Control and its Application in Supercapacitors, J. Power Sources 243 (2013) 396-402.

[27] D. L. Jiang, Q. Xu, S. C. Meng, C. k. Xia, M. Chen, Construction of Cobalt Sulfide/Graphitic Carbon Nitride Hybrid Nanosheet Composites for High Performance Supercapacitor Electrodes, J. Alloys Compd. 706 (2017) 41-47.

[28] B. Chen, R. Li, G. Ma, X. Gou, Y. Zhu, Y. Xia, Cobalt Sulfide/N,S Codoped Porous Carbon Core-shell Nanocomposites as Superior Bifunctional Electrocatalysts for Oxygen Reduction and Evolution Reactions, Nanoscale 7 (2015) 20674-20684.

[29] X. Q. Meng, H. Sun, J. W. Zhu, H. P. Bi, Q. F. Han, X. H. Liu, X. Wang, Graphene-based Cobalt Sulfide Composite Hydrogel with Enhanced Electrochemical Properties for Supercapacitors, New J. Chem. 40 (2016) 2843-2849.

[30] S. N. Bhange, S. M. Unni, S. Kurungot, Nitrogen and Sulphur Co-doped Crumbled Graphene for The Oxygen Reduction Reaction with Improved Activity and Stability in Acidic Medium, J. Mater. Chem. A 4 (2016) 6014-6020.

[31] H. R. Naderi, P. Norouzi, M. R. Ganjali, Electrochemical Study of a Novel High Performance Supercapacitor based on MnO_2 /Nitrogen-doped Graphene Nanocomposite, Appl. Surf. Sci. 366 (2016) 552-560.

[32] K. J. Huang, L. Wang, Y. J. Liu, Y. M. Liu, H. B. Wang, T. Gan, L. L. Wang, Layered MoS_2–graphene Composites for Supercapacitor Applications with Enhanced Capacitive Performance, Int. J. Hydrogen Energy 38 (2013) 14027-14034.

[33] J. Yan, J. P. Liu, Z. J. Fan, T. Wei, L. J. Zhang, High-performance Supercapacitor Electrodes Based on Highly Corrugated Graphene Sheets, Carbon 50 (2012) 2179-2188.

[34] Y. Liu, J. Zhang, S. Wang, K. Wang, Z. Chen, Q. Xu, Facilely Constructing 3D Porous $NiCo_2S_4$ Nanonetworks for High-performance Supercapacitors, New J. Chem. 38 (2014) 4045-4048.

[35] N. Cao, Y. Zhang, Study of Reduced Graphene Oxide Preparation by Hummers' Method and Related Characterization, J. Nanomater. 2015 (2015) 1-5.

[36] M. Zhang, Y. Wang, D. Pan, Y. Li, Z. Yan, and J. Xie, Nitrogen-Doped 3D Graphene/MWNTs Nanoframework-Embedded Co_3O_4 for High Electrochemical Performance Supercapacitors, ACS Sustain. Chem. Eng. 5 (2017) 5099-5107.

[37] R. Ramachandran, M. Saranya, P. Kollu, B. P. C. Raghupathy, S. K. Jeong, A. N. Grace, Solvothermal Synthesis of Zinc Sulfide Decorated Graphene (ZnS/G) Nanocomposites for Novel Supercapacitor Electrodes, Electrochim. Acta 178 (2015) 647-657.

[38] J. Z. Chen, J. L. Xu, S. Zhou, N. Zhao, C. P. Wong, Facile and Scalable Fabrication of Three-dimensional $Cu(OH)_2$ Nanoporous Nanorods for Solid-State Supercapacitors, J. Mater. Chem. A 3 (2015) 17385-17391.

[39] Y. He, W. Chen, X. Li, Z. Zhang, J. Fu, C. Zhao, E. Xie, Freestanding Three-Dimensional Graphene/MnO_2 Composite Networks as Ultralight and Flexible Supercapacitor Electrodes, ACS Nano 7 (2013) 174-182.

CHAPTER 3. FACILE FABRICATION OF ZnCoS NANOMATERIAL FOR FLEXIBLE ASYMMETRIC SUPERCAPACITOR

3.1 Introduction

Metal sulfides, known as being analogous to metal oxides, are expected to provide a much higher specific capacitance than traditional carbon materials, because of their reversible faradaic redox reactions. However, the poor-rate capability and/or cycling stability caused by poor intrinsic conductivity and agglomeration of mono-metal sulfide materials greatly affected their applications. To resolve these disadvantages, two feasible methods could be used to improve the conductivity and stability, namely the synthesis of materials on conducting matrix and the combination of mono-metal sulfides. In our previous work, we found that the introduction of conducting matrix (rGO or PF-9) had a very limited ability to improve the electrochemical performance of mono-metal sulfide (CoS). Thus, we speculate that doping of other elements into the crystal lattices of mono-metal sulfides would be promising for achieving satisfactory supercapacitor performance.

Among various types of metal sulfide electrode materials such as NiS [1, 2], CoS [3, 4] and ZnS [5-7], ZnS, a wide bandgap material (3.5-3.8 eV), has attracted huge attention in the field of energy storage [6, 7]. However, ZnS-based materials face some limitations, such as low specific capacitance and poor conductivity for practical commercial usage [8]. According to previous studies, designing of binary metal sulfides, such as NiCoS [9-11], $CuCo_2S_4$ [12] and MnCoS [13], has been regarded as one of the most feasible ways to obtain an enhanced electrochemical performance because of richer redox reactions occurring during the charging and discharging processes. Based on recent reports, Co-based sulfides demonstrated a high theoretical specific capacitance [14, 15]. Therefore, in this study, we investigated the electrochemical properties of ZnCoS, prepared by an easy method, as positive electrode material in supercapacitors. By introducing cobalt into Zn-based sulfides, it is expected to achieve improved electrochemical performance.

3.2 Preparation of ZnS

ZnS electrode materials are prepared through the following two different methods: hydrothermal or ion-exchange sulfurization method (**Fig. 3.1**).

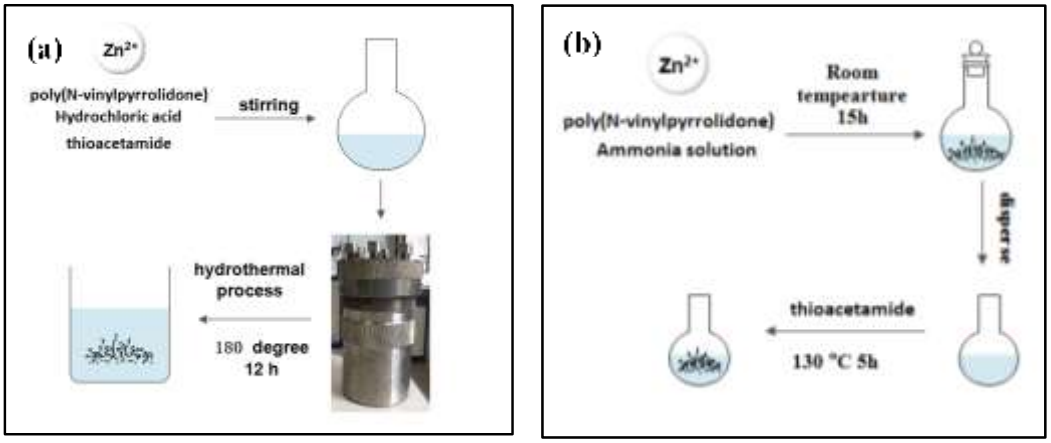

Figure 3.1: Illustration of the synthesis route of ZnS electrode materials, (a) one-step hydrothermal method, (b) two-step ion-exchange sulfurization method.

Hydrothermal method (**Fig. 3.1a**): 1g of PVP was dissolved in 30 mL Milli-Q water under magnetic stirring for 30 min. After that, 660 mg of $Zn(CH_3COO)_2•2H_2O$ and 300 mg of thioacetamide (TAA) were successively added into the above solution. After stirring for 30 min, 30 μL of HCl (37 wt%) was slowly added into the above solution. Finally, the aqueous solution was placed into 125 mL sealed Teflon autoclave and the whole system was heated at 180 ℃ for 12 h. After cooling down to room temperature, the formed precipitate was washed sequentially with Milli-Q water and ethanol until the pH was about 7.

Two-step ion-exchange sulfurization method (**Fig. 3.1b**): 1g of PVP was dissolved in 15 mL Milli-Q water at room temperature (solution A). At the same time, 660 mg of $Zn(CH_3COO)_2•2H_2O$ was dissolved in 15 mL Milli-Q water (solution B). After mixing the solution A and B, 286.5 μL of ammonia (35 wt%) was dropped into the solution under strong magnetic stirring and kept overnight to yield a precipitate. The precipitate was washed sequentially with Milli-Q water and ethanol until the pH was about 7. The obtained product was re-dispersed in 30 mL aqueous solution for further use.

100 mg of TAA was dissolved in 10 mL Milli-Q water and then mixed with 10 mL of the above solution under magnetic stirring. After that, the solution was maintained at 130 ℃ for 5 h. After natural cooling to room temperature, the resulting black solid product was collected through centrifugation, washed with Milli-Q water and ethanol, and dried at 60 ℃ overnight. The sample was labeled as ZnS two-step.

3.3 Characterizations of ZnS

3.3.1 Structure characterization of ZnS

The success of the reaction is confirmed by XRD analysis (**Fig. 3.2**). Diffraction peaks at 2θ values of ~28.6 °, 47.6 °and 56.5 °corresponding to the (111), (220) and (311) crystal planes, respectively can be depicted in the XRD patterns of as-obtained ZnS electrode materials, and all of them are well indexed to the diffraction of face centered cubic sphalerite structure of ZnS (JCPDS 05-0566) [5, 16, 17].

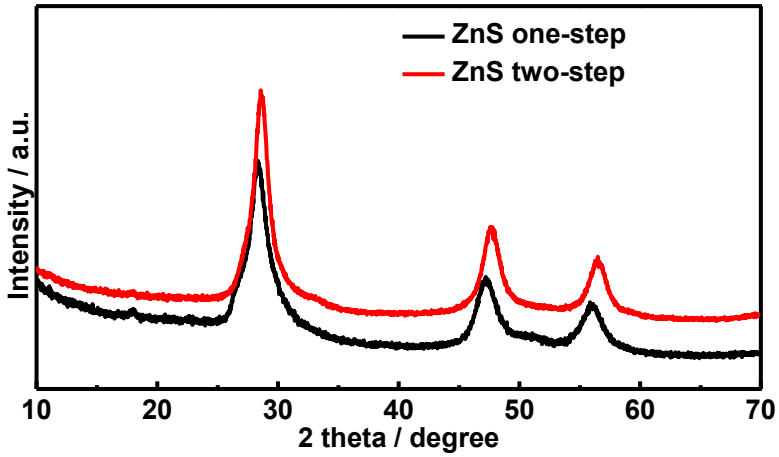

Figure 3.2: XRD patterns of as-obtained ZnS electrode materials.

The scanning electron microscopy (SEM) images of ZnS material synthesized through the two-step method are displayed in **Fig. 3.3**. The SEM images indicate that the obtained ZnS electrode material exhibits a sheet-like structure with a smooth surface.

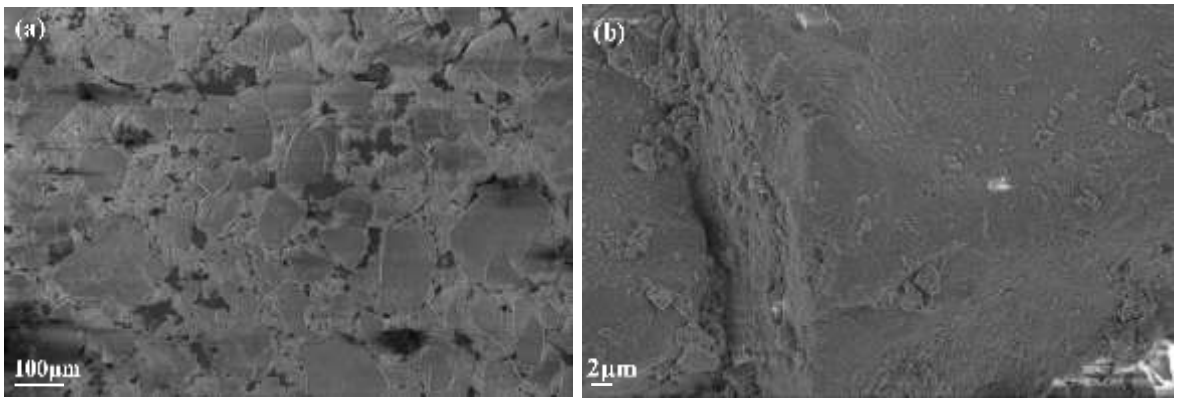

Figure 3.3: SEM images of the ZnS two-step at different magnifications.

3.3.2 Electrochemical performance of ZnS

The electrochemical behavior of ZnS electrode materials is investigated using a 3-electrode system comprising ZnS coated on nickel foam as a working electrode, Pt foil as a counter electrode, and Hg/HgO as a reference electrode.

The CV curves of ZnS (one-step) electrode at different scan rates are depicted in **Fig. 3.4a**. Obvious oxidation and reduction peaks could be detected within the potential range of 0 to +0.55 V, which is believed to be caused by the reversible faradic redox reaction of Zn-S-OH [18]:

$$ZnS + OH^- \leftrightarrow ZnSOH + e^-$$

Furthermore, the current response (current density) enhances as the scan rate increases from 5 to 100 mV/s, while the general shape of the CV curves is not altered, indicating that the electrodes exhibit a good rate capability. **Fig. 3.4b** depicts the CV curves of ZnS (two-step) electrode, which are similar to those of ZnS (one-step) electrode, except that the current response of ZnS (two-step) electrode is larger than that of ZnS (one-step) electrode.

The CV curves of ZnS (one-step) and ZnS (two-step) electrodes at a scan rate of 10 mV/s are also depicted in **Fig. 3.4c**. Obviously, the current response and the integrated area of ZnS (two-step) electrode within the potential window are much larger than those of ZnS (one-step) electrode, indicating that the ZnS electrode material prepared through a two-step method has higher electrochemical activity. Moreover, the specific capacity, calculated from the CV curves (**Fig. 3.4d**), further confirmed an enhanced specific capacity of ZnS (two-step) electrode material.

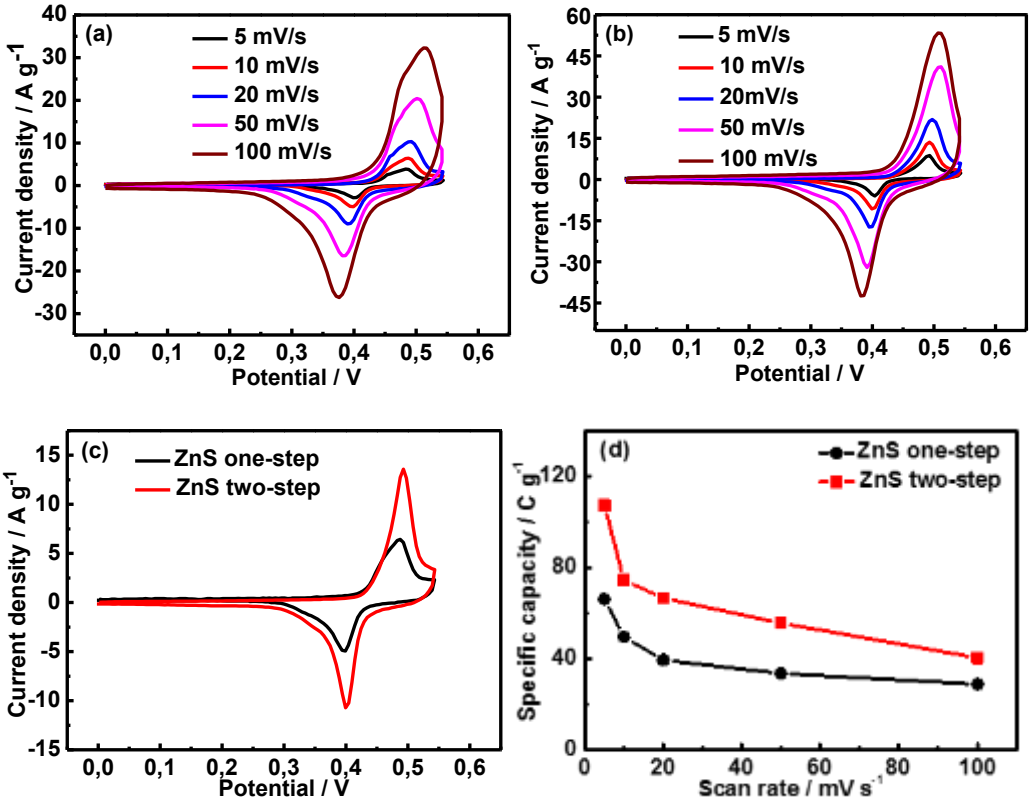

Figure 3.4: CV curves at different scan rates of ZnS one-step (a), ZnS two-step (b), comparison of CV curves at a scan rate of 10 mV/s (c), specific capacity at different scan rates (d).

GCD curves are further acquired to investigate the rate capability and specific capacity. The GCD curves of ZnS (one-step) electrode recorded at various current densities increasing from 0.5 to 10 A g^{-1} in a potential window 0 to +0.55 V are shown in **Fig. 3.5a**. The GCD curves of ZnS (two-step) electrode obtained under the same conditions are also presented in **Fig. 3.5b**. Notably, all GCD curves exhibit nonlinearities and potential plateaus, demonstrating typical faradaic battery-type electrochemical behavior.

Fig. 3.5c presents the GCD curves of ZnS (one-step) and ZnS (two-step) electrodes at a current density of 1 A g^{-1}. Consistent with obtained results from the CV curves, ZnS (two-step) electrode displays a prolonged time for charging/discharging process, demonstrating its higher electrochemical activity. The specific capacity values of ZnS (two-step) electrode are ~85, 82, 77, 76, 71, 70, 69 C g^{-1} at 0.5, 1, 2, 3, 5, 7, and 10 A g^{-1}, respectively, higher than the values obtained for ZnS (one-step) electrode at the same current densities (~48, 46, 45, 42, 40, 37, 31 C g^{-1}) (**Fig. 3.5d**). As the current density increases from 0.5 to 10 A g^{-1}, ~ 81% of the capacity is maintained for ZnS (two-step) electrode, higher than ~64% retained by ZnS (one-step)

electrode, demonstrating the good rate capability. The results from GCD curves further confirmed that ZnS (two-step) electrode has better electrochemical performance.

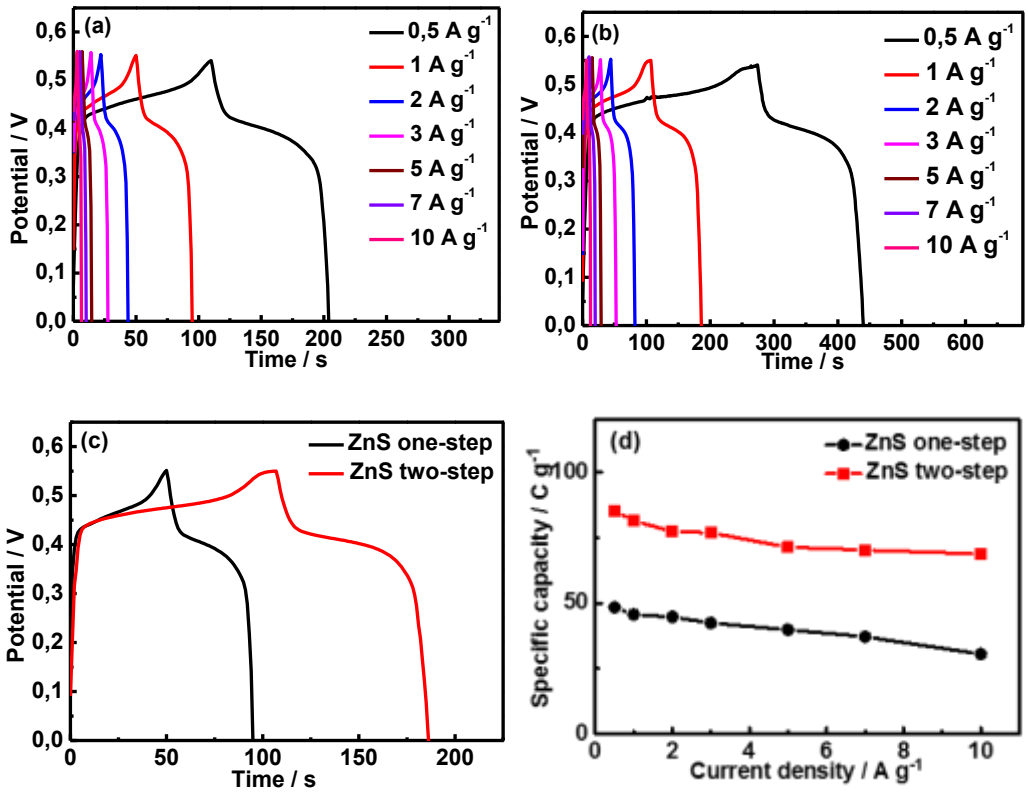

Figure 3.5: GCD curves at different current densities of ZnS (one-step) (a), ZnS (two-step) (b), comparison of GCD curves at a current density of 1 A g^{-1} (c), specific capacity at different current densities (d).

EIS analysis is used to investigate the frequency-dependent behavior of both ZnS electrodes. **Fig. 3.6a** depicts Nyquist plots where the intercept on the real impedance Z' axis in the high-frequency area represents the series resistance. Here, both ZnS electrodes are found to have a similar series resistance. In the fitted equivalent circuit (**Fig. 3.6b**), R_{ct} values of 894.40 and 4598.00 ohm cm^{-2} are determined for ZnS (two-step) and ZnS (one-step) electrodes, respectively, indicating that both prepared ZnS electrodes exhibit a poor electrical conductivity.

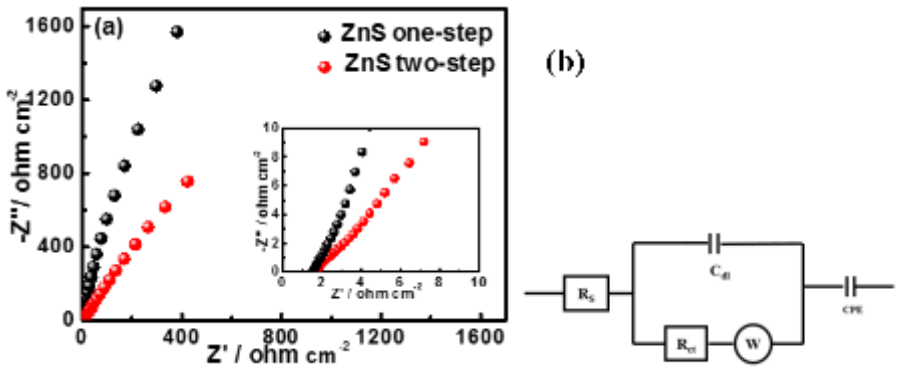

Figure 3.6: Nyquist plots of ZnS electrodes (a), the corresponding equivalent circuit (b).

It is reasonable to suspect that the poor electrical conductivity of ZnS electrode material restricts full electrochemical reactions, and therefore results in a relatively low specific capacity. To overcome this drawback, a simple method for doping Co into Zn-based sulfides is expected to form ZnCoS composites with smaller charge transfer resistance, and therefore, enhance the supercapacitive performance.

3.4 Preparation of ZnCoS

Based on the above results on the electrochemical characterization of both ZnS electrodes, the two-step ion sulfurization method is chosen to prepare ZnCoS electrode materials (**Fig. 3.7**).

Here, a solution A consisting of 1 g of PVP and 15 mL Milli-Q water, and a solution B made up of different mole ratios of $Zn(CH_3COO)_2•2H_2O$ and $CoCl_2•6H_2O$ (the total amount of both precursors is fixed at 3 mmol) were prepared. After mixing solutions A and B, 286.5 µL of ammonia (35 wt%) was dropped into the mixture and maintained overnight at a certain temperature (RT, 50, or 80 ℃). A precipitate was formed and washed with Milli-Q water and ethanol until the pH was about 7. The obtained product was re-dispersed into 30 mL aqueous solution for further use.

100 mg of thioacetamide (TAA) was dissolved in 10 mL Milli-Q water and then mixed with 10 mL of the above solution under magnetic stirring. After that, the mixture was heated at 130 ℃ for 5 h. After natural cooling to room temperature, the resulting black solid product was collected through centrifugation, washed with Milli-Q water and ethanol, and dried at 60 ℃ overnight.

The obtained samples are labeled based on the initial mole ratio of the Zn and Co precursors and the temperature during the chemical precipitation process. For example, the sample Zn: Co 1:2 50 means the initial mole ratio of the Zn and Co precursor was 1:2, and the chemical precipitation temperature was 50 ℃.

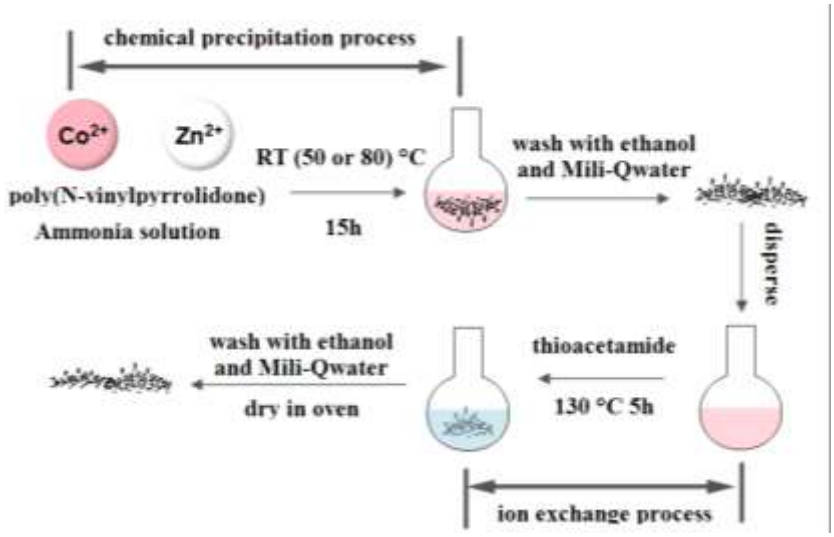

Figure 3.7: Illustration of the synthesis route of ZnCoS electrode materials through a two-step ion-exchange sulfurization method.

To understand the effect of the initial Co/Zn mole ratio and the temperature during the chemical precipitation, the electrode materials were synthesized under different parameters and a systematic investigation was performed to optimize each parameter. The following **Table 3-1** summarizes the preparation conditions of the ZnCoS electrode materials.

Table 3-1: Preparation conditions of ZnCoS electrode materials.

Sample	Initial Zn/Co mole ratio	Temperature during the chemical precipitation process (℃)
Zn:Co (1:1) RT	1:1	RT
Zn:Co (1:2) RT	1:2	RT
Zn:Co (1:3) RT	1:3	RT
Zn:Co (1:2) 50	1:2	50
Zn:Co (1:2) 80	1:2	80

3.5 Characterization of ZnCoS

3.5.1 Structural characterization of ZnCoS prepared at room temperature (RT)

XPS analysis was performed on Zn: Co (1:2) RT to gain information on the chemical composition and oxidation state of surface elements on its surface. The XPS full spectrum of Zn: Co (1:2) RT is depicted in **Fig. 3.8a**. It comprises peaks attributed to Co, Zn, and S, while other elements (C, N, O) due to the PVP stabilizer are also detected.

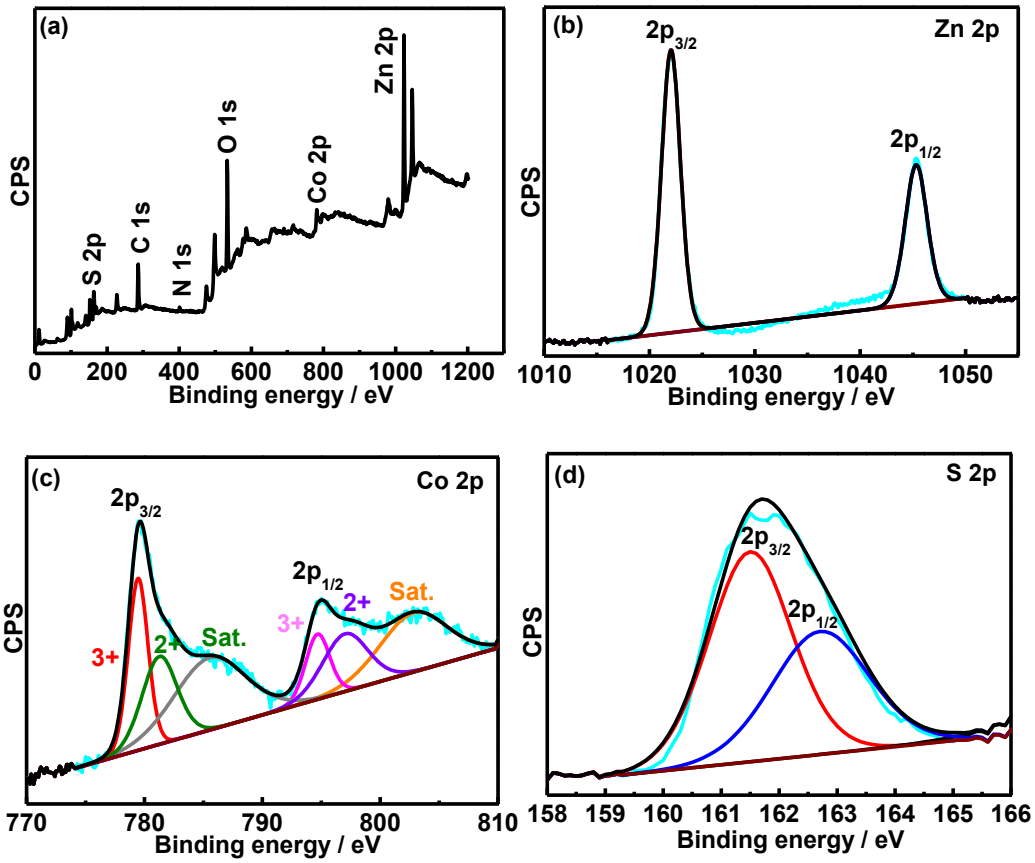

Figure 3.8: XPS analysis of Zn: Co (1:2) RT electrode material: (a) full spectrum, high resolution spectra of (b) Zn_{2p}, (c) Co_{2p} and (d) S_{2p}. "Sat." in the **Fig. 3.8** denotes satellite peaks.

In the XPS high-resolution spectrum of Zn_{2p} (**Fig. 3.8b**), two prominent peaks at 1022.0 and 1045.3 eV due to $Zn_{2p3/2}$ and $Zn_{2p1/2}$, respectively are observed, indicating the presence of Zn^{2+} [5, 6]. The Co_{2p} high-resolution XPS spectrum of Zn: Co (1:2) RT consists of $Co_{2p3/2}$ and $Co_{2p1/2}$ spin-orbit doublets and two shakeup satellites (**Fig. 3.8c**). The bands at ~779.4 and 781.2 eV are assigned to $Co_{2p3/2}$ of Co^{3+} and Co^{2+}, respectively. The bands at binding energies of ~794.6 and 797.0 eV are characteristic of $Co_{2p1/2}$ of Co^{3+} and Co^{2+}, respectively. The difference of the

binding energy between $Co_{2p1/2}$ and $Co_{2p3/2}$ is larger than 15 eV, revealing the co-existence of Co^{3+} and Co^{2+} in Zn: Co (1:2) RT electrode material. The bands at binding energies of ~786.0 and 803.3 eV are the shakeup satellites [19-21]. The XPS high-resolution spectrum of S_{2p} can be deconvoluted in two bands at ~161.5 and 162.7 eV due to $S_{2p3/2}$ and $S_{2p1/2}$, respectively (**Fig. 3.8d**). From XPS analysis results, the obtained Zn: Co (1:2) RT consists of Zn^{2+}, Co^{2+}, Co^{3+}, and S^{2-}.

The existence of Co and Zn in the prepared ZnCoS RT samples is further confirmed by ICP-AES analysis (**Table 3-2**). The influence of the initial Co/Zn mole ratio on the final composition of ZnCoS RT electrode materials is also investigated. The amount of Co in the prepared ZnCoS RT electrode materials increases from 22.66 to 31.73 wt%, as the initial Co/Zn mole ratio increases and the final ratio of Co/Zn (wt%/wt%) increases from 0.45 to 0.73, indicating that more Zn^{2+} ions are replaced by $Co^{2+/3+}$ as the initial Co/Zn mole ratio increases. Furthermore, the exact chemical composition of the obtained ZnCoS RT electrode materials is deduced, based on the ICP-AES results.

Table 3-2: Co and Zn composition obtained by ICP-AES analysis.

Sample	Zn (wt%)	Co (wt%)	Co/Zn (wt%/wt%)	Formula
Zn: Co (1:1) RT	50.80	22.66	0.45	$Zn_{0.70}Co_{0.30}S$
Zn: Co (1:2) RT	45.72	25.36	0.55	$Zn_{0.65}Co_{0.35}S$
Zn: Co (1:3) RT	43.40	31.73	0.73	$Zn_{0.58}Co_{0.42}S$

The crystal structure of the synthesized ZnCoS electrode materials with different initial Co/Zn mole ratios is determined by XRD technique (**Fig. 3.9**), and for comparison, XRD patterns of both ZnS two-step (from **Fig. 3.2**) and CoS electrode materials (from **Fig. 2.3a**) are also given. For Zn: Co RT (1:1), (1:2), (1:3) electrode materials, diffraction peaks at 2Θ= ~28.6 °, 47.8 °, and 56.7 ° corresponding to the (111), (220), and (311) crystal planes, respectively can be well indexed to the diffraction patterns of cubic planes of $Zn_{0.76}Co_{0.24}S$ (ZnCoS) (JCPDS card No. 47-1656). From XRD results, it could be concluded that XRD patterns of the Zn: Co RT (1:1), (1:2), (1:3) electrode materials is very close to that of ZnS (two-step) electrode material, except that diffraction peaks became slightly broader. Therefore, we can hypothesize that during the synthesis process, partial substitution of Zn^{2+} by $Co^{2+/3+}$ ions in the ZnS lattice took place, instead of the substitution of Co^{2+}/Co^{3+} by Zn^{2+} ion in CoS lattice. Indeed, the size

of Zn^{2+} ion (74 pm) is slightly larger than that of Co^{2+} (70 pm) or Co^{3+} (60 pm) ions; therefore, partial substitution of Zn^{2+} by $Co^{2+/3+}$ ions would not significantly affect the cell parameters.

Furthermore, the interplanar distance d of the samples is calculated according to the Bragg's law:

$$2dsin\theta = n\lambda \qquad 3\text{-}1$$

Where θ is the scattering angle, n is a positive integer and λ=1.54056 Å.

The interplanar distance d of diffraction peaks 2θ at values of ~28.6 °, 47.6 ° and 56.5 ° corresponds to ~0.30, 0.19 and 0.16 nm, respectively.

The particle size D of ZnCoS samples is calculated by using the Debye-Scherrer formula [6]:

$$D = \frac{0.94\lambda}{\beta Cos\theta} \qquad 3\text{-}2$$

Where β is the full width at half maximum intensity, θ is the scattering angle and λ = 1.54056 Å.

Based on the full width at half maximum of diffracted peaks of Zn: Co (1:0) RT sample, the calculated average particle size is 7 nm using the (111) diffraction peak.

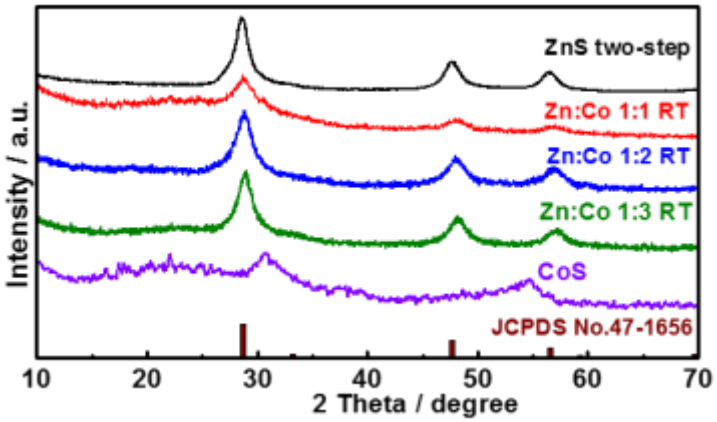

Figure 3.9: XRD patterns of ZnCoS electrode materials with different initial Co/Zn mole ratios.

The morphology and detailed microstructures of the prepared Zn: Co (1:1) RT sample are examined by scanning electron microscopy (SEM). As shown in **Fig. 3.10**, it can be evidently seen that the Zn: Co (1:2) RT sample has a sheet-like structure (**Fig. 3.10a**). The high magnified

SEM image of Zn: Co (1:2) 50 sample (**Fig. 3.10b**) reveals that the surface of those sheets has a porous structure, which is expected to provide more electroactive sites between the active material and the electrolyte**.**

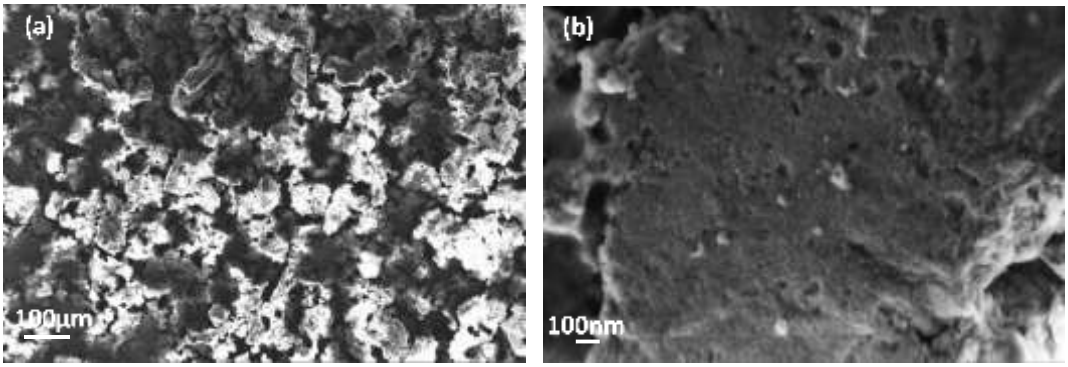

Figure 3.10: SEM images at different magnifications of Zn: Co (1:2) RT sample.

The specific surface area (SSA) and porous texture of Zn: Co (1:2) RT electrode material are examined by nitrogen adsorption-desorption isotherms (**Fig. 3.11**). The nitrogen adsorption-desorption isotherms of Zn: Co (1:2) RT electrode material is identified as type IV, according to the IUPAC (International Union of Pure and Applied Chemistry) classification. A hysteresis loop in the 0.5-0.9 relative pressure region is observed (**Fig. 3.11a**), suggesting the existence of mesoporous structures, which are further investigated in the pore diameter distribution profile (**Fig. 3.11b**), determined from the desorption isotherm using the BJH model. The Zn: Co (1:2) RT sample possesses a BET specific surface area of 76.6 m^2 g^{-1} with an average pore size of around 6 nm. Based on these results, it is reasonable to assume that this porous structure may have potential applications in electrochemical supercapacitors.

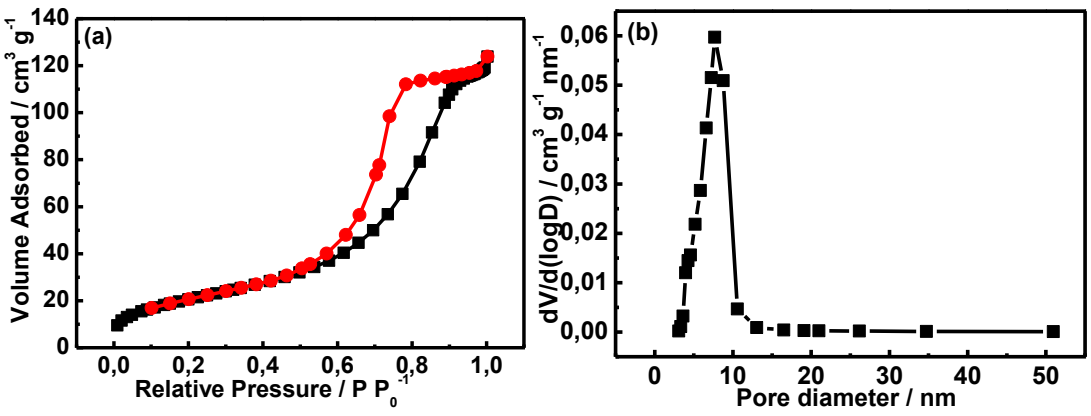

Figure 3.11: Nitrogen adsorption/desorption isotherm (a), and pore size distribution curve (b) of Zn: Co (1:2) RT electrode material.

3.5.2 Electrochemical performance of ZnCoS RT

The electrochemical behavior of ZnCoS RT electrode materials is investigated using a 3-electrode system comprising of ZnCoS RT as a working electrode, Pt foil as a counter electrode, and Hg/HgO as a reference electrode.

The CV curves of Zn: Co (1:1) RT electrode at different scan rates are depicted in **Fig. 3.12a**. The observed redox peaks are believed to be caused by the reversible faradaic redox reaction of Zn-S-OH, CoS to CoSOH and CoSOH to CoSO, as summarized below:

$$ZnS + OH^- \leftrightarrow ZnSOH + e^-$$

$$CoS + OH^- \leftrightarrow CoSOH + e^-$$

$$CoSOH + OH^- \leftrightarrow CoSO + H_2O + e^-$$

Furthermore, the current response (current density) is enhanced as the scan rate increases from 5 to 100 mV/s, while the general shape of the CV curves is not altered, indicating that the electrodes exhibit a good rate capability. **Fig. 3.12b** and **c** depict the CV curves of Zn: Co (1:2) RT and Zn: Co (1:3) RT electrodes, which are similar to those of Zn: Co (1:1) RT electrode except the current response. Obviously, the current response of Zn: Co (1:2) RT electrode within the potential window is much larger than that of Zn: Co (1:1) RT and Zn: Co (1:3) RT electrodes, indicating that Zn: Co (1:2) RT electrode material has higher electrochemical activity.

The CV curves of ZnCoS RT electrodes at a scan rate of 10 mV/s are also displayed in **Fig. 3.12d**, and for comparison, the CV curves of ZnS two-step (from **Fig. 3.4c**) and CoS electrodes (from **Fig. 2.11a**) are also provided. It is evident that Zn: Co (1:2) RT electrode shows the largest integrated area under the CV curve as compared to the other ZnCoS RT electrodes at a scan rate of 10 mV/s, and the order of the integrated area is Zn: Co (1:2) RT > CoS > Zn: Co (1:3) RT > Zn: Co (1:1) RT > ZnS two-step. Since the specific capacity of an electrode is proportional to the area under the CV curve, the order of the specific capacity of ZnCoS RT electrodes is also Zn: Co (1:2) RT (~205 C g^{-1})> CoS (~176 C g^{-1})> Zn: Co (1:3) RT (~148 C g^{-1})> Zn: Co (1:1) RT (~121 C g^{-1})> ZnS two-step (~74 C g^{-1}) (**Fig. 3.12e**), further confirming that the partial substitution of Zn^{2+} by $Co^{2+/3+}$ ions in ZnS lattice could lead to an enhanced electrochemical performance.

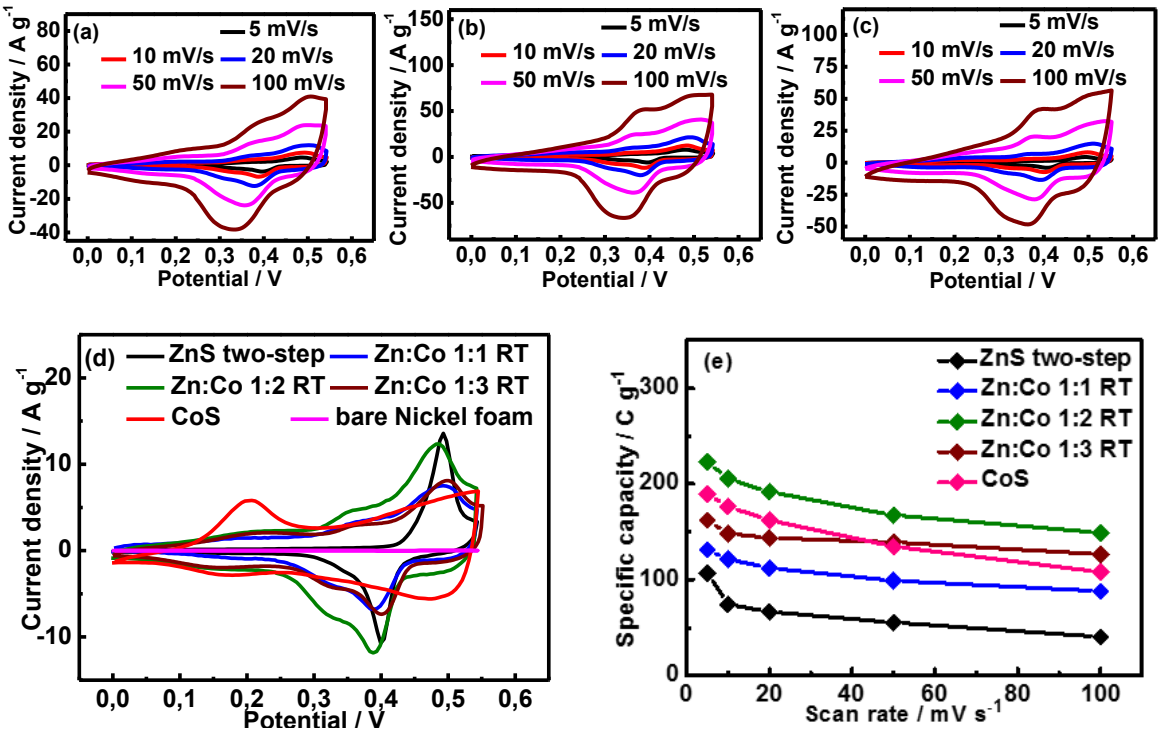

Figure 3.12: CV curves at different scan rates of ZnCoS RT electrodes, (a) Zn: Co (1:1) RT, (b) Zn: Co (1:2) RT, (c) Zn: Co (1:3) RT, (d) comparison of the CV curves recorded at a scan rate of 10 mV/s, (e) specific capacity at different scan rates.

GCD curves are further acquired to investigate the rate capability and specific capacity. The GCD curves of Zn: Co (1:1) RT electrode recorded at various current densities from 0.5 to 10 A g^{-1} in a potential window 0 to +0.55 V are shown in **Fig. 3.13a**, and GCD curves of Zn: Co (1:2) RT and Zn: Co (1:3) RT electrodes are presented in **Fig. 3.13b** and **c**, respectively. Notably, all GCD curves exhibit nonlinearities and potential plateaus, demonstrating typical faradaic battery-type electrochemical behavior.

Fig. 3.13d depicts the GCD curves of ZnCoS RT electrodes at a current density of 1 A g^{-1}, and for comparison, the GCD curves of ZnS two-step (from **Fig. 3.5c**) and CoS (from **Fig. 2.11d**) electrodes are also given. Consistent with obtained results from the CV curves, Zn: Co (1:2) RT electrode displays a prolonged time for charging/discharging process, demonstrating higher electrochemical activity. Specific capacity values of Zn: Co (1:2) RT electrode are determined to be ~225, 220, 213, 211, 206, 198 and 194 C g^{-1} at 0.5, 1, 2, 3, 5, 7 and 10 A g^{-1}, respectively, higher than those achieved by other ZnCoS RT electrodes (**Fig. 3.13e**). As the current density increases from 0.5 to 10 A g^{-1}, ~86% of the initial capacity of Zn: Co (1:2) RT electrode is maintained, higher than that of bare ZnS (two-step) (~81%) and bare CoS (~51%) electrodes, demonstrating the good rate capability. The results of GCD curves further confirm

that the partial substitution of Zn^{2+} by $Co^{2+/3+}$ ions in ZnS lattice could enhance the electrochemical performance.

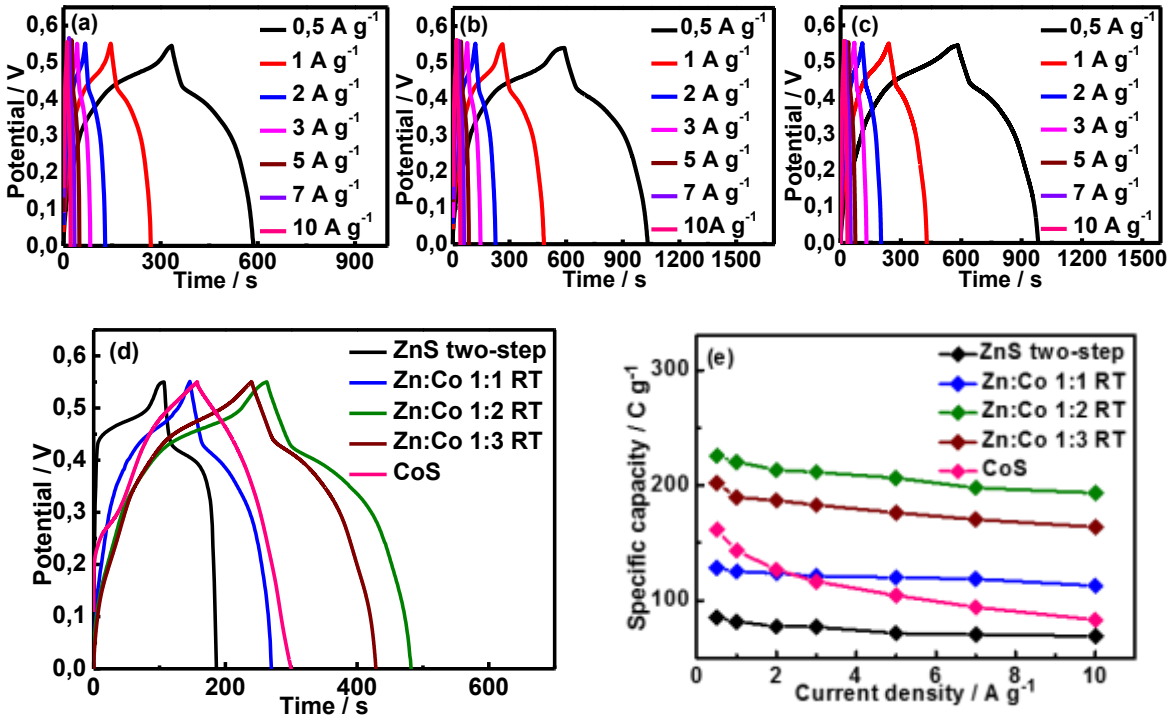

Figure 3.13: GCD curves of ZnCoS RT electrodes at different current densities. (a) Zn: Co (1:1) RT, (b) Zn: Co (1:2) RT, (c) Zn: Co (1:3) RT, (d) comparison of GCD curves at a current density of 1 A g^{-1}, (e) specific capacity at different current densities.

EIS is used to investigate the frequency-dependent electrochemical behavior of the electrode/electrolyte interface of the prepared ZnCoS RT electrodes. **Fig. 3.14a** shows the Nyquist plots of ZnCoS RT electrodes, and for comparison, the Nyquist plots of ZnS two-step (from **Fig. 3.6a**) and CoS (from **Fig. 2.4e**) electrodes are also recorded. The intercept on the real impedance Z' axis in the high-frequency area represents the series resistance, which includes the intrinsic resistance of the electrode material, the resistance of the 2M KOH electrolyte, and the contact resistance at the active electrode material and nickel foam interface. The depressed semi-circle in the high-medium frequency area is attributed to the faradaic charge-transfer resistance between the electrode material and the electrolyte. Subsequently, the slope line, observed in the low-frequency area, suggests the electrolyte ion diffusion in the electrode material. The Zn: Co (1:2) RT electrode shows a smaller value of the intercept on the real impedance Z' axis and a steeper slope compared with other ZnCoS RT electrodes.

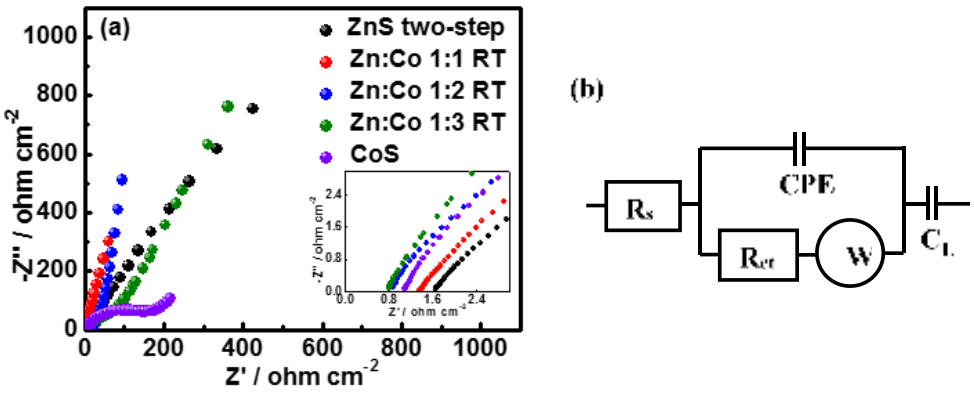

Figure 3.14: Nyquist plots of ZnCoS RT electrodes (a), the corresponding equivalent circuit (b).

The equivalent circuit is also depicted in **Fig. 3.14b**. The corresponding values of R_s and R_{ct} of ZnCoS RT electrodes are summarized in **Table 3-3**, showing that Zn: Co (1:2) RT electrode exhibits the smallest series resistance (0.79 ohm cm^{-2}) and charge transfer resistance (28.54 ohm cm^{-2}).

Table 3-3: Values of R_s and R_{ct} for ZnCoS RT electrodes.

Electrode	R_s (ohm·cm^{-2})	R_{ct} (ohm·cm^{-2})
ZnS (two-step)	1.56	894.40
Zn:Co (1:1) RT	1.29	26.56
Zn:Co (1:2) RT	0.79	28.54
Zn:Co (1:3) RT	0.74	86.57
CoS	1.07	143.10

Moreover, the stability of ZnCoS RT electrodes is examined at 5 A g^{-1} for 2,500 cycles (**Fig. 3.15a**). It should be noticed that the ZnCoS RT electrodes achieve specific capacity retention of ~120%, 132% and 108% for Zn: Co (1:1) RT, Zn: Co (1:2) RT and Zn: Co (1:3) RT electrodes after 2,500 cycles at 5 A g^{-1}, respectively. The Zn: Co (1:2) RT electrode offers the highest specific capacity of ~280 C g^{-1} after 2,500th cycle at 5 A g^{-1} (~212 C g^{-1} for 1st cycle) (**Fig. 3.15b**).

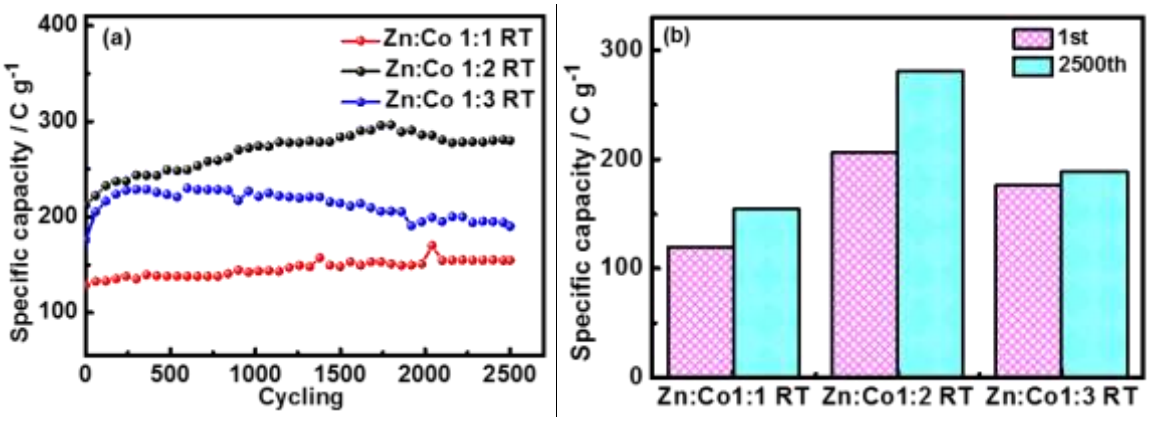

Figure 3.15: Cycling performance of ZnCoS RT electrodes for 2,500 charge/discharge cycles at 5 A g^{-1} (a), specific capacity of ZnCoS RT electrodes before and after stability test at a current density of 5 A g^{-1} in 2M KOH aqueous solution (b).

Based on the results of electrochemical characterizations, the initial mole ratio Co/Zn = 2 provides the best electrochemical performance when the temperature during the precipitation process was fixed at room temperature.

3.5.3 Structural characterization of ZnCoS (1:2)

The chemical and surface states of elements in obtained samples are assessed by XPS. The XPS full spectrum of Zn: Co (1:2) 50 is depicted in **Fig. 3.16a**. Like the full spectrum observed in **Fig. 3.8a**, it comprises peaks attributed to Co, Zn, and S, while other elements (C, O, N) due to the PVP stabilizer are also detected.

The Co_{2p} high-resolution XPS spectrum of Zn: Co (1:2) 50 consists of $Co_{2p3/2}$ and $Co_{2p1/2}$ spin-orbit doublets and two shakeup satellites (**Fig. 3.16b**). The peaks at ~779.3 and 783.1 eV are assigned to $Co_{2p3/2}$ of Co^{3+} and Co^{2+}, respectively. The peaks at binding energies of ~794.5 and 798.1 eV are characteristic of $Co_{2p1/2}$ of Co^{3+} and Co^{2+}, respectively. The difference of the binding energy between $Co_{2p1/2}$ and $Co_{2p3/2}$ is larger than 15 eV, suggesting the co-existence of Co^{3+} and Co^{2+} in Zn: Co (1:2) 50. The peaks at binding energies of ~787.6 and 803.4 eV are the shakeup satellites, in agreement with the literature data for bimetallic sulfides [22-24].

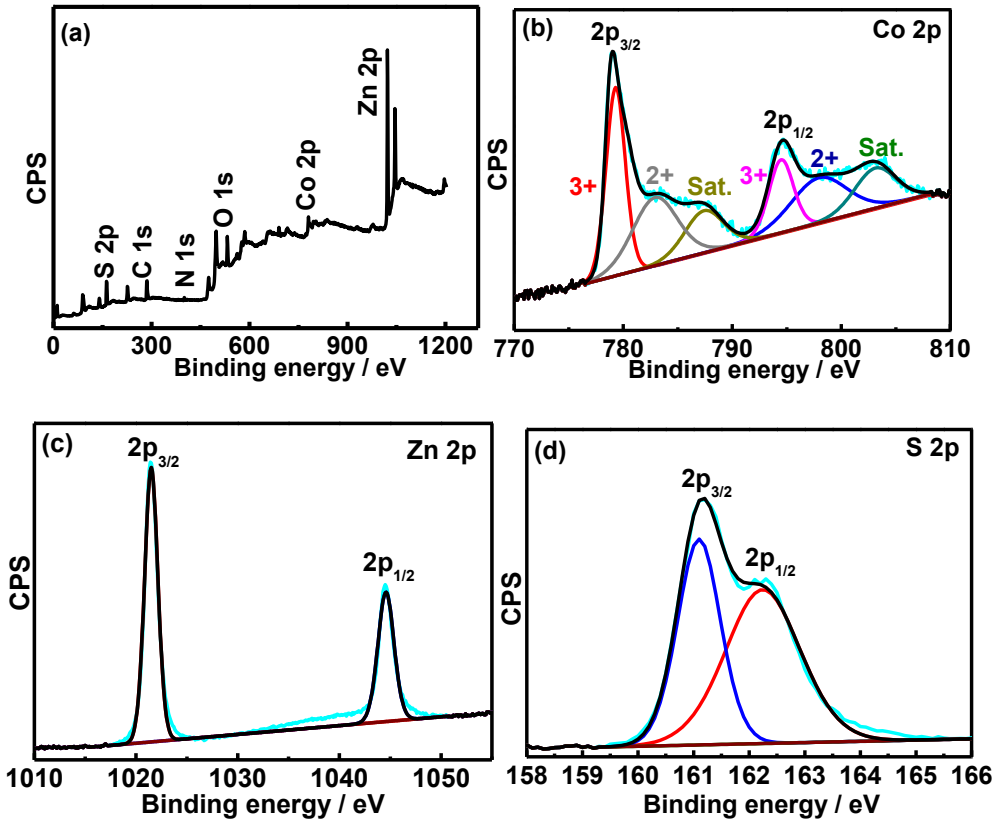

Figure 3.16: XPS analysis of Zn: Co (1:2) 50 electrode material: (a) full spectrum, and high resolution spectra of (b) Co_{2p}, (c) Zn_{2p}, (d) S_{2p}. "Sat." in the **Fig. 3.15** denotes satellite peaks.

In the high-resolution XPS spectrum of Zn_{2p}, two prominent peaks at ~1021.5 and 1044.5 eV due to $Zn_{2p3/2}$ and $Zn_{2p1/2}$, respectively are observed, indicating the presence of Zn^{2+} (**Fig. 3.16c**) [5-7]. The high-resolution XPS spectrum of S_{2p} can be deconvoluted in two peaks at ~161.1 and 162.2 eV due to $S_{2p3/2}$ and $S_{2p1/2}$, respectively (**Fig. 3.16d**). The absence of components at higher binding energies clearly indicates that sulfur is not oxidized. From XPS analysis results, the obtained Zn: Co (1:2) 50 consists of Zn^{2+}, Co^{2+}, Co^{3+}, and S^{2-}.

The crystal structure of the as-prepared Zn: Co (1:2) 50 electrode material is determined by the XRD technique (**Fig. 3.17**); for comparison, the XRD pattern of Zn: Co (1:2) RT electrode is also given. Similar to the XRD pattern of Zn: Co (1:2) RT, diffraction peaks at ~28.6 °, 47.8 °, and 56.7 ° corresponding to the (111), (220), and (311) crystal planes, respectively, could be observed. However, the diffraction peaks become much broader as the temperature during the precipitation process increases. It is reasonable to deduce that the poor crystallinity of obtained ZnCoS electrode materials is due to the increase of the temperature during the precipitation process. Furthermore, the interplanar distance d of Zn: Co (1:2) 50 sample is calculated using equation **3-1**. The interplanar distance d of the diffraction peaks at 2θ values of ~28.6 °, 47.6 °,

and 56.5 ° corresponds to ~0.30, 0.19 and 0.16 nm, respectively. The particle size of ZnCoS sample is determined using the equation **3-2**. Based on the full width at half maximum of diffracted peaks of Zn: Co (1:2) 50, the calculated average particle size was 5 nm using the (111) diffraction peak.

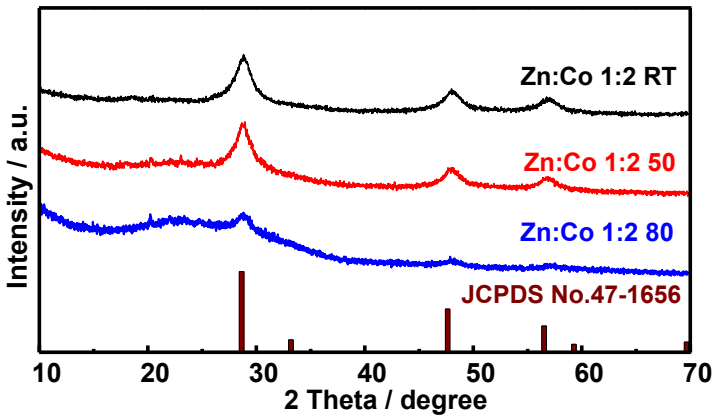

Figure 3.17: XRD patterns of the prepared Zn: Co (1:2) electrode materials at different temperatures during the precipitation process.

The existence of Co and Zn in the prepared Zn: Co (1:2) electrode materials is confirmed by ICP-AES analysis (**Table 3-4**). The influence of temperature during the chemical precipitation process on the final ratio of Co/Zn (wt%/wt%) of ZnCoS is also investigated. When the initial Co/Zn mole ratio is fixed at 2, the final ratio of Co/Zn (wt%/wt%) increases from 0.55 to 1.25 when the temperature is increased from room temperature (RT) to 80 ℃, indicating that much more Zn^{2+} ions are replaced by Co^{2+}/Co^{3+} ions as the chemical precipitation temperature increases. It is worth noting that the final ratio of Co/Zn (wt%/wt%) of ZnCoS sample synthesized at higher chemical precipitation temperature is significantly larger than that prepared at room temperature. Therefore, improving the chemical precipitation temperature is believed to be much more effective to obtain a much higher ratio of Co/Zn (wt%/wt%) in ZnCoS lattice.

Table 3-4: Co and Zn composition obtained by ICP-AES analysis.

Sample	Zn (wt%)	Co (wt%)	Co/Zn (wt%/wt%)	Formula
Zn: Co (1:2) RT	45.72	25.36	0.55	$Zn_{0.65}Co_{0.35}S$
Zn: Co (1:2) 50	37.62	43.54	1.16	$Zn_{0.46}Co_{0.54}S$
Zn: Co (1:2) 80	29.68	36.97	1.25	$Zn_{0.45}Co_{0.55}S$

The morphology and detailed microstructures of the prepared Zn: Co (1:1) 50 are examined by TEM and SEM. The TEM image of Zn: Co (1:2) 50 exhibits a quasi-sheet-like structure (**Fig. 3.18a**). The SAED image displays rings and dots, which are indicative of the crystalline nature of the material (**Fig. 3.18b**). The calculated interplanar distance d values from SAED are ~0.30, 0.19, and 0.16 nm, agreeing well with the distance of the (111), (220), and (333) crystal planes, respectively (**Fig. 3.17**). From the HRTEM images in **Fig. 3.18c** and **d**, the lattice fringes of 0.19 nm (**Fig. 3.18c**) and 0.30 nm (**Fig. 3.18d**) also match well with the interplanar distance d calculated from the XRD pattern of Zn: Co (1:2) 50 sample (**Fig. 3.17**). The results are in accordance with the XRD measurements. The high-resolution TEM image in **Fig. 3.18c** also suggests that the sheet-like structure is made up of several nanoparticles. The low magnified SEM images of Zn: Co (1:2) 50 sample (**Fig. 3.18e, f**) revealed that its surface is very rough and has a porous structure, which is expected to provide more electroactive sites between the active material and the electrolyte**.**

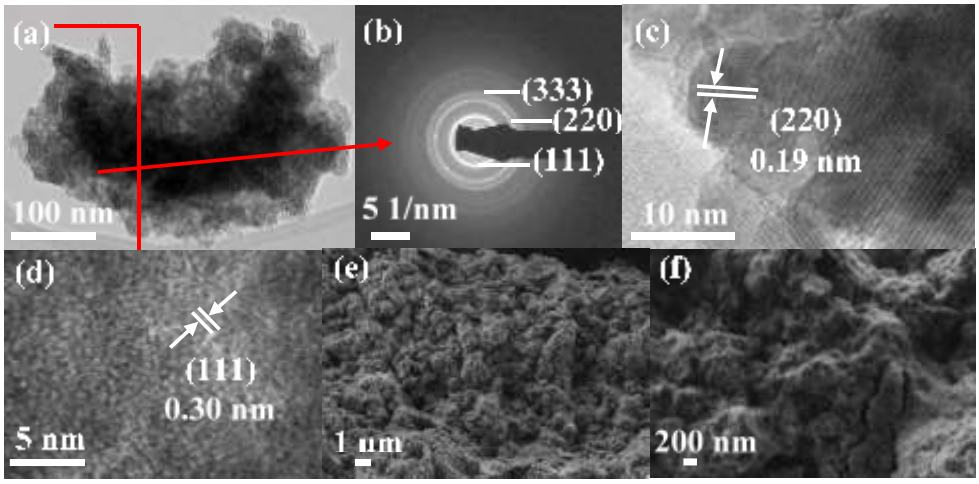

Figure 3.18: TEM images (a), SAED pattern (b), HRTEM images (c, d), and SEM images (e, f) of Zn: Co (1:2) 50.

The SSA and porous texture of obtained Zn: Co (1:2) electrode materials are investigated by nitrogen adsorption-desorption isotherms (**Fig. 3.19**); for comparison, the SSA and porous texture of Zn: Co (1:2) RT are also shown. The nitrogen adsorption-desorption isotherms of ZnCoS samples are identified as type IV. The hysteresis loops in the relative pressure region of 0.5-0.9 could be observed (**Fig. 3.19a**), suggesting the existence of mesoporous structures, which are further investigated in the pore diameter distribution profile (**Fig. 3.19b**), calculated from the desorption isotherm using the BJH model. The pore diameter peaks observed at around 6, 6 and 10 nm also prove the presence of a mesoporous structure in the Zn: Co (1:2) RT, Zn:

Co (1:2) 50, Zn: Co (1:2) 80 samples, respectively. The BET SSA of Zn: Co (1:2) 50 is 112.4 $m^2 g^{-1}$, much higher than that of Zn: Co (1:2) RT (76.6 $m^2 g^{-1}$) and Zn: Co (1:2) 80 (62.2 $m^2 g^{-1}$) samples. This confirms that the temperature during the chemical precipitation process has an influence on the SSA value and the sample prepared at 50 ℃ offers the highest SSA value. This value is larger than that reported for metal sulfides such as hollow ellipsoid Ni-Mn sulfides (48.1 $m^2 g^{-1}$) [25], $NiCo_2S_4$ (42.8 $m^2 g^{-1}$) [26], $ZnS/NiCo_2S_4/Co_9S_8$ (28.1 $m^2 g^{-1}$) [27], and $CuCo_2S_4$ nanoparticles (12.2 $m^2 g^{-1}$) [28].

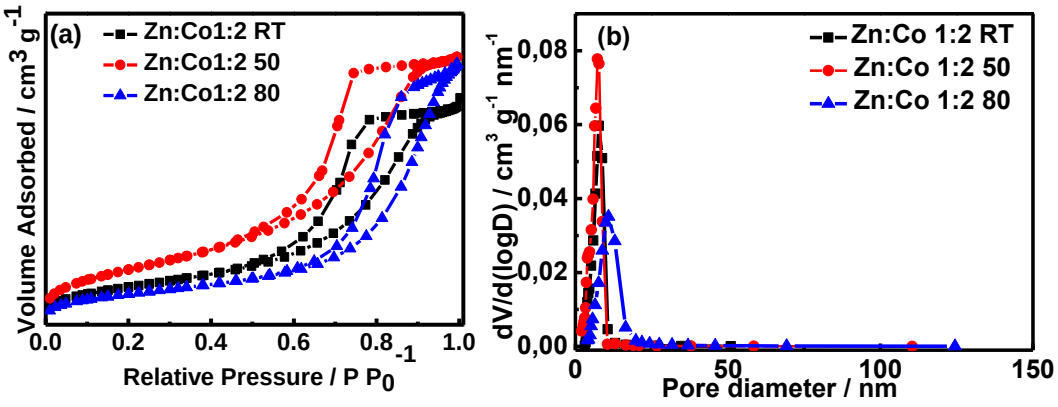

Figure 3.19: Nitrogen adsorption-desorption isotherms (a), and pore size distribution curves (b) of ZnCoS samples.

3.5.4 Electrochemical performance of ZnCoS (1:2) electrodes

The CV curves of ZnCoS (1:2) electrodes, prepared at different temperatures during the precipitation process, are recorded, and the corresponding CV curves acquired at different scan rates are displayed in **Fig. 3.20a** and **b**. Here, redox peaks could be detected in all CV curves, and the maximum current density of Zn: Co (1:2) 50 electrode is obviously larger than that of Zn: Co (1:2) 80 electrode. The CV curves of ZnCoS (1:2) electrodes at a scan rate of 10 mV/s are also depicted in **Fig. 3.20c**, and for comparison, the CV curves of Zn: Co (1:2) RT electrode (from **Fig. 3.12d**) are also provided. It is evident that Zn: Co (1:2) 50 electrode shows the largest integrated area under the CV curve as compared to the other ZnCoS (1:2) electrodes in the following order: Zn: Co (1:2) 50 > Zn: Co (1:2) 80 > Zn: Co (1:2) RT.

Since the specific capacity of the electrode is proportional to the integrated area under the CV curves, the order of the specific capacity of ZnCoS (1:2) electrode at the scan rate of 5 mV/s is as follows: Zn: Co (1:2) 50 (~566 C g^{-1})> Zn: Co (1:2) 80 (~294 C g^{-1})> Zn: Co (1:2) RT (~223 C g^{-1}) (**Fig. 3.20d**), which further confirms that ZnCoS electrode material prepared at 50 ℃ (temperature during the precipitation process) leads to enhanced electrochemical

performance. Furthermore, one clearly sees that as the scan rate increases, the specific capacity of all electrodes gradually decreases. This is believed to be caused by the reduction of effective interaction between the ions and electrode surface; the time for OH^- ion to intercalate through the interface between the electrolyte and electrode is quite reduced at a larger scan rate [29].

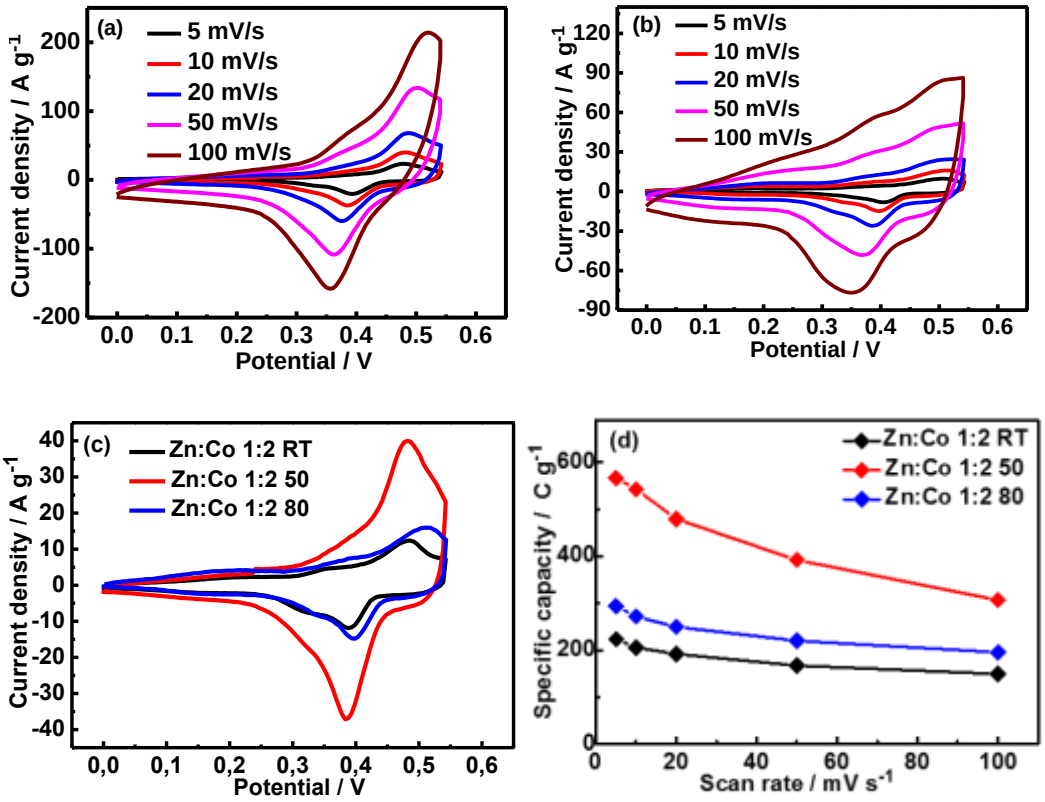

Figure 3.20: CV curves acquired at different scan rates of ZnCoS (1:2) electrodes. (a) Zn: Co (1:2) 50, (b) Zn: Co (1:2) 80, (c) comparison of the CV curves at a scan rate of 10 mV/s, (d) specific capacity at different scan rates.

GCD curves of ZnCoS (1:2) electrodes, prepared at different temperatures during the precipitation process, are recorded at different current densities (**Fig. 3.21a** and **b**). Here, potential plateaus could be detected in all GCD plots. Consistent with obtained results of CV, Zn: Co (1:2) 50 electrode (**Fig. 3.21c**) displays a prolonged time for the charging/discharging process, demonstrating higher electrochemical activity. The specific capacity values of the Zn: Co (1:2) 50 electrode are calculated to be ~624, 556, 534, 529, 522, 513 and 506 C g^{-1} at 1, 3, 5, 7, 10, 15 and 20 A g^{-1}, respectively, higher than those of other ZnCoS (1:2) electrodes (**Fig. 3.21d**). As the current density increases from 1 to 20 A g^{-1}, ~ 81% of the initial capacity is retained, demonstrating a good rate capability. The Zn: Co (1:2) 50 electrode exhibits a maximum specific capacity of ~624 C g^{-1} at a current density of 1 A g^{-1}, which is ~ 1.9 times

than that of Zn: Co (1:2) 80 (~328 C g^{-1}) and 2.8 times than that of Zn: Co (1:2) RT (~220 C g^{-1} at 1 A g^{-1}) electrodes. Using the same initial mole ratio of Co/Zn (2:1), the Zn: Co (1:2) 50 displayed a larger specific capacity compared to that of samples prepared at RT and 80 ℃, indicating that the temperature also has a pronounced effect on the electrochemical properties.

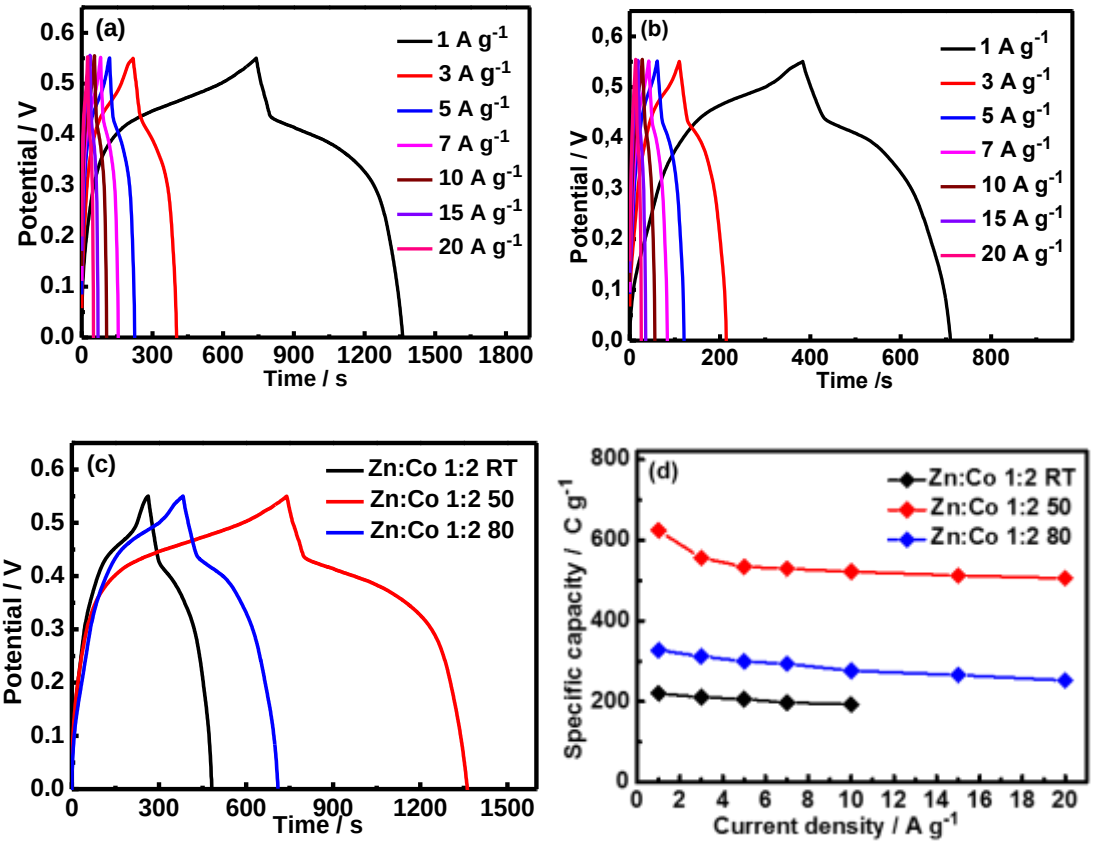

Figure 3.21: GCD curves of ZnCoS (1:2) electrodes at different current densities. (a) Zn: Co (1:1) 50, (b) Zn: Co (1:2) 80, (c) comparison of GCD curves at a current density of 1 A g^{-1}, (d) specific capacity at different current densities.

EIS was used to investigate the frequency-dependent electrochemical properties of the electrode/electrolyte interface of ZnCoS (1:2) electrodes. **Fig. 3.22a** shows the Nyquist plots of Zn: Co (1:2) electrodes; for comparison, the Nyquist plots of Zn: Co (1:2) RT electrode is also provided (from **Fig. 3.14a**). The intercept on the real impedance Z' axis in the high-frequency area represents the series resistance, which includes the intrinsic resistance of the electrode materials, the resistance of the 2M KOH electrolyte, and the contact resistance at the active electrode material and nickel foam interface.

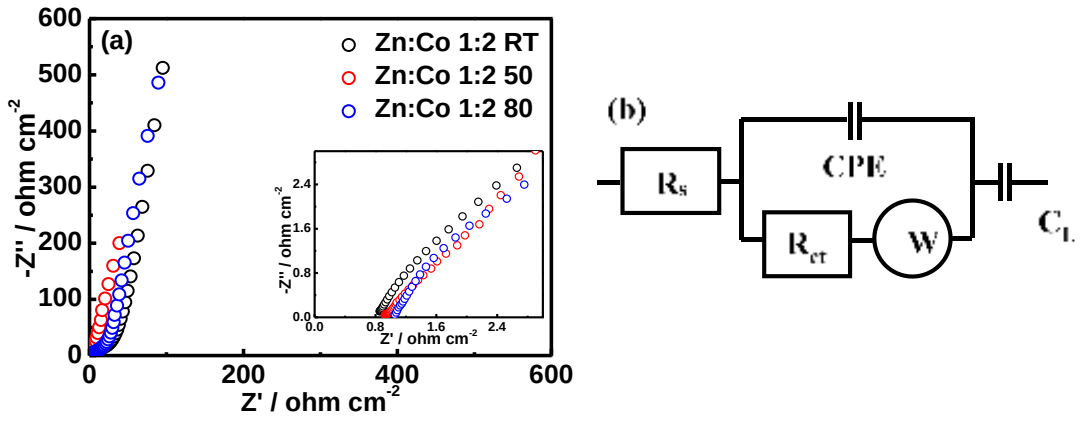

Figure 3.22: Nyquist plots of Zn: Co (1:2) electrodes (a), and the corresponding equivalent circuit (b).

The equivalent circuit is depicted in **Fig. 3.22b**. The calculated values of R_s and R_{ct} of ZnCoS (1:2) electrodes are summarized in **Table 3-5**, showing that all Zn: Co (1:2) electrodes exhibit a small series resistance value, while Zn: Co (1:2) 50 displays the smallest charge transfer resistance (2.68 ohm cm^{-2}).

Table 3-5: Values of R_s and R_{ct} for all Zn: Co (1:2) electrodes.

Electrode	R_s (ohm·cm^{-2})	R_{ct} (ohm·cm^{-2})
Zn:Co (1:2) RT	0.79	28.54
Zn:Co (1:2) 50	0.92	2.68
Zn:Co (1:2) 80	1.05	19.49

Furthermore, the stability of the Zn: Co (1:2) electrodes is examined for 2,500 cycles (**Fig. 3.23a**). In comparison, the stability of the Zn: Co (1:2) 50 electrode is tested at different current densities using the following sequence: 10 A g^{-1} for the first 1,000 cycles and 20 A g^{-1} for additional 1,500 cycles. Retention of ~115% is obtained at 10 A g^{-1}, which slightly drops to ~103% when the current is increased to 20 A g^{-1}. According to the cycling performance examination, even after 2,500 cyclings, the Zn: Co (1:2) 50 electrode still offers the highest specific capacity (~521 C g^{-1} at 20 A g^{-1}). In contrast, Zn: Co (1:2) 80 electrode retains ~87% of the initial capacity after 2,500 charge-discharge cycles at 10 A g^{-1}. Given that the time for discharging process affects the capacity ability of electrode materials, a longer discharging time indicates a much larger specific capacity. Based on the GCD curves of Zn: Co (1:2) 50 electrode after the 1st and 2,500th cycle, acquired at a current density of 5 A g^{-1} (**Fig. 3.23b**), longer

charging and discharging times are observed. From the GCD curves, it can be concluded that a much larger specific capacity is reached after 2,500 cycles.

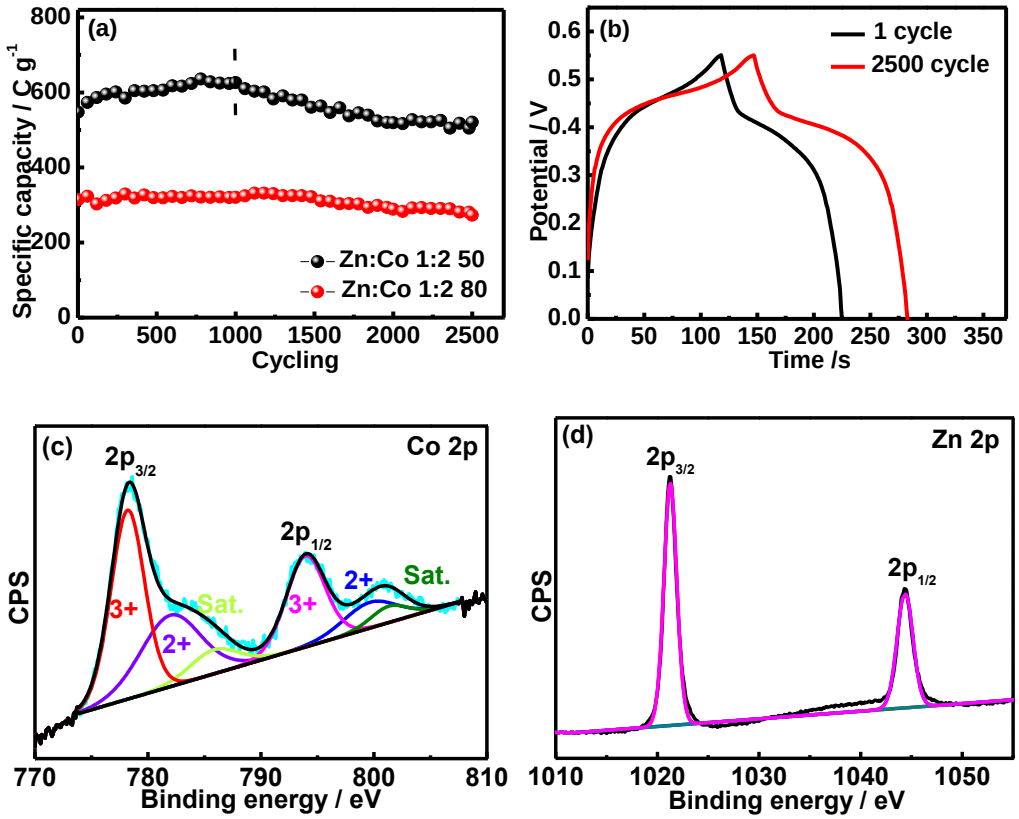

Figure 3.23: (a) Cycling performance of Zn: Co 1:2 electrodes; (b) GCD curves after the first and 2,500th cycle acquired at a current density of 5 A g^{-1}; high resolution XPS spectrum of the Co_{2p} (c) and Zn_{2p} (d) after 2,500 cycles of Zn: Co (1:2) 50.

Furthermore, the chemical composition of the electrode material after cycling stability is examined by XPS. **Fig. 3.23c** and **d** depict the XPS high-resolution spectra of the Co_{2p} and Zn_{2p} of Zn: Co (1:2) 50 after 2,500 cycles. The spectrum of Co_{2p} can be fitted with two spin-orbit peaks at 779.0 and 794.7 eV attributed to $Co^{3+}{}_{2p3/2}$ and $Co^{3+}{}_{2p1/2}$, respectively. Another two broadened peaks can be assigned to $Co^{2+}{}_{2p3/2}$ at ~782.8 eV, $Co^{2+}{}_{2p1/2}$ at ~800.5 eV, and two satellite peaks at ~786.6 and 802.1 eV are also evident in the spectrum. The decrease of the intensity of the Co^{2+} (**Fig. 3.23c**), compared with the initial XPS high-resolution spectrum of the Co_{2p} of Zn: Co (1:2) 50 (**Fig. 3.16b**), suggests an electrochemical transformation of Co^{2+}/Co^{3+} during the supercapacitor operation (charge/discharge cycling). In the spectrum of Zn_{2p} (**Fig. 3.23d**), two prominent peaks at 1021.3 and 1044.4 eV due to $Zn_{2p3/2}$ and $Zn_{2p1/2}$, respectively are observed, indicating the presence of Zn^{2+}.

Furthermore, the stability of the Zn: Co (1:2) 50 electrode is examined at a current density of 20 A g^{-1} for 6,000 cycles (**Fig. 3.24**). It should be noticed that the specific capacity of the electrode increases from ~506 C g^{-1} to 604 C g^{-1} in the first 500 cycles, most likely due to the complete activation of the active electrode material. After 6,000 cycles, the electrode achieves a high specific capacity of ~503 C g^{-1}, indicating good cycling stability.

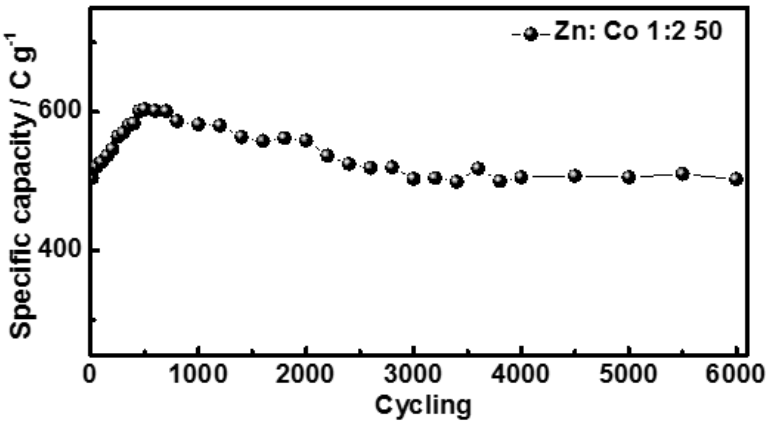

Figure 3.24: Cycling performance of Zn: Co 1:2 50 electrode at 20 A g^{-1} for 6,000 cycles.

3.6 Preparation of negative electrode materials (reduced graphene oxide (rGO) and porous reduced graphene oxide (PrGO))

rGO material prepared in **Chapter 2** is used directly.

PrGO is synthesized according to the work of Chen et al. [30]. A homogeneous (25 mL, 2.5 wt%) GO aqueous solution (**Chapter 2**) was prepared by ultrasonication for 30 min. After that, 160 mg of $KMnO_4$ were introduced with vigorous stirring, and the mixture was kept in a covered beaker for 2 h. Then, 3 mL of HCl (37 wt%) and 5 mL of H_2O_2 (30 wt%) were added. The obtained product was collected after reacting for another 3 h and washed with Milli-Q water. The second step was the reduction of the obtained product. Here, 1.26 mL of ammonia (35 wt%) was added into 21 mL (2.3 wt%) of the above GO aqueous solution under mechanical stirring. After 60 min, 84 μL of hydrazine was added to the mixture and kept under mechanical stirring for another 1 h. Then, the flask was heated at 90 ~100 ℃. After 12 h, the resulting black precipitate was washed with Milli-Q water and ethanol until the pH reached 7. The sample was labeled as PrGO.

3.7 Characterization of rGO and PrGO negative electrodes

The morphology and detailed microstructures of the prepared rGO and PrGO electrode materials are examined by TEM. **Fig. 3.25a** and **b** present TEM images of rGO and PrGO (prepared by pre-oxidation treatment) before the reduction process at 90 °C~100 °C, respectively. The TEM image of rGO (**Fig. 3.25a**) depicts winkles and folded morphology without any pores on the surface, whereas the TEM image of PrGO (**Fig. 3.25b**) is clearly showing the formation of uniform pores over the surface.

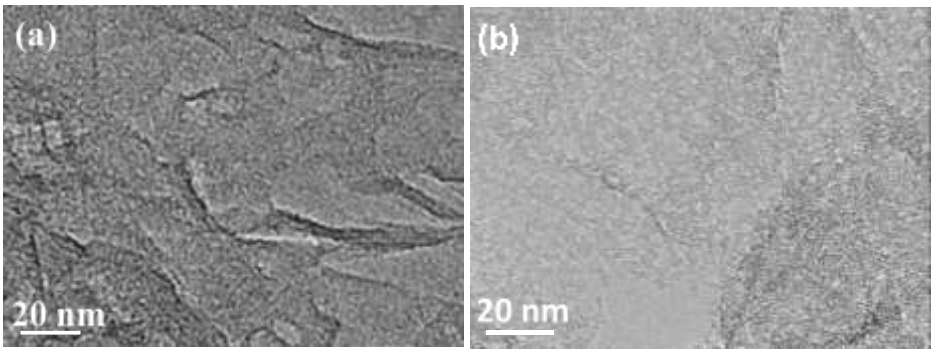

Figure 3.25: TEM images of reduced graphene oxide (rGO) (a), and porous reduced graphene oxide (PrGO) (b).

The electrochemical performance of the two prepared electrode materials is evaluated by CV, GCD, and Nyquist plots in a 3-electrode system in 2M KOH aqueous electrolyte. No obvious oxidation/reduction peaks could be seen in the selected potential region (**Fig. 3.26a** and **b**), suggesting that energy storage takes place mainly through double-layer capacitance. The CV curves of both electrodes still remain nearly rectangular without obvious distortion, even as the scan rate increases to 100 mV/s, revealing that an efficient electric double layer is established in the electrode. The CV curves of rGO and PrGO electrodes recorded at 50 mV/s are shown in **Fig. 3.26c**, revealing a much larger maximum current density and integrated area from the CV curve of PrGO electrode, as compared with that of rGO electrode, indicating an enhanced electrochemical activity.

To further investigate the specific capacitance of the two prepared electrode materials, GCD tests are also performed in the operating potential from -0.9 to +0.1V. Typical GCD curves of rGO and PrGO electrodes at different current densities are shown in **Fig. 3.26d** and **e** respectively. All charge/discharge curves present a triangle-like shape, proving that no redox pseudocapacitive behavior occurs. The GCD curves of rGO and PrGO electrodes at a current

density of 0.5 A g^{-1} are depicted in **Fig. 3.26f**. The PrGO electrode offers a much longer charging/ discharging times (940 s at 0.5 A g^{-1}) than that of rGO electrode (200 s at 0.5 A g^{-1}). Using equation **7-3**, the specific capacitance of both electrodes, based on **Fig. 3.26d** and **e**, is determined (**Fig. 3.26g**). The PrGO electrode provides a much higher specific capacitance (~271 F g^{-1} at 0.5 A g^{-1}) than that of rGO electrode (~62 F g^{-1} at 0.5 A g^{-1}). The results reveal that the oxidation process of GO followed by reduction with ammonia and hydrazine enhances the electrochemical activity of rGO.

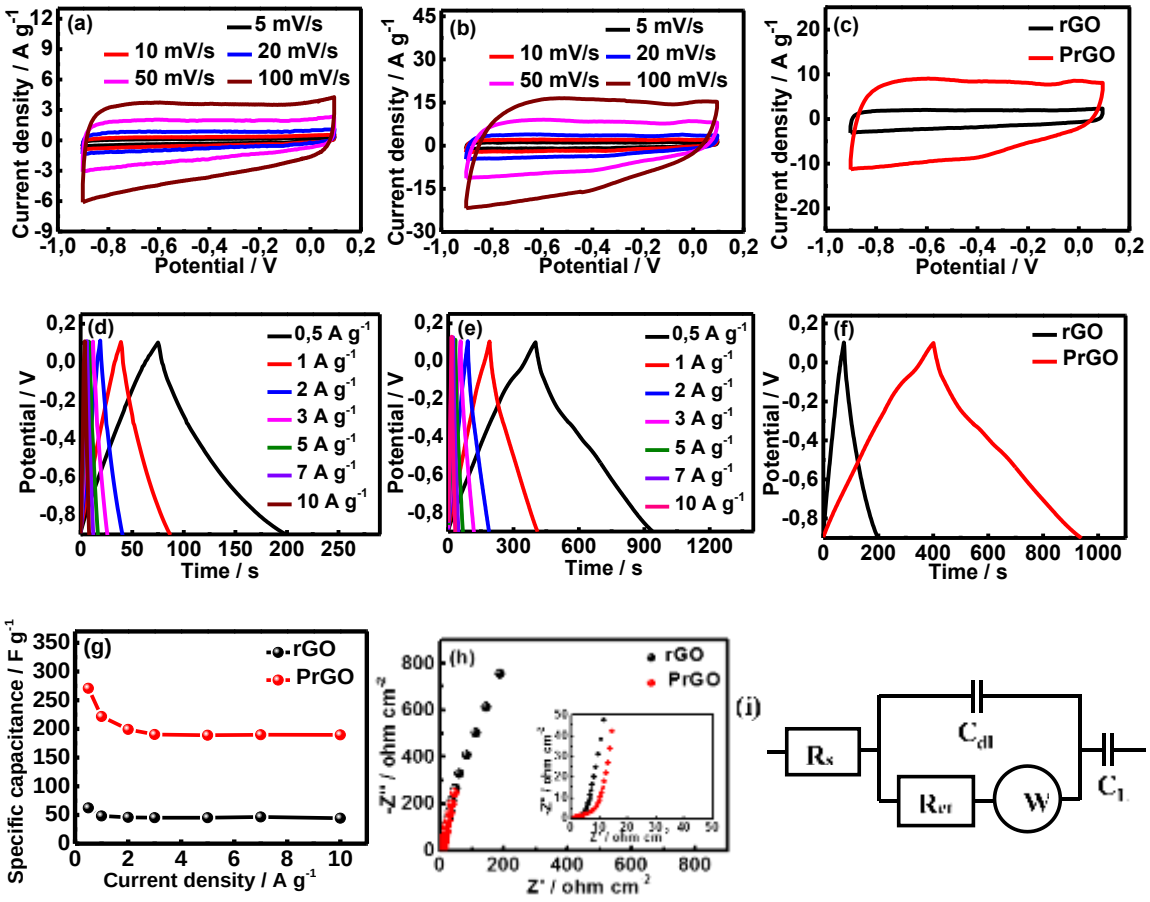

Figure 3.26: Electrochemical properties of rGO and PrGO in 2 M KOH: CV curves of rGO (a) and PrGO (b), CV curves of rGO and PrGO electrodes at a scan rate of 50 mV s^{-1} in the potential range of -0.9 to +0.1V (c); GCD plots of rGO (d) and PrGO (e), GCD plots of rGO and PrGO electrodes at a current density of 0.5 A g^{-1} in the potential range of -0.9 to +0.1 V (f); the corresponding specific capacitance values at different current densities (0.5-10 A g^{-1}) (g); Nyquist plots (h), and the corresponding equivalent circuit (i).

Fig. 3.26h displays the Nyquist plots of rGO and PrGO electrodes and the corresponding equivalent circuit (**Fig. 3.26i**). The PrGO electrode has a slightly lower R_s (about 1.12 ohm·cm^{-2}) as compared to rGO (about 1.85 ohm·cm^{-2}), suggesting the porous structure could reduce the series resistance effectively. Similarly, PrGO exhibits a much smaller R_{ct} (about 2.53 ohm·cm^{-}

^{2}) as compared to rGO (about 496.81 ohm·cm^{-2}), indicating a faster charge transfer speed during the electrochemical process. The enhanced electrochemical activity is assigned to the unique porous structure of PrGO, as evidenced by the TEM image in **Fig. 3.25b**. This porous structure should allow convenient pathways for the transportation of ions and electrons between the active material and electrolyte and provide efficient and fast ion diffusion.

3.8 Electrochemical evaluation of an asymmetric supercapacitor (PrGO// Zn: Co (1:2) 50)

To further investigate the prepared Zn: Co (1:2) 50 electrode for practical application, an asymmetric supercapacitor (ASC) device is fabricated by selecting the Zn: Co (1:2) 50 electrode as the positive electrode and PrGO as the negative electrode in 2M KOH aqueous electrolyte. (**Fig. 3.27a**).

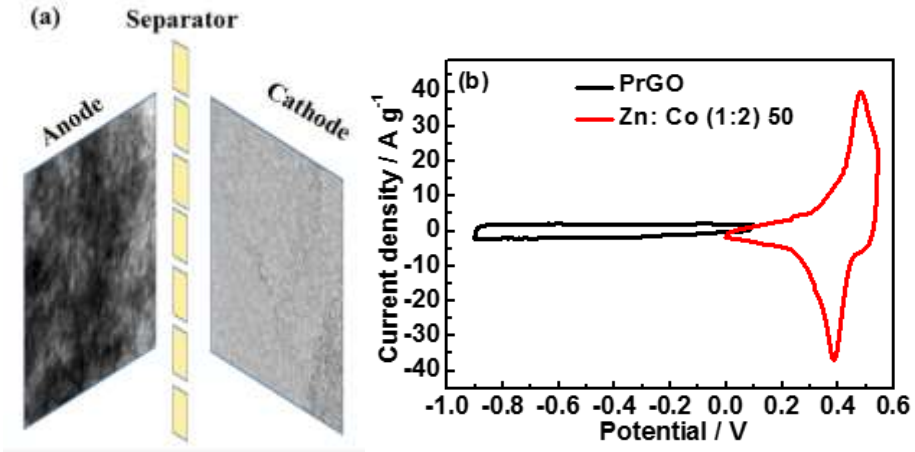

Figure 3.27: Schematic diagram of an asymmetric PrGO//Zn: Co (1:2) 50 supercapacitor cell (a), CV curves of PrGO and Zn: Co (1:2) 50 electrodes at a scan rate of 10 mV s^{-1} (b).

The cell voltages window of the PrGO//Zn: Co (1:2) ASC is optimized based on the working potential range of Zn: Co (1:2) 50 and PrGO in a 3-electrode system. **Fig. 3.27b** displays the working potential window of PrGO (-0.9 ~ +0.1 V *vs.* Hg/HgO) and Zn: Co (1:2) 50 (0 ~ +0.55 V *vs.* Hg/HgO) electrode at a scan rate of 10 mV/s. According to the individual electrode potential range, the cell voltage of the fabricated ASC is fixed at 1.45 V.

In order to investigate the range of operating cell voltages, a series of CV curves of the assembled ASC device at different cell voltages were recorded at 50 mV/s (**Fig. 3.28a**). The shape of the CV curves is not affected by the cell voltage increase, showing the redox peaks within the cell voltages window. The GCD curves at various cell voltages acquired at a current

density of 3 A g^{-1} are also depicted in **Fig. 3.28b**. Both CV and GCD plots reveal that the cell voltages window of PrGO//Zn: Co (1:2) 50 asymmetric supercapacitor could be extended up to 1.6 V even though 1.5 V is chosen as the cell voltage for further characterization of the electrochemical properties of the device.

Fig. 3.28c depicts the CV curves of the ASC at a cell voltage of 1.5 V as a function of the scan rate from 10 to 75 mV s^{-1}. No obvious change in the shape of the CV curves is observed. The variation of the specific capacity, calculated based on obtained CV curves, is given in **Fig. 3.28d**. A maximum specific capacity of the flexible ASC device is determined to be about ~50 C g^{-1} at a scan rate of 10 mV s^{-1}. The GCD curves of the ASC device are also investigated to calculate E_d and P_d (**Fig. 3.28e**). The Ragone plot relating E_d and P_d is displayed in **Fig. 3.28f**. The fabricated flexible ASC cell exhibits a remarkably high energy density and power density of about 17.7 W h kg^{-1} and 435 W kg^{-1}, respectively. Even at a high current density of 10 A g^{-1}, the fabricated ASC cell delivers an energy density of 13.2 W h kg^{-1} at a high power density of 11699 W h kg^{-1}. This result reveals an improved energy density at high power density compared with other supercapacitor devices: NiS_x//AC (53.5 W kg^{-1} and 4.1 W h kg^{-1}) [1], MCS/GNF//AC (74.87 W kg^{-1} and 14.33 W h kg^{-1}) [13], NiS//NiS (250 W kg^{-1} and 16.5 W h kg^{-1}) [31], CoS//CoS (150 W kg^{-1} and 4.8 W h kg^{-1}) [32], $CusbS_2$//$CusbS_2$ (341 W kg^{-1} and 2.6 Wh kg^{-1}) [33], $NiCo_2S_4$//C 160 W kg^{-1} and 22.8 Wh kg^{-1}) [34]. **Fig. 3.28g** presents the Nyquist plot of the fabricated PrGO//Zn: Co (1:2) 50 ASC device. The series resistance (R_s) of the fabricated ASC device is determined to be ~0.2 ohm·cm^{-2}, while the R_{ct} value due to the charge-transfer resistance is ~24.1 ohm·cm^{-2}.

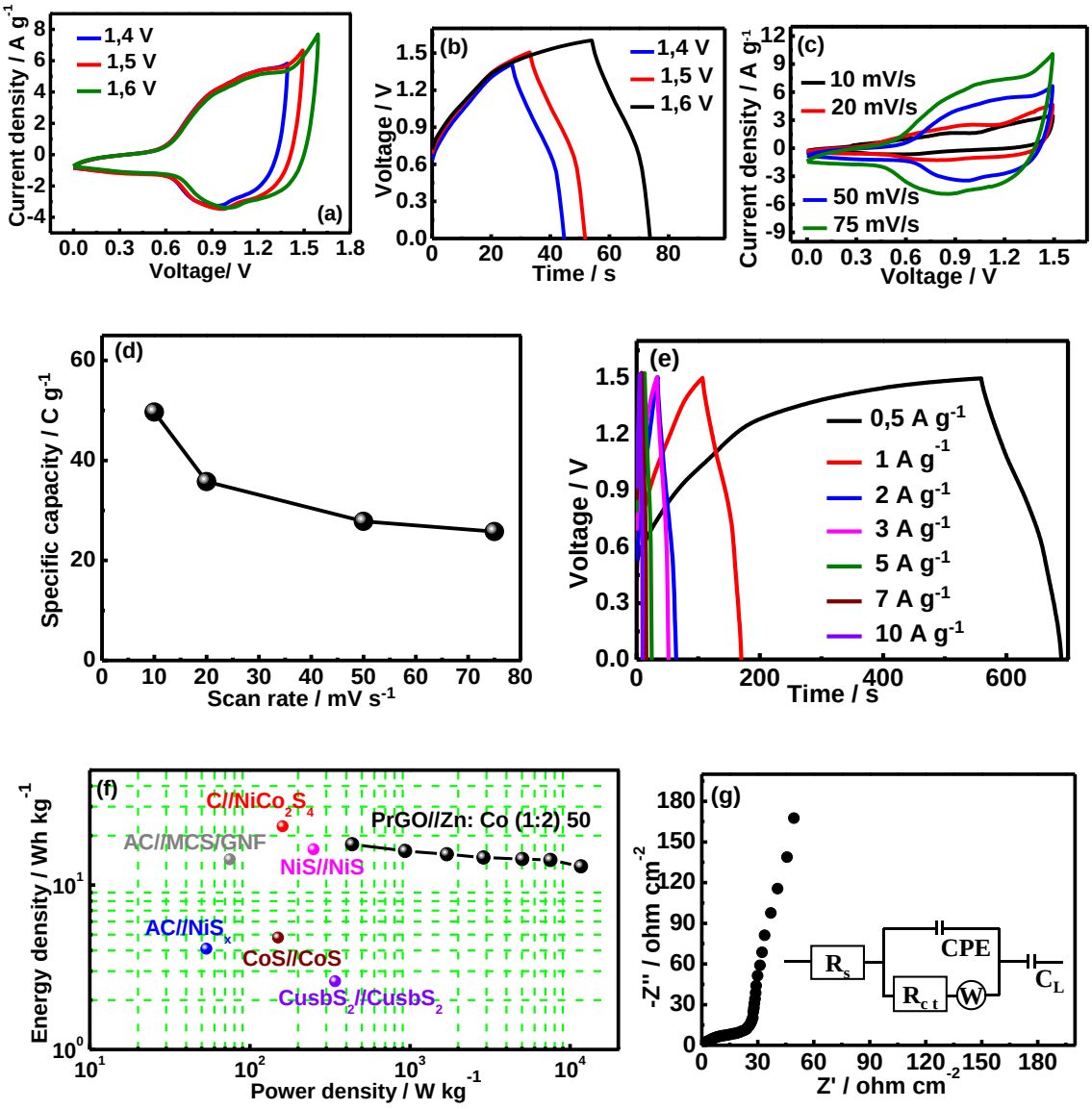

Figure 3.28: (a) CV and (b) GCD curves at different cell voltage values, (c) CV curves at various scan rates, (d) variation of the specific capacity as a function of scan rate, (e) GCD curves at various current densities, (f) typical Ragone plot, (g) Nyquist plot of the fabricated asymmetric supercapacitor device, the inset in (g) is the corresponding equivalent circuit.

In addition, the performance of the fabricated ASC device under mechanical strain is examined by recording the CV curves at different bending angles. **Fig.3.29a** and **b** depict the CV curves of the flexible ASC device as a function of the bending angle (0 to 135 °) recorded at a cell voltage of 1.5 V and a scan rate of 50 mV s^{-1}. No significant distortion of CV curves is apparent even when the bending angle is as high as 135 °, which confirms the good flexibility of the fabricated ASC cell. For viable applications, supercapacitors should have long term electrochemical stability. Furthermore, the stability of the fabricated flexible ASC is evaluated

for 5,000 cycles (**Fig.3.29c**). It should be noticed that in the first 400 cycles, the capacity retention is ~ 122%, most likely due to the complete activation of both electrode materials. After 5,000 cycles, the capacity retention rate of the prepared flexible ASC device is ~ 84%, indicating the good cycling stability of the fabricated flexible ASC device.

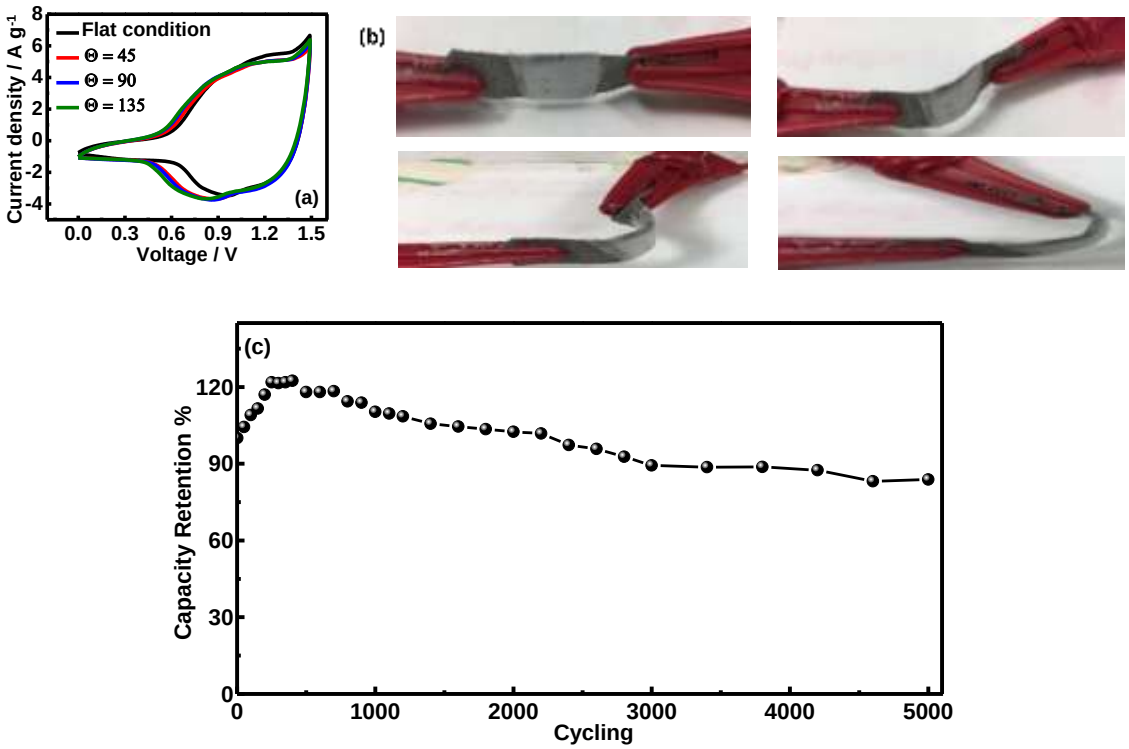

Figure 3.29: CV curves of the ASC at 50 mV/s under different bending angles of 0-135 °in 2 M KOH solution (a), images of the bent cells (b), cycling performance of the fabricated flexible ASC device at 2 A g^{-1} for 5,000 cycles (c).

3.9 Conclusion

In summary, a series of ZnCoS nanomaterials are synthesized by controlling the initial Co/Zn mole ratio and the temperature during the chemical precipitation process. Under optimized conditions, the Zn: Co (1:2) 50 electrode exhibits a specific capacity of ~624 C g^{-1} at a current density of 1 A g^{-1}, with good rate capability (~81% retention from 1 A g^{-1} to 20 A g^{-1}) and excellent cycling stability (almost no obvious decrease of the capacity at a current density of 20 A g^{-1} after 6,000 cycles) in 2M KOH aqueous electrolyte. In addition, Zn: Co (1:2) 50 electrode displays an improved electrochemical performance than the bare ZnS electrode. Furthermore, a PrGO//Zn: Co (1:2) 50 asymmetric supercapacitor (ASC) device is assembled. The device demonstrates a good electrochemical performance within a voltage window of 1.5 V along with good energy and power densities. Moreover, the absence of a significant distortion

of the CV curves at different bending angles indicates the good flexibility of the fabricated ASC device. The results obtained in the present work suggest that Zn: Co (1:2) 50 can be applied as a positive electrode material for designing flexible supercapacitors with high performance.

3.10 References

[1] J. Wang, K. Y. Ma, J. Zhang, F. Liu, J. P. Cheng, Template-free Synthesis of Hierarchical Hollow NiS_x Microspheres for Supercapacitor, J. Colloid Interface Sci. 507 (2017) 290-299.

[2] X. F. Li, J. F. Shen, N. Li, M. X. Ye, Template-Free Solvothermal Synthesis of NiS_2 Microspheres on Graphene Sheets for High-Performance Supercapacitors, Mater. Lett. 139 (2015) 81-85.

[3] R. Ren, M. S. Faber, R. Dziedzic, Z. H. Wen, S. H. Jin, S. Mao, J. H. Chen, Metallic CoS_2 Nanowire Electrodes for High Cycling Performance Supercapacitors, Nanotechnology 26 (2015) 494001.

[4] Q. H. Wang, L. F. Jiao, H. M. Du, W. X. Peng, Y. Han, D. W. Song, Y. C. Si, Y. J. Wang, H. T. Yuan, Novel Flower-like CoS Hierarchitectures: One-pot Synthesis and Electrochemical Properties, J. Mater. Chem. 21 (2011) 327-329.

[5] B. B. Wei, H. F. Liang, R. R. Wang, D. F. Zhang, Z. B. Qi, Z. C. Wang, One-step Synthesis of Graphitic-C_3N_4/ZnS Composites for Enhanced Supercapacitor Performance, J. Energy Chem. 27 (2018) 472-477.

[6] R. Ramachandran, M. Saranya, P. Kollu, B. P. C. Raghupathy, S. K. Jeong, A. N. Grace, Solvothermal Synthesis of Zinc Sulfide Decorated Graphene (ZnS/G) Nanocomposites for Novel Supercapacitor Electrodes, Electrochim. Acta 178 (2015) 647-657.

[7] H. Yan, T. Li, Y. Lu, J. Cheng, T. Peng, J. Xu, L. Yang, X. Hua, Y. Liu, Y. Luo, Template-free Synthesis of Ordered ZnO@ZnS Core-shell Arrays for High Performance Supercapacitors, Dalton Trans. 45 (2016) 17980-17986.

[8] N. S. Arul, L. S. Cavalcante, J. In Han, Facile Synthesis of ZnS/MnS Nanocomposites for Supercapacitor Applications, J. Solid State Electrochem. 22 (2017) 303-313.

[9] J. Pu, F. Cui, S. Chu, T. Wang, E. Sheng, Z. Wang, Preparation and Electrochemical Characterization of Hollow Hexagonal $NiCo_2S_4$ Nanoplates as Pseudocapacitor Materials, ACS Sustain. Chem. Eng. 2 (2013) 809-815.

[10] C. Liu, X. Wu, $NiCo_2S_4$ Nanotube Arrays Grown on Flexible Carbon Fibers as Battery-type Electrodes for Asymmetric Supercapacitors, Mater. Res. Bull. 103 (2018) 55-62.

[11] C. Liu, X. Wu, H. Xia, Flexible Mn-decorated $NiCo_2S_4$ Core–shell Nanowire Arrays for a High Performance Hybrid Supercapacitor Electrode with a Long Cycle Life, CrystEngComm. 20 (2018) 4735-4744.

[12] W. Xu, J. Lu, W. Huo, J. Li, X. Wang, C. Zhang, X. Gu, C. Hu, Direct Growth of $CuCo_2S_4$ Nanosheets on Carbon Fiber Textile with Enhanced Electrochemical Pseudocapacitive Properties and Electrocatalytic Properties Towards Glucose Oxidation, Nanoscale 10 (2018) 14304-14313.

[13] M. Yu, X. Li, Y. Ma, R. Liu, J. Liu, S. Li, Nanohoneycomb-like Manganese Cobalt Culfide/Three Dimensional Graphene-nickel Foam Hybid Electrodes for High-rate Capability Supercapacitors, Appl. Surf. Sci. 396 (2017) 1816-1824.

[14] G. C. Huang, T. Chen, Z. Wang, K. Chang, W. X. Chen, Synthesis and Electrochemical Performances of Cobalt Sulfides/Graphene Nanocomposite as Anode Material of Li-ion Battery, J. Power Sources 235 (2013) 122-128.

[15] B. Chen, R. Li, G. Ma, X. Gou, Y. Zhu, Y. Xia, Cobalt Sulfide/N,S Codoped Porous Carbon Core-shell Nanocomposites as Superior Bifunctional Electrocatalysts for Oxygen Reduction and Evolution Reactions, Nanoscale 7 (2015) 20674-20684.

[16] M. Javed, J. Chen, L. Chen, Y. Xi, C. Zhang, B. Wan, C. Hu, Flexible Full-solid State Supercapacitors Based on Zinc Sulfide Spheres Growing on Carbon Textile with Superior Charge Storage, J. Mater. Chem. A 4 (2016) 667-674.

[17] B. Sarma, R. S. Ray, M. Misra, Charge Storage in Flower-like ZnS Electrochemically Deposited on TiO_2 Nanotube, Mater. Lett. 139 (2015) 77-80.

[18] C. Z. Wei, Q. L. Ru, X. T. Kang, H. Y. Hou, C. Cheng, D. J. Zhang, Self-template Synthesis of Double Shelled ZnS-$NiS_{1.97}$ Hollow Spheres for Electrochemical Energy Storage, Appl. Surf. Sci. 435 (2018) 993-1001.

[19] U. M. Patil, J. S. Sohn, S. B. Kulkarni, S. C. Lee, H. G. Park, K. V. Gurav, J. H. Kim, S. C. Jun, Enhanced Supercapacitive Performance of Chemically Grown Cobalt–nickel Hydroxides on Three-dimensional Graphene Foam Electrodes, ACS Appl. Mater. Interfaces 6 (2014) 2450-2458.

[20] Y. Liu, J. N. Zhang, S. P. Wang, K. X. Wang, Z. M. Chen, Q. Xu, Facilely Constructing 3D Porous $NiCo_2S_4$ Nanonetworks for High-performance Supercapacitors, New J. Chem. 38 (2014) 4045-4048.

[21] X. J. Chen, D. Chen, X. Y. Guo, R. M. Wang, H. Z. Zhang, Facile Growth of Caterpillar-like $NiCo_2S_4$ Nanocrystal Arrays on Nickle Foam for High-performance Supercapacitors, ACS Appl. Mater. Interfaces 9 (2017) 18774-18781.

[22] J. S. S. U. M. Patil, S. B. Kulkarni, S. C. Lee, H. G. Park, K. V. Gurav, J.H. Kim, and S. C. Jun, Enhanced Supercapacitive Performance of Chemically Grown Cobalt−nickel Hydroxides on Three-Dimensional Graphene Foam Electrodes, ACS Appl. Mater. Interfaces 2014 (2014) 8.

[23] Y. Liu, J. Zhang, S. Wang, K. Wang, Z. Chen, Q. Xu, Facilely Constructing 3D Porous $NiCo_2S_4$ Nanonetworks for High-performance Supercapacitors, New J. Chem. 38 (2014) 4045-4048.

[24] X. Chen, D. Chen, X. Guo, R. Wang, H. Zhang, Facile Growth of Caterpillar-like $NiCo_2S_4$ Nanocrystal Arrays on Nickle Foam for High-performance Supercapacitors, ACS Appl. Mater. Interfaces 9 (2017) 18774-18781.

[25] C. Cheng, D. Kong, C. Wei, W. Du, J. Zhao, Y. Feng, Q. Duan, Self-template Synthesis of Hollow Ellipsoid Ni-Mn Sulfides for Supercapacitors, Electrocatalytic Oxidation of Glucose and Water Treatment, Dalton Trans. 46 (2017) 5406-5413.

[26] Y. Zhu, Z. Wu, M. Jing, X. Yang, W. Song, X. Ji, Mesoporous $NiCo_2S_4$ Nanoparticles as High-performance Electrode Materials for Supercapacitors, J. Power Sources 273 (2015) 584-590.

[27] Y. Sui, Y. Zhang, H. Hu, Q. Xu, F. Yang, Z. Li, High Energy Density Asymmetric Supercapacitor Based $ZnS/NiCo_2S_4/Co_9S_8$ Nanotube Composites Materials, Adv. Mater. Interfaces 5 (2018) 1800018.

[28] Y. Zhu, X. Chen, W. Zhou, K. Xiang, W. Hu, H. Chen, Controllable Preparation of Highly Uniform $CuCo_2S_4$ Materials as Battery Electrode for Energy Storage with Enhanced Electrochemical Performances, Electrochim. Acta 249 (2017) 64-71.

[29] H. R. Naderi, P. Norouzi, M. R. Ganjali, Electrochemical Study of a Novel High Performance Supercapacitor based on MnO_2 /Nitrogen-doped Graphene Nanocomposite, Appl. Surf. Sci. 366 (2016) 552-560.

[30] S. Chen, J. Duan, Y. Tang, S. Zhang Qiao, Hybrid Hydrogels of Porous Graphene and Nickel Hydroxide as Advanced Supercapacitor Materials, Chem. Eur. J. 19 (2013) 7118-7124.

[31] S. Nandhini, A. Mary, G. Muralidharan, Facile Microwave-hydrothermal Synthesis of NiS Nanostructures for Supercapacitor Applications, Appl. Surf. Sci. 449 (2018) 485-491.

[32] H. Z. Wan, X. Ji, J. J. Jiang, J. W. Yu, L. Miao, L. Zhang, S. W. Bie, H. C. Chen, Y. J. Ruan, Hydrothermal Synthesis of Cobalt Sulfide Nanotubes: The Size Control and its Application in Supercapacitors, J. Power Sources 243 (2013) 396-402.

[33] R. K. G. K. Ramasamy, H. Sims, S. Palchoudhury, S. Ivanova and A. Gupta, Layered Ternary Sulfide $CuSbS_2$ Nanoplates for Flexible Solid-state Supercapacitors, J. Mater. Chem. A 3 (2015) 13263-13274.

[34] W. Kong, C. Lu, W. Zhang, J. Pu, Z. Wang, Homogeneous Core–shell $NiCo_2S_4$ Nanostructures Supported on Nickel Foam for Supercapacitors, J. Mater. Chem. A 3 (2015) 12452-12460.

CHAPTER 4. SELF-TEMPLATE SYNTHESIS OF ZnS/Ni_3S_2 AS ADVANCED ELECTRODE MATERIAL FOR HYBRID SUPERCAPACITORS

4.1 Introduction

Based on our previous works, the ZnCoS electrode material, synthesized under optimized conditions (i.e. Zn/Co molar ratio and precipitation temperature) exhibited a good electrochemical performance with a maximum specific capacity of ~624 C g^{-1} at 1 A g^{-1}, good rate capability (~81% retention from 1 A g^{-1} to 20 A g^{-1}) and excellent cycling stability (almost no obvious decrease of the capacity at a current density of 20 A g^{-1} after 6,000 cycles). The results revealed that the incorporation of other elements into the crystal lattice of mono-metal sulfide could be promising for achieving satisfactory supercapacitor performance. Except for Co-based sulfides, Ni-based sulfides also have received extensive attention, because of their high theoretical specific capacity values, rich oxidation states, and cost-effectiveness. Additionally, the preparation of Ni-based bimetal sulfides/selenides has proven to enhance their electrochemical performance as electrode materials for supercapacitors. Thus, various materials such as Ni_3S_2@Co_9S_8 and NiS@$NiSe_2$ [1], Ni_3S_2@β-NiS [2], Ni_3S_2-NiS nanowires [3], Ni_3S_2-$Cu_{1.8}S$ nanosheets [4], hollow Ni_3S_2-NiS@Ni_3S_4 core/shell sub-microspheres [5], and Ni_3S_2-NiS/N-doped graphene [6] have been prepared and investigated as electrodes for supercapacitors.

Unlike nickel sulfides, the preparation of Ni-Zn electrodes has been described only in a few reports [7, 8]. Zhao *et al.* were the first to report the synthesis of ZnS/Ni_3S_2@Ni composite with a core–shell structure using a two-step method consisting of solution reduction and template method and applied the resulting material for electromagnetic absorption [7]. In a recent report, Li *et al.* adopted a two-step hydrothermal method to produce cactus-like ZnS/Ni_3S_2 hybrid with a high electrochemical performance for supercapacitors [8]. The ZnS/Ni_3S_2 electrode displayed a specific capacitance of 2093 F g^{-1} at 1 A g^{-1} and cycling stability of 64% after 5,000 cycles at a current density of 3 A g^{-1}. Therefore, it is desirable to synthesize Zn-Ni sulfides to achieve good electrochemical energy storage performance.

4.2 Preparation of ZnS/Ni_3S_2

ZnS/Ni_3S_2 electrode materials are prepared through the following methods: hydrothermal and ion-exchange sulfurization (**Fig. 4.1**).

1g of PVP was dissolved in 15 mL Milli-Q water under magnetic stirring at room temperature (solution A). At the same time, a solution B was prepared by successive dissolution of 1 mmol of $Zn(CH_3COO)_2•2H_2O$ and 2 mmol of $NiCl_2•6H_2O$ in 5 mL Milli-Q water. The solutions A and B were mixed and 286.5 μL of ammonia (35 wt%) was added dropwise to this mixture under magnetic stirring at room temperature. The reaction was kept overnight at 50 ℃ in an oven after which a precipitate was formed. The precipitate was rinsed copiously with ethanol and Milli-Q water until the pH is ~7. The obtained product was re-dispersed in 30 mL Milli-Q water for further use.

100 mg of thioacetamide (TAA) was dissolved in 10 mL Milli-Q water and then mixed with 10 mL of the above solution under magnetic stirring at room temperature. After 30 min of stirring, the solution was heated at 130 ℃ for 5 h. After cooling to room temperature, the resulting black solid product was collected through centrifugation, rinsed with Milli-Q water and ethanol, and dried at 60 ℃ overnight. The sample was labeled as ZnS/Ni_3S_2.

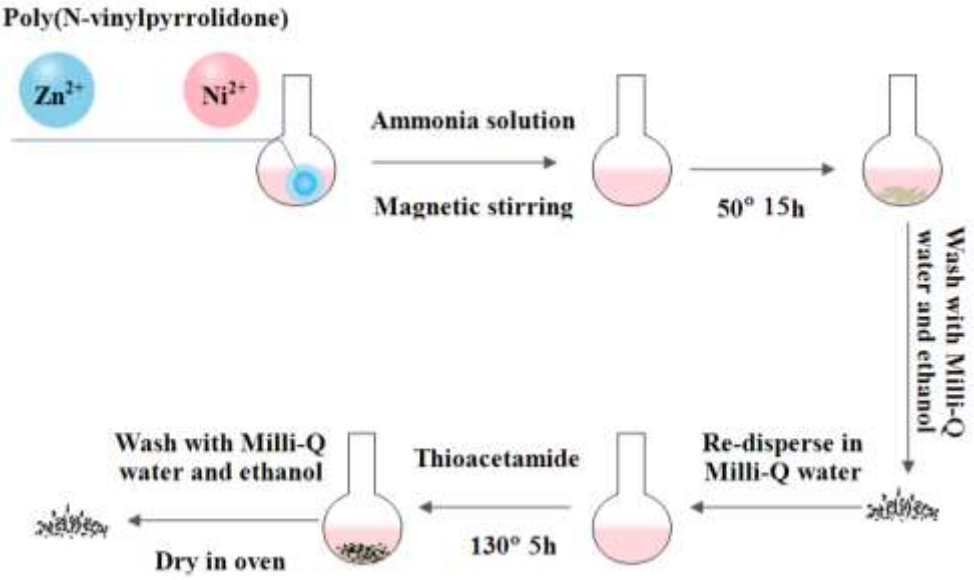

Figure 4.1: Schematic of the synthetic route of ZnS/Ni_3S_2 electrode materials.

4.3 Characterizations of ZnS/Ni_3S_2

4.3.1 Structure characterization of ZnS/Ni_3S_2

Information on the chemical composition and oxidation states of surface elements of the synthesized samples were assessed using XPS. The XPS full spectrum of the obtained ZnS/Ni_3S_2 is depicted in **Fig. 4.2a**, revealing the presence of Zn, Ni, and S. The presence of C, O, N in the XPS spectrum originates from residual PVP stabilizer.

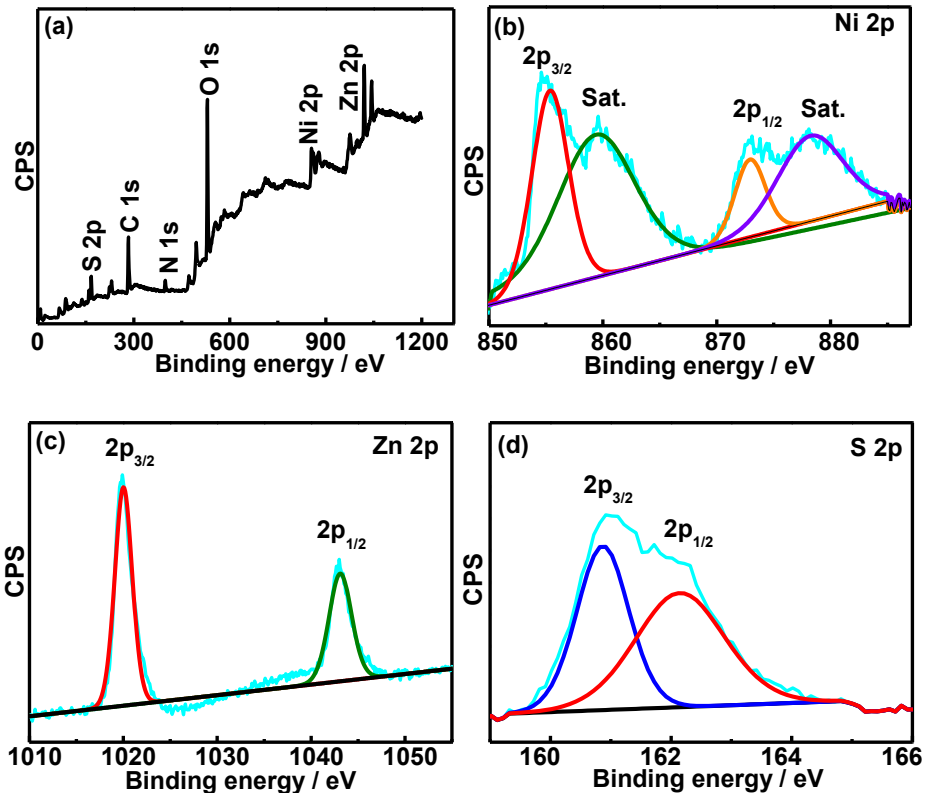

Figure 4.2: XPS analysis of ZnS/Ni_3S_2: (a) full spectrum; (b), (c) and (d) are respectively the Ni_{2p}, Zn_{2p} and S_{2p} high resolution spectra. "Sat" in Fig. 4.2b denotes satellite peaks.

The high-resolution XPS spectra of the Ni_{2p}, Zn_{2p}, and S_{2p} elements are additionally provided (**Fig. 4.2b-d**). The Ni_{2p} XPS high-resolution spectrum (**Fig. 4.2b**) comprises $Ni_{2p3/2}$ and $Ni_{2p1/2}$ spin-orbit doublets along with two shakeup satellite peaks. The $Ni_{2p3/2}$ at ~855.0 eV, $Ni_{2p1/2}$ at ~872.9 eV, and the two shake-up satellite peaks at ~859.6 and ~878.5 eV are characteristic of Ni^{2+} [9, 10]. In the Zn_{2p} XPS high-resolution spectrum (**Fig. 4.2c**), two strong peaks at ~1021.3 and ~1044.3 eV attributed to Zn^{2+} are visible, suggesting the presence of Zn^{2+} in the synthesized sample. The S_{2p} high-resolution XPS spectrum (**Fig. 4.2d**) can be fitted with two peaks at ~160.9 and 162.1 eV assigned to $S_{2p3/2}$ and $S_{2p1/2}$, respectively [11, 12].

The crystalline phase of the as-synthesized ZnS/Ni_3S_2 was investigated by XRD analysis (**Fig. 4.3a**). Two different phases could be observed. The diffraction peaks at ~28.6 °, 47.6 °, and 56.5 °, attributed to the (111), (220) and (311) crystal planes match the diffraction peaks of

the face-centered cubic sphalerite ZnS structure (JCPDS 05-0566) [13]. Additionally, the diffraction peaks at 2θ values of ~21.8 °, 31.0 °, 49.4 °, and 55.1 °are assigned to the (101), (110), (113) and (122) crystal planes of Ni_3S_2 (JCPDS 44-1418) [9, 14, 15]. The observed diffraction peaks indicate that the product is a mixture of ZnS and Ni_3S_2 phases. In addition, using the Bragg's law (equation **3-1**), the interplanar distance d values of the diffraction peaks at 2θ of ~21.8 °, 28.6 °, 31.0 °, 47.6 °, 49.4 °, 55.1 °, and 56.5 °are determined to be ~0.40, 0.30, 0.28, 0.19, 0.18, 0.17, and 0.16 nm, respectively. Furthermore, the crystallite size of the synthesized sample is determined using the Scherrer formula (equation **3-2**). Using the FWHM of the (111) peak, an average crystallite size of 8 nm is estimated.

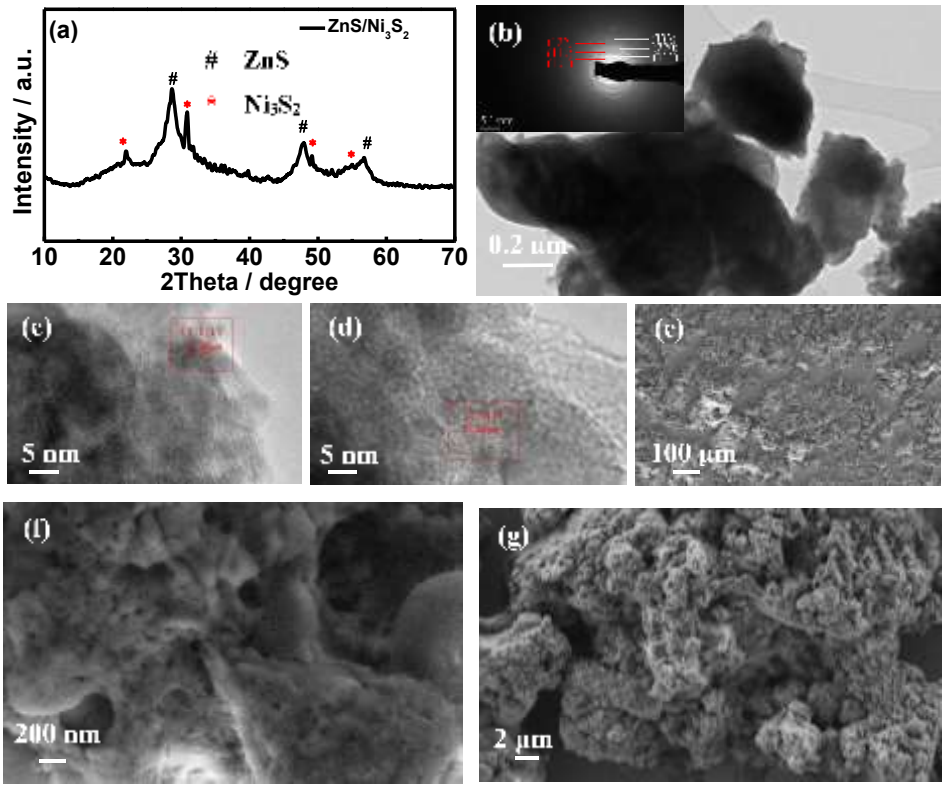

Figure 4.3: (a) XRD pattern, (b) TEM image, (c, d) HRTEM images and (e, f, g) SEM images of ZnS/Ni_3S_2; the inset in (b) is the SAED pattern.

Fig. 4.3b-d depict typical TEM images of as-prepared ZnS/Ni_3S_2. **Fig. 4.3b** shows a low resolution TEM image, from which a quasi-sheet-like structure can be observed. Furthermore, the selected area electron diffraction (SAED) pattern reveals rings and dots, suggesting good crystallinity of the ZnS/Ni_3S_2 nanoparticles (inset in **Fig. 4.3b**). The interplanar distance d values of the lattice fringes, calculated from the SAED pattern, are ~0.30, 0.19, 0.16 nm, in accordance with the (111), (220), and (333) lattice planes of ZnS. Moreover, additional three lattice fringes of ~0.40, 0.28, 0.17 nm due to the (101), (110) and (122) lattice planes of Ni_3S_2

are also detected. HRTEM images of ZnS/Ni_3S_2 are displayed in **Fig. 4.3c** and **d**. The clear lattice fringe spacing of ~0.30 nm (**Fig. 4.3c**) matches well with the (111) lattice plane of ZnS phase, while the lattice fringe spacing of ~0.28 nm is in good accordance with the (110) lattice plane of Ni_3S_2 phase (**Fig. 4.3d**). The results corroborate the XRD analysis.

SEM images of ZnS/Ni_3S_2 are depicted in **Fig. 4.3e-g**. Unlike the smooth surface of bare ZnS sample (**Fig. 3.1**), the SEM image of ZnS/Ni_3S_2 sample, at a lower magnification, reveals that the surface is very rough, suggesting that addition of Ni enhances the surface roughness (**Fig. 4.3e**). Furthermore, it could be clearly observed that this rough structure is composed of numerous loose particles and porous structure (**Fig. 4.3f-g**). This roughness combined with a loose and porous structure is expected to provide more electroactive sites between active material and electrolyte [16, 17].

The synthesized ZnS/Ni_3S_2 is expected to exhibit a large specific surface area (SSA), owing to its unique roughness and loose structure. Nitrogen adsorption-desorption isotherms are used to assess the SSA and porous texture of ZnS/Ni_3S_2 (**Fig. 4.4**), which are identified as the typical type IV, according to the IUPAC classification. Additionally, hysteresis loops in the 0.6-0.9 relative pressure region are apparent (**Fig. 4.4a**). The results indicate the presence of mesoporous structures in the sample, as evidenced by the pore diameter distribution profile (**Fig. 4.4b**), determined from the desorption isotherm using the BJH model. The presence of a pore diameter peak at ~10 nm is a good indication of the presence of mesopores in ZnS/Ni_3S_2. The BET SSA of ZnS/Ni_3S_2 is 147.9 $m^2\ g^{-1}$. The SSA of ZnS/Ni_3S_2 sample, prepared through our method, is found to be larger than that reported for metal sulfides such as ZnS-$NiS_{1.97}$ (105.3 $m^2\ g^{-1}$) [18], $Zn_xCo_{1-x}S$ (77.2 $m^2\ g^{-1}$) [19], $Zn_{0.76}Co_{0.24}S$@Ni_3S_2 (89.1 $m^2\ g^{-1}$) [20], $ZnCo_2S_4$ core-shell nanospheres (117.3 $m^2\ g^{-1}$) [21] and flowerlike Sb_2S_3 (14.7 $m^2\ g^{-1}$) [22]. Accordingly, the porous structure and large specific surface area are necessary to achieve electrode materials with good electrochemical energy storage performance [23, 24]. Therefore, it is quite reasonable to hypothesize that the as-synthesized ZnS/Ni_3S_2 with such roughness and loose structure may have promising applications in electrochemical supercapacitors.

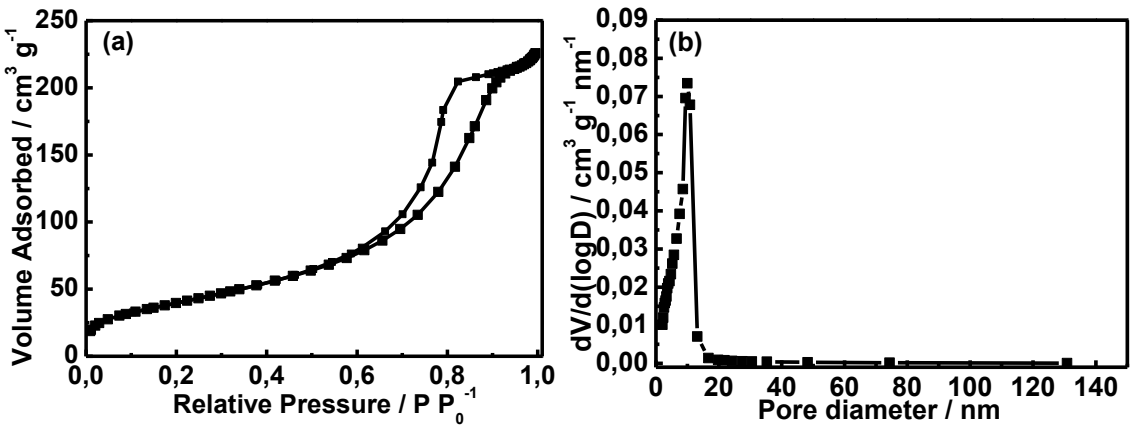

Figure 4.4: (a) Nitrogen adsorption-desorption isotherm and (b) pore size distribution curve of ZnS/Ni_3S_2.

4.3.2 Electrochemical properties of ZnS/Ni_3S_2

In order to investigate the operating potential window of ZnS/Ni_3S_2 electrode, CV curves along with cathodic and anodic peak current densities *vs.* the square root of sweep rate at various scan rates (10 - 100 mV s^{-1}) in the 0 to 0.7 V potential window are recorded (**Fig. 4.5**). CV curves exhibit obvious redox peaks (**Fig. 4.5a**), indicating a faradic battery-type characteristic of the ZnS/Ni_3S_2 electrodes [25]. Additionally, when the scan rate increases (**Fig. 4.5a**), the current density is enhanced without affecting the shape of the CV curves. The results suggest a good rate capability of the ZnS/Ni_3S_2 electrode. Furthermore, when the scan rate increases, the oxidation peaks shift to higher potential and the reduction peak moves towards lower potential. This phenomenon is most likely due to electrochemical polarization during the surface redox reaction of the electrodes [35].

The relationship between the cathodic and anodic peak current densities *vs.* the square root of sweep rate (**Fig. 4.5b**) is also recorded to determine if the capacity is related to surface redox processes or bulk diffusion. The linear relationship confirms that the redox reactions of ZnS/Ni_3S_2 are under OH^- diffusion control rather than surface redox processes [26].

CV curves of ZnS/Ni_3S_2 electrodes over different potential windows are also acquired at a scan rate of 50 mV s^{-1} (**Fig. 4.5c**). Redox peaks, observed in all CV curves, are attributed to the electrochemical redox reactions of (Zn, Ni) species at the interfaces between electrolyte and electrode. However, when the potential window is extended above 0.6 V, a significant increase of the current attributed to oxygen evolution reaction (OER) is observed. A potential window (0 to +0.55 V) and a scan rate ranging from 5 to 50 mV s^{-1} are chosen to avoid the polarization and OER of the prepared ZnS/Ni_3S_2 electrode.

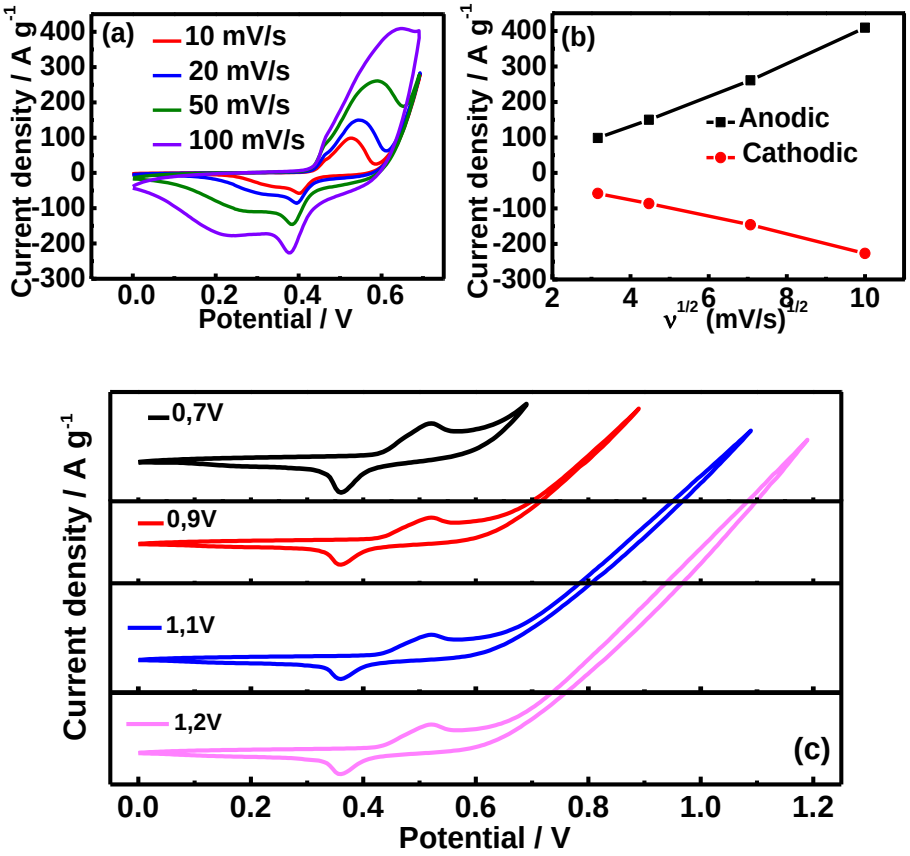

Figure 4.5: Electrochemical properties of ZnS/Ni_3S_2 electrode within the potential range of 0 to +0.7 V in 2 M KOH: (a) CV curves, (b) the anodic and cathodic peak current densities *vs.* the square root of scan rate, (c) CV curves of ZnS/Ni_3S_2 electrodes recorded in different potential windows at a scan rate of 50 mV s^{-1}.

Furthermore, the CV curves of ZnS/Ni_3S_2 electrode and bare nickel foam are measured at a scan rate of 10 mV s^{-1} in the potential range of 0 to +0.55 V (**Fig. 4.6**). The CV curve of bare nickel foam is almost a straight line, indicating that the capacity of bare nickel foam is almost negligible under our experimental conditions. In addition, redox peaks observed in the CV curve of ZnS/Ni_3S_2 electrode are likely due to the reversible faradic redox reaction of (Zn, Ni)S-OH. Therefore, the redox peaks seen in the CV curve of ZnS/Ni_3S_2 electrode are attributed to the following faradaic redox reactions [20, 27-29]:

$$ZnS + OH^- \leftrightarrow ZnSOH + e^-$$

$$ZnSOH + OH^- \leftrightarrow ZnSO + H_2O + e^-$$

$$Ni_3S_2 + 3OH^- \leftrightarrow Ni_3S_2(OH)_3 + 3e^-$$

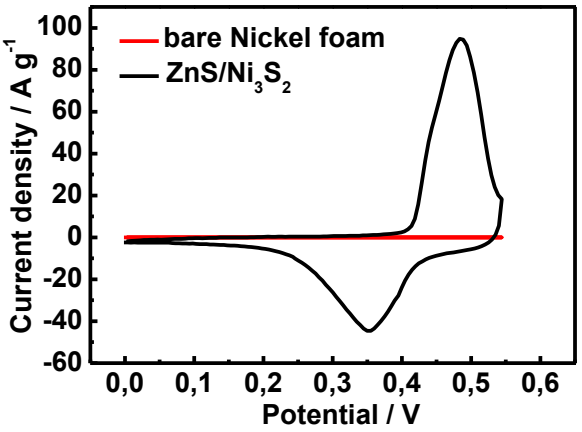

Figure 4.6: CV curves of ZnS/Ni_3S_2 electrodes and bare nickel foam at a scan rate of 10 mV s^{-1} in the potential range of 0 to +0.55 V.

The Faradic battery-type behavior of the ZnS/Ni_3S_2 electrode is investigated by recording the CV curves at different scan rates (5 - 50 mV s^{-1}) (**Fig. 4.7a**). Redox peaks could be seen in the CV curves in the potential window of 0 to +0.55 V, indicating faradaic battery-type behavior of the electrode. The position of anodic and cathodic peaks for ZnS/Ni_3S_2 electrode are given in **Table 4-1**.

Fig. 4.7b depicts the GCD plots of ZnS/Ni_3S_2 electrode within the current density span of 1 to 20 A g^{-1}. Clear potential plateaus, due to the electrochemical redox reactions of (Zn, Ni) species at the interfaces between electrolyte and electrode, are visible in the charge and discharge processes in all GCD curves. The potential plateaus match the redox characteristics observed in the CV curves, indicating strong faradaic battery-type characteristics of the electrode. All GCD curves provide almost symmetric characteristics, revealing the good charge-discharge columbic efficiency during electrochemical capacitive and reversible redox processes of the prepared ZnS/Ni_3S_2 electrode.

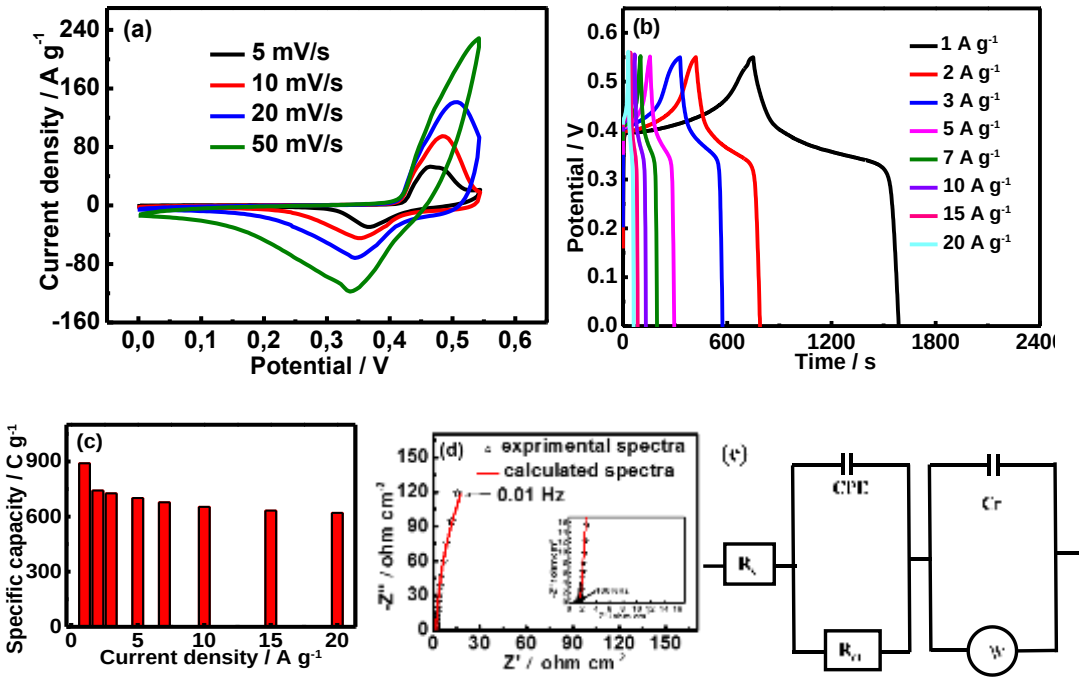

Figure 4.7: Electrochemical properties of ZnS/Ni_3S_2 electrode in 2 M KOH: (a) CV curves at different scan rates (5 to 50 mV s^{-1}), potential=0 to +0.55V; (b) GCD profiles at various current densities of 1, 2, 3, 5, 7, 10, 15 and 20 A g^{-1}; (c) the corresponding specific capacities within the current density span of 1 to 20 A g^{-1}; (d) Nyquist plots; (e) the corresponding equivalent circuit.

Table 4-1: The anodic and cathodic peak potentials of ZnS/Ni_3S_2 at various scan rates ranging from 5 to 50 mV s^{-1}.

Scan rate (mV s^{-1})	Potential of the anode peak (V *vs.* Hg/HgO)	Potential of the cathodic peak (V *vs.* Hg/HgO)
5	0.4692	0.3645
10	0.4836	0.3550
20	0.5082	0.3446
50	0.5421	0.3370

Specific capacity values, determined from GCD curves (**Fig. 4.7b**) and equation **1-4**, are displayed in **Fig. 4.7c**. The ZnS/Ni_3S_2 electrode provides specific capacity values of ~890, 742, 727, 701, 678, 653, 632, and 620 C g^{-1} at current densities of 1, 2, 3, 5, 7, 10, 15 and 20 A g^{-1}, respectively. When the current density increases from 1 to 20 A g^{-1}, the ZnS/Ni_3S_2 electrode retains about 70% of its initial specific capacity value, revealing a good rate capability. Moreover, the specific capacity of ZnS/Ni_3S_2 electrode is superior to that of many metal sulfide-

based electrode materials (**Table 4-2**). Such a desirable performance of the ZnS/Ni_3S_2 electrode indicates its potential usage for energy storage devices.

Table 4-2: Comparison of the specific capacity values of metal-sulfide based electrode materials for energy storage applications.

Electrode material	Specific capacity ($C\ g^{-1}$)	Capacity retention (%)	Ref
$Zn_{0.76}Co_{0.24}S$	-	86.4 (2k cycles at 5.0 A g^{-1})	[19]
rGO-Ni_3S_2	616.0 (1.0 A g^{-1})	92.7 (5k cycles at 5.0 A g^{-1})	[30]
Ni_3S_2/carbon nanotube	-	80 (1k cycles at 3.2 A g^{-1})	[31]
$ZnCo_2S_4$	-	95.5 (5k cycles at 4.0 A g^{-1})	[21]
ZnS-NiS_2	-	87 (1k cycles at 5.0 A g^{-1})	[32]
NiS_2	-	123.0% (10k cycles at 20.0 Ag^{-1})	[33]
$Zn_xNi_{1-x}S$/NF	-	81.5 (4k cycles at 2.0 A g^{-1})	[34]
ZnS-$NiS_{1.97}$	696.8 (5.0 A g^{-1})	Less 5.5% loss (6k cycles at 10.0 A g^{-1})	[18]
Co-S-80	-	86.5 (1k cycles at 0.5 A g^{-1})	[35]
ZnS/Ni_3S_2	-	64 (5k cycles at 3 A g^{-1})	[32]
ZnS/Ni_3S_2	**890 (1.0 A g^{-1})**	**81.7 (6k cycles at 10.0 A g^{-1})**	**Our work**

EIS analysis is used to investigate the frequency-dependent behavior of ZnS/Ni_3S_2 electrode materials. **Fig. 4.7d** depicts Nyquist plots with frequencies of some selected points and the corresponding fitted spectra of ZnS/Ni_3S_2 electrode. An equivalent circuit, based on reported works [36-39], and the corresponding calculated circuit parameters are also depicted in **Fig. 4.7e** and **Table 4-3**, respectively. According to the fitted equivalent circuit, the obtained series resistance (R_s), related to the high frequency region>10^4 Hz (intercept at the real axis), is about 1.03 ohm cm^{-2}; the charge-transfer resistance (R_{ct}), related to the depressed-semicircle in the high-to-medium frequency region (10^4 to 1 Hz), is about 1.01 ohm cm^{-2}. The appearance of CPE may be attributed to the porosity of the prepared ZnS/Ni_3S_2 electrode material and the calculated value is about 0.26 $sec^{1/n}/cm^2$ (n=0.47) and the faradaic capacitance is found to be 0.13 F/cm^2. Moreover, in the lower frequency region (< 1 Hz), the inclined line of the Warburg

line, which is related to the electrolyte ion (OH^-) diffusion from the electrolyte (2 M KOH) into the loose and porous ZnS/Ni_3S_2 electrode surface [40], represents a low diffusion resistance of 0.0046 $sec^{1/2}/cm^2$. The slop of the Warburg line is higher than 45 °, indicating the easy access of OH^- electrolyte for fast and reversible faradaic redox reaction and more ideal capacitor behavior [41, 42], which further confirms that the ZnS/Ni_3S_2 electrode can retain good capacitive performance.

Table 4-3: Impedance parameters determined from EIS spectra.

Sample	R_s (ohm·cm^{-2})	R_{ct} (ohm·cm^{-2})	CPE (S $sec^{1/n}/cm^2$)	n	C_F (F/cm^2)	W (S $sec^{1/2}/cm^2$)
ZnS/Ni_3S_2	1.03	1.01	0.26	0.47	0.13	0.0046

The cycling stability of ZnS/Ni_3S_2 electrode is established by repeated 6,000 charging/discharging cycles at a current density of 10 A g^{-1} (**Fig. 4.8a**). Encouragingly, the retention of the ZnS/Ni_3S_2 electrode is ~ 82% of its initial capacity after 6,000 charge/discharge cycles, which is better than 64% achieved by cactus-like ZnS/Ni_3S_2 at 3 A g^{-1} [8].

XPS analysis is conducted to assess the chemical changes that have occurred during the stability test. **Fig. 4.8b** depicts the XPS high-resolution spectrum of the Ni_{2p} of the ZnS/Ni_3S_2 electrode after 6,000 charging-discharging cycles. The spectrum can be deconvoluted with two spin-orbit peaks at ~856.4 and 874.3 eV assigned to $Ni^{2+}{}_{2p3/2}$ and $Ni^{2+}{}_{2p1/2}$, respectively. The presence of two satellite peaks (~862.1 and 880.1 eV), characteristic of Ni^{2+}, reveals the excellent reversible redox process during the charge-discharge cycling.

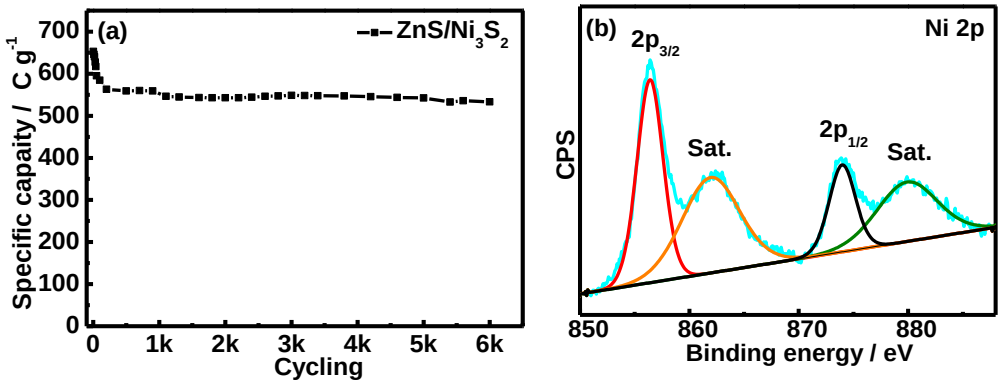

Figure 4.8: (a) Stability test of ZnS/Ni_3S_2 electrode at 10 A g^{-1} for 6,000 cycles; (b) Ni_{2p} high resolution XPS spectrum after 6,000 cycles. "Sat" in Fig. 6b denotes satellite peaks.

4.4 Fabrication of a hybrid supercapacitor (PrGO//ZnS/Ni_3S_2)

Hybrid supercapacitors are believed to combine the advantage of faradaic battery-type electrode material as a positive electrode and double-layer capacitor electrode material as a negative electrode; the combination of these two types of electrode materials is supposed to be able to enlarge the cell's operating voltage greatly and thus improve its energy density [25, 43, 44]. To further assess the practical utilization of the prepared ZnS/Ni_3S_2 electrode, a hybrid supercapacitor is assembled using ZnS/Ni_3S_2 electrode material as a positive electrode and porous reduced graphene oxide (PrGO) electrode material as a negative electrode (**Chapter 3.6**).

A 3-electrode system is used to determine the optimal operating cell voltage window of the hybrid supercapacitor based on the ZnS/Ni_3S_2 and PrGO working potential range. **Fig. 4.9a** depicts the working potential window *vs.* Hg/HgO of ZnS/Ni_3S_2 (0 to +0.55 V) and PrGO (-0.9 to +0.1 V) at a scan rate of 10 mV s^{-1}. Based on these values, the cell voltage of the fabricated hybrid supercapacitor is fixed at 1.45 V.

Fig. 4.9b displays a series of CV curves of the hybrid supercapacitor at different cell voltages at a scan rate=50 mV s^{-1}. Interestingly, increasing the cell voltage does not seem to affect the shape of the CV curves. Additionally, redox peaks are obvious for all investigated voltage windows. However, the polarization becomes much more obvious as the cell voltage is extended to 1.8 V. CV curves of the PrGO//ZnS/Ni_3S_2 hybrid supercapacitor *vs.* the scan rate (10 to 100 mV s^{-1}) at a cell voltage of 1.6 V are displayed in **Fig. 4.9c**. Again, under these experimental conditions, the shape of CV curves is not altered. GCD curves are also recorded at various cell voltage values (current density=5 A g^{-1}) to determine the Ragone plot (P_d vs. E_d) (**Fig. 4.9d**). Both CV and GCD analysis indicate that the PrGO//ZnS/Ni_3S_2 hybrid supercapacitor operating cell voltage window could be extended up to 1.8 V. However, a cell voltage of 1.6 V is used for further investigation of the electrochemical properties of the PrGO//ZnS/Ni_3S_2 hybrid supercapacitor, considering the energy density and the polarization of assembled hybrid supercapacitor.

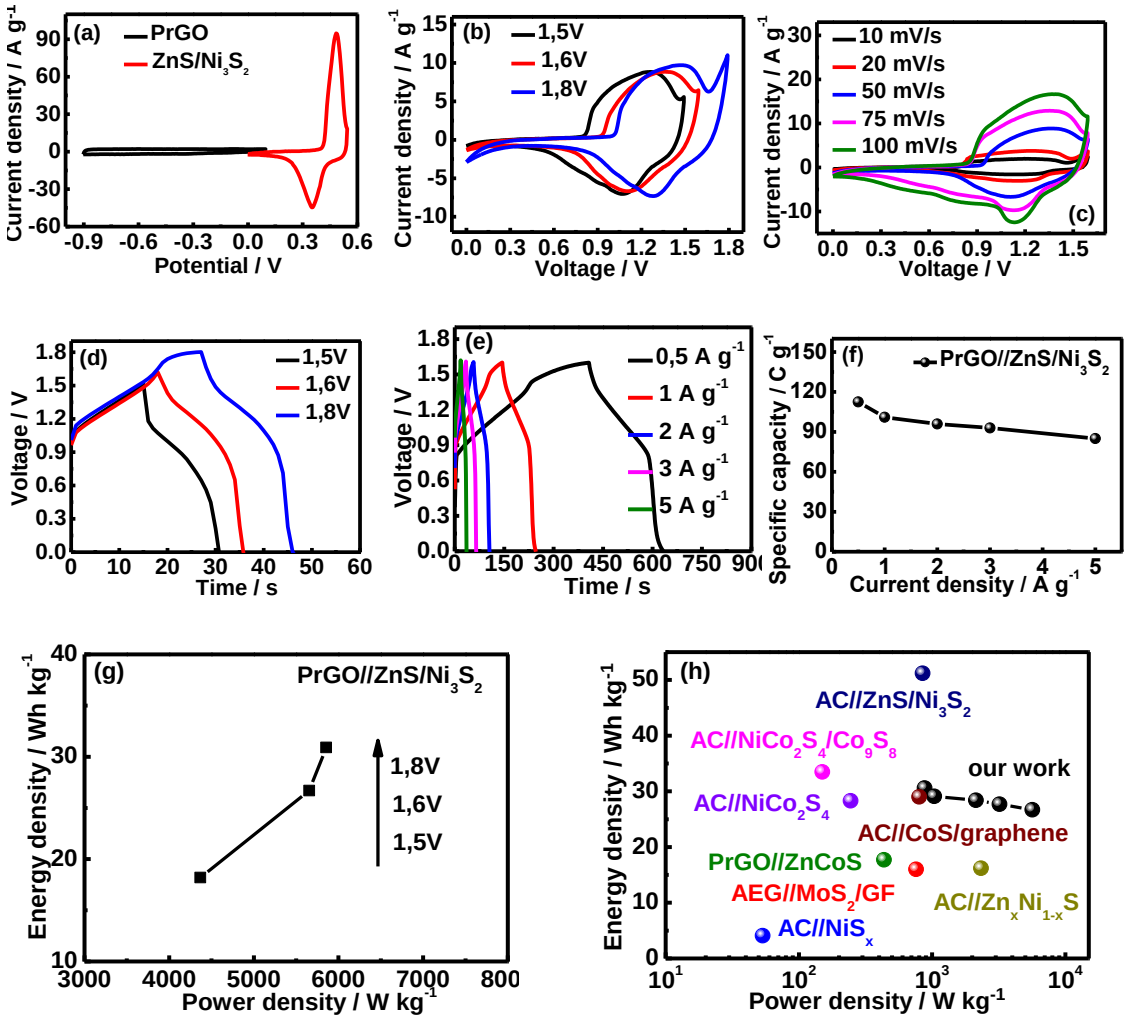

Figure 4.9: (a) CV curves of the positive and negative electrodes at a scan rate of 10 mV s^{-1}; (b) CV curves recorded at different cell voltages; (c) CV curves at different scan rates; (d) GCD curves recorded at different cell voltages; (e) GCD plots recorded as a function of current density; (f) the corresponding specific capacity as a function of current density; (g) the corresponding Ragone plot of the hybrid supercapacitor for different cell voltages (current density=5 A g^{-1}); (h) typical Ragone plot of the hybrid supercapacitor.

The GCD curves (**Fig. 4.9e**) of the hybrid supercapacitor are also recorded to estimate the specific capacity, P_d and E_d. The variation of the specific capacity, determined from the GCD curves and equation **1-4**, is summarized in **Fig. 4.9f**. The hybrid supercapacitor exhibits a maximum specific capacity of ~113 C g^{-1} at a current density of 0.5 A g^{-1}. Moreover, **Fig. 4.9g** depicts the Ragone plot of the PrGO//ZnS/Ni_3S_2 hybrid supercapacitor at various cell voltage values (current density = 5A g^{-1}). It could be clearly seen that higher the applied cell voltage, larger energy density the hybrid supercapacitor could offer (30.9 W h kg^{-1} at 1.8 V, 26.7 W h kg^{-1} at 1.6 V and 18.2 W h kg^{-1} at 1.5 V).

Additionally, **Fig. 4.9h** depicts the Ragone plot of the PrGO//ZnS/Ni_3S_2 hybrid supercapacitor. The hybrid supercapacitor exhibits relatively high energy density and power density values of 30.6 W h kg^{-1} and 880 W kg^{-1} at 0.5 A g^{-1}. The performance of the hybrid supercapacitor is also good even at a high current density of 5 A g^{-1}; indeed, the hybrid supercapacitor attains an energy density of 26.7 W h kg^{-1} at a high power density of 5659 W h kg^{-1}. These values are comparable to and even better than those reported in the literature for many other supercapacitor devices (**Table 4-4**).

Table 4-4: Comparison with other metal sulfide hybrid supercapacitors.

Electrode material	Working voltage / V	Energy density / Wh kg^{-1}	Power density / W kg^{-1}	Reference
Active carbon (AC)//CoS/graphene	1.6	29	800	[45]
AC//NiS_x	1.6	4.1	53.5	[16]
PrGO//ZnCoS	1.5	17.7	435	[46]
AC//$NiCo_2S_4$	1.5	28.3	245	[41]
AEG//MoS_2/GF	1.4	16	758	[47]
AC//$Zn_xNi_{1-x}S$	1.6	16.2	2330	[48]
AC//$NiCo_2S_4$/Co_9S_8	1.5	33.5	150	[11]
AC//ZnS/Ni_3S_2	1.6	51.2	849.4	[32]
PrGO//ZnS/Ni_3S_2	**1.6**	**30.6**	**880**	**Our work**

The practical application of the asymmetric supercapacitor is further demonstrated through powering yellow, red, and green LEDs using two asymmetric supercapacitors connected in series. As can be seen in **Fig. 4.10**, the yellow, red, and green LEDs can be sequentially illuminated upon connection to fully charged supercapacitors.

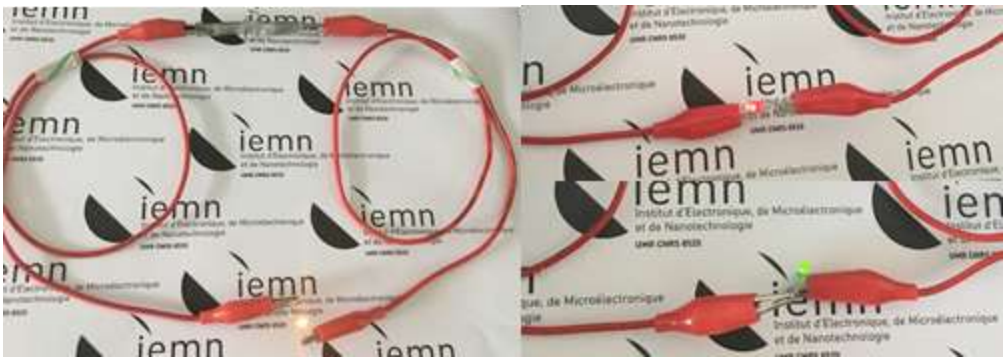

Figure 4.10: Photographs of the LEDs (yellow, red and green) powered by two asymmetric supercapacitor connected in series.

4.5 Conclusion

In summary, ZnS/Ni_3S_2 electrode material with a high specific surface area is synthesized using a self-template method. The ZnS/Ni_3S_2 electrode exhibits a high specific capacity of ~890 C g^{-1} at 1 A g^{-1}, with good cycling stability (~82% of capacity retention) at a current density of 10 A g^{-1} after 6,000 cycles in 2M KOH aqueous electrolyte. Furthermore, a PrGO//ZnS/Ni_3S_2 hybrid supercapacitor is fabricated to investigate the potential usage of the developed material for energy storage. Under an optimized cell voltage window (1.6 V), the hybrid supercapacitor achieves a good electrochemical performance such as a good energy density of 30.6 W h kg^{-1} at a power density of 880 W kg^{-1}. Moreover, for practical application, yellow, red, and green LEDs could be powered sequentially by using two ASC connected in series. The results reported in the present work hold promise for practical application of ZnS/Ni_3S_2 as a positive electrode material for assembling high-performance hybrid supercapacitors.

4.6 References

[1] W. T. Wei, L. W. Mi, Y. Gao, Z. Zheng, W. H. Chen, X. X. Guan, Partial Ion-exchange of Nickel-sulfide-derived Electrodes for High Performance Supercapacitors, Chem. Mater. 26 (2014) 3418-3426.

[2] W. Li, S. L. Wang, L. P. Xin, M. Wu, X. J. Lou, Single-crystal β-NiS Nanorod Arrays with a Hollow-structured Ni_3S_2 Framework for Supercapacitor Applications, J. Mater. Chem. A 4 (2016) 7700-7709.

[3] X. X. Zang, Z. Y. Dai, J. Yang, Y. Z. Zhang, W. Huang, X. C. Dong, Template-assisted Synthesis of Nickel Sulfide Nanowires: Tuning the Compositions for Supercapacitors with Improved Electrochemical Stability, ACS Appl. Mater. Interfaces 8 (2016) 24645-24651.

[4] Y. D. Liu, G. Q. Liu, X. Nie, A. Q. Pan, S. Q. Liang, T. Zhu, In Situ Formation of Ni_3S_2–$Cu_{1.8}S$ Nanosheets to Promote Hybrid Supercapacitor Performance, J. Mater. Chem. A 7 (2019) 11044-11052.

[5] L. L. Cheng, Y. Y. Hu, L. Ling, D. D. Qiao, S. C. Cui, Z. Jiao, One-step Controlled Synthesis of Hierarchical Hollow Ni_3S_2/NiS@Ni_3S_4 Core/shell Submicrospheres for High-performance Supercapacitors, Electrochim. Acta 283 (2018) 664-675.

[6] Y. Y. Luo, W. X. Que, C. H. Yang, Y. P. Tian, Y. W. Yang, X. T. Yin, Nitrogen-doped Graphene/Multiphase Nickel Sulfides Obtained by Ni-$C_3N_3S_3$ (Metallopolymer) Assisted

Synthesis for High-performance Hybrid Supercapacitors, Electrochim. Acta 301 (2019) 332-341.

[7] B. Zhao, G. Shao, B. Fan, W. Zhao, S. Zhang, K. Guan, R. Zhang, In Situ Synthesis of Novel Urchin-like ZnS/Ni_3S_2@Ni Composite with a Core–shell Structure for Efficient Electromagnetic Absorption, J. Mater. Chem. C 3 (2015) 10862-10869.

[8] X. X. Li, J. K. Sun, L. Y. Feng, L. J. Zhao, L. Ye, W. Q. Zhang, L. F. Duan, Cactus-like ZnS/Ni_3S_2 Hybrid with High Electrochemical Performance for Supercapacitors, J. Alloys Compd. 753 (2018) 508-516.

[9] T. Zhu, L. Zhu, J. Wang, G. Ho, In Situ Chemical Etching of Tunable 3D Ni_3S_2 Superstructures for Bifunctional Electrocatalysts for Overall Water Splitting, J. Mater. Chem. A 4 (2016) 13916-13922.

[10] M. Li, J. Cheng, F. Liu, X. Zhang, In Situ Growth of Nickel-cobalt Oxyhydroxide/Oxide on Carbon Nanotubes for High Performance Supercapacitors, Electrochim. Acta 178 (2015) 439-446.

[11] L. Hou, Y. Shi, S. Zhu, M. Rehan, G. Pang, X. Zhang, C. Yuan, Hollow Mesoporous Hetero-$NiCo_2S_4$/Co_9S_8 Submicro-spindles: Unusual Formation and Excellent Pseudocapacitance Towards Hybrid Supercapacitors, J. Mater. Chem. A 3 (2017) 133-144.

[12] X. Chen, D. Chen, X. Guo, R. Wang, H. Zhang, Facile Growth of Caterpillar-like $NiCo_2S_4$ Nanocrystal Arrays on Nickle Foam for High-performance Supercapacitors, ACS Appl. Mater. Interfaces 9 (2017) 18774-18781.

[13] M. Javed, J. Chen, L. Chen, Y. Xi, C. Zhang, B. Wan, C. Hu, Flexible Full-solid State Supercapacitors based on Zinc Sulfide Spheres Growing on Carbon Textile with Superior Charge Storage, J. Mater. Chem. A 4 (2016) 667-674.

[14] X. Xiog, B. Zhao, D. Ding, D. Chen, C. Yang, Y. Lei, M. Liu, One-step Synthesis of Architectural Ni_3S_2 Nanosheet-on-nanorods Array for Use as High-performance Electrodes for Supercapacitors, NPG Asia Mater. 8 (2016) 1-7.

[15] F. Chen, H. Wang, S. Ji, V. Linkov, R. Wang, High-performance All-solid-state Asymmetric Supercapacitors based on Sponge-like NiS/Ni_3S_2 Hybrid Nanosheets, Mater. Today Energy 11 (2019) 211-217.

[16] J. Wang, K. Y. Ma, J. Zhang, F. Liu, J. P. Cheng, Template-free Synthesis of Hierarchical Hollow NiS_x Microspheres for Supercapacitor, J. Colloid Interface Sci. 507 (2017) 290-299.

[17] G. Park, J. Cho, Y. Kang, Sodium-ion Storage Properties of Nickel Sulfide Hollow Nanospheres/Reduced Graphene Oxide Composite Powders Prepared by a Spray Drying Process and The Nanoscale Kirkendall Effect, Nanoscale 7 (2015) 16781-16788.

[18] C. Z. Wei, Q. L. Ru, X. T. Kang, H. Y. Hou, C. Cheng, D. J. Zhang, Self-template Synthesis of Double Shelled ZnS-$NiS_{1.97}$ Hollow Spheres for Electrochemical Energy Storage, Appl. Surf. Sci. 435 (2018) 993-1001.

[19] J. Yang, Y. Zhang, C. C. Sun, G. L. Guo, W. P. Sun, W. Huang, Q. Y. Yan, X. C. Dong, Controlled Synthesis of Zinc Cobalt Sulfide Nanostructures in Oil Phase and Their Potential Applications in Electrochemical Energy Storage, J. Mater. Chem. A 3 (2015) 11462-11470.

[20] Y. M. Lv, A. F. Liu, Z. X. Shi, H. W. Che, J. B. Mu, Z. C. Guo, X. L. Zhang, Construction of Hierarchical Zinc Cobalt Sulfide@Nickel Sulfide Core-shell Nanosheet Arrays for High-performance Asymmetric Solid-state Supercapacitors, Chem. Eng. J. 349 (2018) 397-407.

[21] C. Cheng, X. Zhang, C. Wei, Y. Liu, C. Cui, Q. Zhang, D. Zhang, Mesoporous Hollow $ZnCo_2S_4$ Core-shell Nanospheres for High Performance Supercapacitors, Ceram. Int. 44 (2018) 17464-17472.

[22] X. Li, J. Bai, B. Zhou, X. Yuan, X. Zhang, L. Liu, High Performance of 3D Symmetric Flowerlike Sb_2S_3 Nanostructures in Dye-Sensitized Solar Cells, Chem. 24 (2018) 11444-11450.

[23] J. Yan, J. P. Liu, Z. J. Fan, T. Wei, L. J. Zhang, High-performance Supercapacitor Electrodes Based on Highly Corrugated Graphene Sheets, Carbon 50 (2012) 2179-2188.

[24] Q. Wang, J. Yan, Y. Xiao, T. Wei, Z. J. Fan, M. L. Zhang, X. Y. Jing, Interconnected Porous and Nitrogen-doped Carbon Network for Supercapacitors with High Rate Capability and Energy Density, Electrochim. Acta 114 (2013) 165-172.

[25] M. R. Lukatskaya, B. Dunn, Y. Gogotsi, Multidimensional Materials and Device Architectures for Future Hybrid Energy Storage, Nat. Commun. 7 (2016) 12647

[26] X. Tian, C. Cheng, L. Qian, B. Zheng, H. Yuan, S. Xie, D. Xiao, M. Choi, Microwave-assisted Non-aqueous Homogenous Precipitation of Nanoball-like Mesoporous α-$Ni(OH)_2$ as a Precursor for NiO_x and its Application as a Pseudocapacitor, J. Mater. Chem. 22 (2012) 8029-8035.

[27] X. B. Wang, J. Hao, Y. C. Su, F. G. Liu, J. An, J. S. Lian, a $Ni_{1-x}Zn_xS$/Ni Foam Composite Electrode with Multi-layers: One-step Synthesis and High Supercapacitor Performance, J. Mater. Chem. A 4 (2016) 12929-12939.

[28] J. Wang, S. Wang, Z. Huang, Y. Yu, High-performance $NiCo_2O_4$@Ni_3S_2 Core/shell Mesoporous Nanothorn Arrays on Ni Foam for Supercapacitors, J. Mater. Chem. A 2 (2014) 17595-17601.

[29] R. Ramachandran, M. Saranya, P. Kollu, B. P. C. Raghupathy, S. K. Jeong, A. N. Grace, Solvothermal Synthesis of Zinc Sulfide Decorated Graphene (ZnS/G) Nanocomposites for Novel Supercapacitor Electrodes, Electrochim. Acta 178 (2015) 647-657.

[30] A. Namdarian, A. Tabrizi, A. Maseleno, A. Mohammadi, S. Moosavifard, One Step Synthesis of rGO-Ni_3S_2 Nano-cubes Composite for High-performance Supercapacitor Electrodes, Int. J. Hydrogen Energy 43 (2018) 17780-17787.

[31] C. S. Dai, P. Y. Chien, J. Y. Lin, S. W. Chou, W. K. Wu, P. H. Li, K. Y. Wu, T. W. Lin, Hierarchically Structured Ni_3S_2/Carbon Nanotube Composites as High Performance Cathode Materials for Asymmetric Supercapacitors, ACS Appl. Mater. Interfaces 5 (2013) 12168-12174.

[32] G. Li, M. Liu, M. Wu, P. Liu, Z. Zhou, S. Zhu, R. Liu, L. Han, MOF-derived Self-sacrificing Route to Hollow NiS_2/ ZnS Nanospheres for High Performance Supercapacitors, RSC Adv. 6 (2016) 103517–103522.

[33] Z. Dai, X. Zang, J. Yang, C. Sun, W. Si, W. Huang, X. Dong, Template Synthesis of Shape-Tailorable NiS_2 Hollow Prisms as High-Performance Supercapacitor Materials, ACS Appl. Mater. Interfaces 7 (2015) 25396-25401.

[34] X. Mao, W. Wang, Z. Wang, Hydrothermal Synthesis of $Zn_xNi_{1-x}S$ Nanosheets for Hybrid Supercapacitor Applications, ChemPlusChem 82 (2017) 1145-1152.

[35] H. Z. Wan, X. Ji, J. J. Jiang, J. W. Yu, L. Miao, L. Zhang, S. W. Bie, H. C. Chen, Y. J. Ruan, Hydrothermal Synthesis of Cobalt Sulfide Nanotubes: The Size Control and its Application in Supercapacitors, J. Power Sources 243 (2013) 396-402.

[36] J. He, Y. Chen, P. Li, F. Fu, Z. Wang, W. Zhang, Self-assembled CoS_2 Nanoparticles Wrapped by CoS_2-quantum-dots-anchored Graphene Nanosheets as Superior-capability Anode for Lithium-ion Batteries, Electrochim. Acta 182 (2015) 424-429.

[37] A. Ivanishchev, I. Bobrikov, I. Ivanishcheva, O. Ivanshina, Study of Structural and Electrochemical Characteristics of $LiNi_{0.33}Mn_{0.33}Co_{0.33}O_2$ Electrode at Lithium Content Variation, J. Electroanal. Chem. 821 (2018) 140-151.

[38] A. Ivanishchev, A. Churikov, I. Ivanishcheva, A. Ushakov, M. Sneha, P. Babbar, A. Dixit, Models of Lithium Transport as Applied to Determination of Diffusion Characteristics of Intercalation Electrodes, Russ. J. Electrochem. 53 (2017) 706-712.

[39] K. Tao, X. Han, Q. Cheng, Y. Yang, Z. Yang, Q. Ma, L. Han, Zinc Cobalt Sulfide Nanosheets Array Derived from 2D Bimetallic Metal-Organic Frameworks for High-performance Supercapacitor, Chem. Eur. J. 24 (2018) 12584-12591.

[40] S. Min, C. Zhao, G. Chen, X. Qian, One-pot Hydrothermal Synthesis of Reduced Graphene Oxide/$Ni(OH)_2$ Films on Nickel Foam for High Performance Supercapacitors, Electrochim. Acta 115 (2014) 155-164.

[41] Y. Zhu, Z. Wu, M. Jing, X. Yang, W. Song, X. Ji, Mesoporous $NiCo_2S_4$ Nanoparticles as High-performance Electrode Materials for Supercapacitors, J. Power Sources 273 (2015) 584-590.

[42] F. Luo, J. Li, H. Yuan, D. Xiao, Rapid Synthesis of Three-dimensional Flower-like Cobalt Sulfide Hierarchitectures by Microwave Assisted Heating Method for High-performance Supercapacitors, Electrochim. Acta 123 (2014) 183-189.

[43] W. H. Jin, G. T. Cao, J. Y. Sun, Hybrid Supercapacitor based on MnO_2 and Columned FeOOH using Li_2SO_4 Electrolyte Solution, J. Power Sources 175 (2008) 686-691.

[44] S. K. Balasingam, J. S. Lee, Y. Jun, Few-Layered $MoSe_2$ Nanosheets as an Advanced Electrode Material for Supercapacitors, Dalton Trans. 44 (2015) 15491–15498

[45] J. H. Shi, X. C. Li, G. H. He, L. Zhang, M. Li, Electrodeposition of High-capacitance 3D CoS/Graphene Nanosheets on Nickel Foam for High-Performance Aqueous Asymmetric Supercapacitors, J. Mater. Chem. A 3 (2015) 20619-20626.

[46] Y. Zhang, N. Cao, S. Szunerits, A. Addad, P. Roussel, R. Boukherroub, Fabrication of ZnCoS Nanomaterial for High Energy Flexible Asymmetric Supercapacitors, Chem. Eng. J. 374 (2019) 347-358.

[47] T. Masikhwa, M. Madito, A. Bello, J. Dangbegnon, N. Manyala, High Performance Asymmetric Supercapacitor Based on Molybdenum Disulphide/Graphene Foam and Activated Carbon from Expanded Graphite, J. Colloid Interface Sci. 488 (2017) 155-165.

[48] X. Q. Mao, W. Z. Wang, Z. H. Wang, Hydrothermal Synthesis of $Zn_xNi_{1-x}S$ Nanosheets for Hybrid Supercapacitor Applications, ChemPlusChem 2017 (2017) 8.

CHAPTER 5. PREPARATION OF PVP-ASSISTED $Sb_2S_3/CoS_2/CrOOH$ COMPOSITE WITH ENHANCED ELECTROCHEMICAL PERFORMANCE FOR HYBRID SUPERCAPACITORS

5.1 Introduction

Based on our previous results, bimetal sulfides electrode materials proved to exhibit an enhanced electrochemical performance than mono metal sulfides. In addition, transition metal oxy-hydroxides have also been regarded as one of the most promising electrode materials. Although several valuable studies related to the transition-metal composites (oxides, sulfides or hydroxides) have been reported, little work was focused on employing the composites of transition-metal sulfides and oxides as electrode materials. Therefore, it is expected that the composites of metal sulfides and oxy-hydroxides could offer a much better electrochemical performance.

Recently, there is great interest in using cobalt chalcogenides, antimony trisulfide, or chrome oxide positive electrodes in electrochemical energy storage and conversion devices (supercapacitors, lithium-ion (LIBs) batteries, and sodium-ion batteries), because of their advantages such as high electrical conductivity, high theoretical specific capacity, chemical stability and so on [1-8]. Moreover, Co-, Cr-, or Sb-based composites have been investigated as battery anodes, supercapacitor electrodes, and electrocatalysts [9-16]. Based on these considerations, SbCoS/CrOOH advanced positive electrode material for supercapacitors was prepared *via* a cost-effective co-precipitation process and anion-exchange.

5.2 Preparation of Sb: Cr: Co composites

The synthesis procedure includes the following chemical co-precipitation and ion-exchange processes (**Fig.5.1**).

Chemical co-precipitation process: 0.156 mmol of $SbCl_3$, 0.469 mmol of $Cr(NO_3)_3\ 9H_2O$ and 0.625 mmol of $Co(NO_3)_2\ 6H_2O$ are dissolved in 10 mL ethylene glycol (EG) under strong magnetic stirring. After that, 10 mL of 1 wt% ammonia solution is dropped into the above solution under magnetic stirring for 30 min. The obtained precipitate is rinsed with Milli-Q water until the pH is ~7 and re-dispersed in 42.5 mL aqueous solution containing 400 mg PVP.

Then, 7.5 mL of 1 wt% ammonia solution is added into the above solution and kept at 50 ℃ for 15 h to yield a precipitate. The precipitate is rinsed sequentially with ethanol and Milli-Q water until the pH is ~7. The obtained product is re-dispersed in Milli-Q water (42 mL) using a horn-type sonotrode (Branson, Ultrasonic-Homogenizer Sonifier II W-450 with a 4.8 mm microtip) for 3 min for further use.

Ion-exchange process: 150 mg thioacetamide (TAA) is dissolved in the solution above and heated at 200 ℃ for 10 h to yield a precipitate. The resulting precipitate is separated through centrifugation, rinsed with ethanol and Milli-Q water, and dried in an oven at 60 ℃ overnight. The sample is referred to as Sb: Cr: Co (1:3:4).

After a similar co-precipitation and ion-exchange process. Samples are obtained and labeled based on the initial mole ratio of the Sb, Cr and Co precursors. For example, the sample Sb: Cr: Co (1:3:4) means that the initial mole ratio of the Sb, Cr and Co precursors is 1:3:4. Similarly, other electrode materials viz. Sb: Cr: Co (1:0:0), Sb: Cr: Co (0:1:0) and Sb: Cr: Co (0:0:1) are synthesized by a similar method. The total amount of all precursors is fixed at 1.25 mmol.

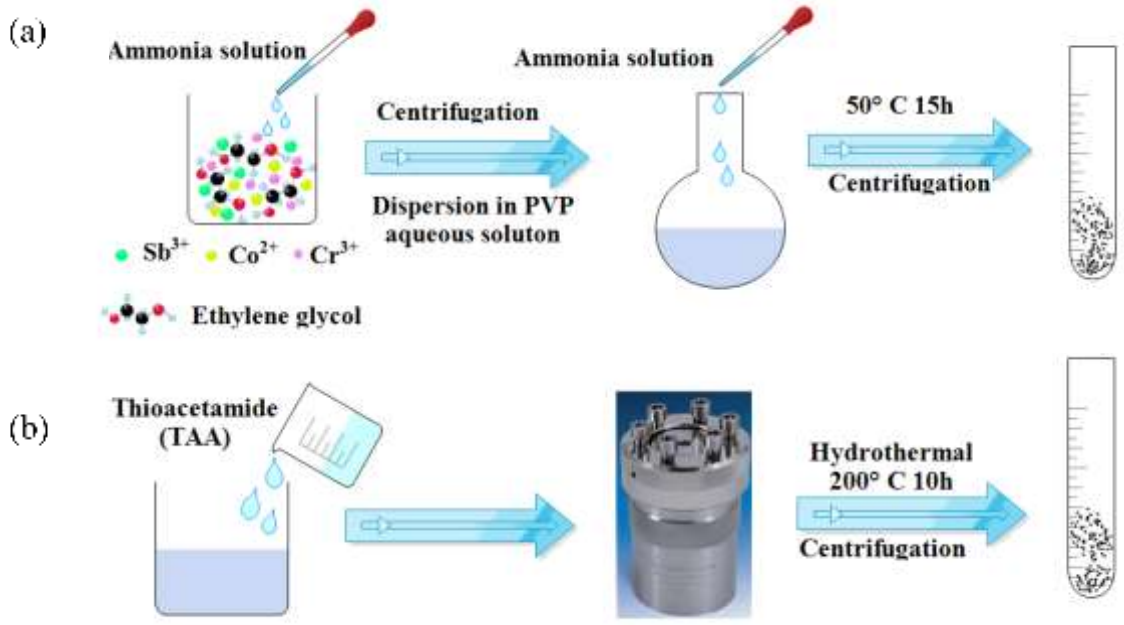

Figure 5.1: Illustration of the synthesis route of the Sb: Cr: Co (1:3:4) electrode by chemical co-precipitation (a) and ion-exchange (b) processes.

5.3 Characterization of Sb: Cr: Co samples

5.3.1 Structure characterization

XRD patterns of as-synthesized Sb: Cr: Co samples, labeled as Sb: Cr: Co (1:0:0), Sb: Cr: Co (0:1:0), Sb: Cr: Co (0:0:1), and Sb: Cr: Co (1:3:4) are presented in **Fig. 5.2**. For Sb: Cr: Co (1:0:0) sample (**Fig. 5.2a**), well-defined diffraction peaks could be well indexed to the diffraction patterns of orthorhombic phase of Sb_2S_3 (JCPDS card No. 42-1393) [4, 7, 17]. The crystal lattice constants are determined using the following equations:

$$2d_{HKL}\sin\theta = n\lambda \quad 5\text{-}1$$

$$d_{HKL} = \frac{1}{\sqrt{\left(\frac{H}{a}\right)^2+\left(\frac{K}{b}\right)^2+\left(\frac{L}{c}\right)^2}} \quad 5\text{-}2$$

Where θ is the scattering angle, (H K L) and d_{HKL} are the corresponding Miller indices, and interplanar distance, respectively, n is a positive integer and λ=1.54056 Å, a, b, c are crystal lattice constants.

The crystal lattice constant, calculated according to the diffraction peaks, are a=11.295Å, b=11.398Å and c= 3.856Å, which are well in agreement with the reported values [6, 17]. Moreover, the sharp and narrow diffraction peaks indicate high crystallinity of the prepared Sb: Cr: Co (1:0:0) samples.

For Sb: Cr: Co (0:1:0) (**Fig. 5.2b**), diffraction peaks at about ~19.3 °, 37.4 °, and 48.1 ° and 62.5 °are well indexed to (003), (012), and (015), and (009) of hexagonal CrO(OH), which has the mineral name Grimaldiite-3R (JCPD card No. 09-0331) [18]. Based on equations **5-1** and **5-3**, the parameters of the hexagonal unit cell of Grimaldiite-3R are: a=b=2.957 Å, c=13.710 Å, which are well in accordance with those of the JCPD card No. 09-0331.

$$d_{HKL} = \frac{1}{\sqrt{\frac{4}{3}\left(\frac{H^2+HK+K^2}{a^2}\right)+\left(\frac{L}{c}\right)^2}} \quad 5\text{-}3$$

The broad and weak diffraction peaks suggest that the resultant material is amorphous. In addition, other diffraction peaks in **Fig. 5.2b** also indicate the formation of sulfur impurities in the sample. Therefore, we can hypothesize that the addition of TAA to the precursor of Sb: Cr: Co (0:1:0), even at 200 ℃, results in the formation of amorphous CrO(OH) and sulfur impurities instead of Cr_2S_3.

For Sb: Cr: Co (0:0:1) sample (**Fig. 5.2c**), diffraction peaks at ~ 27.8 °, 32.3 °, 36.2 °, 39.8 °, 46.4 °, 55.0 °, 57.8 °, 60.2 °, 62.7 °(labelled as*) are well indexed respectively to the (111), (200),

(210), (211), (220), (311), (222), (230), and (321) diffractions planes of cubic CoS_2 (JCPDS card No. 41-1471)[19, 20]. Based on equations **5-1** and **5-4**:

$$d_{HKL} = \frac{a}{\sqrt{(H)^2+(K)^2+(L)^2}} \qquad 5\text{-}4$$

The parameters of the cubic CoS_2 are: a=b=c= 5.538 Å, which match well with those of the JCPDS card No. 41-1471. In addition, other diffraction peaks in **Fig. 5.2c** indicate the formation of $CoSO_4$ impurities in the sample.

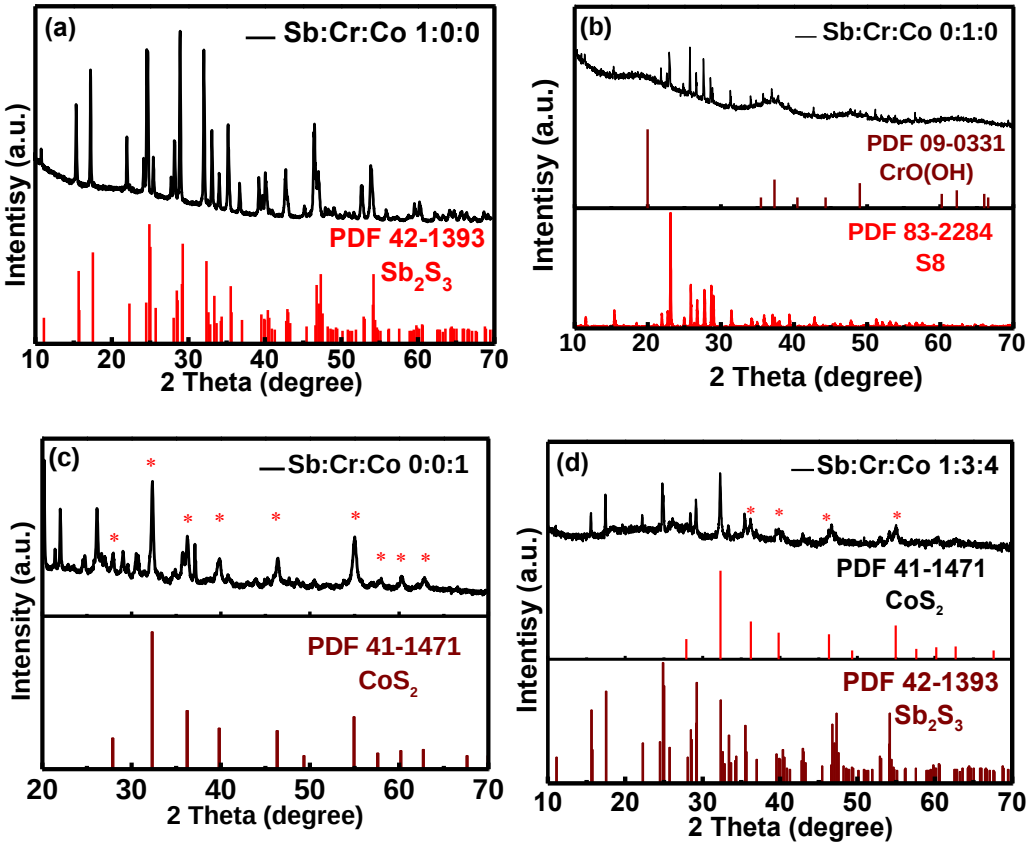

Figure 5.2: XRD patterns of the prepared Sb: Cr: Co samples.

For Sb: Cr: Co (1:3:4) sample (**Fig. 5.2d**), most of the detected diffraction peaks match well with the orthorhombic phase of Sb_2S_3 (JCPDS card No. 42-1393). The peaks centered at ~36.2 °, 46.3 °, and 55.0 °(labelled as*) correspond to the (210), (220) and (311) planes of CoS_2 (JCPD card No. 41-1471). All diffraction peaks confirm the formation of Sb_2S_3 and CoS_2 in Sb: Cr: Co (1:3:4) sample. However, no obvious peaks due to Cr(ш) compounds could be detected in **Fig. 5.2d**. Based on the XRD pattern of Sb: Cr: Co (0:1:0) sample (**Fig. 5.2b**), it could be hypothesized that amorphous CrO(OH) is also formed.

X-ray photoelectron spectroscopy (XPS) is further used to investigate the chemical composition and oxidation states of surface elements of the synthesized Sb: Cr: Co (1:3:4) sample. The XPS full spectrum of Sb: Cr: Co (1:3:4) is depicted in **Fig. 5.3a**. Peaks attributed to Sb, Cr, Co and O, and S could be observed, while C and N peaks due to the stabilizer PVP are also detected.

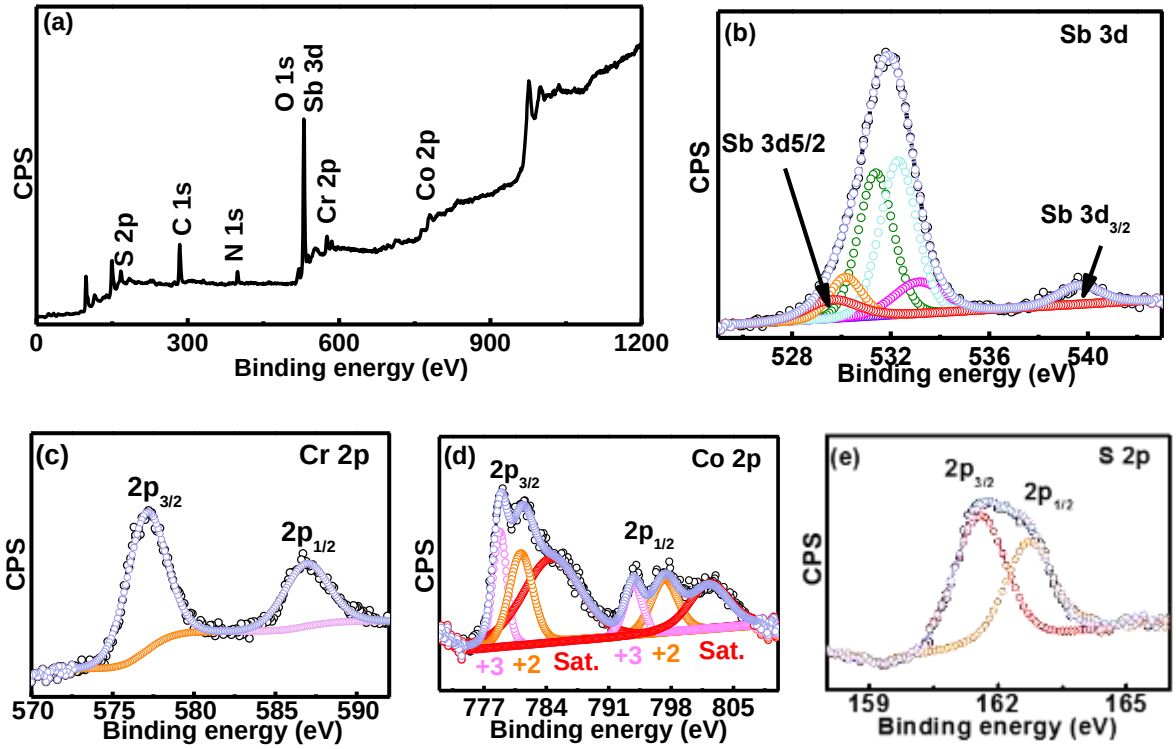

Figure 5.3: XPS analysis of Sb: Cr: Co (1:3:4): (a) survey spectrum, (b), (c) (d) and (e) are the high-resolution spectra of Sb_{3d} (O_{1s}), Cr_{2p} and Co_{2p} and S_{2p}, respectively. "Sat" in Fig. d denotes satellite peaks.

In **Fig. 5.3b**, the XPS high resolution spectrum of Sb_{3d} and O_{1s} are dissociated because the $Sb_{3d5/2}$ peak overlap with O_{1s}. Here, two typical peaks ascribed to $Sb_{3d5/2}$ (~529.7 eV) and $Sb_{3d3/2}$ (~539.7 eV) suggest the existence of Sb^{3+} oxidation state in Sb_2S_3. The results are similar to the reported values of Sb_2S_3 in the literature [4, 5, 11]. Besides, four peaks at ~530.2, 531.4 and 532.3 and 533.2 eV are assigned to O_{1s}, and attributed to O^{2-} in CrO(OH), OH^- in oxyhydroxide or hydroxide, physisorbed moisture and organic C=O in PVP, respectively [18, 21].

In the high resolution XPS spectrum of Cr_{2p} (**Fig. 5.3c**), two prominent peaks at ~577.2 and 587.1 eV due to $Cr_{2p3/2}$ and $Cr_{2p1/2}$, respectively are observed, which are associated with the Cr^{3+} trivalent hydroxide state, in accordance with the reported Cr^{3+} in CrO(OH) [21, 22]. The Co_{2p} core level spectrum (**Fig. 5.3d**) could be well fitted with two spin-orbit doublets together with

two shake-up satellites (identified as Sat.). The peaks located at ~777.9 and 793.8 eV are assigned to Co^{3+}, and the peaks at ~781.2 and 797.3 eV are attributed to Co^{2+} [23-25]. Furthermore, the binding energy difference between $Co_{2p3/2}$ and $Co_{2p1/2}$ is larger than 15 eV, indicating the co-existence of Co^{3+} and Co^{2+} in Sb: Cr: Co (1:3:4). The XPS high resolution spectrum of S_{2p} is fitted with two peaks at ~161.5 and 162.7 eV, attributed to $S_{2p3/2}$ and $S_{2p1/2}$, respectively (**Fig.5.3e**) [15], which are typical of metal-sulfur bonds in the Sb: Cr: Co (1:3:4) sample. According to the results of XRD and XPS, after extensive literature review, it could be hypothesized that the addition of TAA to the precursors of Sb: Cr: Co (1:3:4), after annealing at 200℃ for 10 h, a mixture of Sb_2S_3, CoS_2 and amorphous CrO(OH) phases are formed.

The morphology of Sb: Cr: Co materials synthesized under varying material compositions was investigated by SEM, and the images are presented in **Fig. 5.4**. They reveal that the morphology is significantly affected by varying the material composition. **Fig. 5.4a** and **b** show the images of as-prepared Sb: Cr: Co (1:0:0) sample, displaying an agglomerated morphology composed of belt-like and granular structures. In contrast to the belt-like structure, the granular structure is believed to be caused by the re-dispersion process. As presented in **Fig. 5.4b**, the obtained Sb: Cr: Co (1:0:0) sample has a very smooth surface. The SEM images of Sb: Cr: Co (0:1:0) and Sb: Cr: Co (0:0:1) are displayed in **Fig. 5.4c-f**. They show the samples in agglomerated form composed of many nano-sized particles. **Fig. 5.4g** and **h** depicts the SEM images of Sb: Cr: Co (1:3:4). In contrast to the agglomerate belt-like structure of sample Sb: Cr: Co (1:0:0) or the agglomerated nano-sized particles of sample Sb: Cr: Co (0:1:0) and Sb: Cr: Co (0:0:1), particles with different sizes could be observed (**Fig. 5.4g**). In addition, numerous granular structures seen on the surface of Sb: Cr: Co (1:3:4) particles results in a rougher surface, as compared with that of Sb: Cr: Co (1:0:0). This granular structure on the surface of Sb: Cr: Co (1:3:4) sample is believed to be caused by the introduction of Co and Cr. Moreover, the rougher surface is also expected to provide more electroactive sites between the active material and the electrolyte.

To confirm the element distribution of prepared Sb: Cr: Co (1:3:4), EDX mapping results evidently identified that Sb, Co, S, Cr, O elements are uniformly distributed throughout the particles, in addition element C caused by stabilizer PVP could also be evidenced (**Fig. 5.4i**).

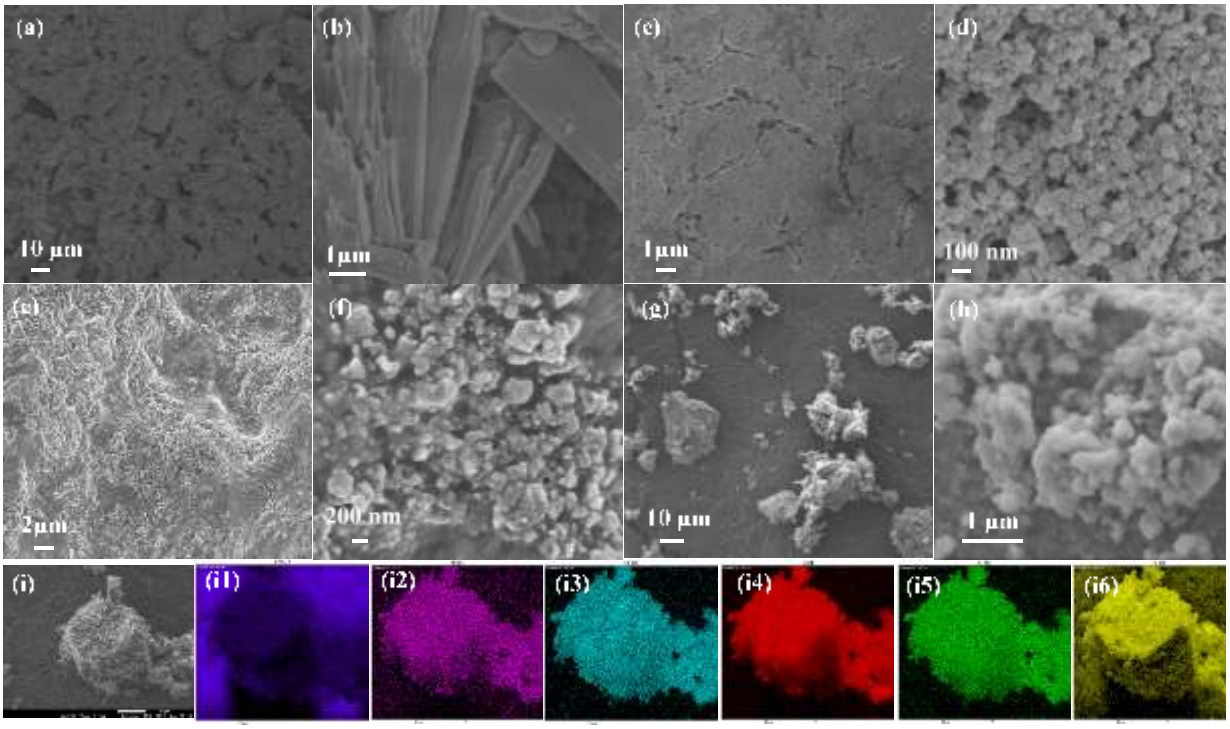

Figure 5.4: SEM images of Sb_2S_3 (a, b), CrOOH (c, d), CoS_2 (e, f) and $Sb_2S_3/CoS_2/CrOOH$ (g, h), and element mappings of C, Sb, Co, S, Cr, O elements recorded from $Sb_2S_3/CoS_2/CrOOH$ (i).

5.3.2 Electrochemical properties of Sb: Cr: Co electrodes

CV and GCD curves of Sb: Cr: Co electrodes are displayed in **Fig. 5.5 a-h**. Obvious redox peaks and potential plateaus are detected in CV and GCD curves of Sb: Cr: Co (1:0:0), (0:1:0) electrodes (**Fig. 5.5 a**, **b**, **e** and **f**), indicating the existence of battery-type behavior. The redox peaks and the humps observed in the CV and GCD curves of Sb: Cr: Co (0:0:1) electrode indicate the existence of faradaic reactions (**Fig. 5.5 c** and **g**). Redox peaks and potential plateaus observed in CV and GCD curves of Sb: Cr: Co (1:3:4) (**Fig. 5.5 d** and **h**) electrode are assigned to the existence of battery-type capacity. Furthermore, the current density response of all electrodes increases when the scan rate is varied from 5 to 100 mV/s, and the shape of CV curves is well-maintained, indicating good rate capability of all Sb: Cr: Co electrodes.

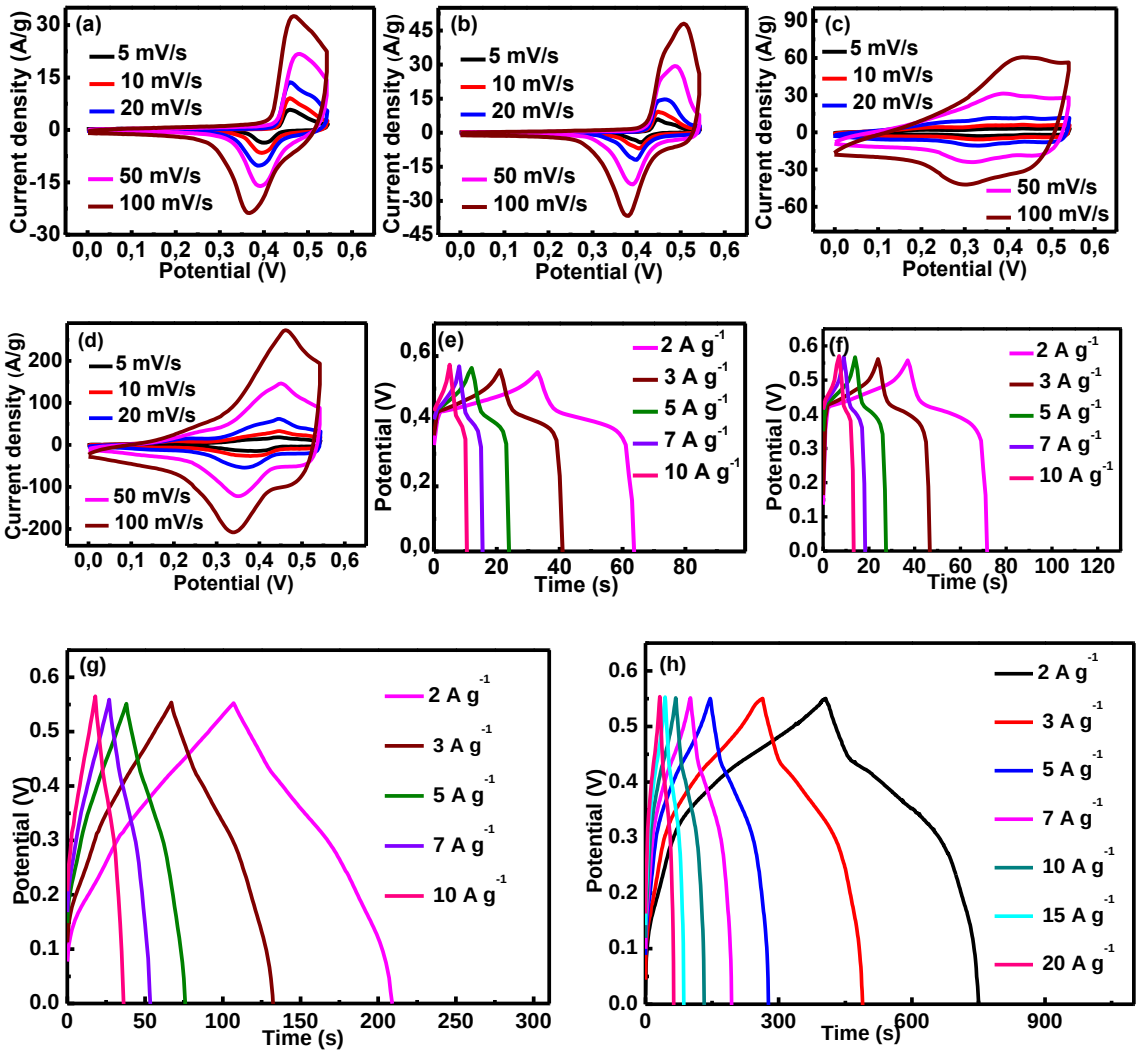

Figure 5.5: Electrochemical properties of Sb: Cr: Co electrode materials in 2 M KOH in the operating potential window (0 - 0.55 V): (a-d) CV curves of Sb: Cr: Co (1:0:0), (0:1:0), (0:0:1), (1:3:4) electrodes recorded at various scan rates (5 -100 mV/s); (e-h) GCD curves of Sb: Cr: Co (1:0:0), (0:1:0), (0:0:1), (1:3:4) electrodes acquired at different current densities (2-20 A g^{-1});

Fig. 5.6 a-f compares CV and GCD curves, specific capacity and Nyquist plots of all Sb: Cr: Co electrodes. Three pairs of redox peaks at about 0.21/0.17 (a/a'), 0.45/0.38 (b/b') and 0.51/0.49 (c/c') V could be observed in the CV curves of Sb: Cr: Co (1:3:4) electrode (**Fig. 5-6a**). As the redox potentials of Sb-S-OH and Cr^{3+}/Cr^{4+} in CV curves of Sb: Cr: Co (1:0:0) and Sb: Cr: Co (0:1:0) electrodes are close to each other, the redox peaks (b/b') in the CV curves of Sb: Cr: Co (1:3:4) are believed to be caused by the reversible faradaic redox reaction of Sb-S-OH and Cr^{3+}/Cr^{4+} together. Redox peaks (a/a', c/c') observed in the CV curve of Sb: Cr: Co (1:3:4) sample agree well with those in the CV curve of Sb: Cr: Co (0:0:1) electrode. Therefore,

they are supposed to be due to the oxidation of CoS_2 to CoS_2OH and CoS_2OH to CoS_2O. The possible reversible redox reactions are presented in **Table 5-1** [2, 26-30].

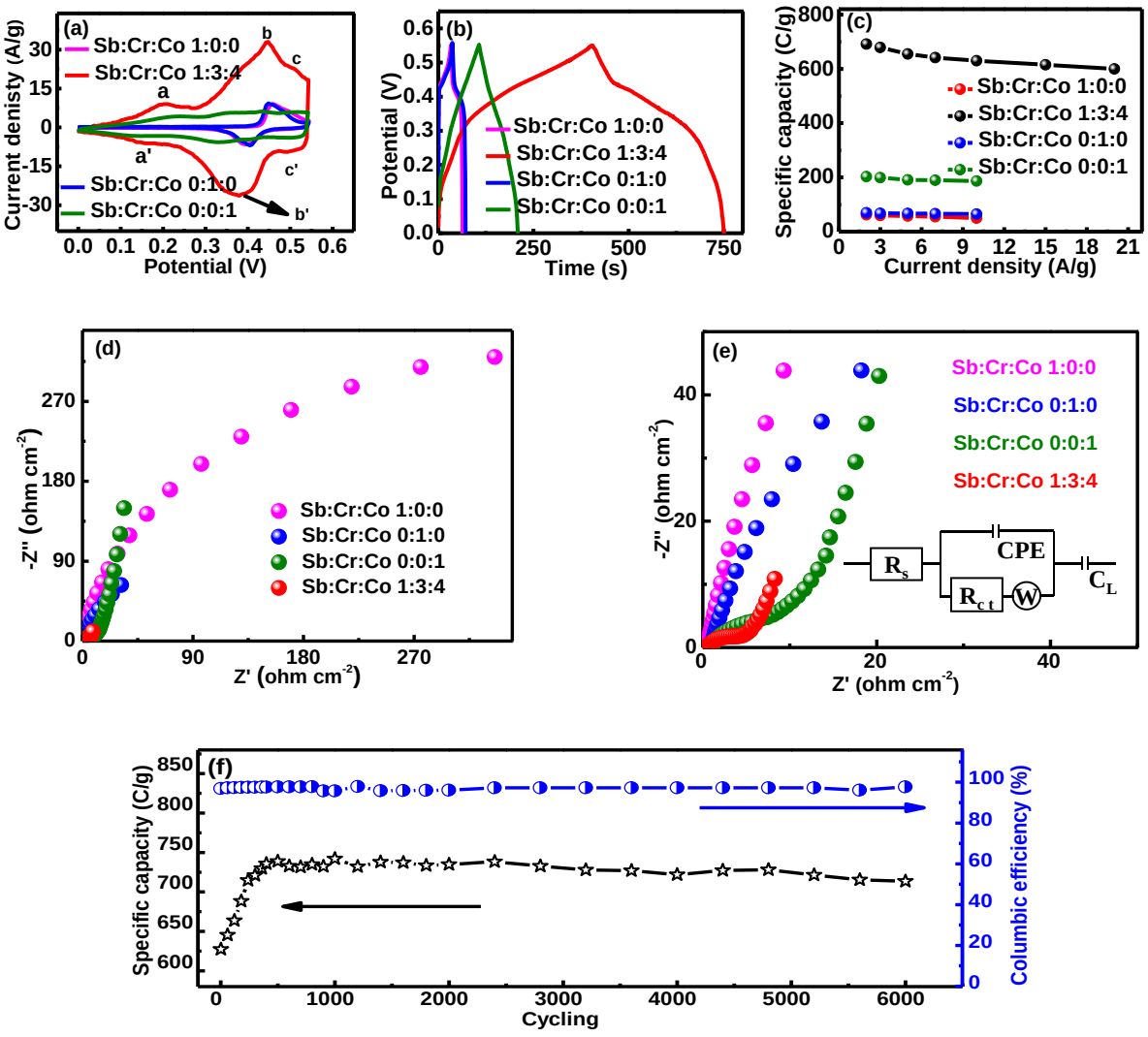

Figure 5.6: (a) CV curves of all electrodes recorded at a scan rate of 10 mV/s; (b) GCD curves recorded of all electrodes at a current density of 2 A g^{-1}; (c) Specific capacity of all electrodes acquired at current densities of 2-20 A g^{-1}; (d, e) Nyquist plots of all Sb: Cr: Co electrodes; (f) cycling performance and columbic efficiency of Sb: Cr: Co (1:3:4) at 20 A g^{-1} for 6,000 cycles, the inset in (e) is the corresponding equivalent circuit.

Table 5-1: Proposed redox reactions of Sb: Cr: Co samples in 2M KOH aqueous electrolyte.

Material	Redox reaction
Sb: Cr: Co (1:0:0)	$Sb_2S_3 + OH^- \leftrightarrow Sb_2S_3OH + e^-$
Sb: Cr: Co (1:3:4)	$Sb_2S_3 + OH^- \leftrightarrow Sb_2S_3OH + e^-$ $CrO(OH) + OH^- \leftrightarrow CrO(OH)_2 + e^-$ $CoS_2 + OH^- \leftrightarrow CoS_2OH + e^-$ $CoS_2OH + OH^- \leftrightarrow CoS_2O + H_2O + e^-$
Sb: Cr: Co (0:1:0)	$CrO(OH) + OH^- \leftrightarrow CrO(OH)_2 + e^-$
Sb: Cr: Co (0:0:1)	$CoS_2 + OH^- \leftrightarrow CoS_2OH + e^-$
	$CoS_2OH + OH^- \leftrightarrow CoS_2O + H_2O + e^-$

Fig. 5.6b compares GCD curves of all Sb: Cr: Co electrodes at a current density of 2 A g^{-1}. The almost symmetric charge/discharge curves demonstrate a good coulombic efficiency of the synthesized composites, owing to the high reversibility of redox reactions during the charge and discharge processes. Furthermore, it is obvious that Sb: Cr: Co (1:3:4) electrode exhibits a much larger maximum current response (current density) and longer time for charge-discharge process. According to the equation **1-4**, the specific capacity of one particular electrode is proportional to the discharge time if the current response is recorded under the same condition. Hence, we can conclude that Sb: Cr: Co (1:3:4) sample could offer a much higher specific capacity compared to Sb: Cr: Co (1:0:0), Sb: Cr: Co (0:1:0) and Sb: Cr: Co (0:0:1) electrodes.

The specific capacity, calculated from discharge curves, is given in **Fig. 5.6c**. The Sb: Cr: Co (1:3:4) sample exhibits the highest value up to ~691 C g^{-1} at 2 A g^{-1}, which is much higher than that of Sb: Cr: Co (1:0:0) (~61 C g^{-1}), Sb: Cr: Co (0:1:0) (~69 C g^{-1}), and Sb: Cr: Co (0:0:1) (~203 C g^{-1}). This could be ascribed to the rough surface of the composite along with synergistic effects of Sb, Cr and Co. Moreover, the specific capacity of Sb: Cr: Co (1:3:4) is slightly lower than or comparable to those previously reported metal sulfides (**Table 5-2**).

Table 5-2: Comparison of specific capacity of metal sulfides electrode materials towards supercapacitor applications			
Electrode materials	Specific capacity (C/g)	Capacitance retention (%)	Ref
Carbon coated CoS_2@Thin carbon layer (CoS_2-C@TCL)	482 (2 A g^{-1})	88 (2k cycles at 5 A g^{-1})	[19]
$Co_3S_4/CoMo_2S_4$ (CMS)-rGO	656 (1 A g^{-1})	97 (2k cycles at 10 A g^{-1})	[27]
Double-shelled hollow hetero-$MnCo_2S_4/CoS_{1.097}$ spheres with carbon coating (SHMCS)	413 (2 A g^{-1})	91.3 (5k cycles at 10 A g^{-1})	[13]
ZnCoS	624 (1 A g^{-1})	No obvious decrease (6k cycles at 20 A g^{-1})	[31]
CdS/Nickel Foam (NF)	397 (2.8 A g^{-1})	104 (5k cycles at 14.2 A g^{-1})	[32]
Pinecone-like and hierarchical manganese cobalt sulfide (PHMCS)	397 (1 A g^{-1})	102.35 (5.5k cycles at 10 A g^{-1})	[33]
Onion-like $NiCo_2S_4$ particles	508 (2 A g^{-1})	87 (10k cycles at 10 A g^{-1})	[34]
CoS	293 (1 A g^{-1})	91 (1k cycles at 3 A g^{-1})	[1]
Sb: Cr: Co (1:3:4)	691 (2 A g^{-1})	**96.6 (6k cycles at 20 A g^{-1})**	**Our work**

EIS was further performed for assessing the electrochemical processes at the electrode/electrolyte interface. **Fig. 5.6d** and **e** displays the Nyquist plots of Sb: Cr: Co electrodes; the corresponding equivalent circuit is shown in the inset. The R_s and R_{ct} values, calculated according to the equivalent circuit, are summarized in **Table 5-3**. Here, the simulated results reveal that the Sb: Cr: Co (1:3:4) electrode displays lower serial resistance and charge transfer resistance than the other samples.

Table 5-3: Values of R_s and R_{ct} for all Sb: Cr: Co electrodes.		
Electrode	R_s (ohm·cm^{-2})	R_{ct} (ohm·cm^{-2})
Sb: Cr: Co (1: 0: 0)	0.88	615.90
Sb: Cr: Co (1: 3: 4)	0.50	4.58
Sb: Cr: Co (0: 1: 0)	0.89	97.50
Sb: Cr: Co (0: 0: 1)	0.84	13.44

Furthermore, the stability and coulombic efficiency of the Sb: Cr: Co (1:3:4) electrode at 20 A g^{-1} for 6,000 cycles are investigated (**Fig. 5.6f**). It should be noticed that in the first 500

cycles, the specific capacity value increases from ~ 627 C g^{-1} to 738 C g^{-1}, most likely due to the complete activation of the electrode material [35-37]. After 6,000 cycles, the electrode achieves a specific capacity of ~ 713 C g^{-1} (~96.6 % of the maximum specific capacity), indicating a good cycling stability. Moreover, the coulombic efficiency (ŋ) of the Sb: Cr: Co (1:3:4) electrode also called charge-discharge efficiency, estimated according to equation **1-9**, remains ~97.7%, indicating a good electrochemical reversibility.

5.3.3 Fundamental electrochemical analysis of electrode Sb: Cr: Co (1:3:4)

The enhanced electrochemical performance of Sb: Cr: Co (1:3:4) electrode could be detected through fundamental electrochemical tests. With respect to investigating the origin of the outstanding performance of Sb: Cr: Co (1:3:4), the electrochemical reaction kinetics are analyzed through the quantification of capacitive and diffusion-controlled charge storage processes.

The total charge originating from the capacitive and diffusion-controlled processes is represented through the area under CV curves, and the contribution ratio of capacitive and diffusion-controlled charge storage processes can be quantified by analyzing the CV curves at different scan rates using the following equations [38, 39]:

$$i = av^b \quad (5\text{-}5)$$

$$log\ i = \mathrm{b}\log \mathrm{v} + \log\ a \quad (5\text{-}6)$$

Here, i and v are the peak current response (peak current density) and scan rate, respectively; a and b are undetermined parameters. The b value could be determined from the slope of *log i vs. log v* at any potential value. Commonly, if the value of b approaches 0.5, the capacity contribution is assigned to the diffusion-controlled process, while if this value approaches 1, the capacity is dominated by capacitive contribution from the surface-controlled process. Therefore, it will be easy to distinguish the diffusion-controlled or capacitive charge storage process based on the value of b.

The fitted curves of *log i vs. log v* for the Sb: Cr: Co (1:3:4) electrode in the range of 5-100 mV/s is given in **Fig. 5.7a**. After linear fitting, both anodic and cathodic peaks exhibit a good linear relationship, and values of b are ~ 0.908 and 0.910 for the cathodic and anodic peaks, respectively. Both values of b are closer to 1, signifying that the capacitive contribution from surface-controlled process is dominant in Sb: Cr: Co (1:3:4).

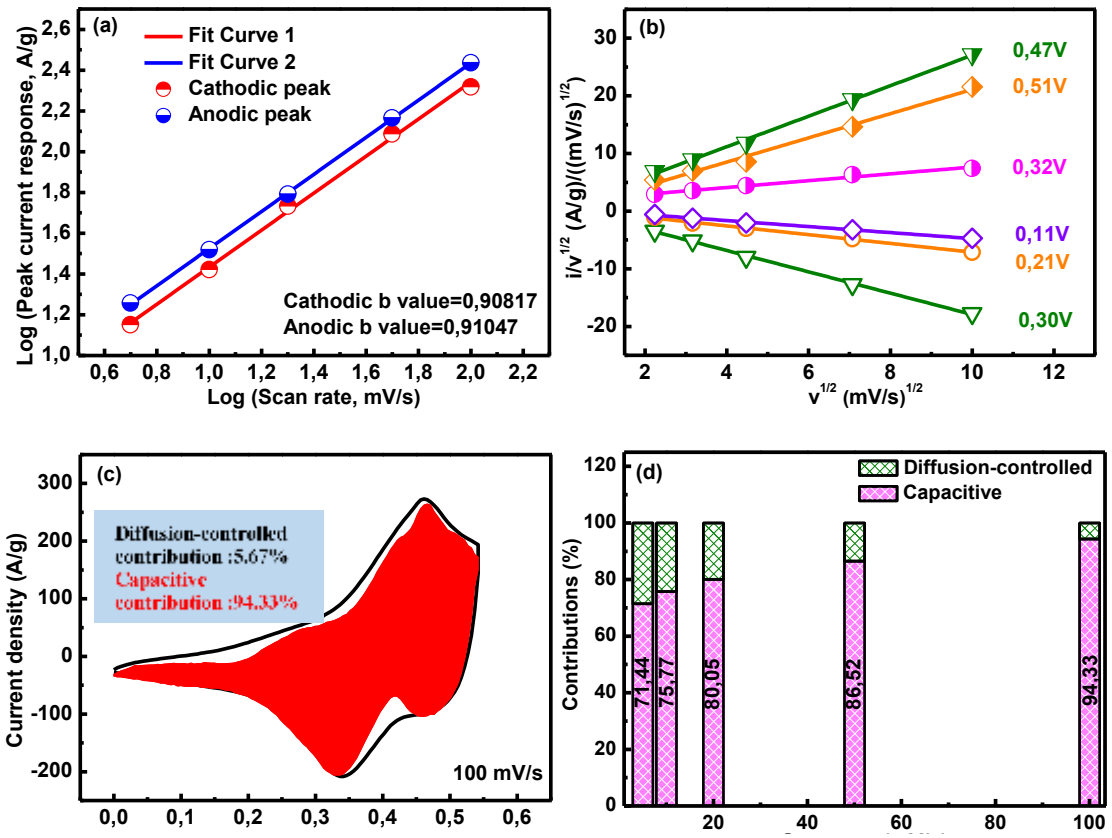

Figure 5.7: log (scan rate) - log (cathodic or anodic peak current response) of Sb: Cr: Co (1:3:4) electrode (a), fitting linear relationship between $i/v^{1/2}$ *vs.* $v^{1/2}$ used to calculate values of k_1 at different potentials (b), CV curves of the Sb: Cr: Co (1:3:4) electrode at a scan rate of 100 mV/s, the shaded area represents the capacitive contribution (c), the normalized contribution ratio of capacitive and diffusion-controlled charge storage of the Sb: Cr: Co (1:3:4) electrode at different scan rates (d).

Furthermore, the Trasatti analysis method is used to quantitatively estimate the contribution ratio based on equation **5-7** [40, 41]:

$$i(V) = k_1 v + k_2 v^{1/2} \qquad 5\text{-}7$$

Where $i(V)$, $k_1 v$, $k_2 v^{1/2}$ are the potential dependent current response (current density), capacitive and diffusion-controlled contributions, respectively.

It is feasible to obtain the contribution ratio of capacitive and diffusion-controlled process by determining the values of k_1 and k_2. The values of k_1 and k_2 could be calculated through fitting the linear relationship of $i(V)/ v^{1/2}$ *vs.* $v^{1/2}$ at various potentials (**Fig. 5.7b**) according to equation **5-8**:

$$i(V)/v^{1/2} = k_1 v^{1/2} + k_2 \quad 5\text{-}8$$

As presented in **Fig. 5.7c**, the shaded area in the CV curve represents the capacitive contribution from the surface-controlled process. It could be seen that capacitive contribution (shaded area with red color) occupies ~ 94.33% of the total charge storage at a scan rate of 100 mV/s. The contribution ratio of capacitive and diffusion-controlled processes of Sb: Cr: Co (1:3:4) electrode at different scan rates is depicted in **Fig. 5.7d**. The capacitive contribution increases with the increase of the scan rate to reach ~ 71.4% of the total charge storage at a scan rate of 5 mV/s, and ~ 94.33% at 100 mV/s. That is to say, the capacitive contribution from the surface-controlled process dominates the charge storage at various scan rates.

5.4 Electrochemical evaluation of PrGO//Sb: Cr: Co (1:3:4) hybrid supercapacitor

To further identify the potential application of the Sb: Cr: Co (1:3:4) electrode, a hybrid supercapacitor, including Sb: Cr: Co (1:3:4) as a positive electrode and PrGO [31] as a negative electrode, is assembled. Based on equations **1-5** and **1-6**, the charges of the positive and negative electrodes are balanced by equilibrating the mass ratio of the positive and negative electrodes.

A series of CV and GCD curves with increasing operation voltage window are performed to investigate the best operating voltage of the fabricated supercapacitor (**Fig.5.8a** and **b**). The operation voltage window is chosen as 1.5 V due to the obvious oxygen evolution as the operation voltage window is extended to 1.6 V.

Fig. 5.8c depicts the CV curves of PrGO//Sb: Cr: Co (1:3:4) hybrid supercapacitor at different scan rates ranging from 5 to 100 mV/s over the voltage window (0 to 1.5 V). CV curves display a relatively inactive region (0 to ~0.3 V) and an active region between ~ 0.3 to 1.5 V. Those two regions are assigned to the double layer capacitance and battery-type capacitive behavior. Initially, PrGO contributes to the relatively small double layer capacitance from 0 to ~0.3 V. When the operation voltage window reaches ~0.3 V, Sb: Cr: Co (1:3:4) starts to provide much more significant faradaic current to the supercapacitor. This results in a rapid increase of the current density in the CV curves. Furthermore, the shape of the CV curves is still maintained as the scan rate increases to 100 mV/s, indicating a good rate capability of the supercapacitor.

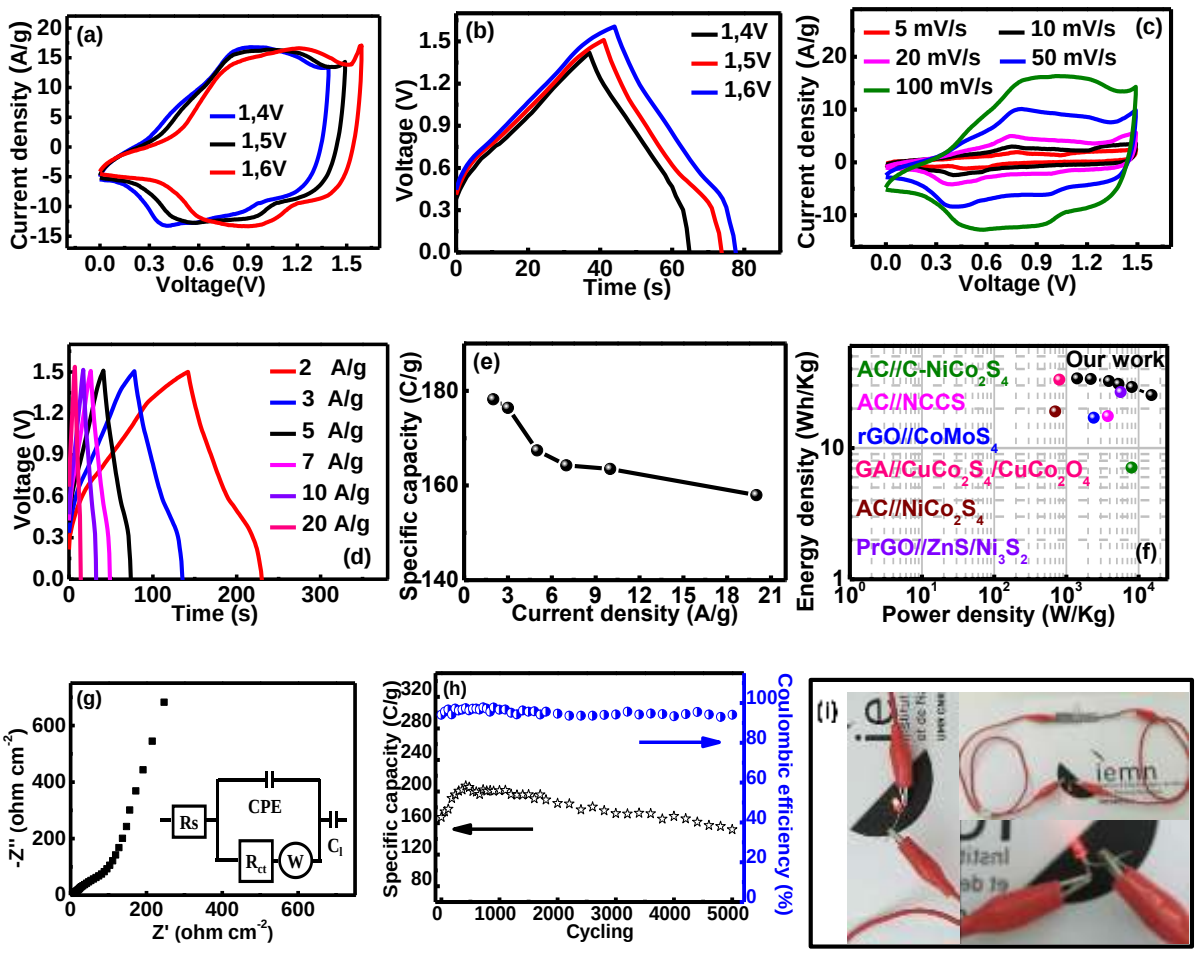

Figure 5.8: Electrochemical properties of the hybrid PrGO// Sb: Cr: Co(1:3:4) supercapacitor: (a) and (b) are the CV and GCD curves at different cell voltage values, respectively, (c) CV curves recorded at various scan rates, (d) GCD curves acquired at various current densities, (e) variation of the specific capacity *vs.* current density, (f) typical Ragone plot of the prepared supercapacitor, (g) Nyquist plot of the prepared supercapacitor, (h) cycling performance and coulombic efficiency of the fabricated supercapacitor at a current density of 5 A g^{-1}, (i) photographs of the red LED lighted up by two connected hybrid supercapacitors.

GCD curves of the fabricated hybrid supercapacitor are also investigated in a wide current density range from 2 to 20 A g^{-1} in the operation voltage window of 0 to 1.5 V (**Fig. 5.8d**). The fabricated supercapacitor delivers a maximum specific capacity of ~178 C g^{-1} at the active mass-normalized current density of 2 A g^{-1} (**Fig. 5.8e**).

The Ragone plot (E_d *vs.* P_d) of the fabricated supercapacitor, calculated based on the GCD curves (**Fig. 5.8d**) and equations **7-4** and **7-5**, is depicted in **Fig. 5.8f**. The fabricated supercapacitor exhibits a maximum energy density of 33.9 Wh kg^{-1} at a power density of 1.4 kW kg^{-1}, and the energy density can even reach 25.3 Wh kg^{-1} at a power density of 15.2 kW kg^{-}

[1]. Data of few typical examples reported recently in the literature are also given for comparison, such as active carbon (AC)//hetero-$NiCo_2S_4/Co_9S_8$ (NCCS) (17.5 Wh kg^{-1} at 3750 W kg^{-1}) [23], AC//$NiCo_2S_4$ (19 Wh kg^{-1} at 703 W kg^{-1}) [42], rGO//$CoMoS_4$ (17 Wh kg^{-1} at 2400 W kg^{-1}) [43], AC//C-$NiCo_2S_4$ (7.1 Wh kg^{-1} at 8 kW kg^{-1}) [44], graphene aerogel (GA)//$CuCo_2S_4/CuCo_2O_4$ (33.2 Wh kg^{-1} at 0.8 kW kg^{-1}) [45] and PrGO//ZnS/Ni_3S_2 (26.7 Wh kg^{-1} at 5659 W kg^{-1}) [46].

EIS is also performed for assessing the electrochemical nature of the processes occurring at the electrode/electrolyte interface of the fabricated supercapacitor. **Fig. 5.8g** displays the EIS curve and the equivalent circuit is depicted in the inset. Here, the simulated results show that the fabricated supercapacitor exhibits R_s of 3.10 ohm cm^{-2} and R_{ct} of 14.21 ohm cm^{-2}. The cycling performance and coulombic efficiency of the fabricated supercapacitor at 5 A g^{-1} for 5,000 charge-discharge cycles are also investigated (**Fig. 5.8h**). The retention of its capacity and coulombic efficiency are ~ 90.7% and 94.1%, respectively, indicating a good electrochemical stability and reversibility.

The practical application of the fabricated supercapacitor is further demonstrated (**Fig. 5.8i**). To achieve higher operation voltage, two fabricated supercapacitors are connected is series, and a red LED can be illuminated upon connection to fully charged supercapacitors.

5.5 Conclusion

In summary, a series of Sb: Cr: Co electrode materials are synthesized by controlling the initial mole ratio of Sb, Cr, and Co during the chemical precipitation process. Under synergistic effects of Sb, Cr, and Co, the Sb: Cr: Co (1:3:4) electrode exhibits a specific capacity of ~691 C g^{-1} at 2 A g^{-1} with excellent cycling stability (~ 96.6% of the maximum specific capacity is maintained at 20 A g^{-1} after 6,000 cycles) in 2M KOH aqueous electrolyte. Furthermore, a PrGO//Sb: Cr: Co (1:3:4) hybrid supercapacitor demonstrates good electrochemical performance within a voltage window of 1.5 V along with high energy of 33.9 Wh kg^{-1} at a power density of 1.4 kW kg^{-1}, and good cycling stability (~ 90.7 % of the maximum specific capacity over 5,000 cycles). Moreover, a red LED can be illuminated by two fabricated supercapacitors in series, demonstrating its practical application. The results obtained in the present work shows the potential for Sb: Cr: Co (1:3:4) electrode as a promising candidate for good performance energy storage devices.

5.6 References

[1] F. Luo, J. Li, H. Yuan, D. Xiao, Rapid Synthesis of Three-dimensional Flower-like Cobalt Sulfide Hierarchitectures by Microwave Assisted Heating Method for High-performance Supercapacitors, Electrochim. Acta 123 (2014) 183-189.

[2] H. Z. Wan, X. Ji, J. J. Jiang, J. W. Yu, L. Miao, L. Zhang, S. W. Bie, H. C. Chen, Y. J. Ruan, Hydrothermal Synthesis of Cobalt Sulfide Nanotubes: the Size Control and its Application in Supercapacitors, J. Power Sources 243 (2013) 396-402.

[3] D. B. Salunkhe, S. S. Gargote, D. P. Dubal, W. B. Kim, B. R. Sankapal, Sb_2S_3 Nanoparticles Through Solution Chemistry on Mesoporous TiO_2 for Solar Cell Application, Chem. Phys. Lett. 554 (2012) 150-154.

[4] W. Luo, X. Ao, Z. S. Li, L. Lv, J. G. Li, G. Hong, Q. H. Wu, C. D. Wang, Imbedding Ultrafine Sb_2S_3 Nanoparticles in Mesoporous Carbon Sphere for High-Performance Lithium-ion Battery, Electrochim. Acta 290 (2018) 185-192.

[5] S. S. Karade, K. Banerjee, S. Majumder, B. R. Sankapal, Novel Application of Non-aqueous Chemical Bath Deposited Sb_2S_3 Thin Films as Supercapacitive Electrode, Int. J. Hydrogen Energy 41 (2016) 21278-21285.

[6] H. J. Zhang, M. Ge, L. T. Yang, Z. Zhou, W. Chen, Q. Z. Li, L. Liu, Synthesis and Catalytic Properties of Sb_2S_3 Nanowire Bundles as Counter Electrodes for Dye-sensitized Solar Cells, J. Phys. Chem. 117 (2013) 10285-10290.

[7] Z. Yi, Q. Han, Y. Cheng, Y. Wu, L. Wang, Facile Synthesis of Symmetric Bundle-like Sb_2S_3 Micron-structures and their Application in Lithium-ion Battery Anodes, Chem. Commun. 52 (2016) 7691-7694.

[8] X. Y. Xu, J. Z. Wu, N. Yang, H. Y. Na, L. Z. Li, J. P. Gao, Cr_2O_3: a Novel Supercapacitor Electrode Material with High Capacitive Performance, Mater. Lett. 142 (2015) 172-175.

[9] A. L. P. James M. Mosby, Direct Electrodeposition of Cu_2Sb for Lithium-ion Battery Anodes, J. Am. Chem. Soc. 130 (2008) 10656–10661.

[10] S. Saadat, Y. Y. Tay, J. X. Zhu, P. F. Teh, S. Maleksaeedi, M. M. Shahjamali, M. Shakerzadeh, M. Srinivasan, B. Y. Tay, H. H. Hng, J. Ma, Q. Y. Yan, Template-free Electrochemical Deposition of Interconnected ZnSb Nanoflakes for Li-ion Battery Anodes, Chem. Mater. 23 (2011) 1032-1038.

[11] S. Dong, C. Li, X. Ge, Z. Li, X. Miao, L. Yin, ZnS-Sb_2S_3@C Core-double Shell Polyhedron Structure Derived from Metal-organic Framework as Anodes for High Performance Sodium Ion Batteries, ACS Nano 11 (2017) 6474-6482.

[12] K. Ramasamy, R. K. Gupta, S. Palchoudhury, S. Ivanov, A. Gupta, Layer-structured Copper Antimony Chalcogenides ($CuSbSe_xS_{2-x}$): Stable Electrode Materials for Supercapacitors, Chem. Mater. 27 (2014) 379-386.

[13] X. Yu, J. L. Yu, L. Hou, A. Gagnoud, Y. Fautrelle, Z. M. Ren, X. Li, Double-shelled Hollow Hetero-$MnCo_2S_4/CoS_{1.097}$ Spheres with Carbon Coating for Advanced Supercapacitors, J. Power Sources 408 (2018) 65-73.

[14] H. Lee, X. Wu, Q. Ye, X. Wu, X. Wang, Y. Zhao, L. Sun, Hierarchical $CoS_2/Ni_3S_2/CoNiO_x$ Nanorods with Favorable Stability at 1 A cm^{-2} for Electrocatalytic Water Oxidation, Chem. Commun. 55 (2019) 1564-1567.

[15] J. G. Hou, B. Zhang, Z. W. Li, S. Y. Cao, Y. Q. Sun, Y. Z. Wu, Z. M. Gao, L. C. Sun, Vertically Aligned Oxygenated-CoS_2–MoS_2 Heteronanosheet Architecture from Polyoxometalate for Efficient and Stable Overall Water Splitting, ACS Catal. 8 (2018) 4612-4621.

[16] Y. Zhu, L. F. Song, N. Song, M. X. Li, C. Wang, X. F. Lu, Bifunctional and Efficient CoS_2–C@MoS_2 Core–shell Nanofiber Electrocatalyst for Water Splitting, ACS Sustain. Chem. Eng. 7 (2019) 2899-2905.

[17] X. Li, J. Bai, B. Zhou, X. Yuan, X. Zhang, L. Liu, High Performance of 3D Symmetric Flowerlike Sb_2S_3 Nanostructures in Dye-sensitized Solar Cells, Chem. 24 (2018) 11444-11450.

[18] D. Vernekar, S. Ratha, C. Rode, D. Jagadeesan, Efficient Bifunctional Reactivity of K-doped CrO(OH) Nanosheets: Exploiting the Combined Role of Cr(iii) and Surface –OH Groups in Tandem Catalysis, Catal. Sci. Technol. 9 (2019) 1154-1164.

[19] M. Jin, S. Y. Lu, L. Ma, M. Y. Gan, Y. Lei, X. L. Zhang, G. Fu, P. S. Yang, M. F. Yan, Different Distribution of In-situ Thin Carbon Layer in Hollow Cobalt Sulfide Nanocages and their Application for Supercapacitors, J. Power Sources 341 (2017) 294-301.

[20] S. Peng, L. Li, H. Tan, R. Cai, W. Shi, C. Li, S. G. Mhaisalkar, M. Srinivasan, S. Ramakrishna, Q. Yan, MS_2(M = Co and Ni) Hollow Spheres with Tunable Interiors for High-Performance Supercapacitors and Photovoltaics, Adv. Funct. Mater. 24 (2014) 2155-2162.

[21] Z. Sun, M. Yuan, H. Yang, L. Lin, H. Jiang, S. Ge, H. Li, G. Sun, S. Ma, X. Yang, 3D Porous Amorphous Gamma-CrOOH on Ni Foam as Bifunctional Electrocatalyst for Overall Water Splitting, Inorg. Chem. 58 (2019) 4014-4018.

[22] M. C. Biesinger, B. P. Payne, A. P. Grosvenor, L. W. M. Lau, A. R. Gerson, R. S. C. Smart, Resolving Surface Chemical States in XPS Analysis of First Row Transition Metals, Oxides and Hydroxides: Cr, Mn, Fe, Co and Ni, Appl. Surf. Sci. 257 (2011) 2717-2730.

[23] L. Hou, Y. Shi, S. Zhu, M. Rehan, G. Pang, X. Zhang, C. Yuan, Hollow Mesoporous Hetero-$NiCo_2S_4/Co_9S_8$ Submicro-spindles: Unusual Formation and Excellent Pseudocapacitance towards Hybrid Supercapacitors, J. Mater. Chem. A 3 (2017) 133-144.

[24] X. Chen, D. Chen, X. Guo, R. Wang, H. Zhang, Facile Growth of Caterpillar-like $NiCo_2S_4$ Nanocrystal Arrays on Nickle Foam for High-Performance Supercapacitors, ACS Appl. Mater. Interfaces 9 (2017) 18774-18781.

[25] A. Farisabadi, M. Moradi, S. Borhani, S. Hajati, M. A. Kiani, S. A. Tayebifard, Synthesis and Electrochemical Properties of Mg-doped Chromium-based Metal Organic Framework/Reduced Graphene Oxide Composite for Supercapacitor Application, J. Mater. Sci-mater. El. 29 (2018) 8421-8430.

[26] Z. Gao, C. Chen, J. Chang, L. Chen, P. Wang, D. Wu, F. Xu, K. Jiang, Porous $Co_3S_4@Ni_3S_4$ Heterostructure Arrays Electrode with Vertical Electrons and Ions Channels for Efficient Hybrid Supercapacitor, Chem. Eng. J. 343 (2018) 572-582.

[27] X. J. Yang, H. M. Sun, P. Zan, L. J. Zhao, J. S. Lian, Growth of Vertically Aligned $Co_3S_4/CoMo_2S_4$ Ultrathin Nanosheets on Reduced Graphene Oxide as a High-performance Supercapacitor Electrode, J. Mater. Chem. A 4 (2016) 18857-18867.

[28] D. Jiang, H. Liang, W. Yang, Y. Liu, X. Cao, J. Zhang, C. Li, J. Liu, J. J. Gooding, Screen-printable Films of Graphene/CoS_2/Ni_3S_4 Composites for the Fabrication of Flexible and Arbitrary-shaped All-solid-state Hybrid Supercapacitors, Carbon 146 (2019) 557-567.

[29] M. Li, J. Cheng, F. Liu, X. Zhang, In Situ Growth of Nickel-cobalt Oxyhydroxide/oxide on Carbon Nanotubes for High Performance Supercapacitors, Electrochim. Acta 178 (2015) 439-446.

[30] M. F. Iqbal, H. Mahmood Ul, M. N. Ashiq, S. Iqbal, N. Bibi, B. Parveen, High Specific Capacitance and Energy Density of Synthesized Graphene Oxide based Hierarchical Al_2S_3 Nanorambutan for Supercapacitor Applications, Electrochim. Acta 246 (2017) 1097-1103.

[31] Y. Zhang, N. Cao, S. Szunerits, A. Addad, P. Roussel, R. Boukherroub, Fabrication of ZnCoS Nanomaterial for High Energy Flexible Asymmetric Supercapacitors, Chem. Eng. J. 374 (2019) 347-358.

[32] P. P. Xu, J. J. Liu, P. Yan, C. X. Miao, K. Ye, K. Cheng, J. Yin, D. X. Cao, K. F. Li, G. L. Wang, Preparation of Porous Cadmium Sulphide on Nickel Foam: a Novel Electrode Material with Excellent Supercapacitor Performance, J. Mater. Chem. A 4 (2016) 4920-4928.

[33] Y. C. Zhao, Z. X. Shi, H. Y. Li, C. A. Wang, Designing Pinecone-like and Hierarchical Manganese Cobalt Sulfides for Advanced Supercapacitor Electrodes, J. Mater. Chem. A 6 (2018) 12782-12793.

[34] B. Y. Guan, L. Yu, X. Wang, S. Song, X. W. Lou, Formation of Onion-like $NiCo_2S_4$ Particles via Sequential Ion-exchange for Hybrid Supercapacitors, Adv. Mater. 29 (2017) 1605051.

[35] X. Q. Lang, H. F. Zhang, X. Xue, C. L. Li, X. C. Sun, Z. T. Liu, H. S. Nan, X. Y. Hu, H. W. Tian, Rational Design of $La_{0.85}Sr_{0.15}MnO_3@NiCo_2O_4$ Core–shell Architecture Supported on Ni Foam for High Performance Supercapacitors, J. Power Sources 402 (2018) 213-220.

[36] T. Y. Wei, C. H. Chen, H. C. Chien, S. Y. Lu, C. C. Hu, A Cost-effective Supercapacitor Material of Ultrahigh Specific Capacitances: Spinel Nickel Cobaltite Aerogels from an Epoxide-driven Sol-gel Process, Adv. Mater. 22 (2010) 347-351.

[37] R. Li, S. L. Wang, Z. C. Huang, F. X. Lu, T. B. He, $NiCo_2S_4@Co(OH)_2$ Core-shell Nanotube Arrays in Situ Grown on Ni Foam for High Performances Asymmetric Supercapacitors, J. Power Sources 312 (2016) 156-164.

[38] B. Jiang, X. Ban, Q. Wang, K. Cheng, K. Zhu, K. Ye, G. Wang, D. Cao, J. Yan, Anionic P-substitution toward Ternary Ni–S–P Nanoparticles Immobilized Graphene with Ultrahigh Rate and Long Cycle Life for Hybrid Supercapacitors, J. Mater. Chem. A 7 (2019) 24374-24388.

[39] D. Chen, M. J. Lu, L. Li, D. Cai, J. Z. Li, J. M. Cao, W. Han, Hierarchical Core–shell Structural $NiMoO_4@NiS_2/MoS_2$ Nanowires Fabricated via an In Situ Sulfurization Method for High Performance Asymmetric Supercapacitors, J. Mater. Chem. A 7 (2019) 21759-21765.

[40] M. S. Javed, H. Lei, J. L. Li, Z. L. Wang, W. J. Mai, Construction of Highly Dispersed Mesoporous Bimetallic-sulfide Nanoparticles Locked in N-doped Graphitic Carbon

Nanosheets for High Energy Density Hybrid Flexible Pseudocapacitors, J. Mater. Chem. A 7 (2019) 17435-17445.

[41] M. S. Javed, H. Lei, H. U. Shah, S. Asim, R. Raza, W. J. Mai, Achieving High Rate and High Energy Density in an All-solid-state Flexible Asymmetric Pseudocapacitor through the Synergistic Design of Binder-Free 3D $ZnCo_2O_4$ Nano Polyhedra and 2D Layered Ti_3C_2Tx-MXenes, J. Mater. Chem. A 7 (2019) 24543-24556.

[42] Y. Li, F. F. An, H. R. Wu, S. M. Zhu, C. Y. Z. Lin, M. D. Xia, K. Xue, D. Zhang, K. Lian, A $NiCo_2S4$ /Hierarchical Porous Carbon for High Performance Asymmetrical Supercapacitor, J. Power Sources 427 (2019) 138-144.

[43] X. Xu, Y. Song, R. Xue, J. Zhou, J. Gao, F. Xing, Amorphous $CoMoS_4$ for a Valuable Energy Storage Material Candidate, Chem. Eng. J. 301 (2016) 266-275.

[44] S. G. Mohamed, I. Hussain, J. J. Shim, One-step Synthesis of Hollow C-$NiCo_2S_4$ Nanostructures for High-performance Supercapacitor Electrodes, Nanoscale 10 (2018) 6620-6628.

[45] X. W. Xu, Y. Liu, P. Dong, P. M. Ajayan, J. F. Shen, M. X. Ye, Mesostructured $CuCo_2S_4/CuCo_2O_4$ Nanoflowers as Advanced Electrodes for Asymmetric Supercapacitors, J. Power Sources 400 (2018) 96-103.

[46] Y. Zhang, N. Cao, M. Li, S. Szunerits, A. Addad, P. Roussel, R. Boukherroub, Self-template Synthesis of ZnS/Ni_3S_2 as Advanced Electrode Material for Hybrid Supercapacitors, Electrochim. Acta 328 (2019) 135065.

CHAPTER 5 PREPARATION OF PVP-ASSISTED $Sb_2S_3/CoS_2/CrOOH$ COMPOSITE WITH ENCHANCED ELECTROCHEMICAL PERFORMANCE FOR HYBRID SUPERCAPACITORS

CHAPTER 6. CONCLUSION AND PERSPECTIVES

Electrochemical supercapacitors (ESs), as convenient electrochemical energy storage devices, are believed to be one of the promising candidates for energy storage, owing to their larger specific capacitance/capacity compared to traditional capacitors, high power storage capability, and much higher charging/discharging rate capability efficiency than primary/secondary batteries, and so on. However, the disadvantages of ESs, including low energy density (E_d) and high production cost, have been identified as major challenges for the further development of ESs technologies. In the past years, specific attention was paid to improve E_d value. It is well-established that E_d predominantly depends on electrode materials, the configuration, and electrolyte of ESs. In addition, the combination of two different storage mechanisms together is expected to offer enhanced performance such as high E_d, P_d, and good cycling stability.

In this thesis, specific attention is currently devoted to the development of two types of electrode materials with improved performance. We have synthesized different types of electrode materials, including negative electrode materials (rGO, PrGO) and positive electrode materials (CoS, CoS/carbonaceous (rGO or PF-9), ZnS, ZnCoS, ZnS/Ni_3S_2, Sb_2S_3, CoS_2, CrOOH, Sb_2S_3/CoS_2/CrOOH). As-prepared materials in this work are used for the investigation of their electrochemical performance and the possibility for practical applications.

In the case of negative electrode materials (rGO, PrGO), the porous structure of PrGO, obtained through pre-oxidation of GO before the reduction process, allows convenient pathways for the transportation of ions and electrons between the active material and electrolyte and provides efficient and fast ion diffusion. Therefore, the PrGO electrode achieved a much higher specific capacitance value (~271 F g^{-1} at 0.5 A g^{-1}), compared with that of rGO (~62 F g^{-1} at 0.5 A g^{-1}) electrode and PF-9 (~75 F g^{-1} at 0.5 A g^{-1}).

In the case of positive electrode materials, composites, and multi-metal compounds ((CoS, CoS/carbonaceous (rGO or PF-9), ZnS, ZnCoS, ZnS/Ni_3S_2, Sb_2S_3, CoS_2, CrOOH, Sb_2S_3/CoS_2/CrOOH)) were prepared and their electrochemical performance was investigated, respectively. Among them, CoS/ carbonaceous (rGO, PF-9) composite materials displayed an enhanced specific capacity (~275 C g^{-1} at 0.5 A g^{-1} for CoS/PF-9, ~243 C g^{-1} at 0.5 A g^{-1} for CoS/rGO), as compared to CoS (~161 C g^{-1} at 0.5 A g^{-1}). Furthermore, bi-metal sulfides (ZnCoS, ZnS/Ni_3S_2) were synthesized and their electrochemical performance was assessed, respectively. The fabricated bi-metal sulfides electrodes exhibit remarkable electrochemical performance

(~624 C g^{-1} at 1 A g^{-1} for ZnCoS, ~890 C g^{-1} at 1 A g^{-1} for ZnS/Ni_3S_2), as compared to ZnS (~85 C g^{-1} at 0.5 A g^{-1}). Moreover, composites of bi-metal sulfides and metal oxyhydroxide ($Sb_2S_3/CoS_2/CrOOH$) were prepared and their electrochemical characteristics were evaluated. The $Sb_2S_3/CoS_2/CrOOH$ electrode achieved an improved specific capacity (~691 C g^{-1} at 2 A g^{-1}), which was much higher than that of Sb: Cr: Co (1:0:0) (~61 C g^{-1}), Sb: Cr: Co (0:1:0) (~69 C g^{-1}), and Sb: Cr: Co (0:0:1) (~203 C g^{-1}). Furthermore, supercapacitor cells of PF-9//CoS, PrGO//ZnCoS, PrGO//ZnS/Ni_3S_2, PrGO// $Sb_2S_3/CoS_2/CrOOH$ were assembled and achieved maximum E_d values of 7.6, 17.7, 30.6 and 33.9 W h kg^{-1}, respectively. These findings represent an important advancement in the utilization of bi-metal sulfides for applications in the field of ESs.

More work still remains to be done in improving the electrochemical performance and facilitating the practical applications of ESs. Considering the practical applications, specific focus should be both on the exploration of suitable electrolytes with low production cost and the development of advanced electrode materials. Regarding the exploration of advanced electrolytes, the limited voltage window provided by aqueous electrolytes and high production costs of organic electrolytes or ionic liquid electrolytes calls for the search for an electrolyte with an extended voltage window that can be produced at low cost.

Based on recently reported results, the use of super-concentrated solutions, such as water-in-salt electrolytes, could be a promising approach to address the issue of limited energy densities of aqueous-based capacitors. In water-in-salt electrolytes, the amount of salt is greater than water, which reduces the kinetics of water splitting reactions and allows for the widening of the cell voltage window. Therefore, the development of advanced electrolytes, especially super-concentrated solutions, could be the most promising approach to obtain a widened voltage window.

With respect to the development of advanced electrode materials, lots of efforts still need to be made to obtain electrode materials with excellent electrochemical performance. Taking nanostructured transition metal compounds as an example, owing to the faradic redox behavior, they have the ability to provide high specific capacitance. However, their agglomeration and poor electrical conductivity significantly limit their electrochemical performance, especially with respect to life cycle and resistance. The results obtained from our work indicate that the construction of composite materials (mono-metal sulfide/carbonaceous, bi-metal sulfides, and bi-metal sulfides/metal oxy-hydroxide) could be a promising approach to improve the electrochemical performance and thus address the issue of agglomeration and poor electrical conductivity. Therefore, the design of multi-metal compounds such as multi-metal sulfides/

oxides (hydroxides), could be an interesting strategy to obtain enhanced electrochemical performance.

Based on the obtained results and published reports, the development of advanced electrode materials and the exploration of suitable electrolytes with large working voltage and low production costs will bring remarkable advances for their application in the field of ESs.

APPENDIX

EXPERIMENTAL SECTION

7.1 Materials

All chemicals are reagent grade or higher and are used as received unless otherwise specified. Graphite power (<20 micrometers), sulfuric acid (H_2SO_4), sodium nitrate ($NaNO_3$), potassium permanganate ($KMNO_4$), hydrazine monohydrate ($NH_2NH_2\times H_2O$), ammonia solution ($NH_3\bullet H_2O$), hydrochloric acid (HCl), hydrogen peroxide (H_2O_2), cobalt dichloride hexahydrate ($CoCl_2\bullet 6H_2O$), zinc acetate dihydrate ($Zn(CH_3COO)_2\bullet 2H_2O$, nickel chloride hexahydrate ($NiCl_2\bullet 6H_2O$), antimony trichloride ($SbCl_3$), chromium nitrate nonahydrate ($Cr(NO_3)_3\ 9H_2O$), cobaltous nitrate hexahydrate ($Co(NO_3)_2\ 6H_2O$), ethylene glycol (EG), thioacetamide (TAA), ethanol (CH_3CH_2OH), 3,4-ethylenedioxythiophene (EDOT), cetyltrimethylammonium bromide (CTAB), ammonium persulfate ($(NH_4)_2S_2O_8$), iron chloride hexahydrate ($FeCl_3\ 6H_2O$), potassium hydroxide (KOH), poly(N-vinylpyrrolidone) (PVP), N-methyl-2-pyrrolidone (NMP) and polyvinylidene fluoride (PVDF) were purchased from Sigma–Aldrich.

Nickel foam is obtained from MTI Corporation, China.

Hg/HgO reference electrode and platinum counter electrode were obtained from China.

The water used throughout the experiments in this thesis is purified with a Milli-Q system from Millipore Co. (resistivity=18 MΩ.cm)

7.2 Preparation of working electrode

All materials prepared in this manuscript are powders, and all active materials are coated on the surface of nickel foam substrate.

The working electrodes are prepared as following:

① The active electrode material and carbon black (conducting agent) were mixed at a mass ratio of 7:2;

② Prepare a homogeneous mixture (active material, carbon black and ethanol) by sonication for 1 h;

③ Dry the above solution in the oven (80℃);

④ A certain amount of polyvinylidene difluoride (PVDF) is dissolved in N-methyl-2-pyrrolidone (NMP) solution; the measured amount of PVDF (A mg) and volume of NMP (B ml) should be recorded for the following calculation;

⑤ Calculate the mass of dried mixture (active material and carbon black), record the value (C mg) and collect the mixture for further use;

⑥ Certain volume in ml of PVDF/NMP (C*B/(9*A)) is taken (B value should be larger than that of C*B/(9*A) value). Make sure the mass ratio of the mixture (active material and carbon black) and PVDF is 9:1.

⑦ A slurry is obtained by manual grinding the mixture of active material and carbon black (C mg) and PVDF/NMP (C*B/(9*A) ml) in a mortar. The slurry should not be too thin or too thick.

⑧ As-prepared slurry is coated on the surface of several pieces of 1*1.5 cm^2 nickel foam. The coated area is 1*1 cm^2.

⑨ Nickel foam coated with slurry is dried in the oven (80℃ overnight).

⑩ The coated nickel foam is chosen to test the electrochemical performance and the corresponding mass of the slurry should also be recorded.

⑪ For other samples, to compare the electrochemical performance (ex. CoS, CoS/rGO, and CoS/PF-9), the nickel foam with similar coated value (around 1 mg/cm^2) should be chosen

7.3 Instrumentation

7.3.1 X-ray diffraction (XRD)

The crystal structure of the synthesized nanomaterials was investigated by powder X-ray diffraction analysis. XRD patterns were recorded using Rigaku X-ray diffractometer (Model: ULTIMA IV, Rigaku, Japan) with a scanning rate of 3 °min^{-1} and 2θ value ranging from 10 to 80 °using Cu Kα (α= 1.54056 Å) as the X-ray source and operated at a generator voltage of 40 kV and a current of 40 mA.

7.3.2 X-ray photoelectron spectroscopy (XPS)

X-ray photoelectron spectroscopy experiments were performed on a PHI 5000 VersaProbe-Scanning ESCA Microprobe (ULVAC-PHI, Japan/USA) instrument at a base pressure below 5×10^{-9} mbar. Monochromatic AlK_α radiation was used and the X-ray beam, focused to a diameter of 100 μm, was scanned on a 250 × 250 μm surface, at an operating power of 25 W (15 kV). Photoelectron survey spectra were acquired using a hemispherical analyzer at pass energy of 117.4 eV with a 0.4 eV energy step. Core-level spectra were acquired at pass energy of 23.5 eV with a 0.1 eV energy step. All spectra were recorded with 90 °between X-ray source and analyzer and with the use of low energy electrons and low energy argon ions for charge neutralization. After subtraction of the linear-type background, the core-level spectra were decomposed into their components with mixed Gaussian-Lorentzian (30:70) shape lines using the CasaXPS software. Quantification calculations were performed using sensitivity factors supplied by PHI.

7.3.3 Raman spectroscopy

Micro-Raman spectroscopy measurements were performed on a Horiba Jobin Yvon LabRam HR Micro-Raman system combined with a 473-nm laser diode as excitation source. Visible light was focused by a 100× objective. The scattered light was collected by the same objective in backscattering configuration, dispersed by a 1800-mm focal length monochromator and detected by a CCD.

Samples were prepared by casting 50 μL aqueous or ethanol suspension of PF-9 or CoS/PF-9 composite on a clean silicon wafer or ITO surface followed by drying in an oven at 80 °C to remove the solvent.

7.3.4 Scanning electron microscopy (SEM)

SEM images were obtained using an electron microscope ULTRA55 (Zeiss) equipped with a thermal field emission emitter and three different detectors (EsB detector with filter grid, high-efficiency In-lens SE detector, Everhart–Thornley secondary electron detector).

7.3.5 Inductively coupled plasma atomic emission spectroscopy (ICP-AES)

The amount of cobalt and zinc in prepared (Zn: Co)S samples was determined with a Varian (liberty II axial view) inductively coupled plasma–atomic emission spectrometer (ICP–AES); the wavelength and detection limit for cobalt were 228.616 nm and 7 μg L^{-1}, respectively; and

the wavelength and detection limit for zinc were 213.856 nm and 2 μg L^{-1}, respectively. The spectrometer was equipped with a pneumatic V-groove nebulizer and Sturmun–Master inert PTFE spray chamber. Sample solutions were driven through columns of resin by means of a multi-channel Gilson peri-staltic pump equipped with 2.28 mm i.d. tubing. Teflon tubing, polyethylene bottles, and a pH meter (WTW) with glass electrode were also used.

7.3.6 Brunauer-Emmett-Teller (BET)

For the BET specific surface area (SSA) analyses, low-pressure volumetric gas adsorption measurements were recorded at 77 K and maintained by a liquid-nitrogen bath on a Quantachrome Quadrasorb automatic volumetric instrument. The pore diameter distribution was calculated by using the Barrett-Joyner-Halenda (BJH) model.

7.3.7 Transmission electron microscopy (TEM)

TEM images were recorded on a FEI, TECNAI G2 F20 instrument. Samples were prepared by dispersing the material in ethanol (0.2 mg mL^{-1}) and then 5 μL of this solution was drop coated on a 200 mesh Cu grid for the high-resolution transmission electron microscopy (HR-TEM) analysis.

7.3.8 Electrochemical measurements

The supercapacitor performance of prepared electrode materials was investigated using a three-electrode system consisting of prepared electrode materials as the working electrode, Hg/HgO as the reference electrode, and platinum foil as the counter electrode. 2M KOH was used as the electrolyte. The cyclic voltammetry (CV) tests were performed using the ModuLab-MTS electrochemical Test Station (Solartron, France). The Galvanostatic charge/discharge (GCD) and electrochemical impedance spectroscopy (EIS) measurements were acquired with an Autolab Galvanostat-Potentiostat instrument between 10 kHz and 0.01 Hz. To ensure that the tested electrodes are completely wetted, each electrode is pre-cycled in the chosen electrolyte through CV tests for hundreds of cycles.

7.3.8.1 Three-electrode system

The specific capacity (*C*) was calculated by integrating the area under the CV curves using the following equation:

$$C = \frac{1}{2Mv}\int_{V_L}^{V_U} I(V)dV \quad 7\text{-}1$$

M is the mass of active material (g), *v* is the scan rate (V s^{-1}), V_U and V_L are the upper and lower voltage limits (V), and *I* is the current (A).

The specific capacitance (*C*) was determined by integrating the area under the CV curves using the following equation:

$$C = \frac{1}{2Mv(V_U - V_L)}\int_{V_L}^{V_U} I(V)dV \quad 7\text{-}2$$

M is the mass of active material (g), *v* is the scan rate (V s^{-1}), V_U and V_L are the upper and lower voltage limits (V), and *I* is the current (A).

The specific capacitance (*C*) was in addition calculated from the GCD curves using the following equation:

$$C = \frac{I\Delta t}{M\Delta v} \quad 7\text{-}3$$

Where *I/M* stands for the current density (A g^{-1}), Δt and Δv is the time and potential of the discharge curve in the GCD curves.

7.3.8.2 Two electrode system

The energy density (E_d) and power density (P_d) are also two important parameters to check the performance of supercapacitors. The values of E and P of the fabricated ASC cells were calculated by the following equations:

$$E_d = \frac{I\int V(t)dt}{3.6M} \quad 7\text{-}4$$

E_d stands for energy density (Wh kg^{-1}), *I/M* is the current density applied to the two electrode system (A g^{-1}), is the integral area of the discharging curve.

$$P_d = \frac{3600E_d}{t} \quad 7\text{-}5$$

P_d stands for power density (W kg^{-1}), E_d stands for energy density (Wh kg^{-1}), *t* stands for the discharging time of the GCD curves (s).

PUBLICATIONS

[1] **Yuan Zhang**, Ning Cao, Sabine Szunerits, Ahemd Addad, Pascal Roussel, Rabah Boukherroub, Fabrication of ZnCoS nanomaterial for high energy flexible asymmetric supercapacitor, *Chemical Engineering Journal*, 374 (2019), 347-358; IF: 8.355

[2] **Yuan Zhang**, Ning Cao, Min Li, Sabine Szunerits, Ahmed Addad, Pascal Roussel, and Rabah Boukherroub, Self-template synthesis of ZnS/Ni_3S_2 as advanced electrode material for hybrid supercapacitors, *Electrochimica Acta*, 328 (2019), 135065; IF: 5.383

[3] Liuqing Pang, Alexandre Barras, **Yuan Zhang**, Mohammed A. Amin, Ahmed Addad, Sabine Szunerits, Rabah Boukherroub, CoO Promoted the Catalytic Activity of Nitrogen-doped MoS_2 Supported on Carbon Fibers for Overal Water Splitting, *ACS Applied Materials & Interfaces*, 11 (2019), 31889-31898; IF: 8.456